2016

Design, Synthesis and Biological Applications of Polypeptoids and Boron Dipyrromethenes

Sunting Xuan
Louisiana State University and Agricultural and Mechanical College, sxuan1@lsu.edu

DESIGN, SYNTHESIS AND BIOLOGICAL APPLICATIONS OF POLYPEPTOIDS AND BORON DIPYRROMETHENES

A Dissertation

Submitted to the Graduate Faculty of the
Louisiana State University and
Agricultural and Mechanical College
in partial fulfillment of the
requirements for the degree of
Doctor of Philosophy

in

The Department of Chemistry

by
Sunting Xuan
B.S., Lanzhou University, 2010
December 2016

ACKNOWLEDGMENTS

I would like to thank my advisor, Prof. Donghui Zhang and Prof. M. Graça H. Vicente for giving me the opportunity to work in their group and for their supervision, encouragement and inspiration during my time at LSU. I would also like to thank my advisory committees, Prof. John Pojman, Prof. Lynne Baggett and Prof. Jennifer Sones for their time and assistance. I would like to thank Prof. Kevin Smith for his suggestion and guidance on the organic synthesis. I would also thank my lab colleagues, Dr. Li Guo, Dr. Brandon Chan, Dr. Jinbao Cao, Ang Li, Albert Chao, Jessica Simpson, Garrett Sternhagen, Zhaoyuan Liu, Dr. Xin Li, Tianyi Yu, David Slefker, Haijun Wang, Jamie Hayes, Daniel LaMaster, Tryslai Williams, Elizabeth Okaoth, Qianli Meng, Maodie Wang, Alex Nguyen and Ning Zhao for their camaraderie and discussions during my PhD years.

I would like to thank Dr. Rafeal Cueto for all the help on DSC, TGA, DLS, and SEC experiments, and Dr. Frank Fronczek for all the help on X-ray analysis. Many thanks are also to my collaborators, Prof. Daniel Hayes, Prof Vijay John, Yueheng Zhang, Cong Chen and Nick Poche. I really enjoying the time working with them.

There are not enough words in me to express how grateful I am to my wonderful parents, my amazing brother, my cute son, and my considerate husband. They are the ones who care about me the most in this world. To my husband, Ning Zhao, your daily encouragement and belief in me gave me the strength to carry on to the next day. Thank you so much for supporting me to pursue my goals.

Thank you to all the amazing people in my PhD time for all of your support, encouragement, and friendship. Without all of you, the dissertation could not have been achieved.

TABLE OF CONTENTS

LIST OF TABLES

LIST OF SCHEMES

LIST OF FIGURES

TABLE OF ABBREVIATIONS

cryo-TEM	cryogenic transmission electron microscopy
DLS	dynamic light scattering
DP_n	(number average) degree of polymerization
DRI	differential refractive index
DSC	differential scanning calorimetry
DCM	dichloromethane
DDQ	2,3-dichloro-5,6-dicyanobenzoquione
DMSO	dimethyl suldoxide
ESI-MS	electrospry ionization mass spectrometry
G’	dynamic storage modulus
G’’	dynamic loss modulus
HRMS	high resolution mass spectrometry
MALDI	matrix-assisted laser desorption/ionization
NMR	nuclear magnetic resonance
PDT	photodynamic therapy
UV-Vis	ultra violet-visible

ABSTRACT

The dissertation is about the design, synthesis and biological applications of polypeptoids and boron dipyrromethenes (BODIPYs). The dissertation is divided into seven chapters reporting various aspects of the background to my field of study and the results obtained during my PhD program.

Chapter 1 is a concise overview of the fundamental concepts of polypeptoids and hydrogels, as well as their recent developments on synthetic strategies, property investigations, and biological applications in different fields.

Chapter 2 presents the design, synthesis and potential application as tissue engineering scaffold of thermoreversible ABC polypeptoid hydrogels. A series of ABC copolypeptoids were synthesized and their gelation behavior were investigated in water and biological media. The potential use of the hydrogel as tissue engineering scaffold to induce chondrogenesis of human stem cells was also investigated.

Chapter 3 describes the synthesis and characterization of a series of highly water soluble PEGylated polypeptoids bearing oligomeric ethylene glycol side chains. Their potential use as antifouling material was investigated.

Chapter 4 reports the solution self-assembly of coil-crystalline diblock copolypeptoids (PNMG-b-PNDG). The relationship between polymer compositions and micelle morphologies was investigated.

Chapter 5 is a brief introduction of BNCT and a concise overview of BODIPYs on their synthetic methodologies, functionalization strategies, and potential applications.

Chapter 6 describes the design, synthesis and in vitro biological studies of a series of carborane-containing BODIPYs. Their ability to cross the BBB was investigated.

Chapter 7 reports the design and synthesis of a series of push-pull BODIPYs. Their spectroscopic and electrochemical properties were investigated by UV-Vis and fluorescence spectroscopy, cyclic voltammetry and DFT calculation.

CHAPTER 1 : INTRODUCTION TO POLYPEPTOIDS AND HYDROGELS

1.1 Introduction to polypeptoids

Polypeptoids, composed of *N*-substituted polyglycine backbones, are structural mimics of polypeptides (Figure 1.1). The polypeptoids are highly structural tunable by tailoring the side chain groups, enabling manipulation over their hydrophilicity and lipophilicity balance (HLB), conformation[1-12], charge characteristics,[13-14] thermal and crystallization properties.[15] In contrast to polypeptides, polypeptoids with the nitrogen being substituted, lack hydrogen bonding interactions and chiral centers along the backbones. Thus, the conformation (*e.g.*, random coils, helix[1-4, 11-12] and β-sheets[5-10]) of polypeptoids is strongly dependent on the backbone rigidity, steric, chirality, and electrostatic characteristics of the side chains, in contrast to the polypeptides whose secondary structure is stabilized by hydrogen bonding. The polypeptoids are thermally processable similar to conventional thermoplastics due to the absence of hydrogen bonding on their backbones, whereas polypeptides undergo thermal degradation before they can be melt-processed due to the extensive hydrogen bonding interactions.[15] In addition, studies of polypeptoids showed their enhanced proteolytic stability relative to polypeptides[16-17], good cytocompatibility[18-19] and degradability under oxidative conditions that mimics tissue inflammation[20]. These combined attributes render polypeptoids an attractive material for biomedical and biotechnological applications. Recent development in the organo-mediated controlled polymerization has enabled access to a variety of well-defined polypeptoid homo and block copolymers. The synthetic methods, structural-property relationship of polypeptoids as well as their potential applications in different fields such as in biotechnological area are under investigation and some related reviews have been published.[15, 21-28]

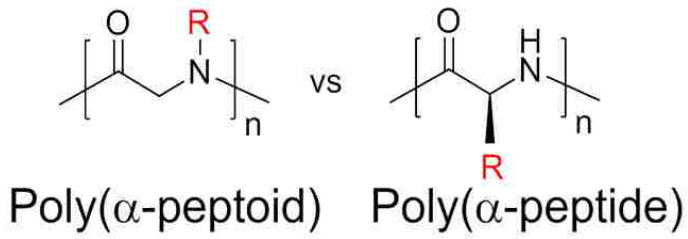

Figure 1.1. Structure of polypeptoids and polypeptides.

1.2 Synthesis of R-NCAs and polypeptoids

1.2.1 Synthesis of *N*-substituted *N*-carboxyanhydride (R-NCA) monomers

A library of *N*-substituted *N*-carboxyanhydride (R-NCA) monomers bearing various side chain structures (*e.g.*, R= methyl, ethyl, allyl etc., Figure 1.2) have been synthesized using two general routes from the *N*-substituted glycine precursors which are obtained from the reaction between primary amine and glyoxylic acid or between ethyl bromoacetate and primary amine (Scheme 1.1). [15, 29-32] The precursor (**1**) is treated with di-*tert*-butyl dicarbonate or chloroformate to obtain the corresponding alkoxycarbonyl protected *N*-substituted glycine (**2**) followed by cyclization to afford the R-NCAs using activating electrophiles (*e.g.*, PCl_3, PBr_3, $SOCl_2$ and $AcCl/Ac_2O$).

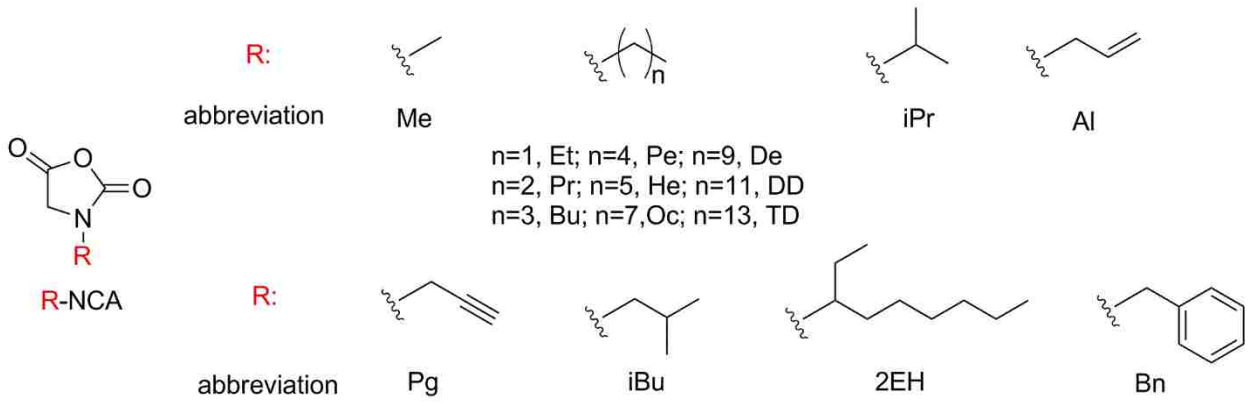

Figure 1.2. Representative chemical structures of *N*-substituted NCA (R-NCA) monomers.

Scheme 1.1. Synthetic procedures of R-NCAs.

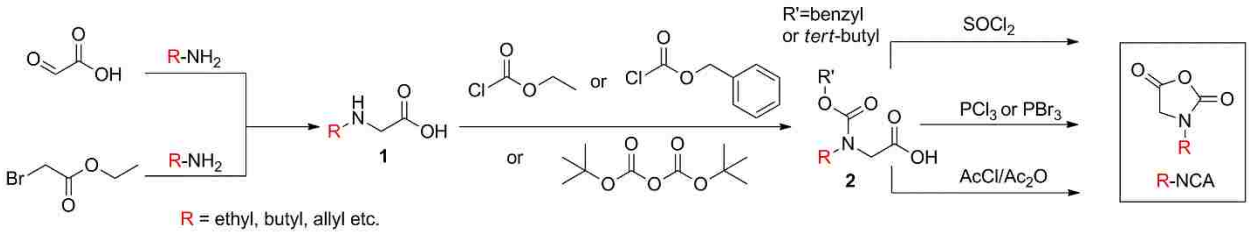

1.2.2 Ring-opening polymerizations of R-NCAs using primary amine initiators

Primary amines are good nucleophiles for the controlled ring-opening polymerization (ROP) of R-NCAs to produce polypeptoids bearing amide end group and secondary amino living chain ends by releasing CO_2 during polymerizations (Scheme 1.2).[15] The nucleophilic ROP mechanism has been extensively studied for the primary amine-initiated ROPs of amino acid-derived NCAs.[33] The primary amine-initiated ROPs have been widely investigated on a variety of R-NCAs. The *N*-methyl-*N*-carboxyanhyride (Me-NCA) was shown to polymerize in a controlled manner without chain transfer or termination events after more than 10 iterative polymerization steps (a.k.a., living polymerization) using benzyl amine as the initiator.[34] The produced polysarcosine (PNMG) analyzed by SEC chromatography, NMR and MALDI-TOF spectroscopy exhibited narrow Poisson distribution (PDI<1.1-1.3) and controllable molecular weight by simply changing the initial monomer to initiator feed ratios. The living chain end of PNMG was further supported by the chain extension experiment with different monomers (*e.g.*, Et-NCA, Pr-NCA, Bu-NCA and Pe-NCA). The living polymerization character of other monomers (*e.g.*, Et-NCA, Pr-NCA, Bu-NCA) was also reported.[29-30] The polymerization behavior of R-NCAs is highly related to their side chain structures. It was shown that iPr-NCA could not (or very slowly) be polymerized in benzylnitrile at room temperature under reduced pressure probably due to the steric hindrance of the relatively bulky propagating species that decrease the statistical probability of the nucleophilic attack at the C5 position of the monomer.[30] Polymerization of monomer in neat above

its melting temperature was attempt, however, the low MW polymer (16 mer) exhibited broad distribution (PDI=1.53). As to *N*-allyl NCA (Al-NCA)[35] and N-2-phenylethyl NCA (2PE-NCA)[12], the chain lengths of the resulting polypeptoids were limited (DP_n<100) probably due to the formation of the corresponding 2,5-diketopiperazine from the intramolecular transamidation that was kinetically competitive relative to the chain propagation.

Scheme 1.2. Mechanism of the primary amine-initiated ROP of R-NCA.

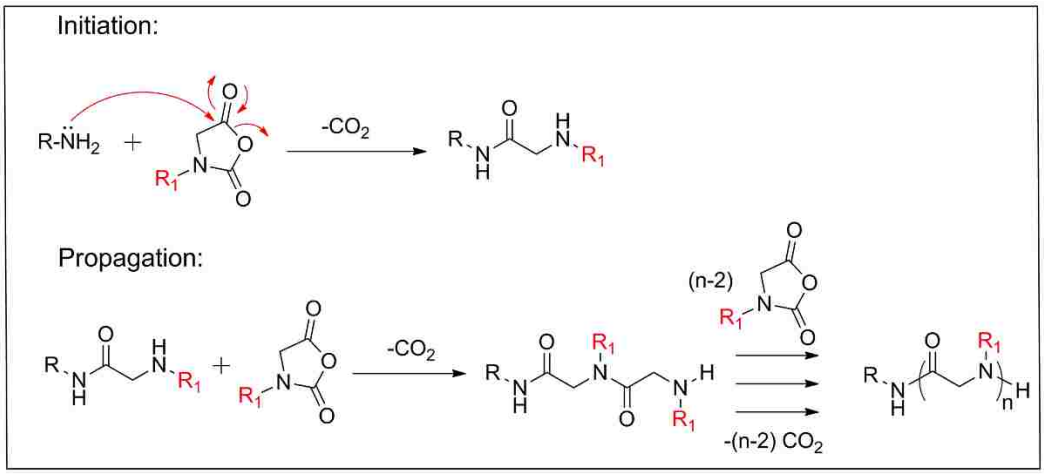

1.2.3 Ring-opening polymerizations of R-NCA using alcohol initiators and 1,1,3,3-tetramethylguanidine

Recently, it was reported that *N*-butyl *N*-carboxyanhydride (Bu-NCA) can be polymerized in low dielectric THF using benzyl alcohol initiator and catalytic amount of 1,1,3,3,-tetramethylguanidine (TMG) promoter to produce poly (*N*-butyl glycine) (PNBG) with controlled molecular weight and narrow molecular weight distribution (PDI=1.04-1.08) by adjusting the initial monomer to initiator ratios.[36] The alcohol alone, however, does not initiate the polymerization of Bu-NCA under the same condition. The proposed mechanism was that the TMG formed a hydrogen bonding complex with the alcohol, which enhanced the nucleophilicity of the alcohols to facilitate the nucleophilic attack of the alcohol to the monomer (Scheme 1.3). The polymerization activities and M_n control are strongly dependent on the steric and electronic

properties of the alcohols. Primary alcohols (*e.g.*, methanol, ethanol, 2-methoxyethanol, propanol and benzyl alcohol) with the presence of TMG promoter can polymerize the Bu-NCA with good to moderate control over M_n and PDI. The resulting PNBG polymers were mainly end-capped with the alcohol initiators, as evidenced by MALDI-TOF spectroscopic analysis. In contrast, the use of more sterically hindered secondary alcohol (*e.g.*, isopropyl alcohol) with the presence of TMG produced PNBG polymers whose M_n were much higher than the theoretically predicated values. Interestingly, no polymerization was observed at different monomer to initiator ratios when using the even more sterically hindered *tert*-butyl alcohol. The polymerization using more electron deficient alcohols with lower pK_a s (*e.g.*, 2,2,2-trifluoroethanol and phenol) were also investigated. It turned out that using 2,2,2-trifluoroethanol in conjugation with TMG lead to PNBG polymers of much higher M_ns relative to the theoretical values, whereas using phenol with TMG yielded no polymerization regardless of the initial monomer to alcohol ratios. The significant deviation of M_ns from the theoretical values suggested that the initiation was much slower relative to the propagation due to significantly reduced nucleophilicity of the alcohol moiety in the hydrogen bonding complexes. The control of polymerization over M_ns was also strongly dependent on the solvent used. In contrast to the polymerization in THF and toluene, polymerization in more polar solvent (*e.g.*, CH_2Cl_2 and DMF) was much less controllable showing comparable M_ns regardless of the initial monomer to alcohol ratios.

1.2.4 Synthesis of cyclic polypeptoids

Cyclic polypeptoids [*i.e.*, poly(*N*-butyl glycine)] were synthesized using *N*-heterocyclic carbenes (NHCs)-mediated zwitterionic ring-opening polymerization (ZROP) of Bu-NCA.[31, 37] The polymer MW and ring size can be easily tuned by controlling the initial monomer to NHC ratios in low dielectric solvents such as THF and toluene. The polymerization was mediated by a zwitterionic propagating intermediate with two proximate oppositely charged chain ends through electrostatic inte-

Scheme 1.3. Mechanism of ROH-initiated ROP with TMG promoter.

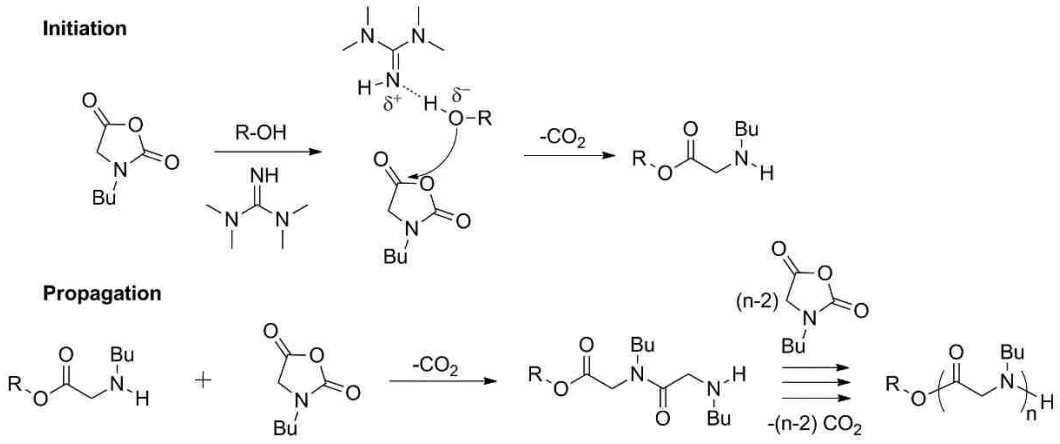

raction (Figure 1.3). The polymerization in high dielectric solvents (*e.g.*, DMF, DMSO) only produced low MW mixtures of linear and cyclic polymers regardless of the initial monomer to initiator ratios, due to the competitive intramolecular transamidation relative to chain propagation. The polymerization in toluene showed a pseudo-first order kinetics and the polymerization rate was dependent on the steric characteristic of the NHC used. A variety of cyclic polypeptoids with varied side chains were synthesized by NHC-mediated ZROP of R-NCAs Me-NCA, Et-NCA, Pg-NCA, Bu-NCA, De-NCA, 2EH-NCA and 2PE-NCA.[11-12] PEG-grafted cyclic random copolypeptoids (PNBG-r-PNPgG) was also reported, which appear as toroid structures in AFM, supporting the cyclic architecture of the polypepotid backbone.[38] 1,8- diazabicyclo[5.4.0]undec-7-ene (DBU), a bicyclic amidine, was also shown to mediated ZROP s of Bu-NCA in a controlled manner similar to NHCs (Figure 1.3).[39] The DBU exhibited enhanced moisture/air stability and availability compared to NHC.

1.3 Physicochemical properties of polypeptoids

1.3.1 Thermal properties of polypeptoids

The side chain structures of polypeptoids greatly affect their thermal properties. Polypeptoids bearing 2 carbon aliphatic side chains were shown to be amorphous, whereas polypeptoids bearing longer linear aliphatic side chains (C3-C14) are highly crystalline.[40] The cyc-

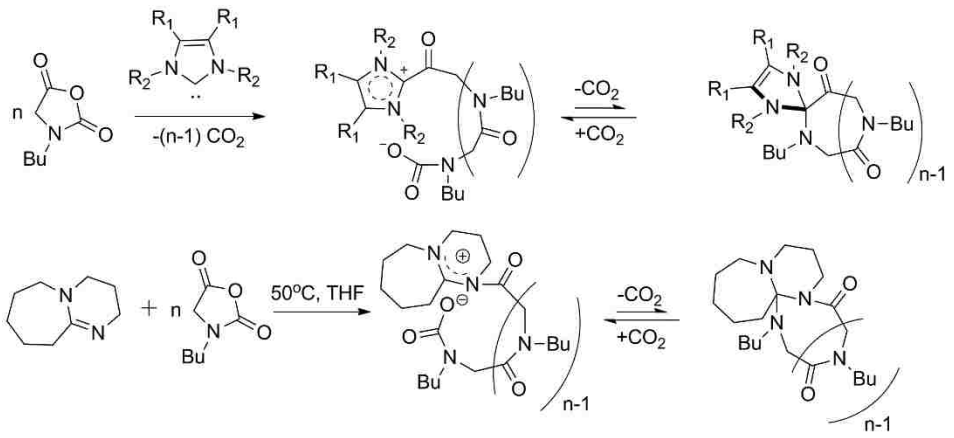

Figure 1.3. NHC- and DBU-mediated ZROPs of Bu-NCA to afford cyclic PNBGs.

lic and linear polypeptoids bearing linear aliphatic side chains (C4-C14) all exhibited two melting points (T_{m1} and T_{m2}) attributed to the side chain and main chain crystallization.[41] The crystallizations of main chain and side chain were strongly coupled: increasing side chain length increased the side chain melting temperature while decreasing the main chain melting temperature (Figure 1.4). The side chain and main chain crystallization of polypeptoid with branched aliphatic side chain (2-ethylhexyl) was shown to be greatly suppressed. The cyclic polypeptoids exhibited higher main chain melting points compared to the linear analog while the polymer architecture does not appreciably affect the side chain melting points. The polymer crystallization was also affected by the thermal history of the polymer.

1.3.2 Thermoresponsive properties of polypeptoids

The hydrophilicity and lipophilicity balance (HLB) of polypeptoids can be readily tailored by controlling the structure of side chains. Amphiphilic polymer solutions, including polypeptoids, often undergo dehydration and subsequent hydrophobic collapse at elevated temperature, the so-called reversible temperature-induced cloud point transition.[42] It was found that poly (*N*-alkyl glycine) with C3 carbon side chains (C3 = n-propyl, allyl, propargyl, and isopropyl) exhibited thermoresponsive behavior in water and their cloud temperatures (T_{cp}s) were dependent on the str-

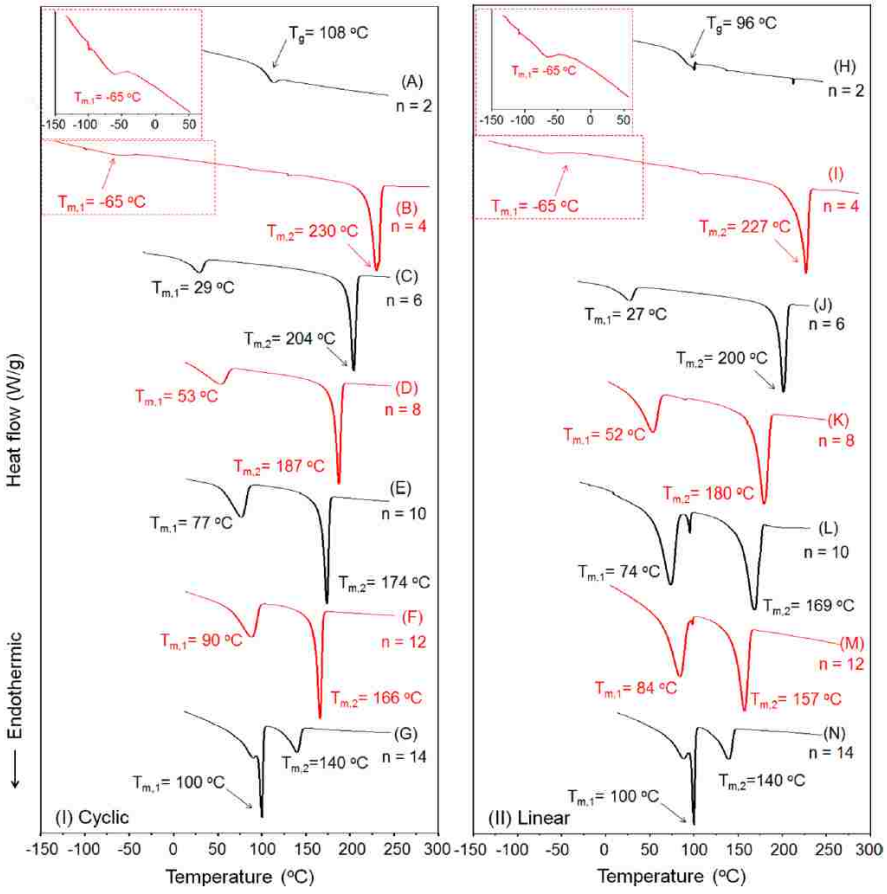

Figure 1.4. DSC thermograms of cyclic (left) and linear poly (*N*-n-alkyl glycine)s (right) during the second heating cycle (n in the plot designates the number of carbons on the n-alkyl side chains). Reproduced from Ref.40 with permission from American Chemical Society.

uctural and electronic properties of the side chain, the backbone length, as well as the solution concentration, whereas poly (*N*-propargyl glycine) was not soluble in water.[30] The T_{cp}s were found to increase in the order C3 = n-propyl (15-25 °C) < allyl (27-54 °C) < isopropyl (47-58 °C). The T_{cp}s were also shown to be concentration-dependent: decrease with increasing solution concentration. Long-term annealing of the aqueous solution of poly (*N*-(n-propyl) glycine) and poly (*N*-allyl glycine) at above their cloud point temperatures lead to the formation of crystalline microparticles and rose bud type morphology driven by the crystallization of the polymer

coacervates. The crystallization mechanism and detailed information of the crystalline structure has not been reported yet.

Another way to tune the cloud point transition temperature is to incorporate both hydrophobic and hydrophilic segments through copolymerization strategy. NHC-mediated or primary amine-initiated copolymerization of Et-NCA and Bu-NCA produced linear or cyclic random copolymers, PNBG-*r*-PNEG, which were thermally responsive in water (Figure 1.5).[43] The cloud point temperature (T_{cp}) in aqueous solution can be readily tailed in the range 20-60^{o}C by controlling the solution concentration, polymer composition, salt added, and polymer architecture (cyclic vs linear). The T_{cp} was systematically shifted to higher temperature with the increase of NEG content in the copolymer, indicating the critical role of hydrophobic effect in the thermoresponsive behavior. The molecular weight of the copolymer with constant composition was shown to have negligible effect on the T_{cp}. Interestingly, the cyclic copolyepeptoids exhibited 4-6 ^{o}C lower T_{cp}s than the linear analogs with identical composition, which is tentatively attributed to the less entropic loss of the cyclic copolymers during the solution phase transition associated with its more compact conformation. The decreased T_{cp}s with increasing concentration of the copolymer solutions indicated that intermolecular aggregation rather than intramolecular coil-to-globule transition was mainly responsible for the reversible phase transition. The T_{cp} depression caused by the addition of various salts is in agreement with the trend of Hofmeister series with Na_2SO_4 decreasing the T_d most, followed by NaCl and NaI.

Bottlebrush copolypeptoids prepared by grafting-through method via the ROMP of norbornenyl-terminated PNEG-*r*-PNBG macromonomers underwent thermoresponsive phase transition in aqueous solution similar to the linear macromonomers (Figure 1.6).[44] In contrast to the linear macromonomers, the bottlebrush copolypeptoids underwent cloud point transition that

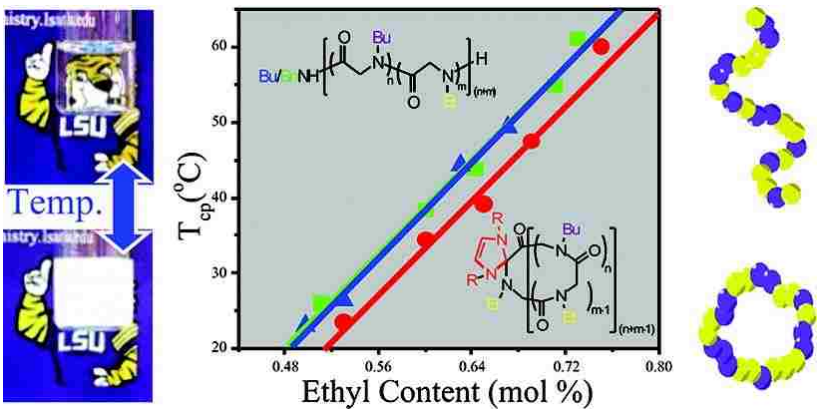

Figure 1.5. Plots of cloud point temperature (T_{cp}) versus the molar fraction of NEG segment in the cyclic and linear P(NEG-r-NBG) random copolymers bearing different end groups and their respective linearly fit curves [cyclic NHC-P(NEG-r-NBG) (●, —), linear Bu-P(NEG-r-NBG) (▲ ,—) and linear Bn-P(NEG-r-NBG) (■, —). Reproduced from Ref.43 with permission from American Chemical Society.

is strongly dependent on the thermal history of the aqueous solutions. Freshly prepared aqueous solutions of the bottlebrush copolypeptoids exhibited no notable phase transition, whereas the solutions underwent sharp and reversible cloud point transition after thermally annealing at high temperature. Interestingly, the aqueous solutions of the bottlebrush copolypeptoids showed normal cloud point transition similar to the linear macromonomer which was independent of the thermal history upon addition of inorganic salt. It was suggested that the conformational reorganization of the bottlebrush copolypeptoids was facilitated upon thermal annealing and addition of salt to favor the hydrophobic collapse and intermolecular aggregation, resulting in a thermoresponsive phase transition.

1.3.3 Solution self-assembly of amphiphilic polypeptoid copolymers

Self-assembly of PNMG-b-poly (*N*-alkyl glycine). Self-assembly of block copolymers have been a long-standing interests both in the fundamental investigation and application perspective. Self-assembly based on many amphiphilic and double hydrophilic hetero-block and graft copolymers, including PNMG-b-polypeptides, PNMG-b-poly (L-lactide) (AB, A_2B, A_3B ar-

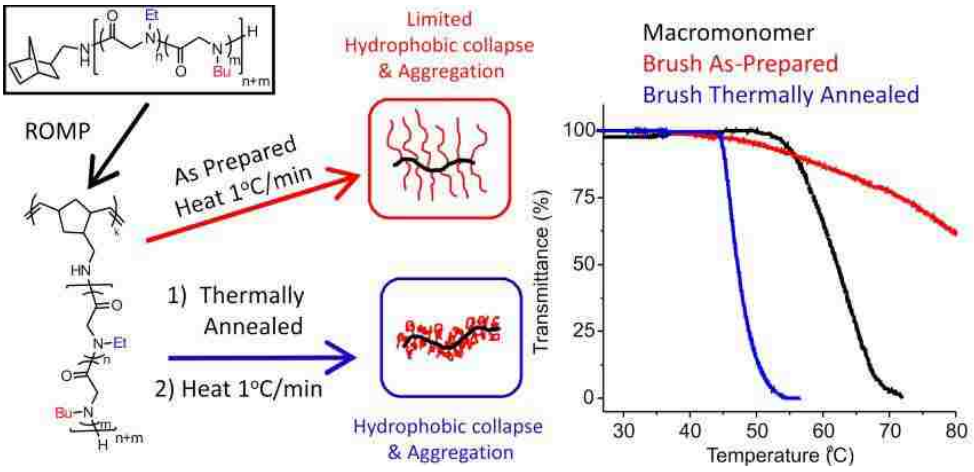

Figure 1.6. Polypeptoid bottlebrush copolymers comprised of linear P(NEG-*r*-NBG) side chains exhibited cloud point transitions that are dependent on the thermal history. Reproduced from Ref.44 with permission from Royal Society of Chemistry.

chitectural types), PEG-b-PNMG and PNMG-b-C_n=12-18, in solution have been studied.[15, 26] The recent report on aggregation behavior of block copolypeptoids, composed of hydrophilic PNMG (DP ~ 50) and poly (*N*-alkyl glycine) with C2-C5 aliphatic side chains, studied the effect of hydrophobicity and chain length of the solvophobic poly (*N*-alkyl glycine) on their critical micelle concentration (CMC) and the size of aggregates formed in aqueous solution.[45] Micellation was observed for the copolypeptoids containing C3-C5 aliphatic side chains with CMC value ranging from 0.6×10^{-6} to 0.1×10^{-3} M. The tendency to form micelles increased with increasing hydrophobicity of the side chains in the solvophobic block (C5>C4>C3). It was also found that increasing the chain length of hydrophobic block resulted in the formation of larger aggregates. The aggregate size and distribution were also strongly dependent on the temperature and solvent with smaller aggregate size in buffer (pH=7.4) than in water.

Redox-responsive polypeptoid micelles. Recently, a redox-sensitive micelle based on poly (*N*-ethyl glycine)-*b*-poly [(*N*-propargyl glycine)-*r*-(*N*-decyl glycine)] (EPgD) synthesized by sequential ROPs of the corresponding monomers using benzyl amine as the initiator, was reported (Figure 1.7).[19] The copolypeptoids underwent micellation in aqueous solution with CMC in the

0.075-0.12 mg/mL range at room temperature. Similarly to previously reported studies, the CMC value was gradually decreased with the increase of the hydrophobic segments. The selected copolypeptoid ($E_{204}Pg_{13}D_{15}$) formed well-defined spherical micelles in aqueous solution which was further crosslinked in the micellar core with two different crosslinkers using copper-mediated alkyne-azido cyclo-addition CuAAC chemistry. The core-crosslinked micelles (CCLMs) bearing a disulfide linkage were cleavable in the presence of reducing agents (*e.g.*, dithiothreitol, DTT), whereas the other micelles permanently crosslinked with 1,4-diazidobutane were not. The CCLMs showed a mono-modal size distribution and a decreased hydrodynamic diameter (d = 42.4 ± 0.8 nm) in comparison to the non-crosslinked micelles (NCLMs) (d = 60.1 ± 0.9 nm), as evidenced by dynamic light scattering (DLS) analysis. As expected, the NCLMs disassembled in DMF, a non-selective solvent for all the blocks, with an increase of the hydrodynamic size, broadening of size distribution (PDI = 0.41) and the appearance of unimers in the DLS analysis. In contrast, the CCLMs maintained the micellar structure with narrow size distribution (d = 59.2 ± 1.6 nm, PDI = 0.19) in DMF due to the covalent crosslinking in the micellar core. Spherical micelles with some short cylinders were observed from TEM analysis of dried CCLMs and NCLMs staining with uranyl acetate with average diameter of the CCLMs (21.1 ± 2.3 nm) comparable to that of the NCLMs (22.8 ± 2.9 nm), suggesting no appreciable change of the micellar morphology after covalent core-crosslinking. Fluorescent dye (1-anilinonaphthalene-8-sulfonic acid (1,8-ANS) or hydrophobic anticancer drug doxorubicin (DOX) was further encapsulated into CCLMs and their releasing behavior were monitored. For the CCLMs with DOX encapsulated, a maximal 23% drug loading capacity and a 37% drug loading efficiency was achieved and the DOX was released in a time-dependent manner associated with the disassembly of the CCLMs upon in contact with DTT. In contrast, minimal releasing of DOX was observed even after 30 h without the presence of DTT,

suggesting that the time-dependent DOX release was based on the cleavage of the disulfide crosslinkers in the micellar core and the subsequent micelle disassembly. The redox-responsive property make the CCLMs to be a potential smart drug delivery vehicle.

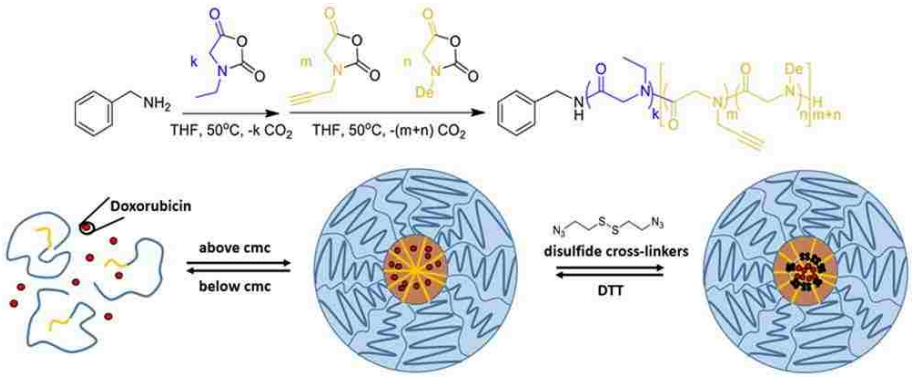

Figure 1.7. Synthesis of redox-responsive and core-cleavable micelles based on amphiphilic block copolypeptoids PNEG-b-P(NPgG-r-NDG) and their potential use for DOX encapsulation. Reproduced from Ref. 19 with permission from American Chemical Society.

Temperature-responsive polypeptoid micelles. Amphiphilic coil-crystalline cyclic diblock copolyeptoids (*c*-PNMG-b-PNDG) and their linear analogue (*l*-PNMG-b-PNDG) were synthesized by NHC-mediated and $BnNH_2$-initiated ROP of the corresponding monomers, respectively, and their self-assembly in methanol at low concentration (1mg/mL) was investigated.[46] Both the cyclic and linear PNMG-b-PNDG were shown to self-assemble into cylindrical micelles with PNDG as the core and PNMG as the shell in uniform diameter in methanol at room temperature over the course of several days after annealing at 70°C (above the first melting temperature of PNDG) (Figure 1.8). The kinetic study of micellation for both cyclic and linear block copolypeptoids in methanol monitored by cryo-TEM at different time intervals revealed the initial formation of amorphous spherical micelles followed by subsequent reorganization into micrometer-long crystalline cylindrical micelles, suggesting that the crystallization of the PNDG hydrophobic core was the driven force for the cylindrical micelle formation. In addition, the spherical-to-cylindrical morphological transition occurred more rapidly for

the linear copolypeptoid than for the cyclic analogue, which was probably due to the retarded crystallization of PNDG core for the cyclic analogue associated with the conformational constraint.

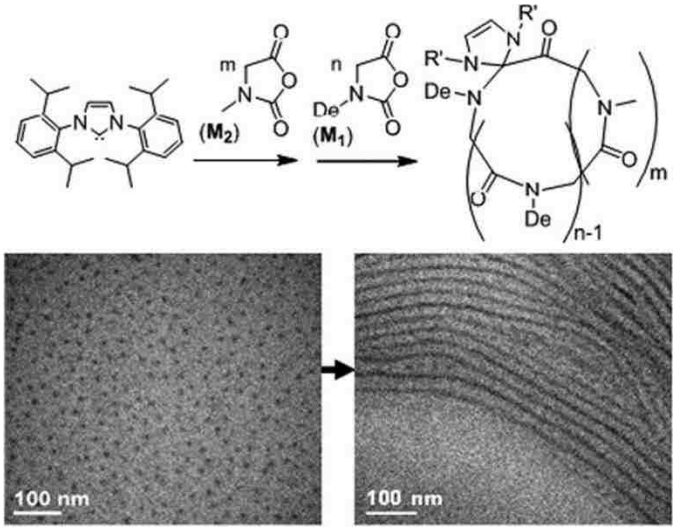

Figure 1.8. Synthesis of c-PNMG105-b-PNDG10 block copolypeptoid and its Cryo-TEM images in dilute methanol solutions after 1 h (spherical micelles) and 15 d (cylindrical micelles). Reproduced from Ref. 46 with permission from American Chemical Society.

At higher concentrations in methanol (5-10 wt%), both cyclic and linear diblock copolyeptoids (PNMG-b-PNDG) were shown to form free-standing gels consisting of entangled fibrils at room temperature. The gelation is thermoreversible that reverse back to isotropic solution upon heating to 70^{o}C, which results in the morphological change of crystalline cylindrical micelles to amporphous spherical micelles or non-associated polymers induced by the melting of the PNDG crystalline domains, as evidenced by both temperature-dependent ^{1}H NMR and DLS analysis. The cyclic polymer gels exhibited higher sol-to-gel transition temperatures and higher gel stiffness compared to the linear analogs, suggesting enhanced crystallinity in the fibrilar network in the formers relative to the latters.

1.4 Biologically relevant properties

1.4.1 Cytotoxicity of polypeptoids

It is important to investigate the cytotoxicity of polypeptoids before being further used in biomedical and biotechnological fields. The cytotoxicity assessment of polysarcosine and its

copolymers as well as other water soluble polypeptoids in different cell lines have been reported. Random copolypeptoid of cyclic P(NEG$_{74}$-*r*-NBG$_{15}$) exhibited minimal cytotoxicity (cell viability > 90 %) towards human embryonic lung fibroblasts (HEL229) up to 5.0 mg/mL concentration after incubation in PBS buffer at 37^{o}C for 24 h, as evidenced by CellTiter-Blue® assay.[43]

The cytotoxicity of the random copolymer of PNMG-*r*-PNEG with different compositions synthesized from primary amine initiated copolymerization of the corresponding NTA monomers (Me-NTA and Bu-NTA) was also evaluated in human heptoblastoma cells (HepG2) using the MTT cell viability asssay.[47] It was found that the relative cell viability was dependent on the polymer composition and concentration. All the polymers investigated showed increased cytotoxicity towards HepG2 cells with increasing polymer concentration from 0.05 to 3.0 mg/mL. P(Sar$_{48}$-*r*-NBG$_{26}$) with relative lower PNBG content displayed higher cell viability (>75%) at the whole concentration range investigated (0.05-3 mg/mL) comparable to that of PNMG, whereas P(Sar$_{47}$-*r*-NBG$_{30}$) and P(Sar$_{42}$-*r*-NBG$_{36}$) with relative higher PNBG content exhibited a significant increase of cytotoxicity at 3.0 mg/mL concentration, presumably due to the partial precipitation of these polymers at this concentration associated with their onset cloud point being close to the incubation temperature.

The homopolymer PNMG (M_n =2.1 kDa, PDI=1.31), diblock and triblock copolypeptoids (PNMG-b-PNprG, PNMG-b-PNpenG, PNMG-b-PNprG-b-PNMG) with MW in the range 3.6-9.6 kDa all exhibited minimal cytotoxicity (cell viability > 90 %) toward HepG2 cells up to 10 mg/mL polymer concentration, as evidenced by WST-1 assay.[45]

The above mentioned core-crosslinked micelles (CCLMs) composed of hydrophobic [P(NPgG-*r*-NDG)] core and hydrophilic (PNEG) corona with redox-responsive disulfide crosslinkers or non-redox responsive permanent crosslinkers all exhibited minimal cytotoxicity (cell viability > 95 %) towards HepG2 cells up to 1.0 mg/mL concentration upon incubation in MEMS medium for 48 h, as evidenced by MTT assay. Both the redox-reponsive and non-redox responsive CCLMs loaded with

the anticancer drug (DOX) displayed time and dosage dependent cytotoxicity towards HepG2 cells. The DOX-loaded redox-responsive CCLMs showed higher cytotoxicity relative to the permanently crosslinked CCLMs through the whole DOX dosage and time investigated, suggesting more efficient release of DOX and more cell death associated with the cleavage of the disulfide crosslinkers of the former under reductive environment in HepG2 cells. The DOX dosage- and time-dependent cytotoxicity of the permanently crosslinked CCLMs, in a relatively lower level, was presumably due to the degradation of polymers in the cellular environment.

1.4.2 Degradation of polypeptoids

Hydrolytic degradation. Polypeptoids, with a tertiary amide linkage on the backbone, are potentially degradable through hydrolysis. polysarcosine-b-poly(L-proline) copolymer was shown to degrade into the corresponding amino acids under highly acidic conditions (6 N HCl, 120 °C, 24 h).[48] Since the hydrolysis of polypeptoids occurred under such a harsh condition, perhaps the hydrolytic degradation of polypeptoids in the cellular environment is minimal and slow.

Enzymatic degradation. The incorporation of tertiary amide bonds is known to enhance protease resistance in peptidomimetic therapeutics.[26] Currently there is no systematic investigation on the enzymatic degradation of high MW polypeptoids. Many studies on peptoid oligomers showed their enhanced protease resistance compared to peptide analogs. In sharp contrast to the peptide analogs that are readily protease degradable, the sequence-specific peptoid oligomers exhibited no protease degradation with the presence of proteases including carboxypeptidase A, papain, pepsin, trypsin, elastase, and chymotrypsin.[16-17] A reasonable hypothesis was made that proline imminopeptidase may also cleave the *N*-sarcosine terminus[26], according to the reported observation that the digestion of the copolymer comprised of L-proline and sarcosine with proline imminopeptidase produced 4.4 times higher free L-proline that of theroretically predicted[49]. Thus, the

enzymatic degradation of (poly) peptoids should not be completely ruled out and more investigations need to be carried out.

Oxidative degradation. It is important and necessary to study the degradation behavior under oxidative conditions as increased local concentration of various reactive oxygenated species (ROS) are generated by oxidative stress in various diseased states under cellular environment.[15] A comparative investigation on the oxidative degradation of PNEG, PEG and poly (2-oxazoline) (Pox) was conducted with the presence of ROS (*e.g.*, $HOO^{\cdot}$, $HO^{\cdot}$) generated from the H_2O_2/Cu^{2+} source.[20] It was found that all polymers investigated were degradable at 50 mM H_2O_2 and Cu^{2+}, with PEG being significantly more stable than the PNEG and POx. Faster degradation rate was observed at higher H_2O_2 concentration. It was also shown that high MW polymer exhibited faster degradation in terms of percentage molecular weight reduction over time in comparison to the corresponding low MW polymer, suggesting chain scission as a main mode of degradation.

1.5 Hydrogels in tissue engineering

Hydrogels are three-dimensional (3 D) hydrophilic polymeric networks that can absorb and retain a considerable amount of water.[50] Hydrogels have received continued interest for encapsulating cells and most recently hydrogels have become especially attractive to be used as tissue engineering scaffolds for repairing and regenerating a variety of tissues due to their highly water-swelled 3 D environment that are similar to soft tissues and allow diffusion of nutrients, metabolites and growth factors through the elastic networks.[50-55]

A major goal of hydrogels in tissue engineering technology is the development of injectable hydrogels. In this case, the hydrogel precursors, bioactive agents and/or drugs are mixed in aqueous solutions and immediately form hydrogels upon injection into targeted sites of body using syringe administration. The injectable hydrogels allow an effective and homogeneous encapsulation of drugs/cells for both in *in vitro* and *in vivo* studies. Moreover, the high moldability

of injectable hydrogels can adapt to the defect shape of tissues. In addition, it provides a convenient and minimally invasive method for *in vivo* surgical operation, causing smaller scar size, less pain and faster recovery for patients.[55-56] The immediate *in situ* gel formation is resulted from ether physical crosslinking in response to environmental stimuli such as pH value, temperature, ionic concentration, or chemical crosslinking through chemical reactions such as Michael addition, Schiff base, disulfide bond formation, *etc*. In contrast to the chemically crosslinked hydrogels which usually undergo significant volume changes during phase transition, the physically crosslinked hydrogels usually exhibit sol-gel transitions without marked volume changes. Besides, the crosslinking agents and/or photo irradiation used, as well as the heat released in chemically crosslinked hydrogels may damage the encapsulated cells and surrounding tissues. Therefore, injectable physical hydrogels have received considerable interests in the recent years for tissue engineering applications.

Another important design criterion of injectable hydrogels is their biocompatibility and biodegradability.[55] The hydrogels should be made of biocompatible materials that are degraded into biocompatible products in body. It is desirable that the degradation rate of hydrogels matches the rate of tissue formation to give enough space for cell activity, oxygen and nutrients migration as well as for the new tissue formed. Meanwhile, the hydrogels should still maintain a relatively stable environment with sufficient strength that match the tissue.

The injectable hydrogels used in tissue engineering should display the following characteristics: 1) nontoxic to the cells encapsulated and the surrounding tissue, 2) hydrolytically and/or enzymatically degradable, 3) controlled degradation rate that matches with that of the tissue formation, 4) controlled mechanical strength to create and maintain a space for tissue development, 5) provide biological cues (*e.g.*, cell adhesion) to facilitate tissue regeneration.[52-53] 6), low viscosity

before gelation for easy encapsulation of cells and drugs, 7) mild while rapid gelation to avoid toxicity and tissue damage, A variety of hydrogels, both naturally occurring hydrogels and synthetic hydrogels, have been developed and investigated as potential tissue engineering scaffolds. No one material will satisfy all the design criteria, but a wide range of hydrogels will provide possible uses in different tissue engineering applications.

1.6 Naturally occurring hydrogels

Naturally occurring hydrogels are made from natural polymer-based materials, such as proteins (*e.g.*, collagen, gelatin and fibrin), and polysaccharides (*e.g.*, alginate, chitosan, agarose and hyaluronic acid), which generally have biocompatibility, cell-controlled degradability, and intrinsic cellular interaction. They may, however, exhibit batch-to-batch variations and have limited tunability to their structure and mechanical properties.[53]

1.6.1 Proteins: collagen, gelatin and fibrin

Collagens are the main protein of extracellular matrices (ECM) of mammalian tissues including skin, bone, cartilage, tendon, and ligament, and comprise 25 % of the total protein mass of most mammals.[53-54] Collagen is basically composed of three polypeptide chains, which wrap around one another to form a three-stranded rope by hydrogen and covalent bonds.[57] Collagen strands can self-assemble into entangled collagen fibers to form fibrillar gels at physiological temperature and pH.[57-58] Collagen, composed of specific combinations of amino acid sequences, can be recognized by cells and degraded by metalloproteases secreted from the cells (*e.g.*, collagenase, serine proteases).[54] Gelatin, a derivative of collagen, is formed by the natural triple-helix structure of collagen into single-stand molecules. Gelatin can form physical thermo-reversible hydrogels by lowering the temperature of its aqueous solution for the chains to undergo coil-to-helix transition.[59] The collagen- and gelatin-based hydrogels, however, are short of

physical strength and have potential immunogenic responses, as well as have variations between produced batches.[53] To increase mechanical strength of the hydrogel, different chemical modification methods, including combining with other natural components[60-61] and chemical crosslinking using carbodiimide[62], nitrocinnamate[63], or glutaraldehyde[64] have been investigated. Collagen and gelatin hydrogels have been used for reconstruction of a variety of organs and tissues including liver, skin and small intestine.[53]

Fibrin, a fibrous and non-globular protein, is an important component of the extracellular matrix involving in wound healing.[55] Fibrin is biocompatible and promotes adhesion and migration of numerous cell types (*e.g.*, fibroblasts). Fibrin is biodegradable through cell-associated enzymatic activity and the degradation rate can be controlled by apronitin, a proteinase inhibitor. Fibrin forms hydrogel by the enzymatic polymerization of fibrinogen in the presence of thrombin.[53, 55] One disadvantage of the fibrin hydrogels is their weak mechanical strength.[53]

1.6.2 Polysaccharides: alginate, chitosan and hyaluronic acid

Alginate, obtained from brown algae, is a linear unbranched polysaccharide (Figure 1.9) which are biocompatible, non-toxic and relatively cheap.[53] Alginate can simply form hydrogels with divalent cations such as Ca^{2+}, Mg^{2+}, Ba^{2+}, and Sr^{2+}.[65] The alginate hydrogels, however, undergo an uncontrollable and unpredictable process involving loss of divalent ions to the surrounding medium and subsequent dissolution.[53] Covalent cross-linking with adipic dihydrazide, methyl ester L-lysine, and PEG-diamines has been investigated to prevent the dissolution process and improve mechanical strength.[66] In addition, many alginates have high molecular weight that are typically above the renal clearance threshold (40 KDa) of the kidney.[67] Moreover, alginate has limited cellular interaction and is unable to specifically interact with mammalian cells.[68]

Hyaluronic acid (HA) , consisted of alternate disaccharide units (Figure 1.9), is the only non-sulfated glycosaminoglycan which plays an important role in wound healing, cell motility, angiogenesis as well as in construction of ECM.[55] Hyaluronic acid is degradable by hyaluronidase, which exists in cells and serum.[69] High molecular hyaluronic acid at high concentrations in solution (*e.g.*, 5 MDa at >0.1 mg/mL) can form viscoelastic entangled molecular networks, but the HA solutions do not have long-lasting mechanical integrity.[70] Hyaluronic acid hydrogels can also be formed by covalent cross-linking with different compounds such as hydrazine derivatives[71] and radical polymerization of glycidyl methacrylate[72], or by physical cross-linking of the thermoresponsive moieties (*e.g.*, PNIPAM) attached[73]. The drawback of hyaluronic acid hydrogel is its low mechanical properties, which limited their application in tissue engineering.[53]

Unlike alginate, agarose which is another type of marine algal polysaccharide, forms thermoreversible hydrogels containing bundles of associated double helices.[53] The physical structure and mechanical strength can be simply tuned by changing the solution concentration of agarose.

Chitosan (Figure 1.9), a copolymer of glusocamine and *N*-acetylglucosamine, is derived from natural chitin.[56] Chitosan is biocompatible and biodegradable with enzymes such as chitosanase and lysozyme.[53] Chitosan forms hydrogel through ionic or chemical cross-linking with glutaradehyde. Chitosan is positively charged at low pH's, while generally insoluble in neutral solutions as well as in most organic solvents. Various modifications of chitosan have been reported to increase its water solubility and processability.

1.7 Synthetic polymer-based hydrogels

In contrast to hydrogels based on naturally occurring biopolymers (*e.g.*, collagen, fibrin, alginate, chitosan and hyaluronic) which have potential immunologic responses, poor mechanical

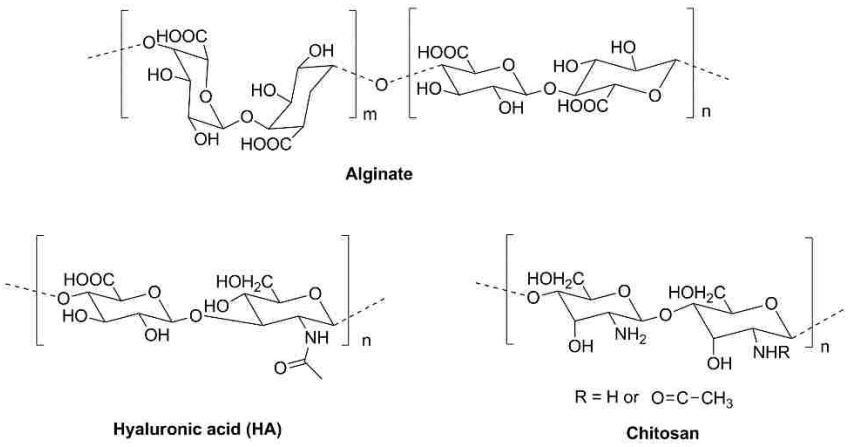

Figure 1.9. Chemical structures of alginate, hyaluronic acid, and chitosan.

strength and variation from batch to batch, synthetic polymer-based hydrogels offer the advantage of adjustable mechanical strength, chemical composition and function, and gel morphologies, as well as their lack of immune responses, making it possible to tune the material properties for specific biomedical and biotechnological applications. Most of the synthetic polymer-based hydrogels, nevertheless, are non-biocompatible and non-degradable in physiological environment, and extensive purification steps may be required to remove any toxic residue that are left from their synthesis or processing. In addition, in contrast to naturally occurring hydrogels, synthetic hydrogels often do not exhibit any substantial biological activities (*e.g.*, cell adhesion) to induce differentiation and proliferation of cells and tissue regeneration. Therefore, the biodegradable and bioactive synthetic polymer-based hydrogels have received special attention in the recent years and various strategies have been applied to endow them bioactivity (*e.g.*, cell adhesion and migration) for various biological applications such as tissue engineering. Importing biological cues such as components of specific tissues (*e.g.*, chondroitin sulfate, hyaluronic acid), growth factors (*e.g.*, TGF-β1), extracellular matrix protein-derived cell-adhesive peptide (*e.g.*, RGD) to the synthetic hydrogels through covalent linkage is a common strategy to incorporate biological activities to synthetic hydrogels.[74-77] This strategy, though effective, has the drawbacks of

enhanced synthetic complexity, potential emergence of cytotoxicity, and altered physicochemical properties of the hydrogels. By contrast, synthetic hydrogels that are inherently biologically active and can modulate cell function and differentiation *de novo* without additional biological cues or factors will not only facilitate the preparation of tissue engineering scaffold but also provide an improved platform to investigate the factors that give rise to the biological activities.[74] For tissue engineering applications, it is desirable that the hydrogel scaffold not only have tunable mechanical stiffness and morphologies that can be made to match those of the native tissues but also exhibit biological activities that can modulate the cell migration, proliferation, and differentiation.[52, 54]

1.7.1 Hydrogels based on amphiphilic block copolymers: AB, ABA and BAB hydrogles

Hydrogels based on AB, ABA and BAB block copolymers, where A and B signify the hydrophobic/thermoresponsive and hydrophilic blocks, respectively, have been widely investigated in the past. The general gelation mechanisms for the amphiphilic block copolymers was the association of formed micelles in aqueous solution with hydrophobic A block as the core and hydrophilic B block as the shell. Among them, the polypeptide and polyester based copolymers were of significant interest due to their biocompatibility and biodegradability.

Hydrogels based on polyesters. Aliphatic polyesters, including poly (glycolic acid) (PGA), poly (L-lactic acid) (PLLA), and copolymers (PLGA), have received long-standing interest in medical applications and are considered to be biocompatible and biodegradable by the FDA.[53, 78-80] Over the last decades, various amphiphilic copolymers of biocompatible PEG and polyesters, including diblock, triblock, multiblock architectures, have been developed as gelators. The block copolymers, PEO-PLLA (BA) and PEO-PLLA-PEO (BAB), formed micelles driven by the hydrophobic interactions of PLLA blocks in aqueous solutions and formed hydrogels at high

concentration levels (> 12wt%) caused by the association of micelles.[81-82] The copolymer solutions exhibited sol-to-gel transition with decreasing temperature from higher temperature to the body temperature (37ºC). The sol-gel transition temperature and the onset gelation concentration can be easily tuned by changing the block length of PLLA. For example, the sol state of PEO-PLLA-PEO (MW, 5000-2040-5000) at 45ºC formed gel upon injection into a rat, making it very promising for drug delivery and/or tissue engineering. The aqueous solution of the ABA type copolymer (PLLA-PEO-PLLA) bearing two hydrophobic blocks can form strong gels at body temperature with elastic moduli greater than 10,000 kPa, which is an order of magnitude higher than previously reported physically associated gels of similar chemistry.[83] These ABA hydrogels showed tunable elastic moduli in the range 100-18,300 Pa at ambient and physiological temperatures by changing the solution concentration and block length of PLLA, render them potential for soft tissue engineering where native tissues have moduli in the kPa range. An equimolar mixture of enantiomeric copolymers, PLLA-PEG/PDLA-PEG or PLLA-PEG-PLLA/PDLA-PEG-PDLA, can form thermoresponsive hydrogels (G'~1000 Pa) with sol-gel transition occurred around 37ºC by the stereo-complexation of the PLLA and PDLA segments.[84-85] Their critical gelation concentrations were considerably lower compared to polymer solutions containing only the single enantiomer. The enantiometic PEG-$(PLA)_8$ star block copolymers (10 wt%, 1.9 kPa) exhibited higher storage moduli than those based on PEG-$(PLA)_2$ (13 wt%, 0.9 kPa).[86] One disadvantage of the stereocomplex hydrogels is the relatively long gelation time.[87] To manipulate the degradation rate of copolymers of PEG and PLA, the ester bond linked the two blocks was changed to an amide bond. It was shown that PEG-(NHCO)-$(PLA)_8$ displayed slow degradation *in vitro* compared to PEG-(OCO)-$(PLA)_8$.[88] Comonomer (glycolic acid) was incorporated to PLA to manipulate the gelation concentration, gelation temperature and gel modulus *etc*.[89] The sequence of lactic acid

and glycolic acid in the copolymer influenced the hydrophobic/hydrophilic balance and thus alters the macroscopic physical gelation in water.[90] Mixing homopolymers or block copolymers to gelator solutions was another simple method to tune the gelation properties. The addition of PEG homopolymer to PLGA-PEG-PLGA aqueous solution lead to a gelation at a lower temperature, probably due to the immiscibility between the PEG and the hydrophobic PLGA block.[91] The recent study showed the effect of molecular weight distribution (MWD) of middle block PEG on the phase transition of the PLGA-PEG-PLGA aqueous solutions: a wider MWD of PEG block enlarged the copolymer micelles and increased the solution viscosity, making it gel at low temperatures.[92]

Poly (ε-caprolactone) (PCL) is another well-known biodegradable polyester and has been extensively investigated in biomedical and biotechnological fields.[93-94] The triblock copolymer PCL-PEG-PCL (ABA) and PEG-PCL-PEG (BAB) (>15 wt%) underwent sol-gel-sol transition as the temperature increases from 10-60^{o}C.[95-96] The mechanism of clear sol-to-turbid gel transition seems to be micellar aggregation, whereas the turbid gel-to-turbid sol transition seems to be due to the higher extent of aggregation driven by an increase in the molecular motion of PCL accompanying the core-shell structure breakage. The gel modulus was increased as the pH increased from 2 to 8 due to the decreased water solubility of the copolymer and hence hardening of the gel modulus. Compared to PEG-PCL-PEG, PCL-PEG-PCL showed a lower sol-to-gel transition temperature and larger gel window (15-32 wt%), which seems to be related to the enhanced intermicellar bridges of PCL-PEG-PCL. The aqueous solutions of these triblock copolymers, however, were not stable at room temperature due to the crystallization of PCL.[97] It was reported that PCTC-PEG-PCTC with incorporation of comonomer (trimethylene carbonate) in PCL blocks[98] or multiblock PEG/PCL copolymer[97] increased the sol stability while keep the

thermogelling property. The chondrocytes encapsulated in PCTC-PEG-PCTC hydrogel showed a higher expression of collagen type II and aggrecan and suppression of collagen type I (fibroblastic gene) compared to the control, as evidenced by RNA extraction and reverse transcription polymerase chain reaction (RT-PCR), suggesting the excellent differentiation of chondrocytes in the hydrogel.[98]

Hydrogels based on polypeptide block copolymers. Polypeptides have emerged as attractive structural elements for hydrogel networks due to their potential biodegradability, a wide range of chemical functionality, and adoption of ordered conformations that can drive structure formation and also respond to stimuli.[99-102] Various hydrogels based on amphiphilic polypeptide copolymers have been reported. Their self-assembled secondary structures (*e.g.*, α-helixes, β-sheets, random coil) in aqueous solutions played a critical role in the sol-to-gel transition.[103-105]

The ionic hydrogels composed of poly-L-lysine-b-poly-L-leucine diblock and poly-L-lysine-b-poly-L-leucine-b-poly-L-lysine triblock copolypeptides formed hydrogel at concentration as low as 0.25% induced by the rod-like helical secondary structure of enantiomerically pure poly-L-leucine blocks.[103] These hydrogels showed high stability in high ionic strength media such as aqueous buffers and cell growth media,[104] however, the copolymers containing positive charges displayed cytotoxicity to *in vitro* cells[106] and were not thermoresponsive in aqueous solutions.

The copolymers of PEG and polyalanine are one of the mostly investigated amphiphilic polypeptide copolymers in hydrogel formation and in both *in vitro* and *in vivo* biological studies. The β-sheet conformation of L-polyalanine plays a critical role in developing a fibrous assemblies in aqueous solutions as well as the sol-to-gel transition of amphphilic PEG-polyananine.[105, 107] It was shown that only the L-isomer showed a sol-to-gel transition in physiological important

temperature window (20-40 ^{o}C) at low concentration (6-12 wt%), while the DL-isomer remained a random coil structure and exhibited much higher gelation concentration (> 16 wt%) and gelation temperature (>70^{o}C).[105] The stereochemistry (L and D) also greatly affect the biological response of polypeptide copolymer hydrogels. The histology study showed that only the hydrogel of L-isomer (PEG-L-PAF) was significantly degraded by cathepsin B and elastase both *in vitro* and *in vivo* and caused milder acute inflammation compared to the D-isomer hydrogel.[108] The PEG-L-PA thermogels were reported to be used as cell scaffolds for cell proliferation, cell differentiation and tissue formation. It was shown that PEG-L-PA hydrogel encapsulated with fibroblasts formed *in situ* improved the formation of collagen types I/III and accelerated the wound closure on incisions of rat skin compared to the controls.[109] The PEG-L-PA hydrogels were also encapsulated with tonsil-derived mesenchymal stem cells (TMSCs) and adipose-tissue-derived stem cells (ADSCs), to facilitate the hepatogenic[110] chondrogenic[111] differentiation, respectively. Efforts were made to control the differentiation pathway of stem cells encapsulated in hydrogels. The recent study incorporated polystyrene microspheres with different functional groups in *in situ* formed PEG-L-PA hydrogels to manipulate the differentiation pathway of TMSCs. The TMSCs preferentially underwent adipogenesis in ammonium (-NH_3^+)- or thiol (-SH)-functionalized polystyrene microsphere incorporated hydrogels; chondrogenesis in the thiol, phosphate (PO_3^{2-})-, or carboxylate (-COO^-)-functionalized polystyrene microsphere incorporated hydrogels; and osteogenesis in phosphate-, carboxylate-functionalized or neat polystyrene microsphere incorporated hydrogels.[112] The PA[113-114], PAF[115] or PAL[116] was end-capped to commercially available PLX to enhance its gel duration for biomedical applications.

γ-esterified Polyglutamates is another common category of hydrophobic polypeptides as hydrogel components. It was revealed that the subtle variation in the length of hydrophobic side

group of polyglutamates greatly affected the gelation behavior of the PEG-Poly (L-glutamate)s copolymers.[117] The copolymers with polyglutamates bearing methyl and ethyl side chains displayed significantly lower critical gelation temperatures (CGTs) compared to those bearing *n*-propyl and butyl side groups due to the increased β-sheet conformation of the formers. In addition, the block copolymers showed no detectable cytotoxicity against HeLa cells and accelerated degradation in buffer containing proteinase K compared to controls. To confer bioactivities to the hydrogels, poly poly (γ-propargyl-L-glutamate) (PPLG) was used to react with azide-modified bioactive molecules, such as biotin and galactose via click chemistry.[118] The hydrogel of PEG-PPLG functionalized with hydrophilic galactose was found to improve cell adhesion, probably due to its adhesion of fibronectin in cell ECM. In contrast, the biotin functionalized hydrogel lead to suppressed effect on cell adhesion compared to galactose functionalized hydrogels, which may due to the relatively hydrophobic character of biotin that tend to aggregate into the micelle core. The galactose and biotin changed the phase transition temperature of the block copolymer as a result of the variation of hydrophilic/hydrophobic balance. The sol-to-gel transitions of these PEG-polyglutamate based copolymers, however, were relatively broad with the transition temperature window larger than 20^{o}C.

The above mentioned hydrogel formation of polypeptide copolymers is driven by dehydration of the PEG segments, as well as the transition of polypeptide segments to β-sheet rich conformation at elevated temperature. The β-sheet structures stabilized hydrogels formation via interchain hydrogen bonding, but also cause limited reversibility of the hydrogel transition.[105, 107, 114-117, 119] The poly(γ-[2-(2-methoxyethoxy)ethyl]-*rac*-glutamate)-block-poly(γ-[2-(2-methoxyethoxy)ethyl]-L-glutamate-*stat*-L-leucine), (rac-E^{P2})-(E^{P2}/L), was currently the only reported thermoreversible hydrogels based solely on synthetic polypeptide components.[120] E^{P2} is

known to be α-helical with a lower critical solution temperature (LCST) above 37ºC in aqueous solutions.[121] The E^{P2} in the E^{P2}/L block of the copolymer was hydrophilic at low T and became hydrophobic with increased temperature which further associated to form 3D hydrogel networks with hydrophilic rac-E^{P2} segments exposed. The sol-gel transition was fully reversible over repeated heating and cooling cycles, presumably due to the stable α-helix conformations of the thermoresponsive domains. In addition, the sol-gel transition temperature and gel stiffness can be well tuned by changing the solution temperature and copolymer compositions. These nonionic thermoreversible polypeptide hydrogels supported the viability of mesenchymal stem cells *in vitro*, in contrast to some reported polyelectrolyte hydrogels which were cytotoxic to cells.[106]

Hydrogels based on PNIPAM. Poly(*N*-isopropylacrylamide) (PNIPAM), showing a LCST in water close to body temperature (~32 °C), is the most commonly investigated thermoresponsive polymer in the design of thermogels.[122-125] The PNIPAM-based copolymers are water-soluble at temperature below LCST and formed thermoreversible hydrogels in aqueous solutions due to hydrophobic interactions between PNIPAM blocks at elevated temperature. The sol-gel transition temperature and gel stiffness can be tuned by changing the solution concentrations and compositions of copolymers. The ABA-typed copolymer (PNIPAM-PMPC-PNIPAM) with the bio-inspired polyphosphorylcholine as the middle block, PNIPAM-PDMA-PNIPAM, PNIPAM-PVP-PNIPAM formed free-standing physical gels (~ 1000 Pa) at 37ºC in PBS at concentrations higher than 10 wt%.[126-127] The hydrogels of PNIPAM-PMPC-PNIPAM were sufficiently biocompatible as a culture medium for V97 cells.[126]

1.7.2 Hydrogels based on ABC block copolymers

The AB-, ABA- or BAB-typed hydrogels often exhibit broad or slow sol-gel transitions or high critical concentration (cgc, where cgc $\geqslant$ 10 wt %). In the ABA- and BAB-type hydrogels,

the inefficient sol-gel transition characteristic has been attributed to the formation of loops, flower micells, and dangling ends in the formation of micellar network.[127-129] Recently, ABC-type hydrogels, where A, B, and C refer to thermoresponsive block with lower critical solution temperature (LCST), hydrophilic and hydrophobic block, respectively, have received considerable interest due to their much sharper so-gel transition and lower cgc. With the formation of separate A and C domains, the intramolecular association of the end blocks to form loop configurations is significantly suppressed, thereby giving rise to a rapid and sharp thermoreversible sol-gel transition at low concentration ($\leq$ 5 wt%) upon a temperature increase.[128] Although ABC triblok copolymer is an attractive structural motif for thermoreversible gelation, studies on the design, characterization, and investigation of potential biomedical uses of ABC hydrogelators have been limited. PNIPAM, showing a LCST in water close to body temperature ($\sim$32 ^{o}C), is the most commonly investigated thermoresponsive polymer in the design of ABC hydrogelators.[128, 130-131] The earlier reported PNIPAM-PMPC-PPO triblock copolymer exhibit sol-gel transition around 37 ^{o}C at high concentration ($\geq$ 20 wt%) with low mechanical strength (G'$\sim$25 Pa).[130] Recently, a 5 wt % aqueous solution of PEP-PEO-PNIPAM (PON) triblock copolymers was shown to undergo thermoreversible sol−gel transition at 42 °C,[128] which is higher than the physiological temperature. The ABC copolymer (PON) was displayed much sharper sol-gel transition at a much lower concentration, compared to the corresponding ABA copolymer (NON). A two-step gelation mechanism was proposed, involving the initial formation of micelles with PEP cores at room temperature and gelation due to PNIPAM block aggregation at elevated temperature. The separation of micellation and gelation in the PON hydrogels greatly suppressed the looping formation which happened in the NON hydrogels. The investigation of the aqueous solutions (1-5 wt%) of PON at different temperatures using cryo-SEM, cryo-TEM, and SANS further confirmed

the two-compartment network structure consisting of distinct spherical PEP and PNIPAM cores upon heating above the critical gelation temperature.[132] Another recently reported cell protective ABC copolymer (PNIPAM−PDMA−PPS) was shown to undergo rapid thermoreversible gelation in PBS buffer at 2.5 wt % with a gelation temperature well below 37 °C.[131] The reported hydrogel was mechanically soft with storage modulus (G') lower than 1 kPa at 7.5 wt % polymer concentration. The reported ABC synthetic polymers were all based on nondegradable polymers.[128, 130-131]

Taking advantage of the synthetic development of polypeptoids, the attractive properties of polypeptoids including the low cytotoxicity and potential biodegradability, and the effcient gelation of ABC triblock copolymers, thermoresponsive ABC triblock copolypeptoids [i.e., poly(*N*-allyl glycine)-b-poly(*N*-methyl glycine)-b-poly(*N*-decyl glycine) (AMD)] with well-defined structure and varying composition have been synthesized by sequential primary amine-initiated ring-opening polymerization of the corresponding *N*-substituted *N*-carboxyanhydride monomers (Al-NCA, Me-NCA, and De-NCA) were synthesized. The ABC block copolypeptoids undergo sol-to-gel transitions with increasing temperature in water and biological media at low concentrations (2.5−10 wt %). Detailed information was presented in Chapter 2. In Chapter 3, the synthesis of highly water soluble polypeptoids bearing oligomeric ethylene glycol side chains and their protein-resistant ability to protein lysozyme was presented. These PEGylated polypeptoids are potentially to be a new benchmark of antifouling material. In Chapter 4, the solution self-assembly of coil-crystalline diblock copolypeptoids (PNMG-b-PNDG) was discussed.

1.8. References

1. Armand, P.; Kirshenbaum, K.; Goldsmith, R. A.; Farr-Jones, S.; Barron, A. E.; Truong, K. T. V.; Dill, K. A.; Mierke, D. F.; Cohen, F. E.; Zuckermann, R. N.; Bradley, E. K. NMR determination of the major solution conformation of a peptoid pentamer with chiral side chains. *Proc. Natl. Acad. Sci.* **1998,** *95* (8), 4309-4314.

2. Kirshenbaum, K.; Barron, A. E.; Goldsmith, R. A.; Armand, P.; Bradley, E. K.; Truong, K. T. V.; Dill, K. A.; Cohen, F. E.; Zuckermann, R. N. Sequence-specific polypeptoids: A diverse family of heteropolymers with stable secondary structure. *Proc. Natl. Acad. Sci.* **1998,** *95* (8), 4303-4308.

3. Wu, C. W.; Sanborn, T. J.; Huang, K.; Zuckermann, R. N.; Barron, A. E. Peptoid Oligomers with α-Chiral, Aromatic Side Chains: Sequence Requirements for the Formation of Stable Peptoid Helices. *J. Am. Chem. Soc.* **2001,** *123* (28), 6778-6784.

4. Wu, C. W.; Sanborn, T. J.; Zuckermann, R. N.; Barron, A. E. Peptoid Oligomers with α-Chiral, Aromatic Side Chains: Effects of Chain Length on Secondary Structure. *J. Am. Chem. Soc.* **2001,** *123* (13), 2958-2963.

5. Kudirka, R.; Tran, H.; Sanii, B.; Nam, K. T.; Choi, P. H.; Venkateswaran, N.; Chen, R.; Whitelam, S.; Zuckermann, R. N. Folding of a single-chain, information-rich polypeptoid sequence into a highly ordered nanosheet. *Peptide Science* **2011,** *96* (5), 586-595.

6. Sanii, B.; Kudirka, R.; Cho, A.; Venkateswaran, N.; Olivier, G. K.; Olson, A. M.; Tran, H.; Harada, R. M.; Tan, L.; Zuckermann, R. N. Shaken, Not Stirred: Collapsing a Peptoid Monolayer To Produce Free-Floating, Stable Nanosheets. *J. Am. Chem. Soc.* **2011,** *133* (51), 20808-20815.

7. Sanii, B.; Haxton, T. K.; Olivier, G. K.; Cho, A.; Barton, B.; Proulx, C.; Whitelam, S.; Zuckermann, R. N. Structure-Determining Step in the Hierarchical Assembly of Peptoid Nanosheets. *ACS Nano* **2014,** *8* (11), 11674-11684.

8. Cai, S.-L.; Zhang, W.-G.; Zuckermann, R. N.; Li, Z.-T.; Zhao, X.; Liu, Y. The Organic Flatland—Recent Advances in Synthetic 2D Organic Layers. *Adv. Mater.* **2015,** *27* (38), 5762-5770.

9. Mannige, R. V.; Haxton, T. K.; Proulx, C.; Robertson, E. J.; Battigelli, A.; Butterfoss, G. L.; Zuckermann, R. N.; Whitelam, S. Peptoid nanosheets exhibit a new secondary-structure motif. *Nature* **2015,** *526* (7573), 415-420.

10. Robertson, E. J.; Battigelli, A.; Proulx, C.; Mannige, R. V.; Haxton, T. K.; Yun, L.; Whitelam, S.; Zuckermann, R. N. Design, Synthesis, Assembly, and Engineering of Peptoid Nanosheets. *Acc. Chem. Res.* **2016,** *49* (3), 379-389.

11. Li, G.; Donghui, Z., Synthesis and Characterization of Helix-Coil Block Copoly(α-peptoid)s. In *Non-Conventional Functional Block Copolymers*, American Chemical Society: 2011; Vol. 1066, pp 71-79.

12. Guo, L.; Li, J.; Brown, Z.; Ghale, K.; Zhang, D. Synthesis and characterization of cyclic and linear helical poly(α-peptoid)s by N-heterocyclic carbene-mediated ring-opening polymerizations of N-substituted N-carboxyanhydrides. *Peptide Science* **2011,** *96* (5), 596-603.

13. Secker, C.; Robinson, J. W.; Schlaad, H. Alkyne-X modification of polypeptoids. *Eur. Polym. J.* **2015,** *62*, 394-399.

14. Murnen, H. K.; Rosales, A. M.; Dobrynin, A. V.; Zuckermann, R. N.; Segalman, R. A. Persistence length of polyelectrolytes with precisely located charges. *Soft Matter* **2013,** *9* (1), 90-98.

15. Chan, B. A. X., S.; Li, A.; Simpson, J. M.; Zhang, D. , Polypeptoid Polymers: Synthesis, Characterization and Properties. Synthesis and Characterization of Biorelated Polymers for Biomedical Applications. 2016.

16. Miller, S. M.; Simon, R. J.; Ng, S.; Zuckermann, R. N.; Kerr, J. M.; Moos, W. H. Proteolytic studies of homologous peptide and N-substituted glycine peptoid oligomers. *Biorg. Med. Chem. Lett.* **1994,** *4* (22), 2657-2662.

17. Miller, S. M.; Simon, R. J.; Ng, S.; Zuckermann, R. N.; Kerr, J. M.; Moos, W. H. Comparison of the proteolytic susceptibilities of homologous L-amino acid, D-amino acid, and N-substituted glycine peptide and peptoid oligomers. *Drug Dev. Res.* **1995,** *35* (1), 20-32.

18. Xuan, S.; Lee, C.-U.; Chen, C.; Doyle, A. B.; Zhang, Y.; Guo, L.; John, V. T.; Hayes, D.; Zhang, D. Thermoreversible and Injectable ABC Polypeptoid Hydrogels: Controlling the Hydrogel Properties through Molecular Design. *Chem. Mater.* **2016,** *28* (3), 727-737.

19. Li, A.; Zhang, D. Synthesis and Characterization of Cleavable Core-Cross-Linked Micelles Based on Amphiphilic Block Copolypeptoids as Smart Drug Carriers. *Biomacromolecules* **2016,** *17* (3), 852-861.

20. Ulbricht, J.; Jordan, R.; Luxenhofer, R. On the biodegradability of polyethylene glycol, polypeptoids and poly(2-oxazoline)s. *Biomaterials* **2014,** *35* (17), 4848-4861.

21. Zuckermann, R. N. Peptoid origins. *Peptide Science* **2011,** *96* (5), 545-555.

22. Zhang, D.; Lahasky, S. H.; Guo, L.; Lee, C.-U.; Lavan, M. Polypeptoid Materials: Current Status and Future Perspectives. *Macromolecules* **2012,** *45* (15), 5833-5841.

23. Luxenhofer, R.; Fetsch, C.; Grossmann, A. Polypeptoids: A perfect match for molecular definition and macromolecular engineering? *J. Polym. Sci., Part A: Polym. Chem.* **2013,** *51* (13), 2731-2752.

24. Sun, J.; Zuckermann, R. N. Peptoid Polymers: A Highly Designable Bioinspired Material. *ACS Nano* **2013,** *7* (6), 4715-4732.

25. Jing, S.; Caroline, P.; Ronald, N. Z., Precision Sequence Control in Bioinspired Peptoid Polymers. In *Sequence-Controlled Polymers: Synthesis, Self-Assembly, and Properties*, American Chemical Society: 2014; Vol. 1170, pp 35-53.

26. Gangloff, N.; Ulbricht, J.; Lorson, T.; Schlaad, H.; Luxenhofer, R. Peptoids and Polypeptoids at the Frontier of Supra- and Macromolecular Engineering. *Chem. Rev.* **2015**.

27. Klinker, K.; Barz, M. Polypept(o)ides: Hybrid Systems Based on Polypeptides and Polypeptoids. *Macromol. Rapid Commun.* **2015,** *36* (22), 1943-1957.

28. Secker, C.; Brosnan, S. M.; Luxenhofer, R.; Schlaad, H. Poly(α-Peptoid)s Revisited: Synthesis, Properties, and Use as Biomaterial. *Macromol. Biosci.* **2015,** *15* (7), 881-891.

29. Fetsch, C.; Grossmann, A.; Holz, L.; Nawroth, J. F.; Luxenhofer, R. Polypeptoids from N-Substituted Glycine N-Carboxyanhydrides: Hydrophilic, Hydrophobic, and Amphiphilic Polymers with Poisson Distribution. *Macromolecules* **2011,** *44* (17), 6746-6758.

30. Robinson, J. W.; Secker, C.; Weidner, S.; Schlaad, H. Thermoresponsive Poly(N-C3 glycine)s. *Macromolecules* **2013,** *46* (3), 580-587.

31. Guo, L.; Zhang, D. Cyclic Poly(α-peptoid)s and Their Block Copolymers from N-Heterocyclic Carbene-Mediated Ring-Opening Polymerizations of N-Substituted N-Carboxylanhydrides. *J. Am. Chem. Soc.* **2009,** *131* (50), 18072-18074.

32. Katchalski, E.; Sela, M., Synthesis and Chemical Properties of Poly-α-Amino Acids. In *Adv. Protein Chem.*, C.B. Anfinsen, M. L. A. K. B.; John, T. E., Eds. Academic Press: 1958; Vol. Volume 13, pp 243-492.

33. Kricheldorf, H. R. Polypeptides and 100 Years of Chemistry of α-Amino Acid N-Carboxyanhydrides. *Angew. Chem. Int. Ed.* **2006,** *45* (35), 5752-5784.

34. Fetsch, C.; Luxenhofer, R. Highly Defined Multiblock Copolypeptoids: Pushing the Limits of Living Nucleophilic Ring-Opening Polymerization. *Macromol. Rapid Commun.* **2012,** *33* (19), 1708-1713.

35. Robinson, J. W.; Schlaad, H. A versatile polypeptoid platform based on N-allyl glycine. *Chem. Commun.* **2012,** *48* (63), 7835-7837.

36. Chan, B. A.; Xuan, S.; Horton, M.; Zhang, D. 1,1,3,3-Tetramethylguanidine-Promoted Ring-Opening Polymerization of N-Butyl N-Carboxyanhydride Using Alcohol Initiators. *Macromolecules* **2016,** *49* (6), 2002-2012.

37. Guo, L.; Lahasky, S. H.; Ghale, K.; Zhang, D. N-Heterocyclic Carbene-Mediated Zwitterionic Polymerization of N-Substituted N-Carboxyanhydrides toward Poly(α-peptoid)s: Kinetic, Mechanism, and Architectural Control. *J. Am. Chem. Soc.* **2012,** *134* (22), 9163-9171.

38. Lahasky, S. H.; Serem, W. K.; Guo, L.; Garno, J. C.; Zhang, D. Synthesis and Characterization of Cyclic Brush-Like Polymers by N-Heterocyclic Carbene-Mediated Zwitterionic Polymerization of N-Propargyl N-Carboxyanhydride and the Grafting-to Approach. *Macromolecules* **2011,** *44* (23), 9063-9074.

39. Li, A.; Lu, L.; Li, X.; He, L.; Do, C.; Garno, J. C.; Zhang, D. Amidine-Mediated Zwitterionic Ring-Opening Polymerization of N-Alkyl N-Carboxyanhydride: Mechanism, Kinetics, and Architecture Elucidation. *Macromolecules* **2016,** *49* (4), 1163-1171.

40. Fetsch, C.; Luxenhofer, R. Thermal Properties of Aliphatic Polypeptoids. *Polymers* **2013,** *5* (1), 112.

41. Lee, C.-U.; Li, A.; Ghale, K.; Zhang, D. Crystallization and Melting Behaviors of Cyclic and Linear Polypeptoids with Alkyl Side Chains. *Macromolecules* **2013,** *46* (20), 8213-8223.

42. Hoogenboom, R.; Schlaad, H. Thermoresponsive poly(2-oxazoline)s, polypeptoids, and polypeptides. *Polymer Chemistry* **2016**.

43. Lahasky, S. H.; Hu, X.; Zhang, D. Thermoresponsive Poly(α-peptoid)s: Tuning the Cloud Point Temperatures by Composition and Architecture. *ACS Macro Letters* **2012,** *1* (5), 580-584.

44. Lahasky, S. H.; Lu, L.; Huberty, W. A.; Cao, J.; Guo, L.; Garno, J. C.; Zhang, D. Synthesis and characterization of thermo-responsive polypeptoid bottlebrushes. *Polymer Chemistry* **2014,** *5* (4), 1418-1426.

45. Fetsch, C.; Flecks, S.; Gieseler, D.; Marschelke, C.; Ulbricht, J.; van Pée, K.-H.; Luxenhofer, R. Self-Assembly of Amphiphilic Block Copolypeptoids with C2-C5 Side Chains in Aqueous Solution. *Macromol. Chem. Phys.* **2015,** *216* (5), 547-560.

46. Lee, C.-U.; Smart, T. P.; Guo, L.; Epps, T. H.; Zhang, D. Synthesis and Characterization of Amphiphilic Cyclic Diblock Copolypeptoids from N-Heterocyclic Carbene-Mediated Zwitterionic Polymerization of N-Substituted N-Carboxyanhydride. *Macromolecules* **2011,** *44* (24), 9574-9585.

47. Tao, X.; Du, J.; Wang, Y.; Ling, J. Polypeptoids with tunable cloud point temperatures synthesized from N-substituted glycine N-thiocarboxyanhydrides. *Polymer Chemistry* **2015,** *6* (16), 3164-3174.

48. Fasman, G. D.; Blout, E. R. Copolymers of L-proline and sarcosine: Synthesis and physical-chemical studies. *Biopolymers* **1963,** *1* (2), 99-109.

49. Sarid, S. B., A.; Katchalski, E. Proline iminopeptidase. *J. Biol. Chem.* **1959,** *234*, 1740−1746.

50. Nguyen, M. K.; Lee, D. S. Injectable Biodegradable Hydrogels. *Macromol. Biosci.* **2010,** *10* (6), 563-579.

51. Hoffman, A. S. Hydrogels for biomedical applications. *Adv. Drug Del. Rev.* **2002,** *54* (1), 3-12.

52. Zhu, J. Bioactive modification of poly(ethylene glycol) hydrogels for tissue engineering. *Biomaterials* **2010,** *31* (17), 4639-4656.

53. Lee, K. Y.; Mooney, D. J. Hydrogels for Tissue Engineering. *Chem. Rev.* **2001,** *101* (7), 1869-1880.

54. Drury, J. L.; Mooney, D. J. Hydrogels for tissue engineering: scaffold design variables and applications. *Biomaterials* **2003,** *24* (24), 4337-4351.

55. Li, Y.; Rodrigues, J.; Tomas, H. Injectable and biodegradable hydrogels: gelation, biodegradation and biomedical applications. *Chem. Soc. Rev.* **2012,** *41* (6), 2193-2221.

56. Hennink, T. V. R. C. W. E. Hydrogels for Protein Delivery. *Chem. Rev.* **2012,** *112* (5), 2853-2888.

57. Lee, C. H.; Singla, A.; Lee, Y. Biomedical applications of collagen. *Int. J. Pharm.* **2001,** *221* (1–2), 1-22.

58. Drzewiecki, K. E.; Parmar, A. S.; Gaudet, I. D.; Branch, J. R.; Pike, D. H.; Nanda, V.; Shreiber, D. I. Methacrylation Induces Rapid, Temperature-Dependent, Reversible Self-Assembly of Type-I Collagen. *Langmuir* **2014,** *30* (37), 11204-11211.

59. Djabourov, M.; Papon, P. Influence of thermal treatments on the structure and stability of gelatin gels. *Polymer* **1983,** *24* (5), 537-542.

60. Choi, Y. S.; Hong, S. R.; Lee, Y. M.; Song, K. W.; Park, M. H.; Nam, Y. S. Study on gelatin-containing artificial skin: I. Preparation and characteristics of novel gelatin-alginate sponge. *Biomaterials* **1999,** *20* (5), 409-417.

61. Zhang, X.; Yang, Y.; Yao, J.; Shao, Z.; Chen, X. Strong Collagen Hydrogels by Oxidized Dextran Modification. *ACS Sustainable Chem. Eng.* **2014,** *2* (5), 1318-1324.

62. Kuijpers, A. J.; Engbers, G. H. M.; Feijen, J.; De Smedt, S. C.; Meyvis, T. K. L.; Demeester, J.; Krijgsveld, J.; Zaat, S. A. J.; Dankert, J. Characterization of the Network Structure of Carbodiimide Cross-Linked Gelatin Gels. *Macromolecules* **1999,** *32* (10), 3325-3333.

63. Gattás-Asfura, K. M.; Weisman, E.; Andreopoulos, F. M.; Micic, M.; Muller, B.; Sirpal, S.; Pham, S. M.; Leblanc, R. M. Nitrocinnamate-Functionalized Gelatin: Synthesis and "Smart" Hydrogel Formation via Photo-Cross-Linking. *Biomacromolecules* **2005,** *6* (3), 1503-1509.

64. Rault, I.; Frei, V.; Herbage, D.; Abdul-Malak, N.; Huc, A. Evaluation of different chemical methods for cros-linking collagen gel, films and sponges. *J. Mater. Sci. Mater. Med.* **1996,** *7* (4), 215-221.

65. Smidsrød, O.; Skja˚k-Brˆk, G. Alginate as immobilization matrix for cells. *Trends Biotechnol. 8*, 71-78.

66. Lee, K. Y.; Rowley, J. A.; Eiselt, P.; Moy, E. M.; Bouhadir, K. H.; Mooney, D. J. Controlling Mechanical and Swelling Properties of Alginate Hydrogels Independently by Cross-Linker Type and Cross-Linking Density. *Macromolecules* **2000,** *33* (11), 4291-4294.

67. Al-Shamkhani, A.; Duncan, R. Radioiodination of Alginate via Covalently-Bound Tyrosinamide Allows Monitoring of its Fate In Vivo. *J. Bioact. Compatible Polym.* **1995,** *10* (1), 4-13.

68. Smetana, K. Cell biology of hydrogels. *Biomaterials* **1993,** *14* (14), 1046-1050.

69. Afify, A. M.; Stern, M.; Guntenhoner, M.; Stern, R. Purification and Characterization of Human Serum Hyaluronidase. *Arch. Biochem. Biophys.* **1993,** *305* (2), 434-441.

70. Xu, X.; Jha, A. K.; Harrington, D. A.; Farach-Carson, M. C.; Jia, X. Hyaluronic acid-based hydrogels: from a natural polysaccharide to complex networks. *Soft Matter* **2012,** *8* (12), 3280-3294.

71. Pouyani, T.; Harbison, G. S.; Prestwich, G. D. Novel Hydrogels of Hyaluronic Acid: Synthesis, Surface Morphology, and Solid-State NMR. *J. Am. Chem. Soc.* **1994,** *116* (17), 7515-7522.

72. Inukai, M.; Jin, Y.; Yomota, C.; Yonese, M. Preparation and Characterization of Hyaluronate-Hydroxyethyl Acrylate Blend Hydrogel for Controlled Release Device. *Chem. Pharm. Bull. (Tokyo)* **2000,** *48* (6), 850-854.

73. Ohya, S.; Nakayama, Y.; Matsuda, T. Thermoresponsive Artificial Extracellular Matrix for Tissue Engineering: Hyaluronic Acid Bioconjugated with Poly(N-isopropylacrylamide) Grafts. *Biomacromolecules* **2001,** *2* (3), 856-863.

74. Park, H.; Guo, X.; Temenoff, J. S.; Tabata, Y.; Caplan, A. I.; Kasper, F. K.; Mikos, A. G. Effect of Swelling Ratio of Injectable Hydrogel Composites on Chondrogenic Differentiation of Encapsulated Rabbit Marrow Mesenchymal Stem Cells In Vitro. *Biomacromolecules* **2009,** *10* (3), 541-546.

75. Hwang, N. S.; Varghese, S.; Theprungsirikul, P.; Canver, A.; Elisseeff, J. Enhanced chondrogenic differentiation of murine embryonic stem cells in hydrogels with glucosamine. *Biomaterials* **2006,** *27* (36), 6015-6023.

76. Nuttelman, C. R.; Tripodi, M. C.; Anseth, K. S. Dexamethasone-functionalized gels induce osteogenic differentiation of encapsulated hMSCs. *J. Biomed. Mater. Res. Part A* **2006,** *76A* (1), 183-195.

77. Jha, A. K.; Xu, X.; Duncan, R. L.; Jia, X. Controlling the adhesion and differentiation of mesenchymal stem cells using hyaluronic acid-based, doubly crosslinked networks. *Biomaterials* **2011,** *32* (10), 2466-2478.

78. Ronneberger, B.; Kao, W. J.; Anderson, J. M.; Kissel, T. In vivo biocompatibility study of ABA triblock copolymers consisting of poly(L-lactic-co-glycolic acid) A blocks attached to central poly(oxyethylene) B blocks. *J. Biomed. Mater. Res.* **1996,** *30* (1), 31-40.

79. Zhu, K. J.; Xiangzhou, L.; Shilin, Y. Preparation, characterization, and properties of polylactide (PLA)–poly(ethylene glycol) (PEG) copolymers: A potential drug carrier. *J. Appl. Polym. Sci.* **1990,** *39* (1), 1-9.

80. Bhatia, S. R.; Tew, G. N., PLA-PEO-PLA Hydrogels: Chemical Structure, Self-Assembly and Mechanical Properties. In *Degradable Polymers and Materials: Principles and Practice (2nd Edition)*, American Chemical Society: 2012; Vol. 1114, pp 313-324.

81. Byeongmoon Jeong, Y. H. B., Doo Sung Lee, Sung Wan Kim *Nature* **1997,** *388*, 860-862.

82. Jeong, B.; Lee, D. S.; Shon, J.-I.; Bae, Y. H.; Kim, S. W. Thermoreversible gelation of poly(ethylene oxide) biodegradable polyester block copolymers. *J. Polym. Sci., Part A: Polym. Chem.* **1999,** *37* (6), 751-760.

83. Aamer, K. A.; Sardinha, H.; Bhatia, S. R.; Tew, G. N. Rheological studies of PLLA–PEO–PLLA triblock copolymer hydrogels. *Biomaterials* **2004,** *25* (6), 1087-1093.

84. Fujiwara, T.; Kimura, Y. Macromolecular Organization of Poly(L-lactide)-block-Polyoxyethylene into Bio-Inspired Nano-Architectures. *Macromol. Biosci.* **2002,** *2* (1), 11-23.

85. Fujiwara, T.; Mukose, T.; Yamaoka, T.; Yamane, H.; Sakurai, S.; Kimura, Y. Novel Thermo-Responsive Formation of a Hydrogel by Stereo-Complexation between PLLA-PEG-PLLA and PDLA-PEG-PDLA Block Copolymers. *Macromol. Biosci.* **2001,** *1* (5), 204-208.

86. Hiemstra, C.; Zhong, Z.; Dijkstra, P. J.; Feijen, J. Stereocomplex Mediated Gelation of PEG-(PLA)2 and PEG-(PLA)8 Block Copolymers. *Macromolecular Symposia* **2005,** *224* (1), 119-132.

87. Hiemstra, C.; Zhong, Z.; Li, L.; Dijkstra, P. J.; Feijen, J. In-Situ Formation of Biodegradable Hydrogels by Stereocomplexation of PEG−(PLLA)8 and PEG−(PDLA)8 Star Block Copolymers. *Biomacromolecules* **2006,** *7* (10), 2790-2795.

88. Buwalda, S. J.; Dijkstra, P. J.; Calucci, L.; Forte, C.; Feijen, J. Influence of Amide versus Ester Linkages on the Properties of Eight-Armed PEG-PLA Star Block Copolymer Hydrogels. *Biomacromolecules* **2009,** *11* (1), 224-232.

89. Jeong, B.; Bae, Y. H.; Kim, S. W. Thermoreversible Gelation of PEG−PLGA−PEG Triblock Copolymer Aqueous Solutions. *Macromolecules* **1999,** *32* (21), 7064-7069.

90. Yu, L.; Zhang, Z.; Ding, J. Influence of LA and GA Sequence in the PLGA Block on the Properties of Thermogelling PLGA-PEG-PLGA Block Copolymers. *Biomacromolecules* **2011,** *12* (4), 1290-1297.

91. Zhang, H.; Yu, L.; Ding, J. Roles of Hydrophilic Homopolymers on the Hydrophobic-Association-Induced Physical Gelling of Amphiphilic Block Copolymers in Water. *Macromolecules* **2008,** *41* (17), 6493-6499.

92. Chen, L.; Ci, T.; Yu, L.; Ding, J. Effects of Molecular Weight and Its Distribution of PEG Block on Micellization and Thermogellability of PLGA–PEG–PLGA Copolymer Aqueous Solutions. *Macromolecules* **2015,** *48* (11), 3662-3671.

93. Pitt, C. G.; Chasalow, F. I.; Hibionada, Y. M.; Klimas, D. M.; Schindler, A. Aliphatic polyesters. I. The degradation of poly(ϵ-caprolactone) in vivo. *J. Appl. Polym. Sci.* **1981,** *26* (11), 3779-3787.

94. Pitt, G. G.; Gratzl, M. M.; Kimmel, G. L.; Surles, J.; Sohindler, A. Aliphatic polyesters II. The degradation of poly (DL-lactide), poly (ε-caprolactone), and their copolymers in vivo. *Biomaterials* **1981,** *2* (4), 215-220.

95. Bae, S. J.; Suh, J. M.; Sohn, Y. S.; Bae, Y. H.; Kim, S. W.; Jeong, B. Thermogelling Poly(caprolactone-b-ethylene glycol-b-caprolactone) Aqueous Solutions. *Macromolecules* **2005,** *38* (12), 5260-5265.

96. Hwang, M. J.; Suh, J. M.; Bae, Y. H.; Kim, S. W.; Jeong, B. Caprolactonic Poloxamer Analog: PEG-PCL-PEG. *Biomacromolecules* **2005,** *6* (2), 885-890.

97. Bae, S. J.; Joo, M. K.; Jeong, Y.; Kim, S. W.; Lee, W.-K.; Sohn, Y. S.; Jeong, B. Gelation Behavior of Poly(ethylene glycol) and Polycaprolactone Triblock and Multiblock Copolymer Aqueous Solutions. *Macromolecules* **2006,** *39* (14), 4873-4879.

98. Park, S. H.; Choi, B. G.; Joo, M. K.; Han, D. K.; Sohn, Y. S.; Jeong, B. Temperature-Sensitive Poly(caprolactone-co-trimethylene carbonate)−Poly(ethylene glycol)−Poly(caprolactone-co-trimethylene carbonate) as in Situ Gel-Forming Biomaterial. *Macromolecules* **2008,** *41* (17), 6486-6492.

99. Altunbas, A.; Pochan, D. J., Peptide-Based and Polypeptide-Based Hydrogels for Drug Delivery and Tissue Engineering. In *Peptide-Based Materials*, Deming, T., Ed. Springer Berlin Heidelberg: Berlin, Heidelberg, 2012; pp 135-167.

100. Jonker, A. M.; Löwik, D. W. P. M.; van Hest, J. C. M. Peptide- and Protein-Based Hydrogels. *Chem. Mater.* **2012,** *24* (5), 759-773.

101. Park, M. H.; Joo, M. K.; Choi, B. G.; Jeong, B. Biodegradable Thermogels. *Acc. Chem. Res.* **2012,** *45* (3), 424-433.

102. Rypáček, F.; Dvořák, M.; Štefko, I.; Machová, L.; Škarda, V.; Kubies, D., Poly(amino acid)s and Ester-Amide Copolymers: Tailor-Made Biodegradable Polymers. In *Biopolymers from Polysaccharides and Agroproteins*, American Chemical Society: 2001; Vol. 786, pp 258-275.

103. Breedveld, V.; Nowak, A. P.; Sato, J.; Deming, T. J.; Pine, D. J. Rheology of Block Copolypeptide Solutions: Hydrogels with Tunable Properties. *Macromolecules* **2004,** *37* (10), 3943-3953.

104. Nowak, A. P.; Breedveld, V.; Pine, D. J.; Deming, T. J. Unusual Salt Stability in Highly Charged Diblock Co-polypeptide Hydrogels. *J. Am. Chem. Soc.* **2003,** *125* (50), 15666-15670.

105. Choi, Y. Y.; Joo, M. K.; Sohn, Y. S.; Jeong, B. Significance of secondary structure in nanostructure formation and thermosensitivity of polypeptide block copolymers. *Soft Matter* **2008,** *4* (12), 2383-2387.

106. Pakstis, L. M.; Ozbas, B.; Hales, K. D.; Nowak, A. P.; Deming, T. J.; Pochan, D. Effect of Chemistry and Morphology on the Biofunctionality of Self-Assembling Diblock Copolypeptide Hydrogels. *Biomacromolecules* **2004,** *5* (2), 312-318.

107. Jeong, Y.; Joo, M. K.; Bahk, K. H.; Choi, Y. Y.; Kim, H.-T.; Kim, W.-K.; Jeong Lee, H.; Sohn, Y. S.; Jeong, B. Enzymatically degradable temperature-sensitive polypeptide as a new in-situ gelling biomaterial. *J. Controlled Release* **2009,** *137* (1), 25-30.

108. Kang, E. Y.; Yeon, B.; Moon, H. J.; Jeong, B. PEG-l-PAF and PEG-d-PAF: Comparative Study on Thermogellation and Biodegradation. *Macromolecules* **2012,** *45* (4), 2007-2013.

109. Yun, E. J.; Yon, B.; Joo, M. K.; Jeong, B. Cell Therapy for Skin Wound Using Fibroblast Encapsulated Poly(ethylene glycol)-poly(l-alanine) Thermogel. *Biomacromolecules* **2012,** *13* (4), 1106-1111.

110. Kim, S.-J.; Park, M. H.; Moon, H. J.; Park, J. H.; Ko, D. Y.; Jeong, B. Polypeptide Thermogels as a Three Dimensional Culture Scaffold for Hepatogenic Differentiation of Human Tonsil-Derived Mesenchymal Stem Cells. *ACS Appl. Mater. Interfaces* **2014,** *6* (19), 17034-17043.

111. Yeon, B.; Park, M. H.; Moon, H. J.; Kim, S.-J.; Cheon, Y. W.; Jeong, B. 3D Culture of Adipose-Tissue-Derived Stem Cells Mainly Leads to Chondrogenesis in Poly(ethylene glycol)-Poly(l-alanine) Diblock Copolymer Thermogel. *Biomacromolecules* **2013,** *14* (9), 3256-3266.

112. Kye, E. J.; Kim, S.-J.; Park, M. H.; Moon, H. J.; Ryu, K. H.; Jeong, B. Differentiation of Tonsil-Tissue-Derived Mesenchymal Stem Cells Controlled by Surface-Functionalized Microspheres in PEG-Polypeptide Thermogels. *Biomacromolecules* **2014,** *15* (6), 2180-2187.

113. Kim, J. Y.; Park, M. H.; Joo, M. K.; Lee, S. Y.; Jeong, B. End Groups Adjusting the Molecular Nano-Assembly Pattern and Thermal Gelation of Polypeptide Block Copolymer Aqueous Solution. *Macromolecules* **2009,** *42* (8), 3147-3151.

114. Oh, H. J.; Joo, M. K.; Sohn, Y. S.; Jeong, B. Secondary Structure Effect of Polypeptide on Reverse Thermal Gelation and Degradation of l/dl-Poly(alanine)–Poloxamer–l/dl-Poly(alanine) Copolymers. *Macromolecules* **2008,** *41* (21), 8204-8209.

115. Kim, E. H.; Joo, M. K.; Bahk, K. H.; Park, M. H.; Chi, B.; Lee, Y. M.; Jeong, B. Reverse Thermal Gelation of PAF-PLX-PAF Block Copolymer Aqueous Solution. *Biomacromolecules* **2009,** *10* (9), 2476-2481.

116. Moon, H. J.; Choi, B. G.; Park, M. H.; Joo, M. K.; Jeong, B. Enzymatically Degradable Thermogelling Poly(alanine-co-leucine)-poloxamer-poly(alanine-co-leucine). *Biomacromolecules* **2011,** *12* (4), 1234-1242.

117. Cheng, Y.; He, C.; Xiao, C.; Ding, J.; Zhuang, X.; Huang, Y.; Chen, X. Decisive Role of Hydrophobic Side Groups of Polypeptides in Thermosensitive Gelation. *Biomacromolecules* **2012,** *13* (7), 2053-2059.

118. Cheng, Y.; He, C.; Xiao, C.; Ding, J.; Cui, H.; Zhuang, X.; Chen, X. Versatile Biofunctionalization of Polypeptide-Based Thermosensitive Hydrogels via Click Chemistry. *Biomacromolecules* **2013,** *14* (2), 468-475.

119. Han, J. O.; Joo, M. K.; Jang, J. H.; Park, M. H.; Jeong, B. PVPylated Poly(alanine) as a New Thermogelling Polymer. *Macromolecules* **2009,** *42* (17), 6710-6715.

120. Zhang, S.; Alvarez, D. J.; Sofroniew, M. V.; Deming, T. J. Design and Synthesis of Nonionic Copolypeptide Hydrogels with Reversible Thermoresponsive and Tunable Physical Properties. *Biomacromolecules* **2015,** *16* (4), 1331-1340.

121. Chen, C.; Wang, Z.; Li, Z. Thermoresponsive Polypeptides from Pegylated Poly-l-glutamates. *Biomacromolecules* **2011,** *12* (8), 2859-2863.

122. Liow, S. S.; Dou, Q.; Kai, D.; Karim, A. A.; Zhang, K.; Xu, F.; Loh, X. J. Thermogels: In Situ Gelling Biomaterial. *ACS Biomater. Sci. Eng.* **2016,** *2* (3), 295-316.

123. He, C.; Kim, S. W.; Lee, D. S. In situ gelling stimuli-sensitive block copolymer hydrogels for drug delivery. *J. Controlled Release* **2008,** *127* (3), 189-207.

124. Tomoko, F.; Yoshiharu, K., Thermo-Sensitive Gels: Biodegradable Hydrogels from Enantiomeric Copolymers of Poly(lactide) and Poly(ethylene glycol). In *Degradable Polymers and Materials*, American Chemical Society: 2006; Vol. 939, pp 216-233.

125. Jeong, B.; Kim, S. W.; Bae, Y. H. Thermosensitive sol–gel reversible hydrogels. *Adv. Drug Del. Rev.* **2002,** *54* (1), 37-51.

126. Li, C.; Tang, Y.; Armes, S. P.; Morris, C. J.; Rose, S. F.; Lloyd, A. W.; Lewis, A. L. Synthesis and Characterization of Biocompatible Thermo-Responsive Gelators Based on ABA Triblock Copolymers. *Biomacromolecules* **2005,** *6* (2), 994-999.

127. Kirkland, S. E.; Hensarling, R. M.; McConaughy, S. D.; Guo, Y.; Jarrett, W. L.; McCormick, C. L. Thermoreversible Hydrogels from RAFT-Synthesized BAB Triblock

Copolymers: Steps toward Biomimetic Matrices for Tissue Regeneration†. *Biomacromolecules* **2008,** *9* (2), 481-486.

128. Zhou, C.; Hillmyer, M. A.; Lodge, T. P. Efficient Formation of Multicompartment Hydrogels by Stepwise Self-Assembly of Thermoresponsive ABC Triblock Terpolymers. *J. Am. Chem. Soc.* **2012,** *134* (25), 10365-10368.

129. de Graaf, A. J.; Boere, K. W. M.; Kemmink, J.; Fokkink, R. G.; van Nostrum, C. F.; Rijkers, D. T. S.; van der Gucht, J.; Wienk, H.; Baldus, M.; Mastrobattista, E.; Vermonden, T.; Hennink, W. E. Looped Structure of Flowerlike Micelles Revealed by 1H NMR Relaxometry and Light Scattering. *Langmuir* **2011,** *27* (16), 9843-9848.

130. Li, C.; Buurma, N. J.; Haq, I.; Turner, C.; Armes, S. P.; Castelletto, V.; Hamley, I. W.; Lewis, A. L. Synthesis and Characterization of Biocompatible, Thermoresponsive ABC and ABA Triblock Copolymer Gelators. *Langmuir* **2005,** *21* (24), 11026-11033.

131. Gupta, M. K.; Martin, J. R.; Werfel, T. A.; Shen, T.; Page, J. M.; Duvall, C. L. Cell Protective, ABC Triblock Polymer-Based Thermoresponsive Hydrogels with ROS-Triggered Degradation and Drug Release. *J. Am. Chem. Soc.* **2014**.

132. Zhou, C.; Toombes, G. E. S.; Wasbrough, M. J.; Hillmyer, M. A.; Lodge, T. P. Structure of Two-Compartment Hydrogels from Thermoresponsive ABC Triblock Terpolymers. *Macromolecules* **2015,** *48* (16), 5934-5943.

CHAPTER 2 : THERMOREVERSIBLE AND INJECTABLE ABC POLYPEPTOID HYDROGELS: CONTROLLING THE HYDROGEL PROPERTIES THROUGH MOLECULAR DESIGN

2.1 Abstract

A series of ABC triblock copolypeptoids [i.e., poly (*N*-allylglycine)-b-poly (*N*-methyl glycine)-b-poly (*N*-decyl glycine) (AMD)] with well-defined structure and varying composition have been synthesized by sequential primary amine-initiated ring-opening polymerization of the corresponding *N*-substituted *N*-carboxyanhydride monomers (Al-NCA, Me-NCA, and De-NCA). The ABC block copolypeptoids undergo sol-to-gel transitions with increasing temperature in water and biological media at low concentrations (2.5−10 wt %). The sol−gel transition is rapid and fully reversible with a narrow transition window, evidenced by the rheological measurements. The gelation temperature (T_{gel}) and mechanical stiffness of the hydrogels are highly tunable: T_{gel} in the 26.2−60.0 °C range, the storage modulus (G') and Young's modulus (E) in the 0.2−780 Pa and 0.5−2346 Pa range, respectively, at the physiological temperature (37 °C) can be readily accessed by controllingthe block copolypeptoid composition and the polymer solution concentration. The hydrogel is injectable through a 24 gauge syringe needle and maintains their shape upon in contact with surfaces or water baths that are kept above the sol−gel transition temperature. The hydrogels exhibit minimal cytotoxicity toward human adipose derived stem cells (hASCs), evidenced from both alamarBlue and PicoGreen assays. Furthermore, quantitative PCR analysis revealed significant up-regulation of the Col2a1 gene and down-regulation of ANGPT1 gene, suggesting that the hydrogel exhibited biological activity in inducing chondrogenesis of hASCs. It was also

* Chapter 2 previously appeared as Xuan, S.; Lee, C.-U.; Chen, C.; Doyle, A. B.; Zhang, Y.; Guo, L.; John, V. T.; Hayes, D.; Zhang, D. Xuan, S.; Lee, C.-U.; Chen, C.; Doyle, A. B.; Zhang, Y.; Guo, L.; John, V. T.; Hayes, D.; Zhang, D. Thermoreversible and Injectable ABC Polypeptoid Hydrogels: Controlling the Hydrogel Properties through Molecular Design. *Chem. Mater*. **2016**, *28* (3), 727-737. It is reprinted by permission of ACS Publisher (see page 260).

demonstrated that the hydrogel can be used to quantitatively encapsulate water-soluble enzymes (*e.g.*, horseradish peroxidase) by manipulating the sol−gel transition. The enzymatic activity of HRP remain unperturbed after encapsulation at 37 °C for up to 7 d, suggesting that the hydrogel does not adversely affect the enzyme structure and thereby the enzymatic activity. These results suggest that the polypeptoid hydrogel a promising synthetic platform for tissue engineering or protein storage applications.

2.2 Experimental

2.2.1 General considerations

All chemicals used were purchased from Sigma-Aldrich and used as received unless otherwise noted. THF, CH_2Cl_2, and acetonitrile used in polymerization reaction were purified by passing through alumina columns under argon. ^{1}H and ^{13}C $\{^{1}H\}$ NMR were recorded on a Bruker AV-400 Nanobay spectrometer, and the chemical shifts in parts per million (ppm) were referenced to protio impurities of $CDCl_3$ and CD_2Cl_2. SEC analyses were performed using an Agilent 1200 system (Agilent 1200 series degasser, isocratic pump, auto sampler and column heater) equipped with three Phenomenex 5 μm, 300 × 7.8 mm columns, a Wyatt OptilabrEX differential refractive index (DRI) detector with a 690 nm light source, and a Wyatt DAWN EOS multiangle light scattering (MALS) detector (GaAs 30mW laser at $\lambda = 690$ nm). DMF with 0.1M LiBr was used as the eluent at a flow rate of 0.5 mL min^{-1}. The column and detector temperature was room temperature. The standard used was twenty three pauci-disperse polystyrene standards (590 $g \cdot mol^{-1}$-1472 $kg \cdot mol^{-1}$ MW, Polymer Laboratories, Inc.). All data analysis was performed using Wyatt Astra V 5.3 software.

2.2.2 Monomer synthesis

All the monomers used were synthesized by adapting reported procedures.[1] *N*-alkyl *N*-carboxyanhydrides (R-NCAs) with allyl, butyl, octyl, decyl, and methoxyethyl, methoxyethoxyethyl side chains were synthesized via synthetic routes (I), whereas Me-NCA was synthesized via route II (Scheme 2.1).

Scheme 2.1.Synthesisof *N*-alkyl *N*-carboxyanhydrides (R-NCAs).

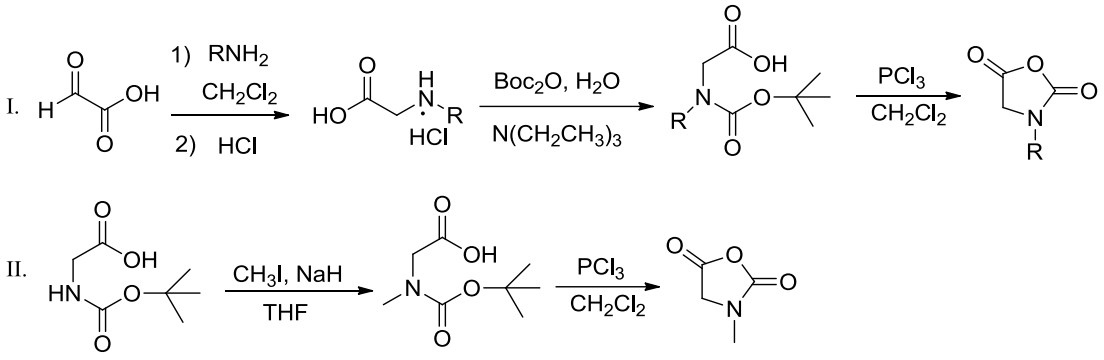

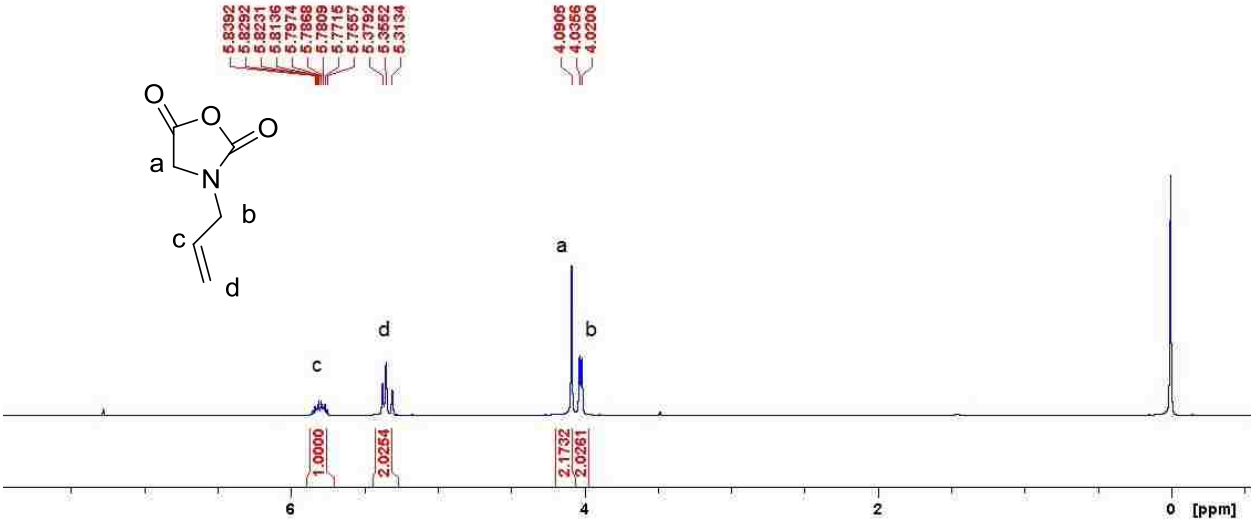

Figure 2.1.[1]H NMR spectrum of allyl-NCA in $CDCl_3$.

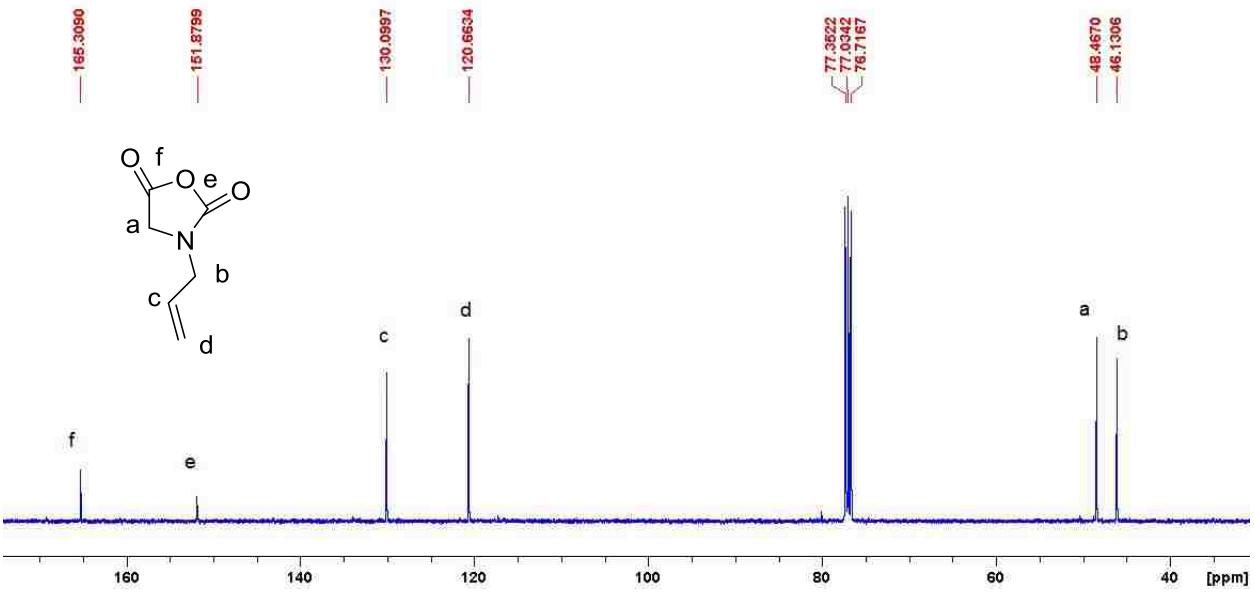

Figure 2.2. ^{13}C {^{1}H} NMR spectrum of allyl-NCA in $CDCl_3$.

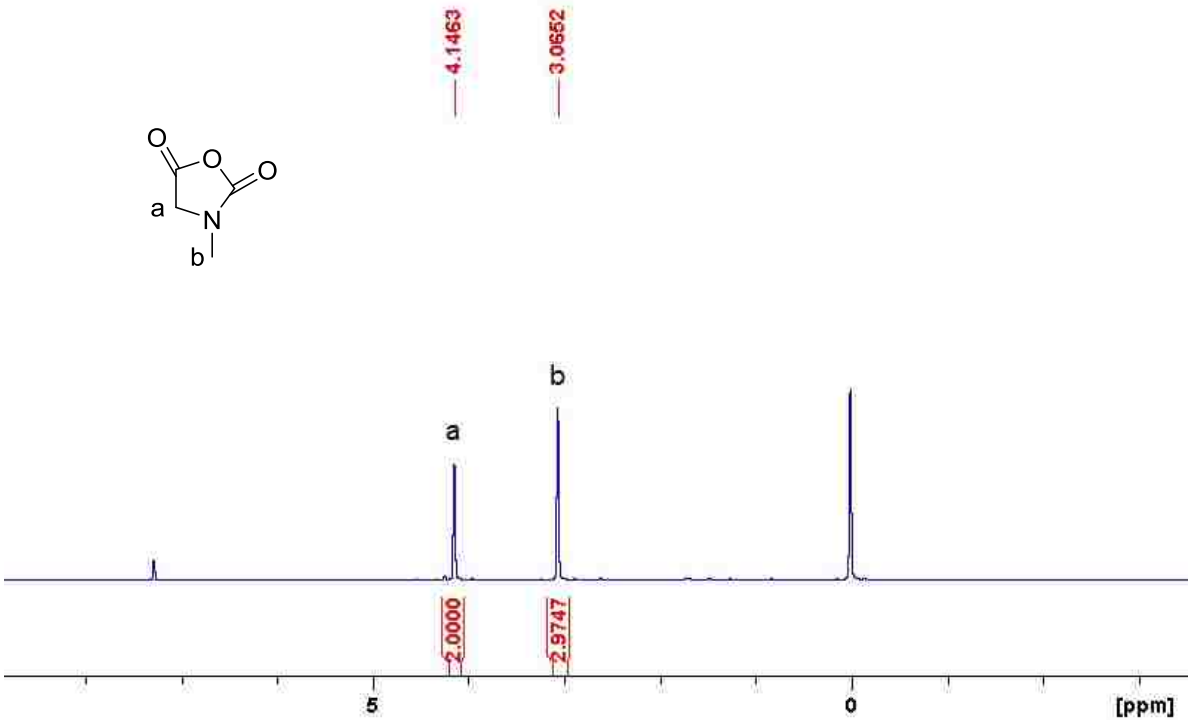

Figure 2.3. ^{1}H NMR spectrum of Methyl-NCA in $CDCl_3$.

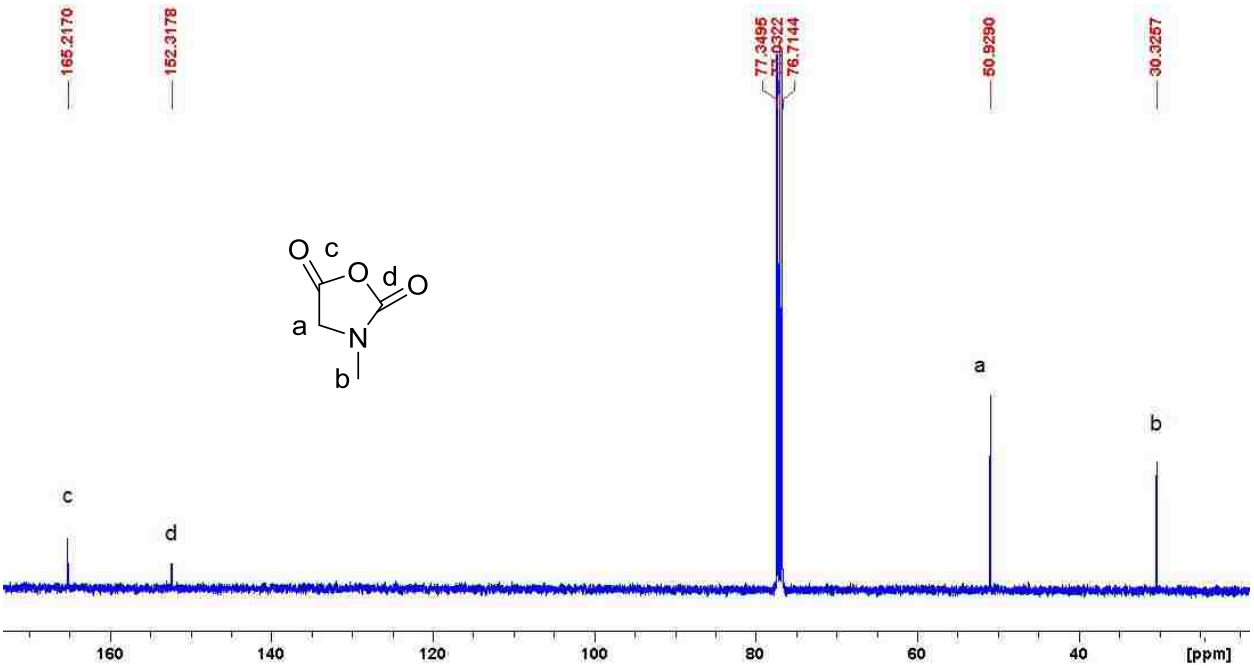

Figure 2.4. ^{13}C {^{1}H} NMR spectrum of Methyl-NCA in $CDCl_3$.

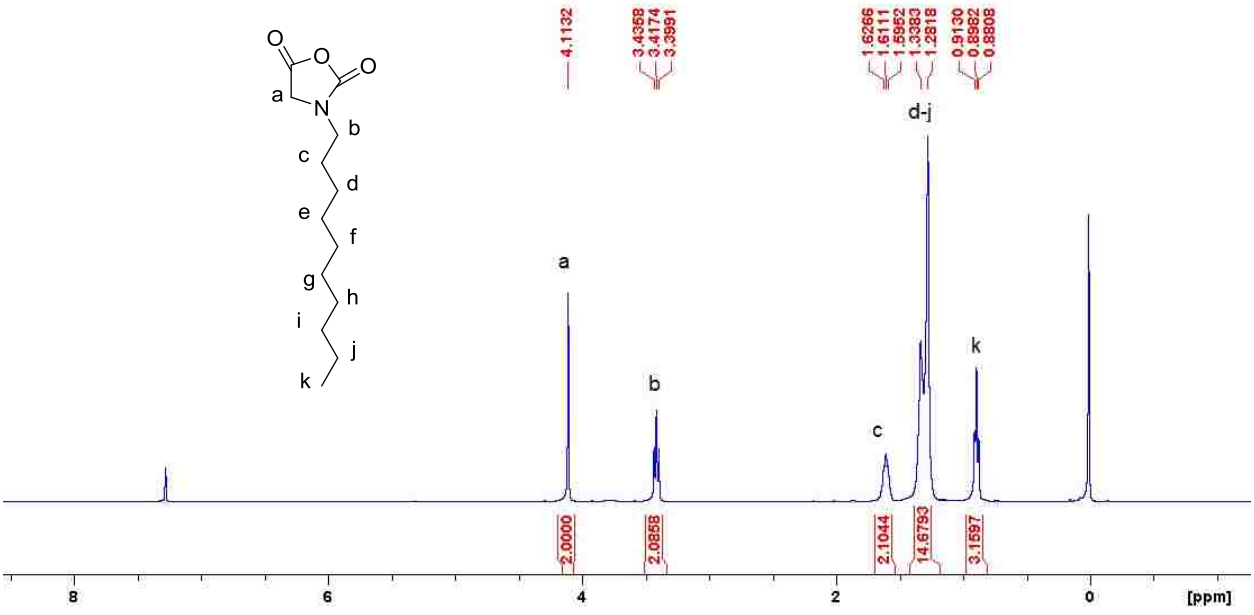

Figure 2.5. ^{1}H NMR spectrum of Decyl-NCA in $CDCl_3$.

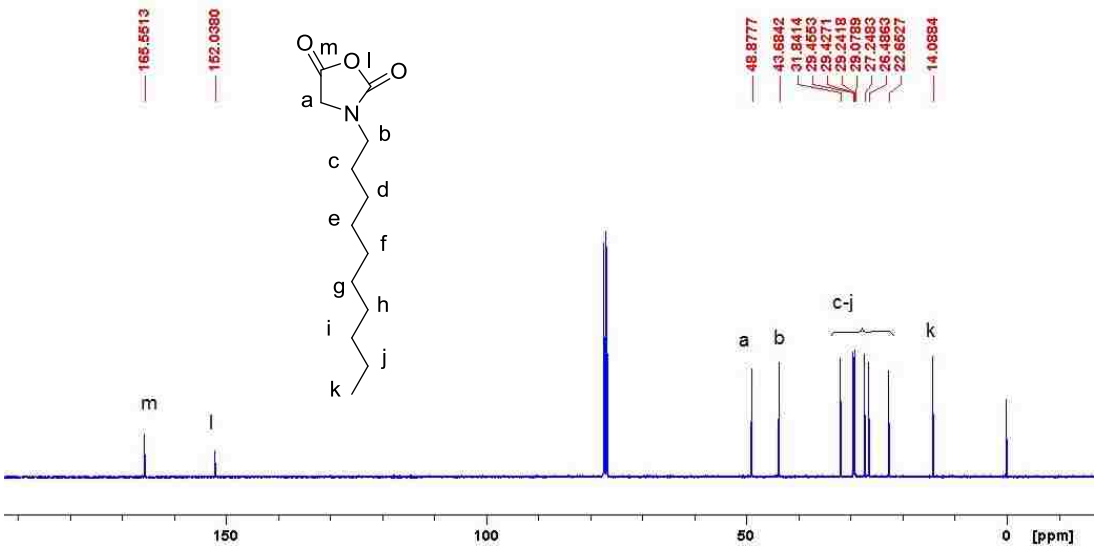

Figure 2.6. ^{13}C {^{1}H} NMR spectrum of Decyl-NCA in $CDCl_3$.

2.2.3 Polymer synthesis

All the ABC triblock copolypeptoids were synthesized by primary amine-initiated ring-opening polymerization of the corresponding *N*-substituted *N*-carboxyany-drides (R-NCAs) in a sequential manner. A representative procedure for the synthesis of $A_{98}M_{98}D_{18}$ was presented. In the glovebox, Al-NCA (136.3 mg, 0.97 mmol, $[M_1]_0$=0.4 M) was dissolved in anhydrous acetonitrile. Stock solution of benzyl amine (104 µL, 92.7 mM, $[M_1]$: $[BnNH_2]_0$=100:1) was added. The reaction mixture was heated at 50 ^oC for 24 h to reach a complete conversion of polymerization. Acetonitrile solution of Me-NCA (2.4 mL, 0.4 M, 0.97 mmol, $[M_1]_0$:$[M_2]_0$: $[BnNH_2]_0$=100:100:1) was added to the above mixture and allowed to stir at room temperature for another 24 h to reach a full conversion. Acetonitrile solution of De-NCA (475 µL, 0.4 M, 0.19 mmol, $[M_1]_0$:$[M_2]_0$:$[M_3]_0$:$[BnNH_2]_0$=100:100:20:1) was added and stirred at room temperature for an additional 24 h. The polymer was precipitated out by the addition of excess THF. The polymer was collected by filtration and washed with ample THF and hexane followed by drying under vacuum (178 mg, 89%). The composition of the polymer was determined by ^{1}H NMR spectroscopy using end-group analysis. The number average degree of polymerization (DP_n) of

each block was calculated based on the integration ratios of characteristic proton peaks due to individual block. DP_n (A) = (5 × integration of –CH=)/(1 × integration of C_6H_5); DP_n (M) = (5 × integration of $^aCH_3$)/(3 × integration of C_6H_5); DP_n (D) = (5 × integration of $^bCH_3$)/(3 × integration of C_6H_5) (a. methyl protons of M block, b. methyl protons of D block).

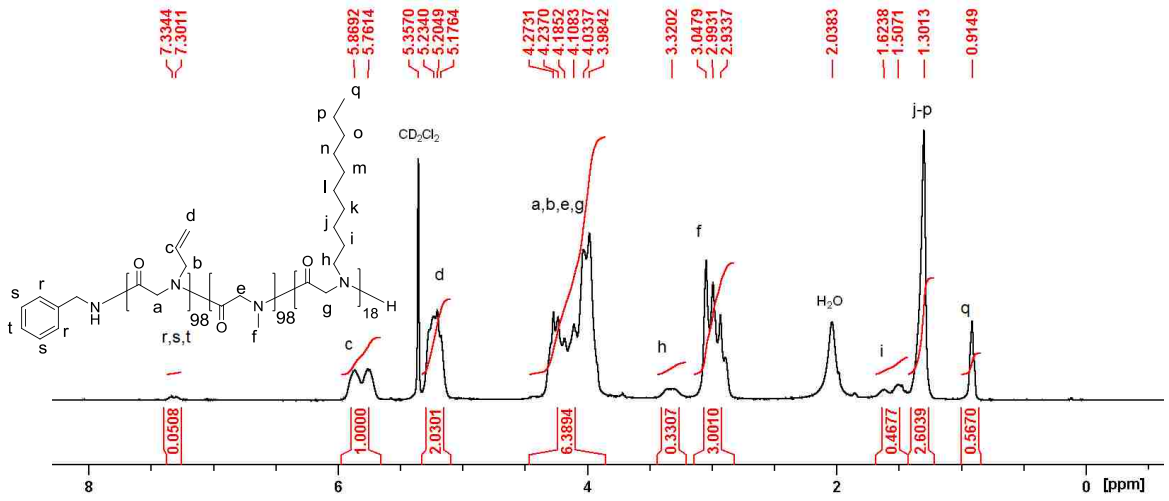

Figure 2.7. ^{1}H NMR spectrum of the $A_{98}M_{98}D_{18}$ triblock copolypeptoid in CD_2Cl_2.

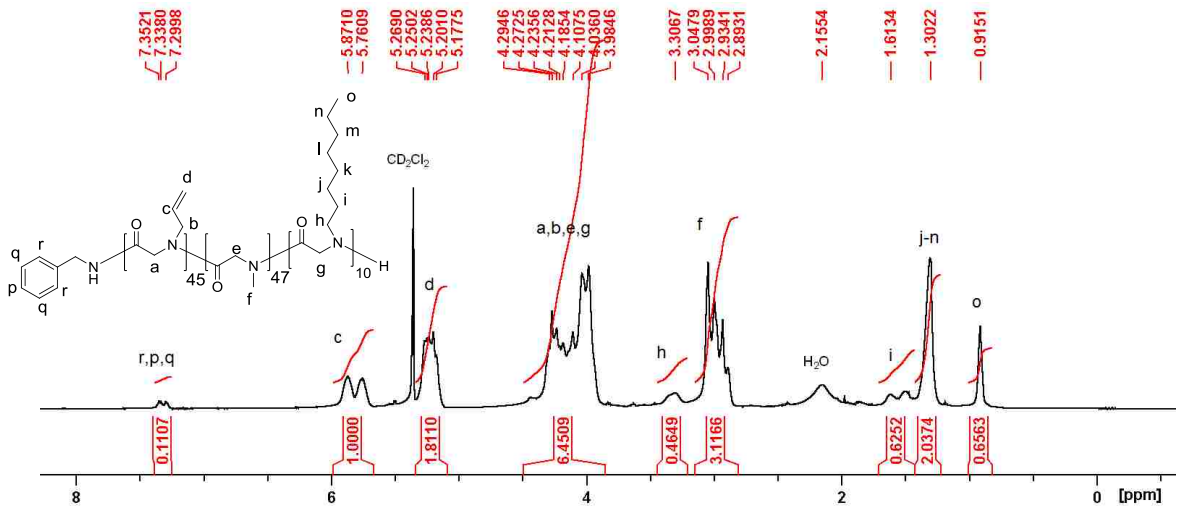

Figure 2.8. ^{1}H NMR spectrum of the $A_{45}M_{47}O_{10}$ triblock copolypeptoid in CD_2Cl_2

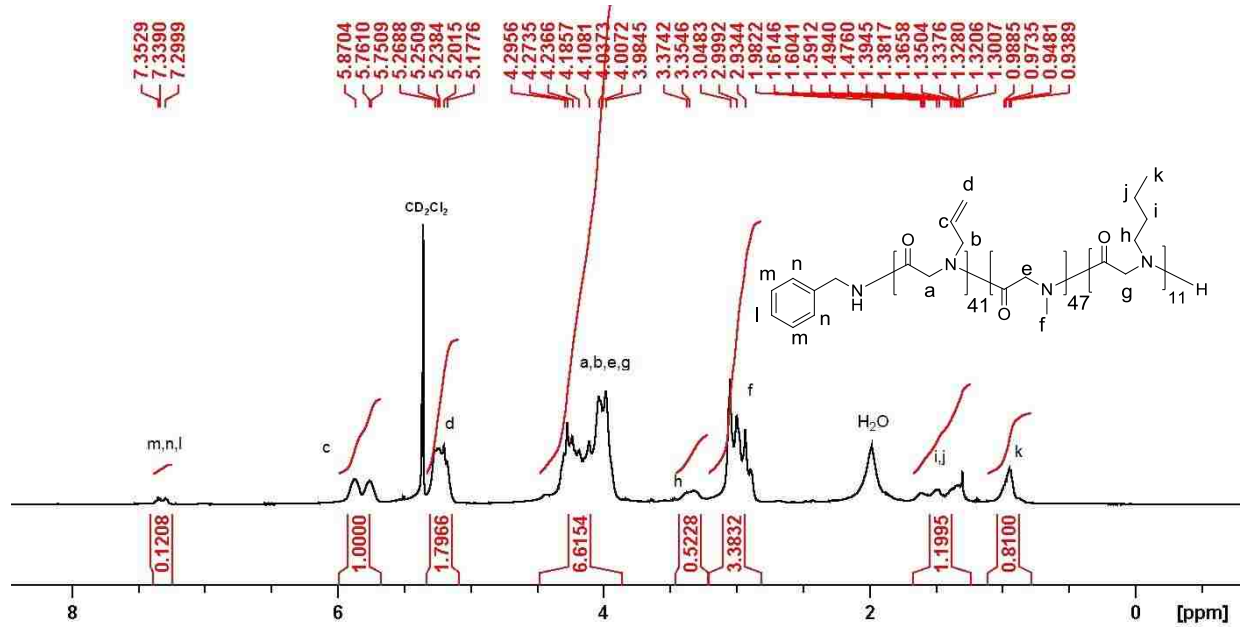

Figure 2.9. ^{1}H NMR spectrum of the $A_{41}M_{47}B_{11}$ triblock copolypeptoid in CD_2Cl_2.

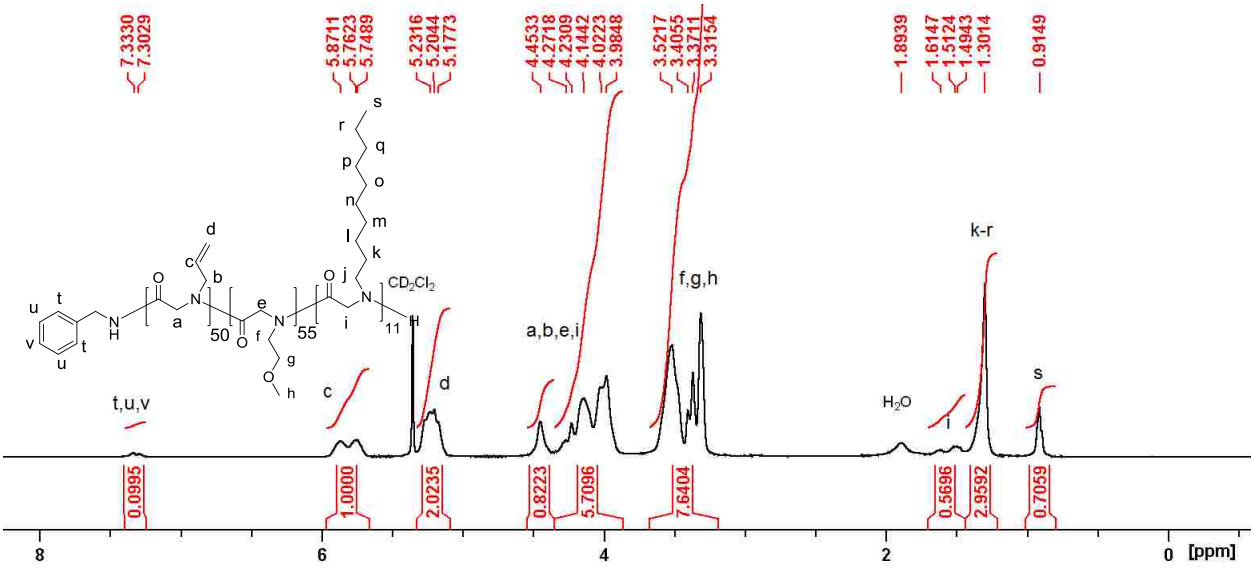

Figure 2.10. ^{1}H NMR spectrum of the $A_{50}m_{55}D_{11}$ triblock copolypeptoid in CD_2Cl_2.

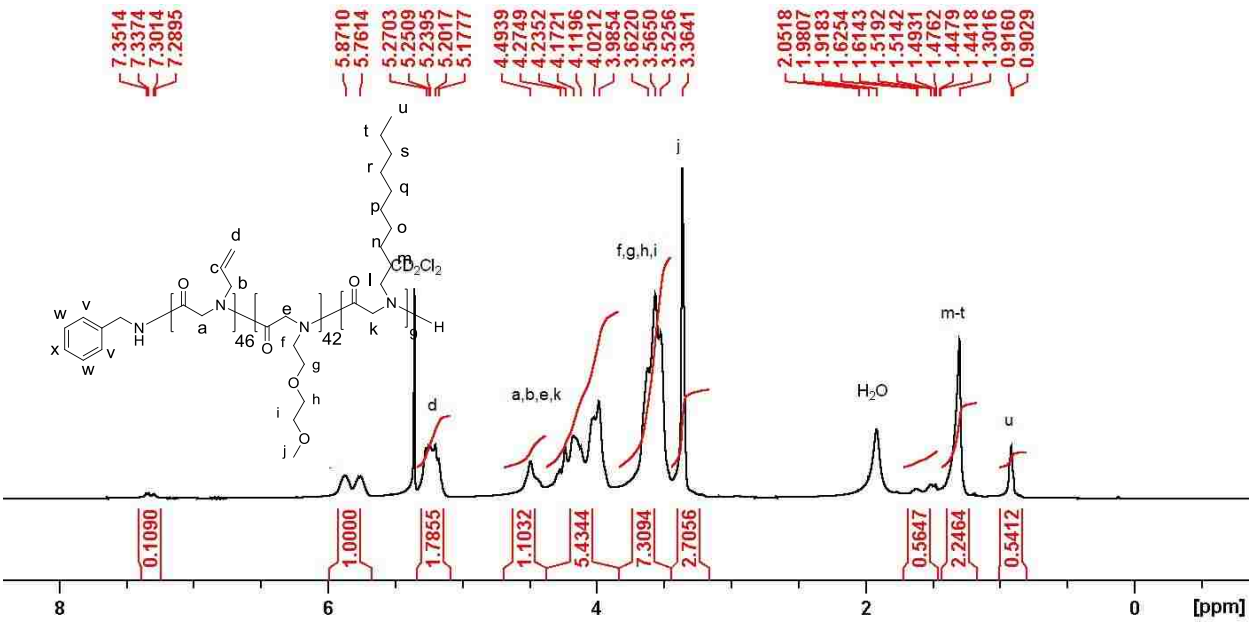

Figure 2.11. ^{1}H NMR spectrum of the $A_{46}d_{42}D_9$ triblock copolypeptoid in CD_2Cl_2.

2.2.4 Hydrogel preparation

The 5 wt% aqueous solution of triblock copolypeptoids used for the rheological measurement was prepared by "thin-film hydration", as reported by Zhou et al.[2] Briefly, a known amount of dry polymer was dissolved in CH_2Cl_2, followed by evaporation of the solvent under a stream of N_2 overnight to form a thin film on the wall of the vial. The thin film was further dried under vacuum for 1 d. Nanopure water was added, and the solution was stirred at room temperature for 3 d before further characterization. 1 wt% and 2.5 wt% aqueous solutions were prepared by direct dilution of the concentrated solution (5 wt%).

2.2.5 Characterization of hydrogel and dilute solution of polymer

Rheological measurements. Rheological study was conducted using a TA AR 2000ex rheometer. A parallel-plate geometry of 40 mm diameter was used. In each experiment, approximately 0.3 mL of the hydrogel sample was loaded between the plates with a gap of 200 μm. The metallic plate covers were then put on the plates that were sealed with highly viscous oil. Dynamic storage modulus (G') and loss modulus (G") were measured by oscillatory shear

experiments. Dynamic strain sweep experiments were conducted at a frequency of 10 rad/s at 25 ^{o}C and 45 ^{o}C to determine the linear viscoelastic regime. Dynamic frequency sweep measurements were conducted within the linear viscoelastic regime with angular frequency from 0.1 to 100 rad/s. Temperature sweep measurements were conducted from 15 ^{o}C to 60 ^{o}C at a heating rate of 1 ^{o}C/min. Below the critical gelation temperature, the solution was measured at a strain of 50 %, and above the gelation temperature at a strain of 0.75 %. The storage moduli (G') show some fluctuation after the sol-gel transition. This could be due to the structural reorganization within the gels.

Dynamic light scattering measurement of dilute solution. An aqueous solution of polymers (0.5 wt% in nanopure water) that was filtered through a 0.22 µm filter. All the DLS measurements were conducted using Malvern Zetasizer Nano-zs (Zen3600). The He-Ne laser operating at 633 nm was utilized, and scattered light intensity was detected at an external angle of 173 ^{o}C using non-invasive backscatter (NIBS) technology. Data from three measurements with 12 scans for each measurement was recorded. At each temperature, the sample was equilibrated for 3 min.

Temperature dependent 1H NMR experiments of polymer solution. The temperature dependent ^{1}H NMR experiments of polymer solution was conducted on a Bruker AV-400 Nanobay spectrometer. The $A_{92}M_{94}D_{12}$ triblock copolypeptoid was dissolved in CD_2Cl_2 and D_2O at 5 wt% respectively. In CD_2Cl_2, the ^{1}H NMR spectrum was obtained at 25 ^{o}C, whereas the spectra were collected at 25, 37 and 60 ^{o}C with increasing temperature in D_2O.

TEM/CryoTEM sample preparation and analysis. FEI Vitrobot was used for the sample preparation of cryo-TEM experiment. 5 µL aqueous solution of ABC copolymer (1 wt%) was applied to a 300 mesh lacey carbon coated TEM grid. Double side blotting to the grid for 2 seconds

leaves a thin film on the grid. The grid then was quickly plunged into liquid ethane chilled by liquid nitrogen. The vitrified sample grid was loaded in a single tilt liquid nitrogen cryo transfer holder, and was then inserted to FEI G2 F30 Tecnal TEM operated at 120keV, with a FEI digital camera and analyzed using FEI Digital Micrograph software. The grids for the regular TEM was prepared by adding 5 μL polymer aqueous solution (0.2 wt%) onto the 300 mesh carbon grid followed by blotting with a filter paper and drying at room temperature. The grids then were stained with uranyl acetate for 1 min.

Cryo-SEM sample preparation and analysis. Aqueous Polymer solution of 5 wt% $A_{92}M_{94}D_{12}$ (~40 μL) was pipetted on top of a metal rivet and was heated up by a hot plate for gel formation, indicated by the color change of the liquid drop from clear to white. The gel sample was then plunged into liquid nitrogen, followed by fracturing at -130 ^{o}C using a flat-edge cold knife. The solvent was sublimated at -95 ^{o}C for 5 min and the sample was sputtered with a platinum-palladium composite at 10 mA for 88 seconds before imaging. The vitrified sample was imaged on a Hitachi S-4800 field emission scanning electron microscope using cryo-mode operated at a voltage of 3 kV.

Cloud point measurement of ABC triblock copolypeptoid solutions. Cloud point measurements of aqueous solutions of both poly(*N*-allyl glycine) homopolymer (A) and $A_{98}M_{98}D_{18}$ triblock copolymers (1 wt%) were conducted using Varian Cary 50 Bio-UV-vis spectrophotometer equipped with a Thermo/Neslab RTE-7 refrigerated bath circulator for temperature control. The experimental temperature range is 15-60 ^{o}C and all UV-vis absorptions were referenced against distilled water. The temperature at 50 % UV-vis transmittance (λ = 450 nm) is defined as the cloud point.

2.2.6. Protein encapsulation study of hydrogel

10 µL of 0.14 mg/mL HRP in PBS buffer was added to 100 µL of aqueous polymer solution (5 wt%) and well mixed. The mixture was incubated at 37 ^{o}C in an oil bath for different time (1 h, 4 h, 7 h, 24 h, and 7 d). After each time period, the mixture was cooled down to room temperature and diluted with PBS buffer using 1.0 ml volumetric flask, which was further used for the kinetic study. To a disposable cuvette, 3 ml of PBS buffer, 20 µL of 0.1 M Guaiacol in PBS buffer and 40 µL of the above diluted solution was added. 20 µL of 0.1 M H_2O_2 in PBS buffer was quickly injected to the above mixture and well mixed. The cuvette was immediately monitored at room temperature every 40 seconds by a Varian Cary 50 Bio-UV-Vis spectrophotometer at a wavelength range of 200-600 nm. All UV-Vis absorptions were referenced against PBS buffer. For comparison, the enzymatic activity of two sets of controls was measured using the same method described above. One control involves incubation of HRP in PBS buffer at 37 ^{o}C for different duration (1, 4, 7, 24 h and 7 d). The other control is the as-received HRP whose enzymatic activity was directly measured in PBS at 25 ^{o}C.

2.2.7. Biological studies of hydrogels and polymer solutions

Adult stem cells isolation and culture. Liposuction aspirates from subcutaneous adipose tissue were obtained from three healthy adult subjects (male = 1 and females = 2) undergoing elective procedures. All tissues were obtained with informed consent under a clinical protocol reviewed and approved by the Institutional Review Board at the LSU Pennington Biomedical Research Center and used under an exempted protocol at LSU A&M College. Isolation of hASC was performed as published.[3] Passage 2 of each individual was used for in vitro hASC evaluation on tissue culture treated plastic or on scaffold of hydrogel. In both cases, hASC were cultured in stromal (control - DMEM, 10 % FBS, and 1 % triple antibiotic solution) media with media

maintenance performed three times a week. For the live control, stem cells were cultured in plain media. For the dead control, stem cells were cultured in media and then introduced to 70 % ethanol.

Extract cytotoxicity Assessment. The extract cytotoxicity study was modified based on FDA protocol.[4] The hydrogel samples (0.1 g) were incubated on an orbital shaker with 5 mL stromal media at 37 ˚C and 200 rpm/min for 7 days. The extractives were filtered (0.22 μm pore size) and pipetted (100 μL/well) into a 96-well plate previously sub-cultured with hASC (2,500 cells/well) and incubated in a CO_2 incubator at 37 ˚C containing 5 % CO_2 for 24 hours. 10 μL alamarBlue® reagent to each well and re-incubated at 37 ˚C in 5 % CO_2 for 2 h. The fluorescence was measured at an excitation wavelength of 530 nm and an emission wavelength of 595 nm using a fluorescence plate reader. The tissue culture treated plastic 96-well plate served as a control substrate.

hASC loading on ABC hydrogel and culture. The ABC hydrogel was filtered through a 0.22 μm filter at 20 ˚C and 100 μL aliquots was mixed with 1×10^4 cells/μL for total volume of 10 μL. The cells and hydrogel mixture was transferred to a 96 well plate afterwards. 100 μL stromal medium was added to each well after the cells/hydrogel mixture was solidified at 37 ˚C.

In vitro hASCs viability on scaffolds with alamarBlue® stain. The viability of cells within ABC hydrogel in stromal media was determined after 3 days using an alamarBlue® metabolic activity assay. The cells/hydrogel mixture were removed from culture, washed three times in PBS, and incubated with 10 % alamarBlue® in Hank's balanced salt solution (HBSS) without phenol red (pH 7) for 90 min. Aliquots (100 μL) of alamarBlue®/HBSS were placed in a 96-well plate in triplicate, and the fluorescence was measured at an excitation wavelength of 530 nm and an emission wavelength of 595 nm using a fluorescence plate reader.

In vitro quantification of DNA on scaffolds. Total DNA content was used to determine the number of cells on each scaffold as previously described.[5] After the scaffolds were minced by a scalpel and the DNA was digested with 0.5 mL 0.5 mg/mL proteinase K (Sigma-Aldrich) at 56 °C overnight, aliquots (50 µL) were mixed with equal volumes of 0.1 g/mL PicoGreen dye solution (Invitrogen) in 96-well plates. Samples were then excited at 480 nm with a plate reader (Wallac 1420 multilabel hts counter). Scaffolds without cells were used as negative controls.

In vitro hASCs Viability on polymer solution with alamarBlue® Stain. The copolymer was dissolved in stem cell media (40 % v/v). The solution was used as a stock solution to dilute and receive concentration values of 20 %, 10 %, 5 %, 2 %, and 1 % copolymer in media. Stem cells were seeded in a 96-well plate at a density of 40,000 cells per well and incubated for 24 h at 37 □C. Culture media (95% Dulbecco's Modified Eagle Medium, 4.5 % fetal bovine serum, 0.5 % penicillin, streptomycin, and amphotericin) was subsequently replaced with serum-free media. Polypeptoids were then added at 40, 20, 10, 5, 2, and 1 % (v/v) per well. Cells were incubated for 4 h before the medium was replaced with serum-containing media. Cell viability was assessed using the standard alamarBlue® cell viability assay 24 h later. Following 4 h of alamarBlue uptake, fluorescence data was collected at an excitation wavelength of 530 nm and an emission wavelength of 595 nm using fluorescence plate reader.

Quantitative real-time polymerase chain reaction (QPCR). Quantitative real-time polymerase chain reaction (QPCR) was utilized to examine the effects of the hydrogel on human adult stem cell (hASC) differentiation. hASC were cultured in 100 µL of hydrogel (5 wt% of $A_{92}M_{94}D_{12}$ in medium) and stromal media (Dulbecco's minimal essential medium (DMEM), 10 % fetal bovine serum (FBS), and 1 % antibiotic solution (penicillin, streptomycin, fungizone)) at 37 °C and 5 % CO_2 in a humidified atmosphere. Following incubation, RNA was extracted with TRI

Reagent® (Sigma) according to the manufacturer's instructions. The isolated RNA was then used to perform QPCR with iScript™ One-Step RT-PCR Kit with SYBR®Green (Bio-Rad) using a MiniOpticon™ Real-Time PCR Detection System (Bio-Rad). Expression of the genes *Col2a1* and *ANGPT1* was used to quantify the hydrogel's ability to induce chondrogenic and angiogenic differentiation, respectively. QPCR samples were normalized against the house keeping gene *18s rRNA* and relative to separate hASC cultures maintained in chondrogenic growth medium (StemPro® Chondrogenesis Differentiation Kit; Life Technologies) and endothelial growth medium (EGM™-2 BulletKit™; Lonza) with SingleQuots™ (Lonza) containing vascular endothelial growth factor (VEGF), human basic fibroblast growth factor (hFGF-b), epidermal growth factor, insulin-like growth factor-1, heparin, ascorbic acid, and 5 % FBS.

Statistical analysis. The results of alamarBlue, PicoGreen and QPCR analysis were reported as mean ± standard deviation. Data was evaluated with one or two way analysis of variance (ANOVA), and analyzed by Tukey's minimum significant difference (MSD) post hoc test for pairwise comparisons of main effects. A P-value < 0.05 was considered significant for all comparisons.[6]

2.3. Results and discussion

2.3.1. Synthesis and characterization of ABC triblock copolypeptoids

A series of ABC triblock copolypeptoids have been synthesized by benzyl amine-initiated ring-opening polymerization of the corresponding *N*-substituted *N*-carboxyanhydrides (R-NCAs) in a sequential manner (Scheme 2.2). Representative ^{1}H and ^{13}C $\{^{1}H\}$ NMR spectra of the monomers were shown in Figure 2.1-2.6 in section 2.2. The hydrophobic C segment consists of poly (*N*-alkyl glycine) where the alkyl groups is varied from butyl (B), octyl (O) to decyl (D) with increasing hydrophobicity. The hydrophilic B segment consists of either poly (*N*-methyl glycine)

(M) or poly(*N*-methoxyethyl glycine) (m) or poly(*N*-methoxyethoxyethyl glycine)(d) with increasing hydrophilicity. The M, m and d homopolymers are highly water soluble with solubility in the 20-200 mg/mL range. The thermoresponsive A segment is based on poly (*N*-allyl glycine) (A) for all samples. Poly(*N*-allyl glycine) has previously been demonstrated to be thermoresponsive with cloud point in the 27-54 °C range, which is dependent on the chain length and concentration.[7]

Scheme 2.2. Synthesis of ABC copolypeptoids.

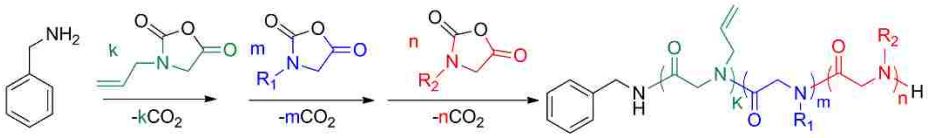

Abbrev.	R_1	Abbrev.	R_2
M		D	
m		O	
d		B	

Copolymer Comp.	R_1	R_2
AMD	M	D
AMO	M	O
AMB	M	B
AmD	m	D
AdD	d	D

All polymerization reactions were conducted in 50 °C anhydrous acetonitrile and were allowed to reach complete conversion prior to the addition of another monomer. The resulting triblock copolymers were purified by precipitation in hexane and dried under vacuum prior to further analysis. The ABC triblock copolypeptoid compositions were determined by ^{1}H NMR spectroscopy (Figure 2.7−2.11). For example, the number-averaged degree of polymerization (DP_n) of the AMD polymers (Entry 1−6, Table 2.1) was determined by the integrations at 0.91, 3.0, and 5.8 ppm due to the methyl protons in D and M blocks as well as the terminal alkenyl protons in the A block relative to the integration of signals at 7.3 ppm due to the benzyl end-group. The triblock copolypeptoids composition can be systematically adjusted by controlling the initial monomer to initiator feed ratio (Table 2.1). The weight fraction of individual block is varied in the 0.31−0.50, 0.34−0.54, and 0.13−0.21 range for the A, B, and C segments, respectively (Table 2.1).

Table 2.1. Molecular Parameters of ABC Triblock Copolypeptoids and the Corresponding Hydrogel Properties.

	Sample composition [a]	$[M_1]_0$:$[M_2]_0$:$[M_3]_0$:$[I]_0$ [b]	M_n(theor.) (kDa) [c]	M_n(NMR) (kDa) [d]	M_n(SEC) (kDa) [e]	PDI [e]	f_1 [f]	f_2 [f]	f_3 [f]	T_{gel} (°C) [g]	G'' (Pa) [h]	G' (Pa) [h]	E (Pa) [i]
1	$A_{98}M_{98}D_{18}$	100:100:20	20.8	20.0	36.7	1.04	0.47	0.35	0.18	26.2±1.2	36±4	251±23	762±68
2	$A_{92}M_{94}D_{12}$	100:100:10	18.9	18.1	36.4	1.09	0.50	0.36	0.14	26.6±0.6	58±8	780±46	2346±139
3	$A_{94}M_{158}D_{16}$	100:150:20	26.0	23.6	41.4	1.09	0.39	0.48	0.13	30.7±1.0	32±1	189±8	573±22
4	$A_{43}M_{92}D_{9}$	50:100:10	14.0	12.6	29.8	1.08	0.33	0.52	0.14	40.9±1.3	- [j]	- [j]	- [j]
5	$A_{45}M_{45}D_{10}$	50:50:10	10.5	9.64	24.1	1.03	0.46	0.34	0.21	31.0±0.3	11±1	125±8	378±23
6	$A_{23}M_{25}D_{5}$	25:25:5	5.29	5.10	10.3	1.15	0.45	0.36	0.20	>60.0	- [j]	- [j]	- [j]
7	$A_{45}M_{47}O_{10}$	50:50:10	10.2	9.50	26.5	1.06	0.46	0.35	0.18	31.4±0.4	4±1	25±9	76±27
8	$A_{41}M_{47}B_{11}$	50:50:10	9.64	8.66	28.2	1.06	0.47	0.39	0.14	32.7±0.7	0.07±0.01	0.2±0.04	0.5±0.1
9	$A_{50}m_{55}D_{11}$	50:50:10	12.7	13.5	26.5	1.07	0.31	0.54	0.15	30.6±0.6	8±1	60±8	182±25
10	$A_{46}d_{42}D_{9}$	50:50:10	14.9	13.0	26.8	1.07	0.36	0.51	0.14	42.6±1.1	- [j]	- [j]	- [j]

[a] The numbers in subscripts correspond to the DP_n of individual block determined by end-group analysis using ^{1}H NMR spectroscopy in CD_2Cl_2; [b] initial monomer to initiator ratio; [c] theoretical molecular weights were calculated from the initial monomer to initiator ratio; [d] determined by ^{1}H NMR analysis; [e] determined by the SEC-DRI method using polystyrene standards (0.1 M LiBr/DMF, room temperature); [f] f_1, f_2, and f_3 refer to the weight fraction of the thermoresponsive A end block, the hydrophilic middle block and the hydrophobic end block respectively; [g] T_{gel} is the crossover point of G' and G" in the plot of G' and G" versus temperature: average of two measurements; [h] G' and G" in the gel state at physiological temperature (37 °C): average of two measurements; [i] Young's modulus is calculated using $E = 2G(1+\nu)$, $G = (G'^2+G''^2)^{1/2}$, $\nu = 0.5$, ν is he Poisson's ratio;[8] [j] The polymer solution did not form a gel at 37 °C.

Size exclusion chromatographic (SEC) analysis of the polymer products obtained after the growth of each block revealed monomodal peaks that are consistently shifted toward lower elution time, in agreement with the block copolymer formation (Figure 2.12). The polymer molecular weight distribution remains narrow with low polydispersity indices (PDI) in the 1.03−1.15 range (Figure

2.13), consistent with the formation of well-defined block copolypeptoid polymers. The molecular parameters of the triblock copolypeptoid samples are summarized in Table 2.1.

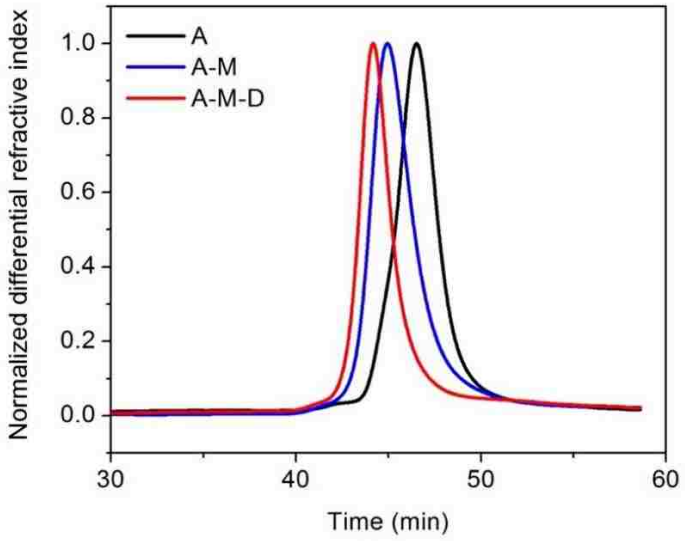

Figure 2.12. Representative SEC chromatograms showing the successful enchainment for the synthesis of the ABC triblock copolypeptoid ($A_{98}M_{98}D_{18}$, Entry 1, Table 2.1).

2.3.2. Preparation of the ABC hydrogels

All aqueous solutions of ABC triblock copolymers were prepared by the "thin film hydration" method, as reported by Zhou et al.[2] All samples underwent thermoreversible gelation in DI water, as evidenced by rheological measurements (*vide infra*). The 5 wt % solutions of selected polymers (Entry 1, 2, 3, 5, 7, and 9, Table 2.1) form free-standing opaque gels at close-to-body temperature, and return to a free-flowing liquid when cooled down to room temperature (Figure 2.14−2.15). The ABC triblock copolymers also underwent sol-to-gel transition in biological media (stromal media) at the same concentrations.The sol-to-gel transition is rapid with the formation of free-standing gels in less than 30 s. Repeated heating and cooling experiments indicate that the sol-to- gel transition is fully reversible. The hydrogels appear opaque, suggesting the occurrence of phase separation to some extent during gelation. The hydrogels are injectable th-

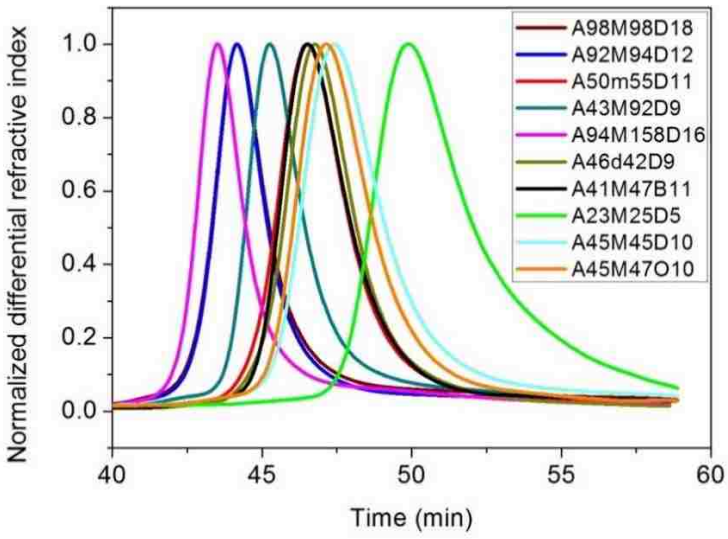

Figure 2.13. Representative SEC chromatograms of all ABC triblock copolypeptoids (Entry 1-10, Table 2.1).

rough a 24 gauge syringe needle and maintain the shape upon contact with 37 °C surfaces or DI water bath.

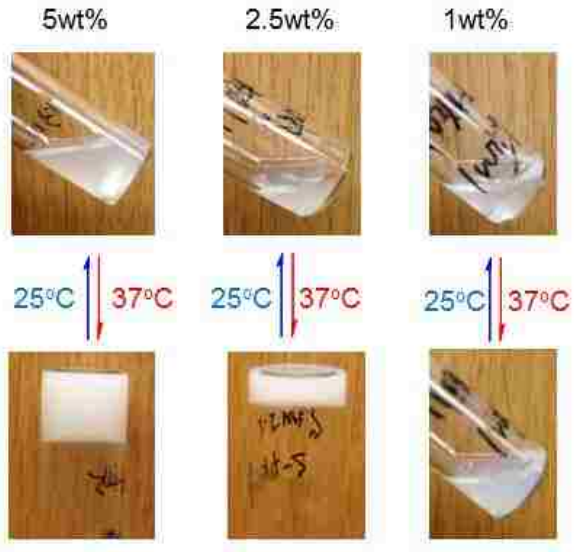

Figure 2.14. Optical images showing the thermoreversible gelation of $A_{98}M_{98}$ D_{18} at different concentration in DI water.

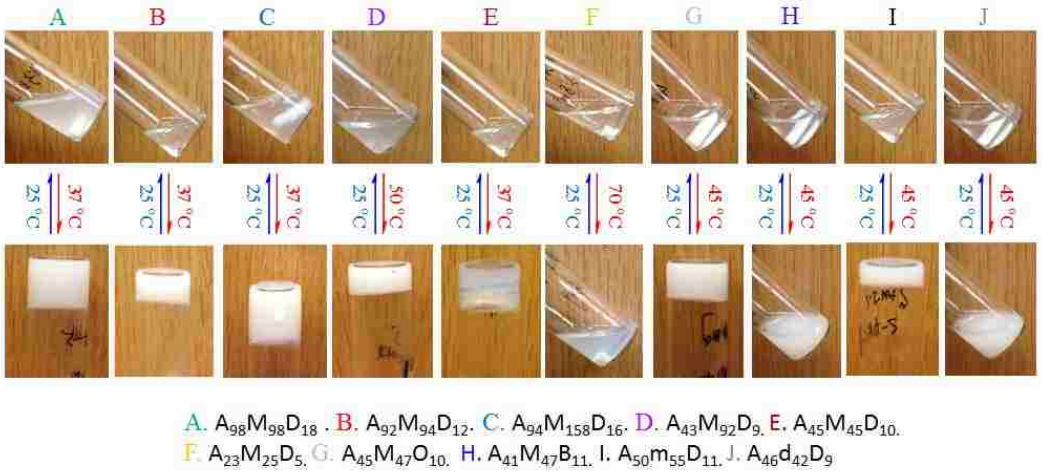

Figure 2.15. Optical images showing the thermoreversible gelation of ABC triblock copolymers at 5 wt% in DI water.

2.3.3. Rheological characterization of the sol−gel transition

Rheological measurements of the ABC polypeptoid hydrogels were conducted to quantify the gelation temperature and assess the relative mechanical stiffness of the hydrogels. Two measurements were conducted for each sample (see representative data in Figures 2.16-2.18). Temperature-dependent dynamic shear moduli (storage moduli G' and loss moduli G") of the polypeptoid aqueous solution were recorded at a frequency of 10 rad/s and heating rate of 1 °C/min over a 15−60 °C temperature range. A representative evolution of G' and G" with increasing temperature is shown in Figure 2.18 for a 5 wt % aqueous solution of $A_{98}M_{98}D_{18}$ (Entry 1, Table 2.1). The storage (G′) and loss modulus (G″) are both low with G″ larger than G′ at low temperature range, which indicates the viscous liquid-like behavior of the solution. As the temperature increases to the transition point, the G′ and G″ of the sample increase sharply to reach a crossover point at which the G′ starts to exceed the G″, indicating an elastic solid-like behavior of the solution beyond the critical temperature point. Here, we define the crossover point of the G′ and G″ as the gelation temperature (T_{gel}). With further increase of the temperature, the G′ and G″ values continue to increase and eventually plateau, suggesting the formation of stable hydrogels with a certain

mechanical stiffness. To investigate the reversibility of the gelation, a second temperature sweep of the G′ and G″ was conducted after the sample was cooled down to the starting temperature (Figure 2.19). The two measurements are nearly overlapped, indicating that the sol−gel transition is reversible.

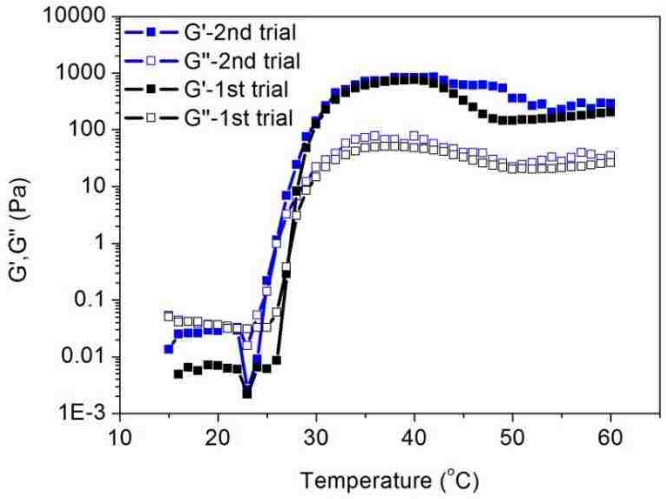

Figure 2.16. Plots of storage (G', filled symbols) and loss moduli (G", open symbols) versus temperature for the $A_{92}M_{94}D_{12}$ (5 wt%): 1st trial (G', ■ ; G", □) and 2nd trial (G', ■ ; G", □).

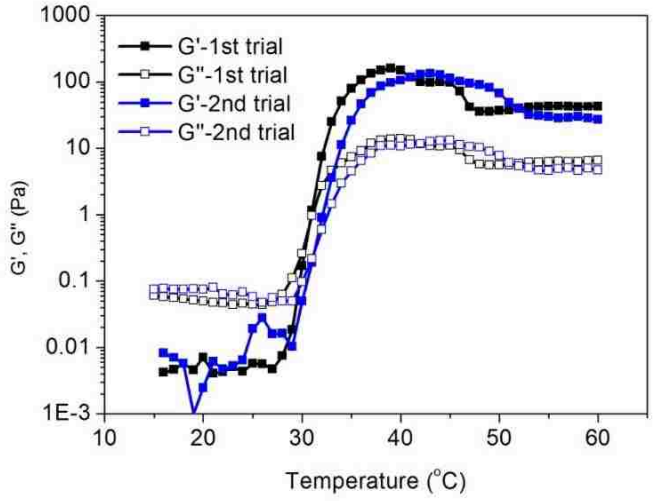

Figure 2.17. Plots of storage (G', filled symbols) and loss moduli (G", open symbols) versus temperature for the $A_{45}M_{45}D_{10}$ (5 wt%): 1st trial (G', ■ ; G", □) and 2nd trial (G', ■ ; G", □).

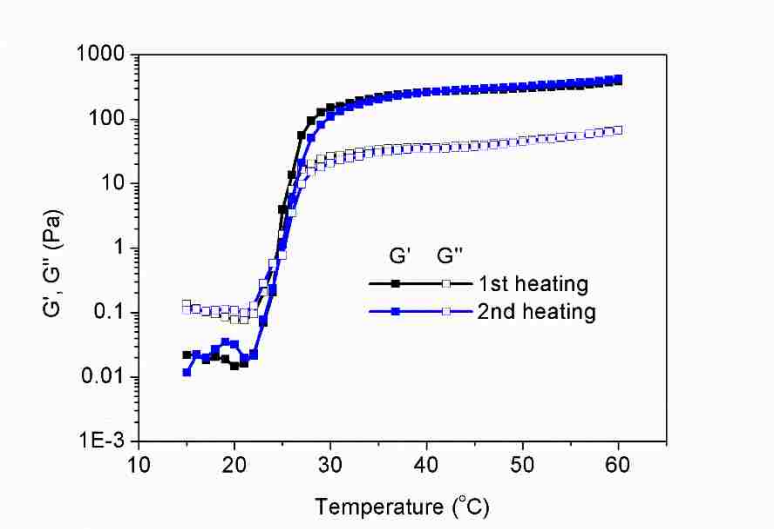

Figure 2.18. Plots of storage (G′, filled symbols) and loss moduli (G″, open symbols) versus temperature for the $A_{98}M_{98}D_{18}$ (5 wt %): first heating (G′, ■ ; G″, □) and second heating (G′, ■ ; G″, □).

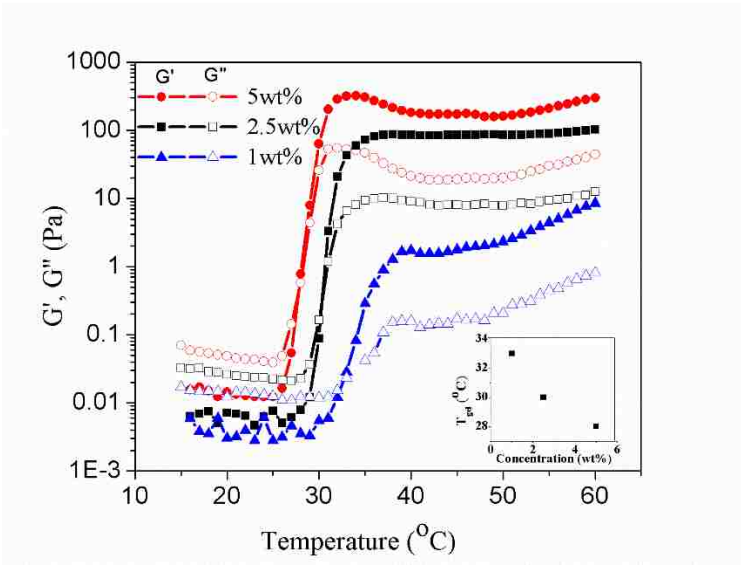

Figure 2.19. Plots of storage (G′, filled symbols) and loss moduli (G″, open symbols) versus temperature for the $A_{98}M_{98}D_{18}$ (Entry 1, Table 2.1) polymer solutions at 1 wt % (G′, ▲; G″ Δ), 2.5 wt % (G′, ■; G″,□), and 5 wt % (G′, ● ; G″, ○). Inset shows the plot of T_{gel} versus polymer concentration.

To further characterize the rheological properties of the sol and the gel based on the $A_{98}M_{98}D_{18}$ triblock copolypeptoid (Entry 1, Table 2.1), measurement of dynamic shear moduli as

a function of angular shearing frequency was conducted (Figure 2.20). At 22 °C, the loss modulus (G″) is larger than the storage modulus (G′) and both moduli are close to zero at low frequency and adapt a terminal rheological behavior indicative of a viscous liquid. At 25 °C, the G′ started to superimpose on the G″ and approaches the critical gelation temperature when G′ and G″ follow a power law with an exponential of approximately 1/2 ($G' \approx G'' \sim \omega^{0.5}$) (Figure 2.20).[2] At 37 °C, G′ is large than G″ through the whole frequency range and is nearly frequency independent, indicating the formation of a stable elastic solid-like hydrogel.

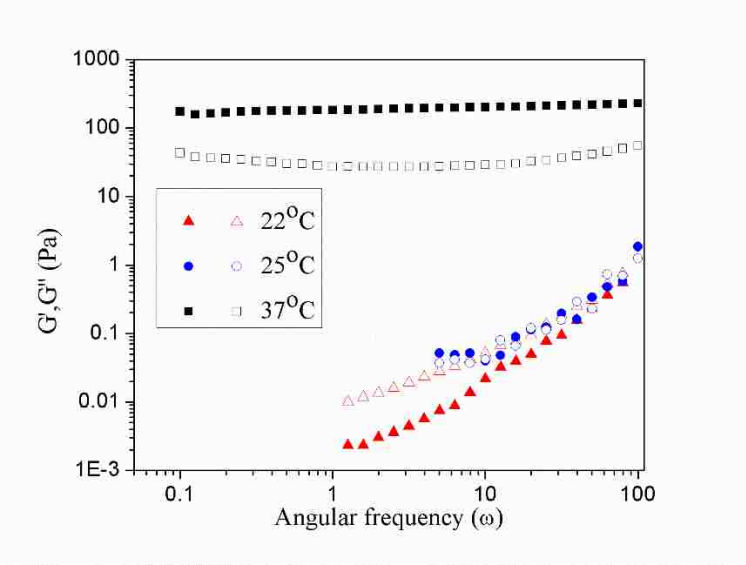

Figure 2.20. Plots of storage modulus (G′, filled symbols) and loss modulus (G″, open symbols) versus angular frequency (ω) for the 5wt % aqueous solution of $A_{98}M_{98}D_{18}$ (Entry 1, Table 2.1) at different temperatures: 37 °C (G′, ■; G″, □), 25 °C (G′, ●; G″, ○), and 22 °C (G′, ▲; G″ Δ).

2.3.4. Microscopic characterization of the hydrogel

To investigate the microscopic structure of the hydrogel, cryo-SEM was conducted on the $A_{92}M_{94}D_{12}$ hydrogel (5 wt %, 2.5wt% and 1 wt%) freshly formed at 37 °C. The cryo-SEM microgram revealed a highly porous structure with large mesh size in the micron regime (>3 μm) (Figure 2.21), consistent with a gel structure formed by phase separation. The pore size of the hydrogel can be easily tailored by controlling the concentration of the polymer solution. As

expected, the pore size of the hydrogel gradually increased with decreasing polymer solution concentration, consistent with the decreased hydrogel stiffness with increasing concentration measured by rheological analysis. The average pore size measured long the longest and shortest axis of at least 50 pores for 5wt% hydrogel (Figure 2.21 A and B) was 3.23 ± 0.68 μm and 7.26 ± 1.46 μm, respectively. As the concentration decreased to 2.5 wt%, the pore size of the hydrogel (Figure 2.21 C) along the longest and shortest axis increased to 3.48 ± 0.82 μm and 10.38 ± 5.06 μm, respectively. As the concentration further decreased to 1wt%, the hydrogel exhibited a lamellar morphology. The average spacing between the lamella was 4.13 ± 0.71 μm, whereas the lamellar morphology spans more than 50 μm continuously.

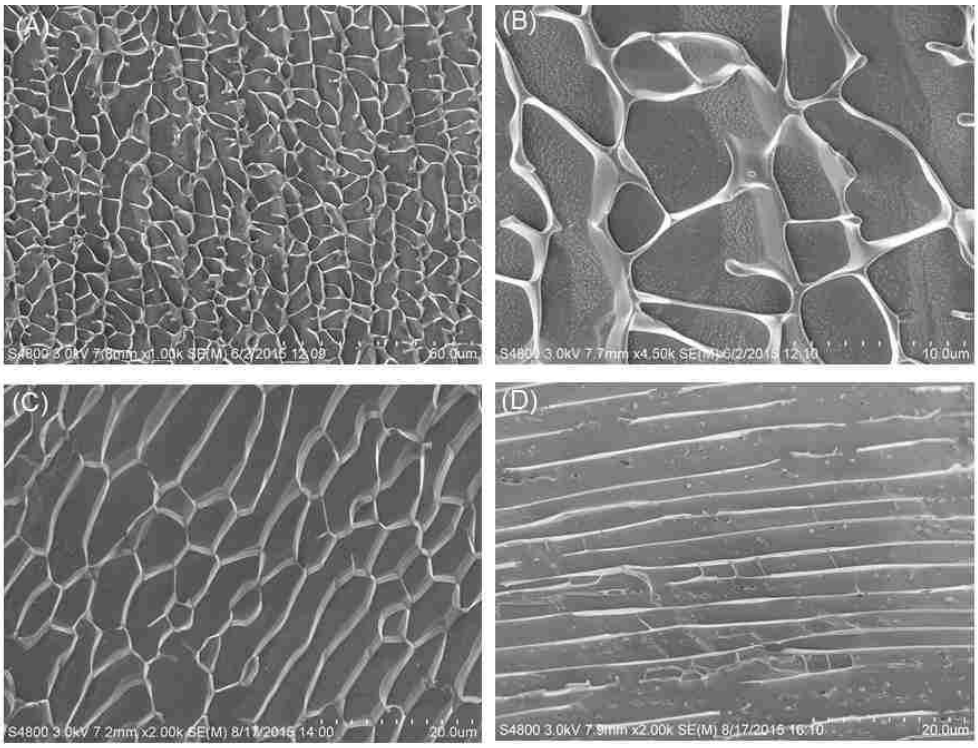

Figure 2.21. Cryo-SEM images of the 5 wt % (A,B), 2.5 wt% (C) and 1wt% (D).$A_{92}M_{94}D_{12}$ hydrogel The scale bar in (A) and (B) is 50.0 and 10.0 μm, respectively. The scale bar in (C) and (D) is 20.0 μm.

2.3.5. Characterization of micellation of ABC triblock copolypeptoids in dilute solution

We hypothesize that the ABC triblock copolypeptoids undergo a thermoreversible sol−gel transition through the formation of micellar networks (Figure 2.22) similar to early studies on other ABC block copolymer systems.[2, 9-10] As the three blocks are mutually immiscible, the C block is hydrophobic and the B and A blocks are water-soluble below the sol−gel transition temperature, the triblock copolymers are expected to form core−shell−corona micelles below T_{gel}. Upon temperature increases, the corona blocks (A) undergo cloud point transition and become dehydrated to form hydrophobic domains. This results in the formation of a three-dimensional micellar network.

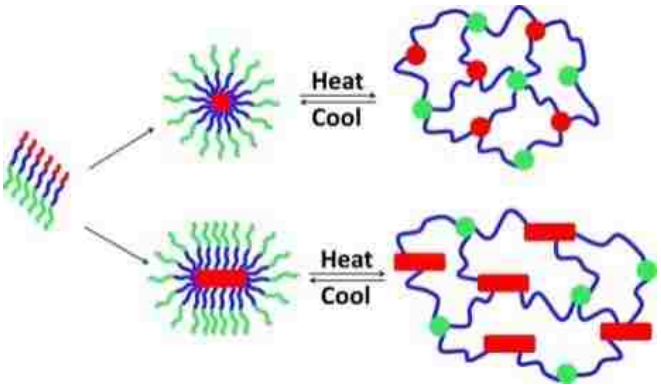

Figure 2.22. Schematic showing the proposed gelation mechanism of aqueous solutions of the ABC triblock copolypeptoids.

The cloud point of the AMD triblock copolypeptoids, as determined from the turbidity measurement, was shown to be higher than of the poly (*N*-allyl glycine) homopolymer (A) itself by 8 °C (Figure 2.23). It is attributed to the attachment of hydrophilic M block at the A terminal, resulting in an increased cloud point of the A segment.

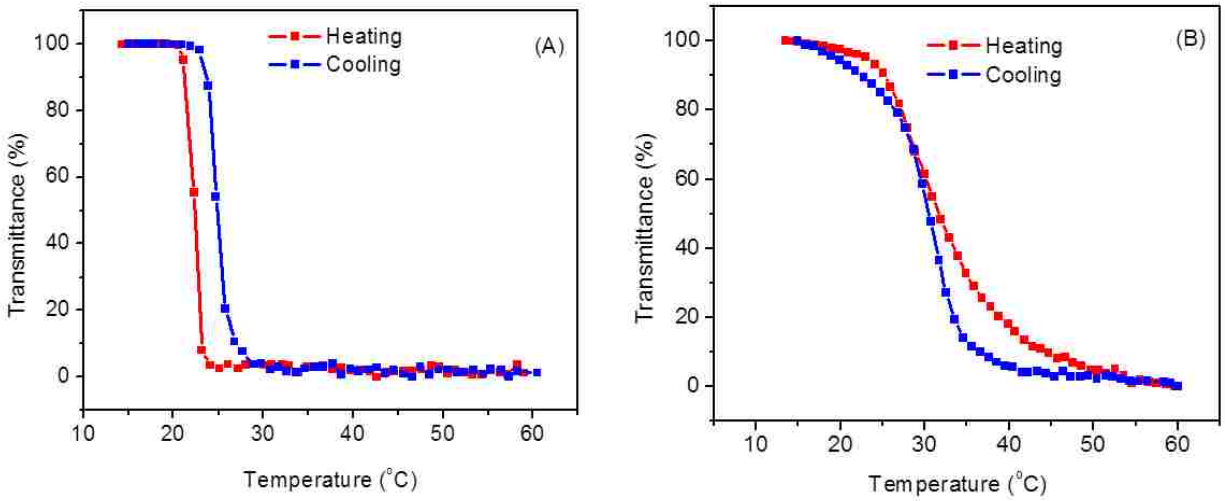

Figure 2.23. (A) Plots of transmittance at λ = 450 nm versus temperature for the aqueous solutions of homopolymer A_{105} and (B) the $A_{98}M_{98}D_{18}$ triblock copolypeptoid (both samples: 1 wt% in DI water).

To verify the micelle formation, TEM analysis of the diluted triblock copolypeptoids solutions were conducted. Spherical micelles with a uniform diameter (13.4 ± 1.1 nm) were observed for the $A_{92}M_{94}D_{12}$ sample (Entry 2, Table 2.1) (Figure 2.24A); for the $A_{98}M_{98}D_{18}$ sample with slightly increased D segmental length (Entry 1, Table 2.1), rod-shape micelles with moderately uniform diameter (16.6 ± 1.7 nm) become notably present (Figure 2.24C). Consistent with the TEM analysis on the dried and uranyl acetate stained micellar samples, Cryo-TEM analysis of a dilute aqueous solution (1 wt %) of the same $A_{92}M_{94}D_{12}$ and $A_{98}M_{98}D_{18}$ sample also confirm the formation of spherical and rod-shape micelles, respectively (Figure 2.24B and D). In addition, DLS analysis of the dilute solution of $A_{98}M_{98}D_{18}$ (0.5 wt %) at 25 °C revealed the presence of particles of a much larger hydrodynamic size than that of $A_{92}M_{94}D_{12}$ (0.5 wt %, Figure 2.25), in accordance with their different micellar morphologies observed by TEM. These results together with the cryo-SEM analysis of the polypeptoid hydrogel (Figure 2.21) suggest that the hydrogel structure is highly hierarchical with spatial features ranging from micron down to nanometer in dimension.

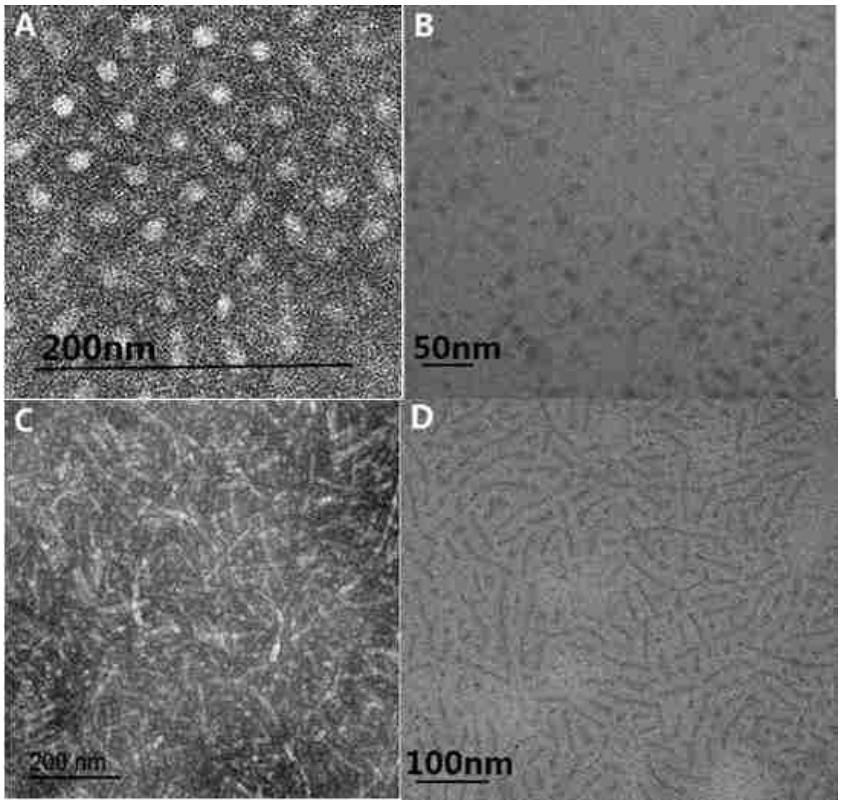

Figure 2.24. (A, C) TEM images of the micelles based on $A_{92}M_{94}D_{12}$ and $A_{98}M_{98}D_{18}$ polymers respectively (stained with uranyl acetate) and (B, D) cryo-TEM image of 1 wt% aqueous solution of the same $A_{92}M_{94}D_{12}$ and $A_{98}M_{98}D_{18}$ polymers respectively.

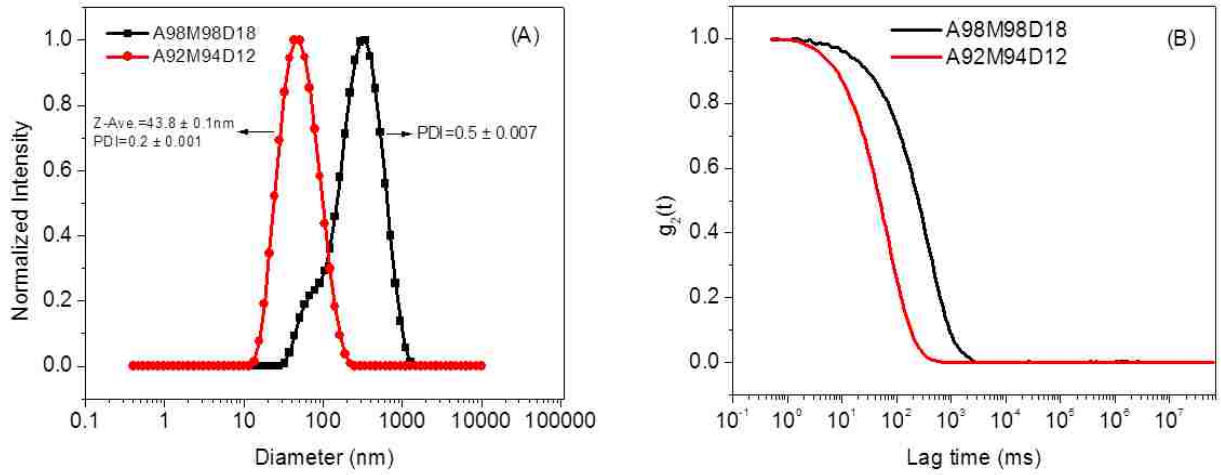

Figure 2.25. (A) Hydrodynamic size distribution of the $A_{92}M_{94}D_{12}$ and $A_{98}M_{98}D_{18}$ micelles (0.5 wt% in nanopure water) at room temperature (below the T_{gel}) and (B) the corresponding correlograms.

The micelle formation is further supported by ^{1}H NMR spectroscopic study of a dilute solution of AMD. (Figure 2.26). In CD_2Cl_2, which is a good and nonselective solvent for all three blocks in the triblock copolypeptoids, proton signals from the three different blocks (A, M, D) are notably present. In D_2O, which is a poor solvent for the D segment and a good solvent for the A and M segments, the proton signals due to the D segment have completely disappeared. This is consistent with micellation where the insoluble D block becomes buried in the core of the micelles. As the temperature is increased to 37 °C, which is above the cloud point of the block copolypeptoids, the proton signals due to the A block was significantly decreased. This indicates the increased dehydration of the A block above the cloud point. The broadening of the proton signals of the M block at elevated temperature was attributed to structural heterogeneity within the gel due to the phase separation during gelation.

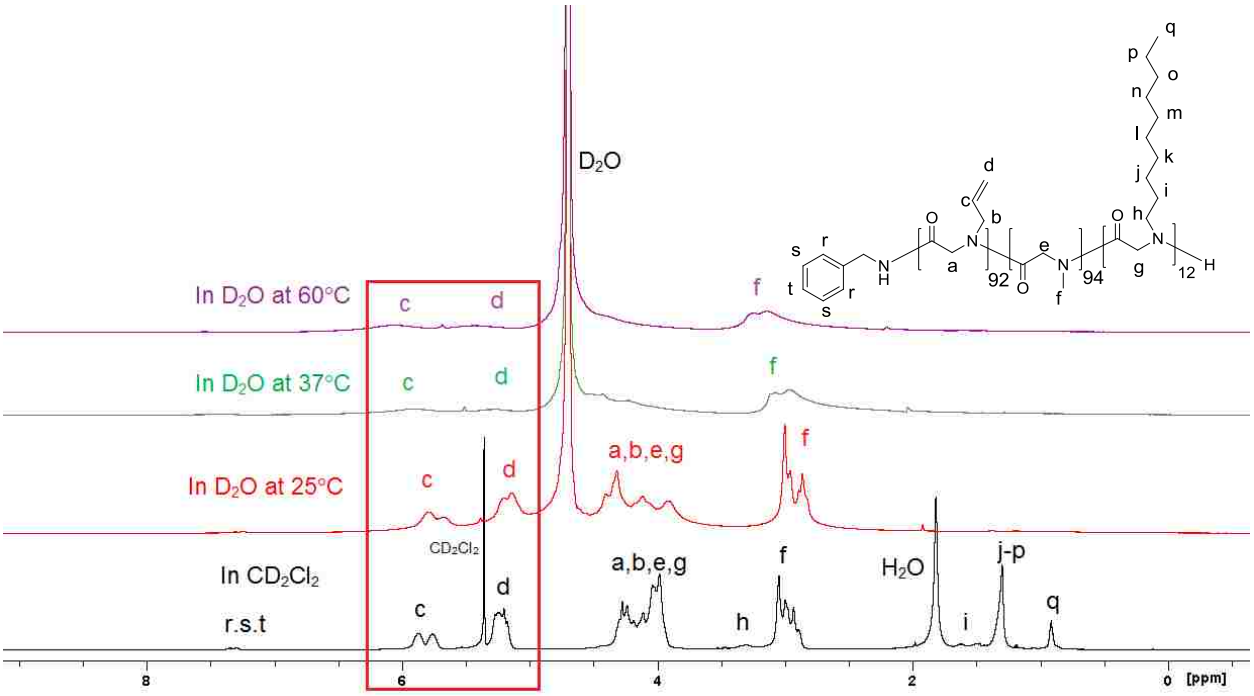

Figure 2.26. ^{1}H NMR spectra of $A_{92}M_{94}D_{12}$ in solvent CD_2Cl_2 and D_2O at different temperature (from below to above the T_{gel}).

To further support the proposed mechanism, a temperature-sweep dynamic light scattering (DLS) measurement within 20−60 °C range was performed on the dilute aqueous solution of $A_{92}M_{94}D_{12}$ (0.5 wt %) (Figure 2.27 and 2.28). At 20 °C, DLS revealed a relatively narrow distribution of micellar sizes with an average 40.6 ± 0.4 nm diameter. As the temperature increases, the average size of the particles also increases (Figure 2.27). Plot of the derived count rate of the micelle solution versus temperature revealed a sharp increase at 27 °C, indicating the onset of micellar aggregation (Figure 2.28A). The temperature- dependent DLS measurement suggests the association of micelles at elevated temperature, in agreement with the proposed gelation mechanism (Figure 2.22).

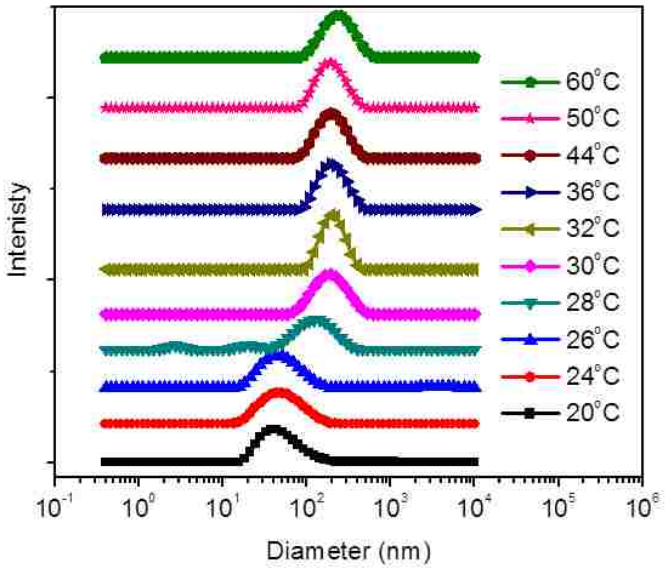

Figure 2.27. Diameter distribution of the $A_{92}M_{94}D_{12}$ micellar solution (0.5 wt%) at different temperature obtained by DLS measurements.

2.3.6. Tuning the Hydrogel Properties

The gelation temperature and mechanical stiffness of the ABC block copolypeptoid hydrogels can be adjusted by controlling the polymer solution concentration and the polymer composition. For example, the aqueous solutions of $A_{98}M_{98}D_{18}$ (Entry 1, Table 2.1) in the 1−5 wt

% range all underwent thermoreversible sol−gel transitions (Figure 2.18). The sol−gel transition temperature can be systematically increased from 26.2 to 33.6 °C as the polymer concentration is

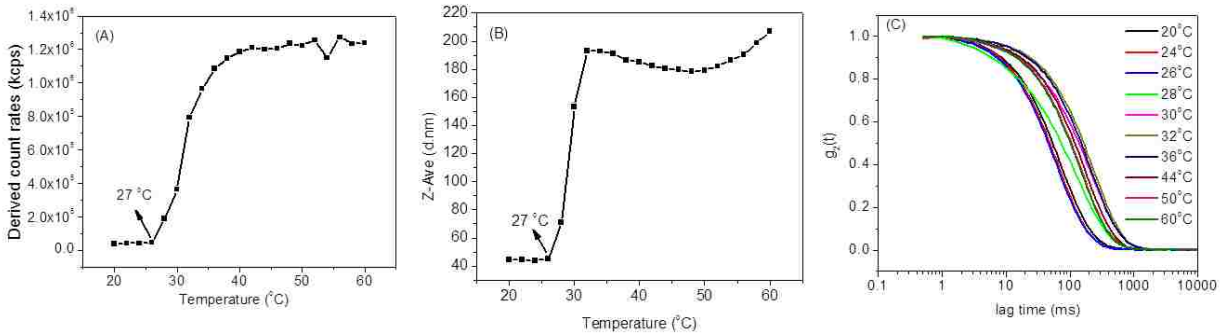

Figure 2.28. (A) Plots of derived count rate and (B) Z-averaged diameter versus temperature for the $A_{92}M_{94}D_{12}$ micellar solution (0.5 wt% in water) together with (C) the corresponding correlograms.

decreased from 5 to 1 wt %. The sol−gel transition window also becomes narrower as the polymer concentration increases. The mechanical stiffness of the hydrogel at 37 ^{o}C, as indicated by storage modulus (G'), increases from approximately 2 to 251 Pa as the polypeptoid concentration increases from 1 to 5 wt %. It corresponds to an increase of Young's modulus from 6 to 762 Pa. This is attributed to the increased cross-linking density at higher concentrations, resulting in micellar networks with increased stiffness.[2] The concentration dependence of the sol−gel transition temperature is consistent with the concentration dependence of the cloud point of block copolymers: the higher the concentration, the lower the cloud point transition.[7, 11]

To investigate the impact of polymer composition on the gelation characteristics, we conducted rheological measurements on the aqueous solutions of triblock copolypeptoids where the chain length of a selective block in the AMD triblock copolypeptoids is systematically varied while the chain length of the remaining two blocks are kept constant. It has been found that the chain length of each block impacts the gelation temperature and gel modulus to different extents. For example, T_{gel} does not change appreciably when the length of the hydrophobic D end block is

increased by 50% from DP_n =12 to 18 (Figure 2.29C), whereas the G' at 37 ^oC decreases from 780 to 251 Pa. By comparison, when the length of the M middle block is increased by 60% from DP_n = 98 to 158 while the chain length of the other two blocks are kept constant, T_{gel} is increased from 26.2 to 30.7 ^oC and the G' value at 37 ^oC was reduced from 251 to 189 Pa (Figure 2.29B). This is consistent with the general observation that increasing the molar fraction of the terminal hydrophilic moiety in thermoresponsive block copolymers enhances the cloud point.[11] By contrast, a dramatic increase of gelation temperature from 26.6 to 40.9 °C occurred (Figure 2.29A) when the length of A block is decreased by 53% from DP_n = 92 to 43. The latter sample did not form a gel at physiological temperature (37 °C). The change in the T_{gel} is in agreement with the previous report where the cloud point of the A homopolymer exhibits chain length dependence: the shorter chain length of A gives rise to a higher cloud point.[7] The gelation temperature (40.9 °C) is much higher than the reported cloud point of the A homopolymer with similar DP_n (30 °C). This is expected as the A segment in the triblock copolypeptoids is directly attached to a long hydrophilic M segment, thereby resulting in an increase in cloud point.[11] Compared to the ABC hydrogelators, the corresponding ABA triblock copolymer exhibit a very different gelation behavior: no gelation occurs up to 60.0 °C (Figure 2.29D). It is probably due to the long-range structural arrangement during the simultaneous micellation and gelation process. In addition, the same end block may cause loops or flower-like conformation that suppresses the formation of bridging structure.[2, 12-13]

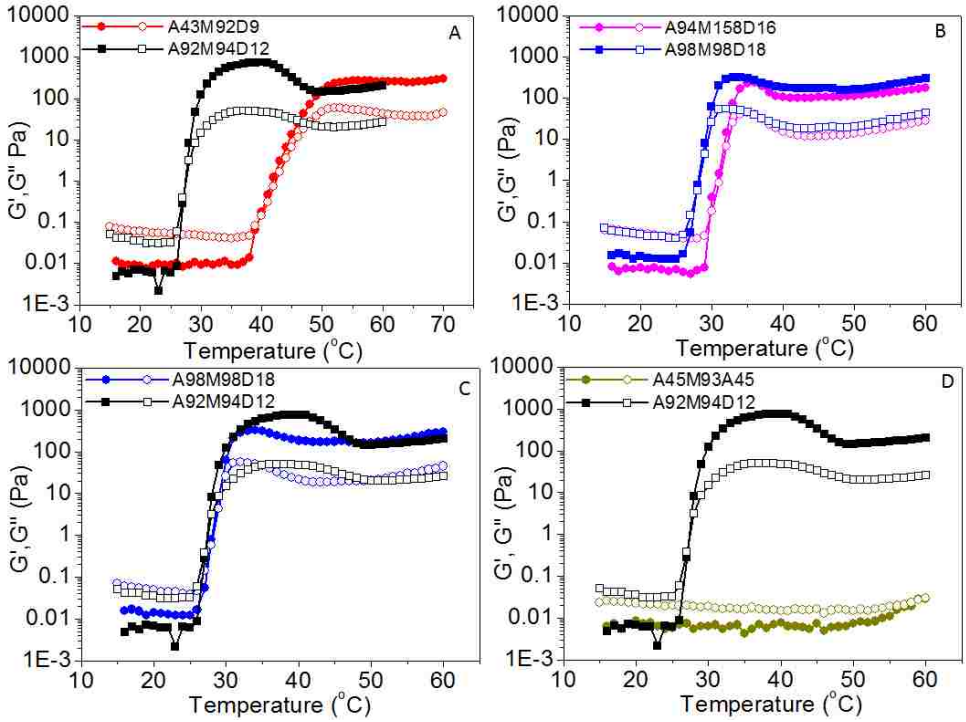

Figure 2.29. Plots of storage (G′, filled symbol) and loss moduli (G″, open symbol) versus temperature for aqueous solutions (5 wt %) of triblock copolypeptoids having varying compositions: $A_{98}M_{98}D_{18}$ (G′, ●; G″, ○), $A_{92}M_{94}D_{12}$ (G′, ■; G″, □), $A_{94}M_{158}D_{16}$ (G′, ●; G″, ○), $A_{43}M_{92}D_9$ (G′, ●; G″, ○), $A_{45}M_{93}A_{45}$ (G′, ●; G″, ○).

To elucidate the influence of the total chain length on the gelation characteristics, rheological measurements were also conducted on aqueous solutions of AMD triblock copolypeptoids where the total polymer chain length is varied while the weight fraction of each block is kept constant (Figure 2.30 and entries 1, 5, and 6 in Table 2.1). The sol−gel transition temperature was shown to systematically increase from 26.2 to 31.0 to >60.0 °C as the total chain length (DP_n) decreases from 214 to 100 to 53. In fact, the shortest chain sample remains a solution at the highest temperature (60.0 °C) that was tested. G' and G" appear to crossover at this temperature limit (Figure 2.30). The chain length dependence of T_{gel} is consistent with the chain length dependence of the cloud point for A homopolymer: shorter chains exhibit higher cloud points.[7] This indicates that tuning the A chain length is the most effective strategy to control the

sol−gel transition temperature in the triblock copolypeptoid system. In addition, the hydrogel stiffness at 37 °C, as indicated by the G' value, is reduced from 251 to 125 Pa with the decrease of total chain length (DP_n) from 214 to 53 (Figure 2.30).

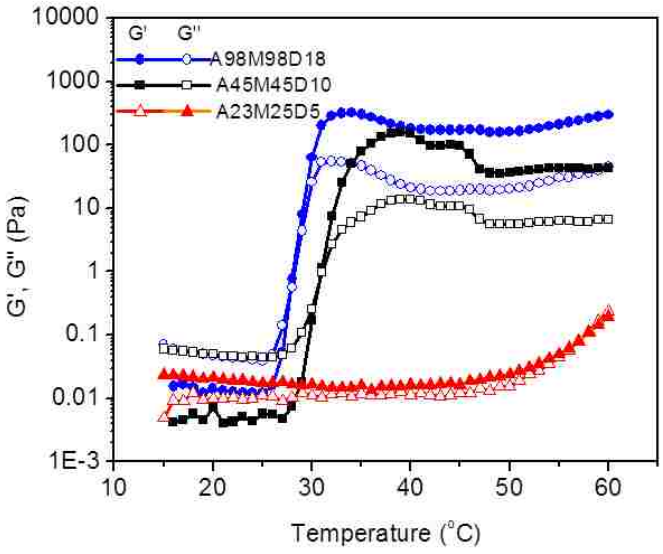

Figure 2.30. Plots of storage (G', filled symbol) and loss moduli (G", open symbol) versus temperature for aqueous solutions (5 wt %) of triblock copolypeptoids with varying block chain length and same block molar ratio: $A_{98}M_{98}D_{18}$ (G', ●; G", ○), $A_{45}M_{45}D_{10}$ (G', ■; G", □), $A_{23}M_{25}D_5$ (G', ▲; G", Δ).

To elucidate how the hydrophobicity of the core block (i.e., C segment) affect the gelation temperature and mechanical stiffness of the hydrogel, rheological measurements were conducted on the aqueous solutions of triblock copolypeptoids where the hydrophobic D end block was replaced with less hydrophobic O and B (Scheme 2.2), whereas the length of each block was kept nearly the same. As the hydrophobicity of the core block decreases (D > O > B), the T_{gel} was slightly increased from around 31.0 to 31.4 to 32.7 °C. The hydrogel at 37 °C shows decreased storage modulus from 125 to 0.2 Pa asthe hydrophobic core block is changed from D to B (Figure 2.31). Thus, the hydrophobicity of the C segment plays an important role in the gelation that increased hydrophobicity lowers the T_{gel} and raises the hydrogel stiffness.

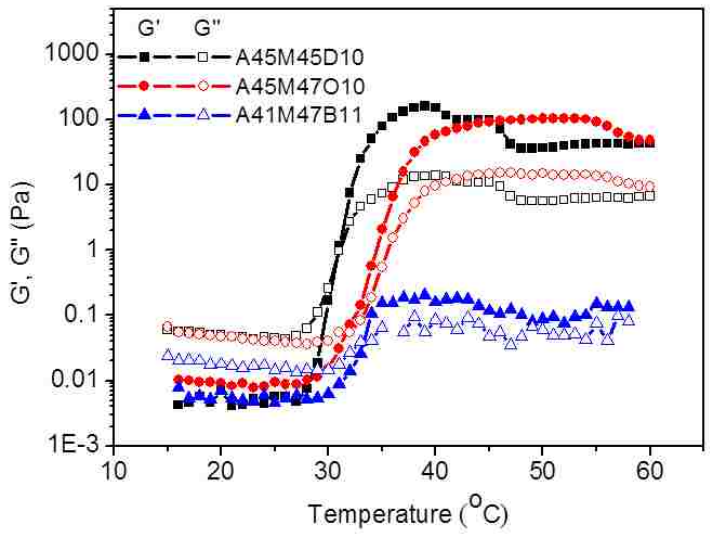

Figure 2.31. Plots of storage modulus (G', filled symbol) and loss modulus (G", open symbol) versus temperature for aqueous solutions (5 wt %) of triblock copolypeptoids having varying hydrophobic end block: $A_{45}M_{45}D_{10}$ (G', ■; G", □), $A_{45}M_{47}O_{10}$ (G', ●; G", ○), $A_{41}M_{47}B_{11}$ (G', ▲; G", Δ).

To further investigate how the hydrophobicity of the B middle block affects the gelation characteristics, rheological measurements were conducted on the aqueous solutions of triblock copolypeptoids where the hydrophilicity of the middle block was altered. As the hydrophilicity of the middle block increases in the following order: M < m < d (Scheme 2.1), the T_{gel} was increased from 31.0 to 42.6 °C. The storage modulus at 37 °C is decreased from 125 to 60 Pa with the increase of the middle block hydrophilicity from M to m (Figure 2.32). In contrast, as the middle block hydrophilicity further increased to d, the polymer solution remains in the sol state at 37 °C. These results strongly indicate that the gelation temperature and stiffness of the gels are highly dependent on the hydrophilicity and hydrophobicity of the constituent block. We are able to adjust the T_{gel} and G' by tuning the polymer composition (i.e., chemistry and molar fraction) for targeted applications.

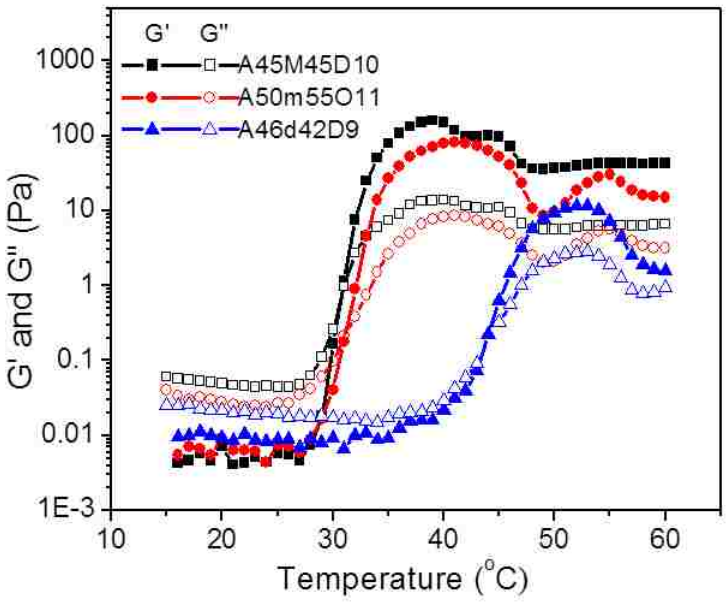

Figure 2.32. Plots of storage (G', filled symbol) and loss moduli (G", open symbol) versus temperature for aqueous solutions (5 wt %) of triblock copolypeptoids with varying middle block: $A_{45}M_{45}D_{10}$ (G', ■; G", □), $A_{50}m_{55}O_{11}$ (G', ●; G", ○), $A_{46}d_{42}D_9$ (G', ▲; G", Δ).

2.3.7. Protein Encapsulation Study

Thermoreversible hydrogels are useful for encapsulation and delivery of water-soluble therapeutics such as proteins/peptides or cells.[14-15] For encapsulation of proteins, it is important that the hydrogels do not adversely affect the protein structure and function. Because the polypeptoids are structurally similar to polypeptides, it is of concern that the hydrogel materials may interact with the proteins and alter the protein functions, even though the polypeptoids only present in low weight fraction in the hydrogel. To assess the suitability of the polypeptoid hydrogel for protein encapsulation, a model water-soluble enzyme (horseradish peroxidases, HRP) was encapsulated in the hydrogel and examined for any functional change over an extended period of time.

HRP is known to catalyze the reaction of guaiacol and H_2O_2, giving rise to colored product (Scheme 2.3).[16] This allows the enzymatic activity of HRP to be readily quantified by measuring the initial reaction rate using an UV−vis spectrometer (Figure 2.33). HRP was encapsulated in the

$A_{92}M_{94}D_{12}$ hydrogel (sample 2, Table 2.1) at 37 °C for up to 7 d, over which period the enzymatic activity was examined and quantified.[16] The HRP encapsulated in hydrogels do not exhibit any appreciable changes in the specific enzymatic activity in the first 24 h of encapsulation (Table 2.2, Figure 2.34). The activities are comparable to thecontrol sets (no gel, Figure 2.34), where the HRP was kept in PBS buffer at 37 °C for the same duration. The encapsulated HRP also shows comparable enzymatic activity to the as-received HRP in PBS buffer at 25 °C without any prolonged incubation (control, Figure 2.34). Increasing the encapsulation to 7 days resulted in a slight decrease of the enzyme activity by 9.4%. This is ascribed to the prolonged heating as the control sample where the enzyme is incubated in buffer at 37 °C without hydrogel shows the similar percentage reduction of activity. The results indicate that the polypeptoid hydrogel does not adversely affect the HRP enzymatic function.

Scheme 2.3. Catalytic Reaction of Guaiacol with HRP and H_2O_2.

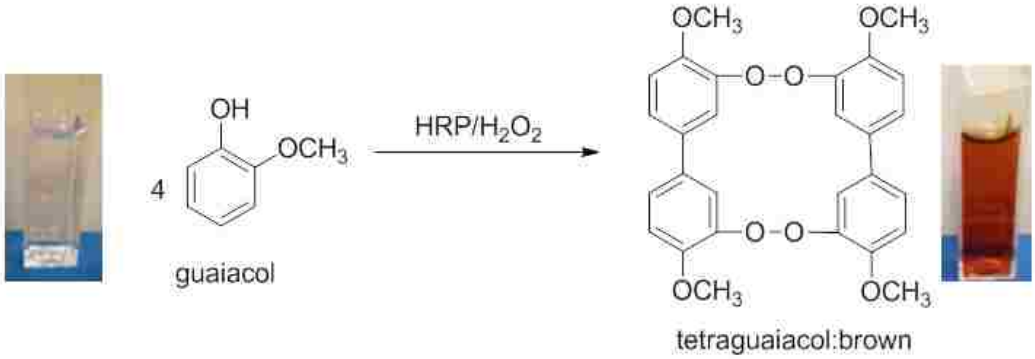

2.3.8. Cytotoxicity Assessment of the Polypeptoid Solution and Hydrogel

AlamarBlue assay was used to assess the cytotoxicity of ABC triblock copolypeptoids diluted solution to human adipose-derived stem cells (hASCs). The diluted polymer solution ($A_{92}M_{94}D_{12}$) was shown to be minimally cytotoxic to hASC with concentration up to 20 mg/mL (Figure 2.35).

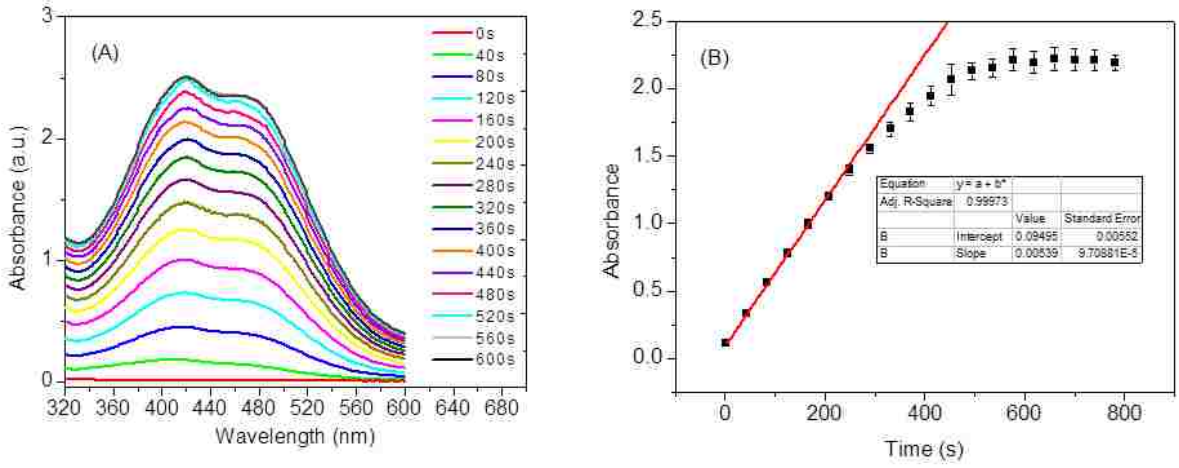

Figure 2.33. (A) Representative UV-Vis spectra of the enzymatic reaction involving Guaiacol, HRP and H_2O_2 showing the absorbance increase over time after incubation of HRP in the $A_{92}M_{94}D_{12}$ hydrogel for 24 h; (B) plot of absorbance at λ = 470 nm versus time.

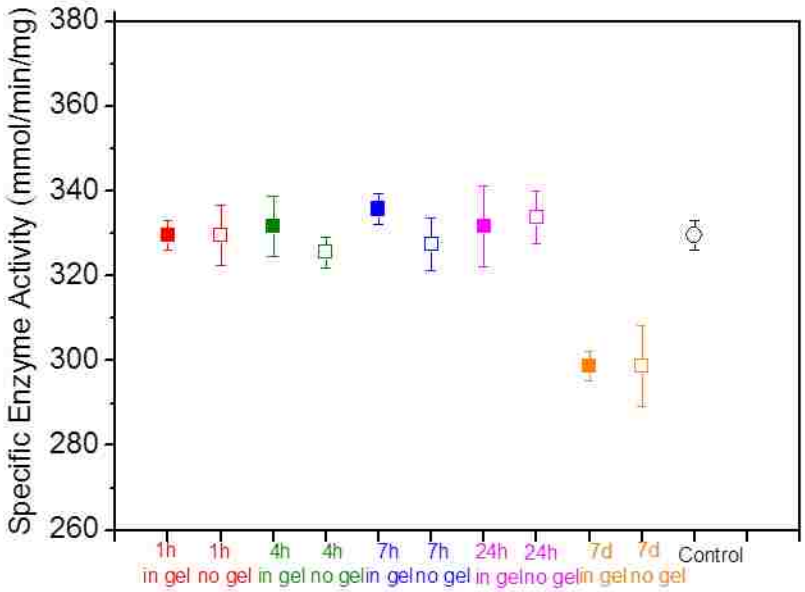

Figure 2.34. Specific enzyme activity with different incubation time at 37 °C: incubation in the $A_{92}M_{94}D_{12}$ hydrogel (sample 2, Table 2.1) (filled symbol: ■) and incubation without the hydrogel (open symbol: □). Control (circular symbol: ○): the enzymatic activity of as-received HRP was measured in PBS buffer at 25 °C without any treatment.

Table 2.2. Systematic study of HRP enzyme activity upon incubation in hydrogel for different time.

Enzyme	**Entry**	**dA/dt (s^{-1}) [d]**	**Enzyme Activity (umol/min) [e]**	**Average Enzyme Activity (umol/min) [f]**	**Specific Enzyme Activity (umol/min/mg) [g]**
1h-in gel[a]	1	0.0054	0.187	0.185±0.002	329.71±3.6
	2	0.0053	0.183		
	3	0.0053	0.183		
1h-no gel[b]	1	0.0054	0.187	0.185±0.004	329.71±7.1
	2	0.0054	0.187		
	3	0.0052	0.180		
4h-in gel[a]	1	0.0055	0.190	0.186±0.004	331.7±7.1
	2	0.0053	0.183		
	3	0.0053	0.183		
4h-no gel[b]	1	0.0053	0.183	0.182±0.002	325.5±3.6
	2	0.0053	0.183		
	3	0.0052	0.180		
7h-in gel[a]	1	0.0055	0.190	0.188±0.002	335.9±3.6
	2	0.0054	0.187		
	3	0.0054	0.187		
7h-no gel[b]	1	0.0054	0.187	0.183±0.003	327.6±6.2
	2	0.0053	0.1837		
	3	0.0052	0.180		
24h-in gel[a]	1	0.0054	0.187	0.186±0.005	331.7±9.4
	2	0.0055	0.190		
	3	0.0052	0.180		
24h-no gel[b]	1	0.0054	0.187	0.187±0.003	333.8±6.2
	2	0.0053	0.183		
	3	0.0055	0.190		
7d-in gel[a]	1	0.0047	0.166	0.167±0.002	298.8±3.6
	2	0.0050	0.173		
	3	0.0048	0.163		
7d-no gel[b]	1	0.0048	0.166	0.167±0.005	298.8±9.4
	2	0.0049	0.170		
	3	0.0048	0.166		
control[c]	1	0.0053	0.183	0.185±0.002	329.7±3.6
	2	0.0054	0.187		
	3	0.0053	0.183		

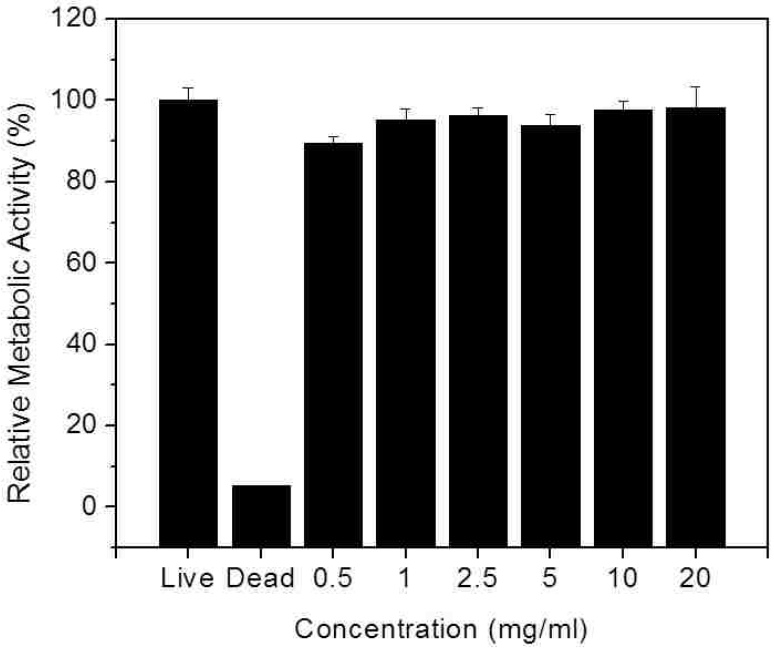

Figure 2.35. Relative metabolic activity of hASC cultured in dilute solutions of $A_{92}M_{94}D_{12}$ triblock copolypeptoids (Entry 2, Table 2.1). The results are normalized to live control.

AlamarBlue assay was further used to investigate the effect of ABC hydrogel on hASCs metabolic activity. After 24 h of culturing in the ABC hydrogel extractives or 3 d of culturing within the hydrogel matrix in direct contacting, hASCs showed a significant decrease (P-value <0.05) of relative metabolic activity compared to the live control (Figure 2.36A). The corresponding total DNA content was quantified using Quanti-T PicoGreen assay to analyze the hASC proliferation on ABC hydrogel (Figure 2.36B). No significant inhibition of hASC proliferation compared to the live control was observed when hASCs exposed to the ABC hydrogel extractives for 24 h or cultured within the hydrogel matrix in direct contact for 3 d. The results indicated that the slight decrease of cells proliferation rate does not correlate with a decrease in metabolic activity and may be indicative of stem cells leaving the proliferative cell cycle to differentiate. The differentiation pathway of hASCs happening within the hydrogel matrix was further indicated by the QPCR analysis (Figure 2.38). Moreover, hASC maintained a healthy spindle shape both when exposed to hydrogel extractives and cultured within hydrogel matrix

(Figure 2.37). Overall, the results demonstrated that ABC hydrogel is a cytocompatible material that can be potentially used as a tissue engineering scaffold.

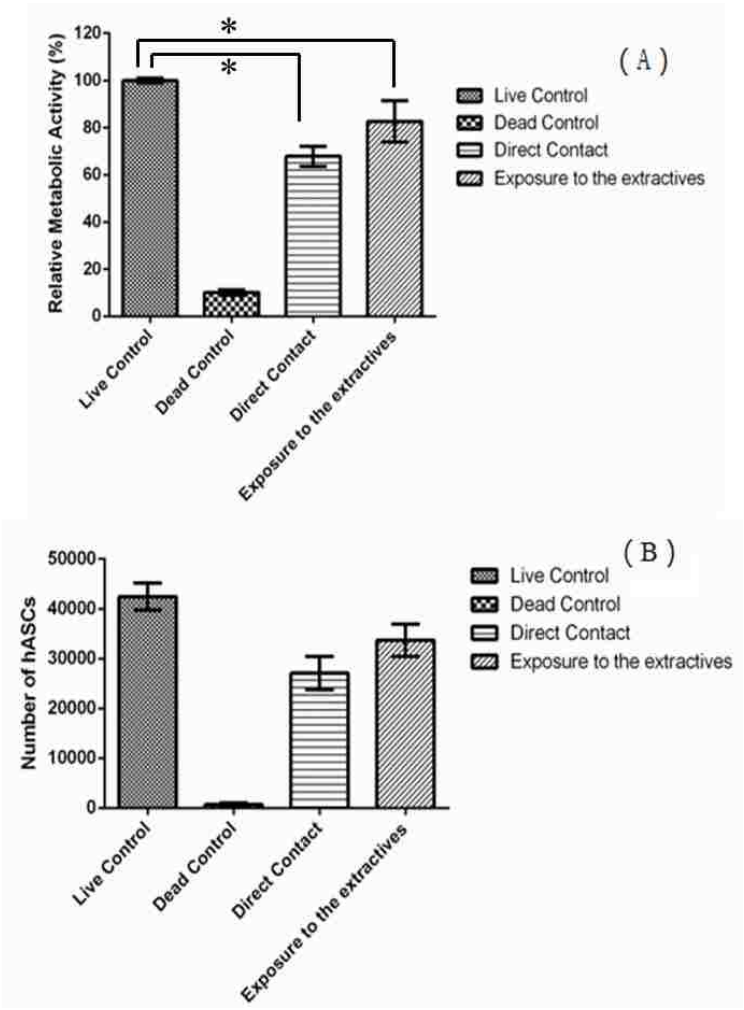

Figure 2.36. (A) Relative metabolic activity of hASC cultured in $A_{92}M_{94}D_{12}$ hydrogel (Entry 2, Table 2.1) (5 wt % in PBS). The results are normalized to positive control. (B) Corresponding number of hASC obtained using Quanti-T PicoGreen assay. Star symbol (*) indicates statistical significant difference between two groups.

2.3.9. QPCR Quantification of Chondrogenesis Markers

To further investigate the effect of hydrogel on stem cell differentiation, quantitative real-time polymerase chain reaction (QPCR) analysis were conducted to quantify the expression of two marker genes, *Col2a1* and *ANGPT1*, for chondrogenesis and endotheliogenesis, respectively.[17-19]

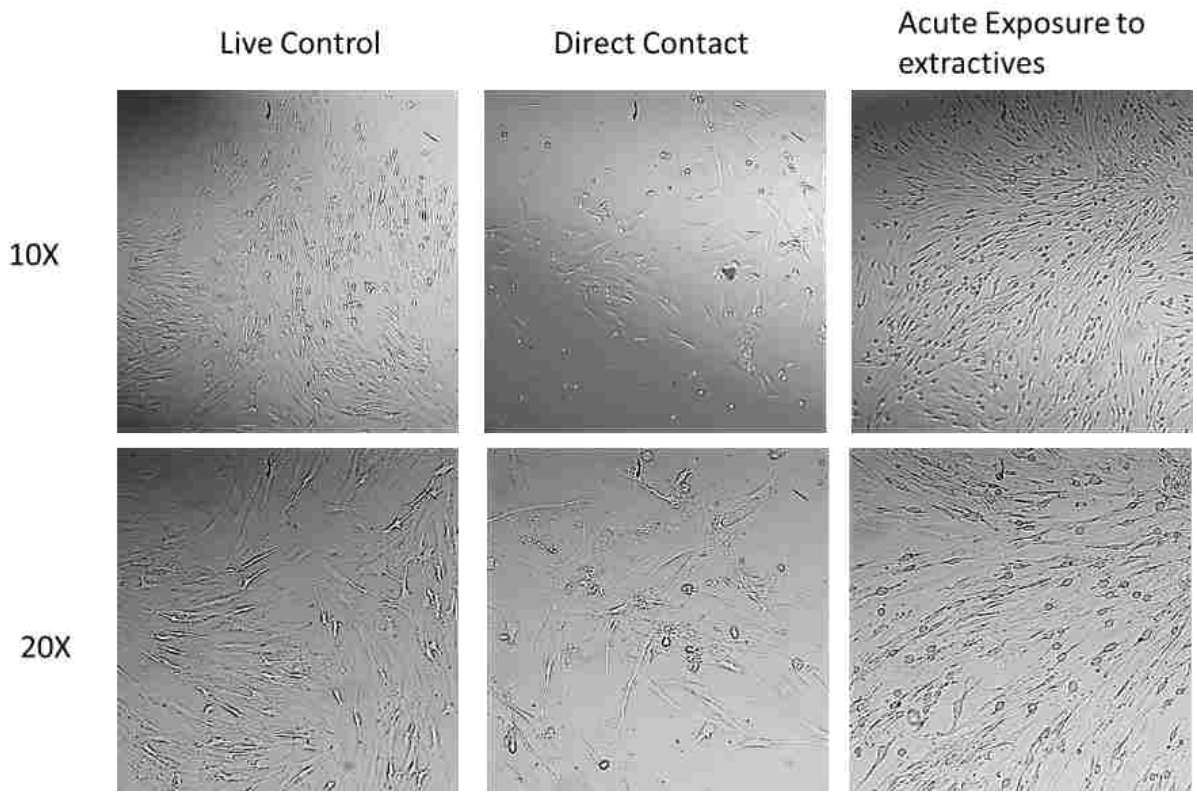

Figure 2.37. Optical microscopic images of hASC with different treatments.

Chondrogenesis is a multistep process characterized cell commitment, expression of chondrogenic markers, condensation, and cellular morphological changes.[17] The product of the *Col2a1* gene is an early and abundant marker of chondrocytes differentiation pathway.[18] The expression of *Col2a1* and *ANGPT1*, a marker of angiogenesis, was assessed by QPCR at the 7 and 21 day time point. The $A_{92}M_{94}D_{12}$ hydrogel was shown to up-regulate the *Col2a1* and down-regulated the *ANGPT1* gene expression of hASCs at 7 and 21 d of the chondrogenesis study (Figure 2.38). Others studies have also shown up-regulation of *Col2a1* and down-regulation of *ANGPT1* gene expression when hASCs committed to chondrogenesis pathway.[17, 19] These results indicate that the polypeptoid hydrogel may have potential use as scaffold or graft materials for stem cell based tissue repair.

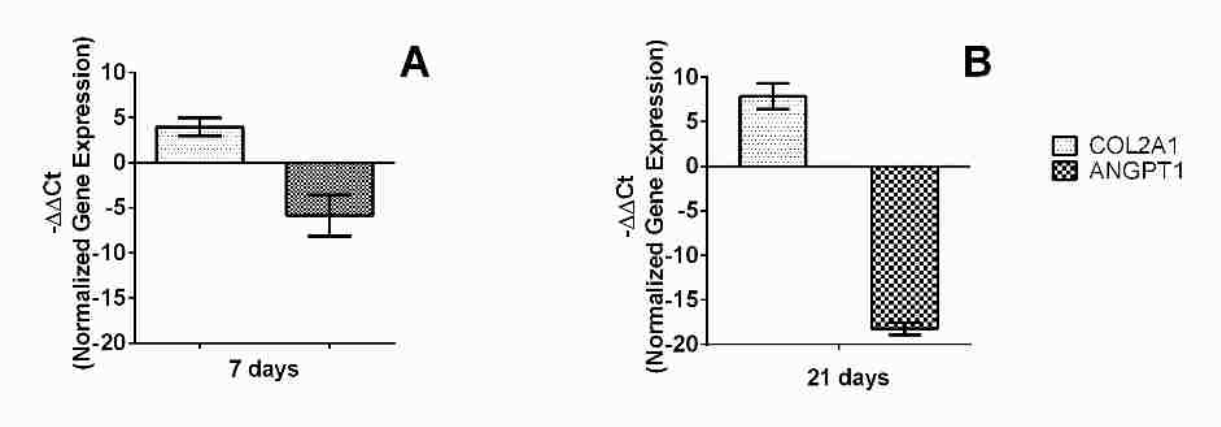

Figure 2.38. QPCR analysis of gene expression within $A_{92}M_{94}D_{12}$ hydrogel matrix (Entry 2, Table 2.1).

Several synthetic hydrogels have previously been reported to influence the differentiation of specific cell lines. For example, polypeptide-based hydrogels (PA-PLX-PA[20]and PEG-L-PA[21]) have led to chondrogenesis of chondrocytes and adipose tissue derived cells. Although many factors [*e.g.*, cell morphologies, proliferation rate, cell density, size of cell aggregation, swelling ratio, gel modulus, gel morphology, functional group (*e.g.*, −COO−, −SH, $-NH_3$), and charge state in the hydrogel as well as degradation rate][20-29] have been suggested to contribute to this unique phenomenon, the exact role of each factor and their complex interplays are not well understood. Our future efforts will be directed toward understanding how the structural characteristics of the polypeptoid hydrogels affect the stem cell differentiation by systematically tuning the hydrogel composition and structure.

2.4. Conclusions

Well-defined amphiphilic ABC triblock copolypeptoids with varying composition and chain length can be synthesized by primary amine-initiated ring-opening polymerization. The polymer aqueous solutions undergo rapid thermoreversible sol−gel transitions. The gelation is attributed to the temperature-induced formation of micellar networks. The hydrogel exhibit shear-thinning behavior and can be injected through 24 gauge syringe needles. The gelation temperature

of the hydrogel can be readily adjusted between 26.2 and 60.0 °C, and the mechanical stiffness (G') at physiological temperature (37 °C) can be tuned from between 0.2 and 780 Pa, corresponding to the Young's modulus in the 0.5−2346 Pa range. Encapsulation of model proteins (HRP) in the polypeptoid hydrogel for up to 7 d does not adversely affect the enzymatic activity. Furthermore, the ABC hydrogel and hydrogel extractives show minimal cytotoxicity to hASCs as indicated by standard metabolic and proliferation assays. The study of chondrogenic marker expression indicated that the hydrogel may have de novo bioactivity and is capable of modulating the expression of chondrogenic differentiation markers in hASCs. The combination of low cytotoxicity and bioactivity renders the polypeptoid hydrogel a highly promising tissue engineering material. The ABC hydrogel motif is highly versatile and structurally tunable. We envision the further functionalization of the hydrogel by photoinitiated thiol-ene addition chemistry to incorporate various biologically active ligands (*e.g.*, peptides) and further enhancement of the mechanical stiffness of the hydrogels by chemical cross-linking. These studies are currently in progress and will be reported in due course.

2.5. Reference

1. Guo, L.; Zhang, D. Cyclic Poly(α-peptoid)s and Their Block Copolymers from N-Heterocyclic Carbene-Mediated Ring-Opening Polymerizations of N-Substituted N-Carboxylanhydrides. *J. Am. Chem. Soc.* **2009,** *131* (50), 18072-18074.

2. Zhou, C.; Hillmyer, M. A.; Lodge, T. P. Efficient Formation of Multicompartment Hydrogels by Stepwise Self-Assembly of Thermoresponsive ABC Triblock Terpolymers. *J. Am. Chem. Soc.* **2012,** *134* (25), 10365-10368.

3. Zanetti, A. S.; McCandless, G. T.; Chan, J. Y.; Gimble, J. M.; Hayes, D. J. Characterization of novel akermanite:poly-ϵ-caprolactone scaffolds for human adipose-derived stem cells bone tissue engineering. *J. Tissue Eng. Regen. Med.* **2015,** *9* (4), 389-404.

4. http://www.fda.gov/downloads/medicaldevices/deviceregulationandguidance/guidan.

5. Liu, Q.; Cen, L.; Yin, S.; Chen, L.; Liu, G.; Chang, J.; Cui, L. A comparative study of proliferation and osteogenic differentiation of adipose-derived stem cells on akermanite and β-TCP ceramics. *Biomaterials* **2008,** *29* (36), 4792-4799.

6. Kanitkar, A.; Smoak, M.; Chen, C.; Aita, G.; Scherr, T.; Madsen, L.; Hayes, D. Synthesis of novel polyesters for potential applications in skin tissue engineering. *J. Chem. Technol. Biotechnol.* **2016,** *91* (3), 733-741.

7. Robinson, J. W.; Secker, C.; Weidner, S.; Schlaad, H. Thermoresponsive Poly(N-C3 glycine)s. *Macromolecules* **2013,** *46* (3), 580-587.

8. Chaudhuri, O.; Koshy, S. T.; Branco da Cunha, C.; Shin, J.-W.; Verbeke, C. S.; Allison, K. H.; Mooney, D. J. Extracellular matrix stiffness and composition jointly regulate the induction of malignant phenotypes in mammary epithelium. *Nat Mater* **2014,** *13* (10), 970-978.

9. Zhou, C.; Toombes, G. E. S.; Wasbrough, M. J.; Hillmyer, M. A.; Lodge, T. P. Structure of Two-Compartment Hydrogels from Thermoresponsive ABC Triblock Terpolymers. *Macromolecules* **2015,** *48* (16), 5934-5943.

10. Gupta, M. K.; Martin, J. R.; Werfel, T. A.; Shen, T.; Page, J. M.; Duvall, C. L. Cell Protective, ABC Triblock Polymer-Based Thermoresponsive Hydrogels with ROS-Triggered Degradation and Drug Release. *J. Am. Chem. Soc.* **2014**.

11. Chung, J. E.; Yokoyama, M.; Aoyagi, T.; Sakurai, Y.; Okano, T. Effect of molecular architecture of hydrophobically modified poly(N-isopropylacrylamide) on the formation of thermoresponsive core-shell micellar drug carriers. *J. Controlled Release* **1998,** *53* (1–3), 119-130.

12. Li, C.; Tang, Y.; Armes, S. P.; Morris, C. J.; Rose, S. F.; Lloyd, A. W.; Lewis, A. L. Synthesis and Characterization of Biocompatible Thermo-Responsive Gelators Based on ABA Triblock Copolymers. *Biomacromolecules* **2005,** *6* (2), 994-999.

13. Ma, Y.; Tang, Y.; Billingham, N. C.; Armes, S. P.; Lewis, A. L. Synthesis of Biocompatible, Stimuli-Responsive, Physical Gels Based on ABA Triblock Copolymers. *Biomacromolecules* **2003,** *4* (4), 864-868.

14. Hennink, T. V. R. C. W. E. Hydrogels for Protein Delivery. *Chem. Rev.* **2012,** *112* (5), 2853-2888.

15. Nguyen, M. K.; Lee, D. S. Injectable Biodegradable Hydrogels. *Macromol. Biosci.* **2010,** *10* (6), 563-579.

16. Hidalgo-Cuadrado, N.; Pérez-Galende, P.; Manzano, T.; De Maria, C. G.; Shnyrov, V. L.; Roig, M. G. Screening of Postharvest Agricultural Wastes as Alternative Sources of Peroxidases: Characterization and Kinetics of a Novel Peroxidase from Lentil (Lens culinaris L.) Stubble. *J. Agric. Food Chem.* **2012,** *60* (19), 4765-4772.

17. Zhao, Q.; Eberspaecher, H.; Lefebvre, V.; de Crombrugghe, B. Parallel expression of Sox9 and Col2a1 in cells undergoing chondrogenesis. *Dev. Dyn.* **1997,** *209* (4), 377-386.

18. Estes, B. T.; Wu, A. W.; Guilak, F. Potent induction of chondrocytic differentiation of human adipose-derived adult stem cells by bone morphogenetic protein 6. *Arthritis Rheum.* **2006,** *54* (4), 1222-1232.

19. Kishiya, M.; Sawada, T.; Kanemaru, K.; Kudo, H.; Numasawa, T.; Yokoyama, T.; Tanaka, S.; Motomura, S.; Ueyama, K.; Harata, S.; Toh, S.; Furukawa, K.-I. A Functional RNAi Screen for Runx2-Regulated Genes Associated With Ectopic Bone Formation in Human Spinal Ligaments. *J. Pharmacol. Sci.* **2008,** *106* (3), 404-414.

20. Choi, B. G.; Park, M. H.; Cho, S.-H.; Joo, M. K.; Oh, H. J.; Kim, E. H.; Park, K.; Han, D. K.; Jeong, B. In situ thermal gelling polypeptide for chondrocytes 3D culture. *Biomaterials* **2010,** *31* (35), 9266-9272.

21. Yeon, B.; Park, M. H.; Moon, H. J.; Kim, S.-J.; Cheon, Y. W.; Jeong, B. 3D Culture of Adipose-Tissue-Derived Stem Cells Mainly Leads to Chondrogenesis in Poly(ethylene glycol)-Poly(l-alanine) Diblock Copolymer Thermogel. *Biomacromolecules* **2013,** *14* (9), 3256-3266.

22. Ko, C.-Y.; Yang, C.-Y.; Yang, S.-R.; Ku, K.-L.; Tsao, C.-K.; Chwei-Chin Chuang, D.; Chu, I. M.; Cheng, M.-H. Cartilage formation through alterations of amphiphilicity of poly(ethylene glycol)-poly(caprolactone) copolymer hydrogels. *RSC Advances* **2013,** *3* (48), 25769-25779.

23. Kye, E. J.; Kim, S.-J.; Park, M. H.; Moon, H. J.; Ryu, K. H.; Jeong, B. Differentiation of Tonsil-Tissue-Derived Mesenchymal Stem Cells Controlled by Surface-Functionalized Microspheres in PEG-Polypeptide Thermogels. *Biomacromolecules* **2014,** *15* (6), 2180-2187.

24. Fei, T.; Xiaoding, X.; Ting, D.; Miao, Y.; Xianzheng, Z.; Jiawei, W. Fabrication of positively charged poly(ethylene glycol)-diacrylate hydrogel as a bone tissue engineering scaffold. *Biomedical Materials* **2012,** *7* (5), 055009.

25. Bryant, S. J.; Durand, K. L.; Anseth, K. S. Manipulations in hydrogel chemistry control photoencapsulated chondrocyte behavior and their extracellular matrix production. *J. Biomed. Mater. Res. Part A* **2003,** *67A* (4), 1430-1436.

26. Tang, J.; Peng, R.; Ding, J. The regulation of stem cell differentiation by cell-cell contact on micropatterned material surfaces. *Biomaterials* **2010,** *31* (9), 2470-2476.

27. Zhang, L.; Yuan, T.; Guo, L.; Zhang, X. An in vitro study of collagen hydrogel to induce the chondrogenic differentiation of mesenchymal stem cells. *J. Biomed. Mater. Res. Part A* **2012,** *100A* (10), 2717-2725.

28. Wolf, F. C., C.; Wendt, D.; Farhadi, J.; Heberer, M.; Martin, I.; Barbero, A. Cartilage Tissue Engineering Using Pre-aggregated Human Articular Chondrocytes. *Eur. Cell Mater.* **2008,** *16*, 92-99.

29. Moreira Teixeira, L. S. L., J. C.; Sobral, J.; Jin, R.; Van Apeldoom, A. A.; Feijen, J.; Van Blitterswijk, C.; Dijkstra, P. J.; Karperien, M. High Throughput Generated Micro-aggregates of Chondrocytes Stimulate Cartilage Formation in Vitro and in Vivo. *Eur. Cell Mater.* **2012,** *5*, 387-399.

CHAPTER 3 : SYNTHESIS OF PEGYLATED POLYPEPTOIDS AS ANTIFOULING POLYMERS

3.1 Introduction

Nonspecific protein adsorption to the surface of biomaterials and medical devices accompanied by slow protein denaturation can induce cascades of biological responses when they get into contact with human blood, including thrombosis, chronic inflammation and fast immunological recognition.[1-4] Those biological responses may hinder the function and effectiveness of biomedical devices and drug delivery vehicles.[1-4] The resistance of nonspecific protein adsorption, therefore, is critical in improving the biocompatibility of biomaterials for various biomedical and biotechnological applications (*e.g.*, tissue engineering, therapeutic delivery)

The mechanisms responsible for non-specific protein adsorption to surfaces are not fully understood and more investigation is needed.[3] The interaction between a protein and a surface is considered to be the result of a balance between van der Waals, electrostatic, hydrophobic, and hydration forces.[3] It is believed that the water layer bound to hydrophilic polymer chains is mainly responsible for resisting protein adsorption.[4-5] Based on the reported studies, a protein-resistant material usually obey four molecular-scale criteria, the so-called "Whitesides rules": 1) hydrophilicity, 2) the presence of hydrogen bond acceptor groups, 3) the absence of hydrogen bond donor groups, and 4) the absence of net charge. [4, 6-7] The "Whitesides rules" have been widely applied for the rational design of protein-resistant materials. Many types of protein-resistant materials have been developed including poly(ethylene glycol) (PEG),[3, 8] oligo/polypeptides,[9-10] polycarbonates,[11] polyoxazolines,[12-14] polyacrylamides[15-16] and zwitterionic polymers[3, 17]. PEG is considered as the gold standard of protein-resistant stealth polymers in polymer-based therapeutic

delivery. The drug-PEG conjugates enhance the water solubility of drugs and decrease their interaction with blood components, leading to increased circulation half-life and decreased toxicity of drugs. However, PEG has obvious drawbacks including non-biodegradability, potential immunological recognition and hypersensitivity provocation, as well as accumulation in tissue when the molecular weight of PEG exceeds 40 KDa.[3-4, 8] Zwitterionic polymers (*e.g.*, zwitterionic polycarbonate[17] and polybetanes[3]) which form a very stable hydration shell through strong ion-dipole bonding with water and absence of net charge are very promising protein-resistant materials.[3-4] They are, nevertheless, minimally soluble in most commonly used organic solvents and thereby enhance their subsequent process complexity especially when conjugation to a hydrophobic drug is desired.[11] Polyoxazolines (*e.g.*, poly(2-methyl-2-oxazoline), with similar stealth behavior as PEG, is not backbone degradable and the potential formation of poly (ethylene imine) from enzymatic degradation of the amide bonds on the side chain may confer cytotoxicity.[14, 18-19] Polyacrylamides are another category of protein-resistant material that is not backbone degradable. Moreover, the thermoresponsive behavior of, in particular, poly (*N*-isopropylacrylamide) makes it absorb proteins at body temperature due to the enhanced hydrophobicity.[15-16, 20] Some oliogomeric[21-24] and polymeric peptides[9, 25-26] were shown to be enzyme degradable, while the problem with the common water-soluble polypeptides (*e.g.*, poly-L-lysine and poly-L-aspartate) is their pH dependency and limited circulation lifetime caused by the aggregation with oppositely charged moieties.[27-28] Besides, the enzymatic proteolysis of peptides may results in short *in vivo* half-lives and therefore limit their use in long-term biological application (*e.g.*, long-term drug delivery). Polycarbonates have attracted considerable attention in the recent years due to their low toxicity, potential biocompatibility and biodegradability;[29]

however, studies showed that polycarbonates are prone to fast degradation (within several days or weeks) both hydrolytically[30-31] and enzymatically[32] and thus limit their long-term biological use.

Poly (*N*-substituted glycine) (a.k.a, polypeptoids), with an *N*-substituted polyglycine backbone, are structural mimics of polypeptides. In contrast to polypeptides, which adopt secondary structures (*e.g*., helix or sheet) stabilized by hydrogen bonding, polypeptoids lack extensive hydrogen bonding and chirality on the backbone and render them excellent thermal processability, good solubility in commonly used solvents, as well as enhanced enzymatic and hydrolytic stability relative to polypeptides.[21-23, 33-34] In addition, some studies showed that polypeptoids exhibit minimal cytotoxicity,[35-38] and are degradable under oxidative conditions that mimics tissue inflammation.[38] These excellent properties make polypeptoids an attractive material for biomedical and biotechnological applications.[33, 39-43] In recent years, oligo polypeptoids ($DP_n \leq 20$) (*e.g*., polysarcocine,[44] polymethoxyethylyglycine,[45-46] polyhydroxyethylglycine[46]) grafted onto TiO_2 surface through a DOPA-Lys surface anchor were shown excellent antifouling characteristic to resist protein (*e.g*., human fibrinogen) adsorption and cell (*e.g*., mammalian cell) attachment. These polypeptoids prepared by solid-phase method appeared to have length limitation to around 50 mer.[41] Surface initiated ring-opening polymerization (SI-ROP) of *N*-substituted glycine *N*-carboxyanhyrides (NNCA) was also reported to tether longer polypeptoid chains (polysarcosine) to the targeted surface for antifouling purpose.[47] Studies of polypeptoids regarding their protein resistance, to our best knowledge, all focused on surface attached polymer chains and there is no study on their protein resistance in bulk solution.

Here, for the first time, we designed and synthesized a series of polypeptoids bearing oligometic ethylene glycol side chains with well-defined structure by primary amine-initiated ring-opening polymerization of the corresponding *N*-substituted *N*-carboxyanhydrides (Scheme 3.2).

These PEGylated polypeptoids are highly water soluble, charge neutral and have hydrogen bond acceptor both on the backbone and side chains, which fulfill all the criteria of the abovementioned "whitesides rule" for protein-resistant materials. The small angle neutron scattering (SANS) and dynamic light scattering (DLS) study indicated there is no obvious adsorption of lysozyme to PNMeOEtG. All the results suggested that the PEGylated polypeptoids are becoming a new benchmark of protein-resistant materials for biological applications.

3.2 Experimental

3.2.1 General considerations

All chemicals were purchased from Sigma Aldrich and used as received unless otherwise noted. All the solvents used in monomer preparation and polymerization were purified by passing through alumina columns under argon. Toluene-d^8 was purified by vacuum transfer after stirring over CaH_2 overnight. ^1H and ^{13}C $\{^1H\}$ NMR spectra were obtained using a Bruker AV-400 Nanobay spectrometer (400 MHz for ^1H NMR and 100 MHz for ^{13}C $\{^1H\}$ NMR) and a Bruker AV-500 spectrometer (500 MHz for ^1H NMR and 125 MHz for ^{13}C $\{^1H\}$ NMR) at 298 K. Chemical shifts (δ) given in parts per million (ppm) were referenced to protio impurities or the ^{13}C $\{^1H\}$ isotopes of deuterated solvents ($CDCl_3$ and D_2O).

3.2.2 Synthesis of MeOEt-NCA and PNMeOEtG

Synthesis of ethyl 2-((2-methoxyethyl)amino)acetate (1). 2-methoxyethylamine (10g, 0.13mol) and triethylamine (18.6 mL, 0.13mol) was dissolved in 100 mL ethyl acetate. Ethyl bromoacetate (14.7 mL, 0.13 mol) dissolved in 50 mL ethyl acetate was added dropwise to the above mixture at room temperature and stirred at room temperature for 4h. The white precipitation was removed by filtration and the filtrate was condensed to obtain the crude product as pale yellow liquid (21.2 g, 99.1%). The crude product was purified by column chromatography performed on

silica gel (230-400 mesh, 60 Å, Sorbent Technologies) using ethyl acetate/methanol as the eluent to afford the desired product as colorless liquid (17.2 g, 82.3 % yield). ^{1}H NMR (δ in $CDCl_3$, 400 MHz, ppm): 1.23-1.26 ppm (t, J = 7.16 Hz, 3H, -$COOCH_2CH_3$); 1.87 ppm (s, 1H, -N*H*-); 2.76-2.79 ppm (t, J = 5.12 Hz, 2H, -$CH_2NHCH_2CH_2$-); 3.33 ppm (s, 3H, -OCH_3); 3.40 ppm (s, 2H, -$NHCH_2COO$-); 3.45-3.48 ppm (t, J = 5.08, 2H, $CH_3OCH_2CH_2$-); 4.14-4.19 ppm (q, J = 7.12 Hz, 2H, -$COOCH_2CH_3$). ^{13}C {^{1}H} NMR (δ in $CDCl_3$, 125 MHz, ppm): 14.2 ppm (-$COOCH_2CH_3$); 48.8 ppm (-$CH_2NHCH_2CH_2$-); 51.0 ppm (-OCH_3); 58.7 ppm (-$NHCH_2COO$-); 60.7 ppm ($CH_3OCH_2CH_2$-); 72.1 ppm (-$COOCH_2CH_3$); 172.3 ppm (-CH_2COOH).

Synthesis of ethyl 2-((2-methoxyethyl)amino)acetic acid hydrochloride (2). Compound **1** (16.5 g, 0.10 mol) was added aqueous HCl (104 mL, 4 M) and heated at 80 ^{o}C for 24 h. The water was removed by rotary evaporation to obtain a colorless oil (12.8 g, 94.1 %yield). ^{1}H NMR (δ in D_2O, 400 MHz, ppm): 3.25-3.27 ppm (t, J = 4.00 Hz, 2H, -$CH_2NHCH_2CH_2$-); 3.30 ppm (s, 3H, -OCH_3); 3.64-3.66 ppm (t, J = 4.00 Hz, 2H, $CH_3OCH_2CH_2$-); 3.91 ppm (s, 2H, -$NHCH_2COO$-). ^{13}C {^{1}H} NMR (δ in D_2O, 125 MHz, ppm): 46.7 ppm (-$CH_2NHCH_2CH_2$-); 47.2 ppm (-OCH_3); 58.3 ppm ($CH_3OCH_2CH_2$-); 66.7 ppm (-$NHCH_2COO$-); 168.8 ppm (-CH_2COOH).

Synthesis of 2-(*N*, *N*-tert-butoxycarbonyl-2-methoxyethyl)amino)acetic acid (3). Compound **2** (16.0 g, 0.09 mol), triethylamine (62.7 mL, 0.45 mol) and *di*-tert-butyl dicarbonate (49 g, 0.23 mol) were mixed in distilled water (200 mL) and stirred at 25 ^{o}C for 24 h. The reaction mixture was extracted with hexane (2 x 200 mL) to remove extra *di*-tert-butyl dicarbonate. The aqueous phase was acidified with aqueous HCl (4 M) at 0^{o}C and extracted with ethyl acetate (3 x 100 mL). The organic phase was washed with brine (1 x 200 mL) followed by drying over anhydrous $MgSO_4$. After filtration, the solvent was removed to obtain the desired product as white solid (18.5 g, 88.2 %). ^{1}H NMR (δ in $CDCl_3$, 400 MHz, ppm): 1.45-1.49 ppm (d, 9H, -$C(CH_3)_3$);

3.35-3.38 ppm (d, 3H, -OC*H*$_3$); 3.47-3.53 (m, 2H, $CH_3OCH_2CH_2$-); 3.59-3.61 ppm (m, 2H, $CH_3OCH_2CH_2$-); 4.01-4.09 (d, 2H, HOOCC*H*2-). ^{13}C {^{1}H} NMR (δ in $CDCl_3$, 125 MHz, ppm): 28.2-28.3 ppm (-C(*C*H_3)$_3$); 48.5-48.7 ppm ($CH_3OCH_2CH_2$-); 50.3-51.6 ppm ($CH_3OCH_2CH_2$-); 58.7-57.4 ppm ($CH_3OCH_2CH_2$-); 71.5-71.6 ppm (HOOC*C*H_2-); 80.9-81.0 ppm (-*C*(CH$_3$)$_3$); 155.0-155.8 ppm (-*C*OOC(CH$_3$)$_3$); 174.2-174.5 ppm (-CH$_2$*C*OOH).

Synthesis of MeOEt-NCA (M$_1$). Compound **3** (10.5 g, 0.045 mol) was dissolved in dry dichloromethane (150 mL) under a nitrogen atmosphere. PCl_3 (3.1 mL, 0.036 mol) was added dropwise to the solution at 0^{o}C and the mixture was stirred at 25^{o}C for 2 h. The solvent was removed under vacuum to obtain yellowish viscous residue. In the glovebox, the residue was extracted with dry dichoromethane (3 x 20 mL) and filtered and the filtrate was stirred with small amount of sodium hydride. After filtration, the filtrate was condensed to afford a pale yellow liquid (5.7 g, 80.5 %). The crude monomer was washed by soxhlet extraction with hexane and further purified by sublimation (50^{o}C, 20-50 militorr) to afford a colorless liquid (4.5 g, 85.1 %). ^{1}H NMR (δ in $CDCl_3$, 400 MHz, ppm): 3.38 ppm (s, 3H, C*H*$_3$O-); 3.60 ppm (s, 2H, $CH_3OCH_2CH_2$-); 4.28 ppm (s, 2H, -OOCC*H*2-). ^{13}C {^{1}H} NMR (δ in $CDCl_3$, 125 MHz, ppm): 43.6 ppm ($CH_3OCH_2CH_2$-); 50.8 ppm ($CH_3OCH_2CH_2$-); 59.0 ppm ($CH_3OCH_2CH_2$-); 70.9 ppm (-OOC*C*H2-); 152.2 ppm (-CH_2OCOOC-); 163.8 ppm (-CH$_2$O*C*OOC-).

Representative synthetic procedure for PNMeOEtG. In the glovebox, **M$_1$** (56.9 mg, 0.36 mmol, $[M]_0$ = 1 M) was dissolved in dry THF (201 µL). A volume of $BnNH_2$/THF stock solution (157 µL, 91.2 mM, $[M]_0$: $[BnNH_2]_0$ = 25 : 1) was added to the monomer solution and heated at 50^{o}C for 24 h under nitrogen atmosphere to reach 100 % conversion checked by FT-IR or NMR spectrascopy. The polymerization was quenched by adding excess hexane. The precipitate was collected and washed with hexane, followed by drying under vacuum to obtain a crispy solid.

Freeze drying yielded a white fluffy solid (34.1 mg, 82.3 %). ^{1}H NMR (δ in D_2O, 400 MHz, ppm): 7.25-7.33 ppm and 2.77-2.82 ppm (benzyl end group); 4.01-4.53 ppm (m, -COC*H*$_2$-); 3.49-3.83 ppm (m, -C*H*$_2$C*H*$_2$OCH$_3$); 3.02-3.31(d, -CH$_2$CH$_2$OC*H*$_3$).

3.2.3 Synthesis of Me(OEt)$_2$-NCA and PNMe(OEt)$_2$G

Synthesis of 2-(2-methoxyethoxy)ethanamine (4). **4** was synthesized by using a reported procedure. overall yield: 61.3%. ^{1}H NMR (δ in $CDCl_3$, 400 MHz, ppm): 3.61-3.64 ppm (m, 2H, -C*H*$_2$CH$_2$NH$_2$); 3.51-3.58 ppm (m, 4H, CH$_3$OC*H*$_2$C*H*$_2$-); 3.40 ppm (s, 3H, C*H*$_3$O-); 2.87-2.90 ppm (t, J=5.28 Hz, 2H, -C*H*$_2$NH$_2$); 1.58 ppm (bs, 2H, -N*H*$_2$).

Synthesis of ethyl 2-((2-(2-methoxyethoxy)ethyl)amino)acetate (5). **5** was synthesized with the same protocol as **1**. Yield: (70.5 %). ^{1}H NMR (δ in $CDCl_3$, 400 MHz, ppm): 4.18-4.24 ppm (q, J= 7.12Hz, 2H, -COOC*H*$_2$CH$_3$); 3.56-3.65 ppm (m, 6H, CH$_3$OC*H*$_2$C*H*$_2$OC*H*$_2$-); 3.45 ppm (s, 2H, -NHC*H*$_2$COO-); 3.41 ppm (s, 3H, C*H*$_3$O-); 2.83-2.86 ppm (t, J=10.6 Hz, 2H, -C*H*$_2$NHCH$_2$-); 1.83 ppm (s, -N*H*-); 1.28-1.31 ppm (t, J=14.3 Hz, 3H, -CH$_2$C*H*$_3$). ^{13}C {^{1}H} NMR (δ in $CDCl_3$, 125 MHz, ppm): 172.3 ppm (-*C*OOCH$_2$CH$_3$); 70.3-71.9 ppm (CH$_3$O*C*H$_2$*C*H$_2$O*C*H$_2$-); 59.0-60.7 ppm (-*C*H$_2$COO*C*H$_2$-); 48.8-51.0 ppm (*C*H$_3$OCH$_2$CH$_2$OCH$_2$*C*H$_2$NH-); 14.2 ppm (-COOCH$_2$*C*H$_3$).

Synthesis of ethyl 2-((2-(2-methoxyethoxy)ethyl)amino)acetate hydrochloride (6). **6** was synthesized with the same protocol as **2** in 95.1%-96.8% yield. ^{1}H NMR (δ in $CDCl_3$, 400 MHz, ppm): 3.91 ppm (s, 2H, -NHC*H*$_2$COOH); 3.55-3.74 ppm (m, 6H, CH$_3$OC*H*$_2$C*H*$_2$OC*H*$_2$-); 3.31 ppm (s, 3H, C*H*$_3$O-); 3.27-3.29 ppm (t, J=9.96 Hz, -C*H*2CH-). ^{13}C {^{1}H} NMR (δ in $CDCl_3$, 125 MHz, ppm): 169.0 ppm (-*C*OOH); 65.3-71.0 ppm (CH$_3$O*C*H$_2$*C*H$_2$OCH$_2$CH$_2$NH*C*H$_2$-); 58.0 ppm (-*C*H$_2$CH$_2$NH-); 46.9-47.3 ppm (*C*H$_3$OCH$_2$CH$_2$OCH$_2$*C*H$_2$-).

Synthesis of 2-(*N*, *N*-tert-butoxycarbonyl-2-(2-methoxyethoxyethyl)amino)acetic acid (7). **7** was synthesized with the same protocol as **3**. Yield: (82.9 %). ^{1}H NMR (δ in $CDCl_3$, 400

MHz, ppm): 4.03-4.11 ppm (d, 2H, HOOCC*H*2-); 3.48-3.69 ppm (m, 8H, -CH_2CH_2OCH_2CH_2OCH$_3$); 3.39 ppm (s, 3H, -OCH_3); 1.45-1.48 ppm (d, 9H, $(CH_3)_3$-). ^{13}C {^{1}H} NMR (δ in $CDCl_3$, 125 MHz, ppm): 28.2-28.4 ppm (-C(*C*$H_3)_3$); 48.4-50.1 ppm (*C*H_3OCH_2CH_2OCH_2*C*H_2-); 58.7-58.8 ppm (CH_3OCH_2CH_2OCH_2CH_2-); 69.9-70.5 ppm (CH_3OCH_2*C*H_2-); 71.9-72.0 ppm (HOOC*C*H_2-); 80.5-80.6 ppm (-*C*$(CH_3)_3$); 155.3-155.7 ppm (-*C*OOC$(CH_3)_3$); 172.6-172.7 ppm (-CH_2*C*OOH).

Synthesis of Me(OEt)$_2$-NCA (M$_2$). **M$_2$** was synthesized with the same protocol as **M$_1$**. Yield: 70.8 %). ^{1}H NMR (δ in $CDCl_3$, 400 MHz, ppm): 4.34 ppm (s, 2H, -OOCC*H*2-); 3.51-3.72 ppm (m, 8H, -C*H*$_2$C*H*$_2$OC*H*$_2$C*H*$_2$O-); 3.38 ppm (-OC*H*$_3$). ^{13}C {^{1}H} NMR (δ in $CDCl_3$, 125 MHz, ppm): 166.1 ppm (-*C*OOCO-); 152.3 ppm (-COO*C*O-); 69.4-71.7 ppm (-OOC*C*H2-, -CH_2CH_2OCH_2*C*H_2O-); 59.1 ppm (-CH_2*C*H_2OCH_2CH_2O-); 50.9 ppm (-*C*$H_2CH_2OCH_2CH_2$O-); 43.5 ppm (-O*C*H_3).

Representative synthetic procedure for PNMe(OEt)$_2$G. In the glovebox, **M$_2$** (66.4 mg, 0.33 mmol, $[M]_0$ = 1 M) was dissolved in dry THF (184 μL). A volume of $BnNH_2$/THF stock solution (143 μL, 91.2 mM, $[M]_0$: $[BnNH_2]_0$ = 25 : 1) was added to the monomer solution and heated at 50^{o}C for 24 h under nitrogen atmosphere to reach 100 % conversion checked by FT-IR or NMR spectrascopy. The polymerization was quenched by adding excess hexane. The precipitate was collected and washed with hexane, followed by drying under vacuum to obtain a crispy solid. Freeze drying yielded a white fluffy solid (46.1 mg, 87.8 %). ^{1}H NMR (δ in D_2O, 400 MHz, ppm): 7.22-7.32 ppm and 2.93-2.94 ppm (benzyl end group); 4.09-4.63 ppm (m, 2H, -COC*H*$_2$-); 3.51-3.60 ppm (m, 8H, -C*H*$_2$C*H*$_2$OC*H*$_2$C*H*$_2$OCH$_3$); 3.26-3.28(m, -OC*H*$_3$).

3.2.4 Synthesis of $Me(OEt)_3$-NCA and $PNMe(OEt)_3G$

Synthesis of 2-(2-(2-Methoxyethoxy)ethoxy)ethylamine (8). 8 was synthesized by using a reported procedure. Yield: 67.2 %. ^{1}H NMR (δ in $CDCl_3$, 400 MHz, ppm): 3.40-3.55 ppm (m, 10H, -C*H*$_2$OC*H*$_2$C*H*$_2$OC*H*$_2$C*H*$_2$OCH$_3$); 3.28 ppm (s, 3H, -OC*H*$_3$); 2.77 ppm (s, 2H, -C*H*$_2$NH$_2$); 1.77 ppm (s, 2H, N*H*$_2$).

Synthesis of ethyl 2-((2-(2-(2-ethoxyethoxy)ethyl)amino)acetate (9). 9 was synthesized with the same protocol as **1** and **5**. Yield: 71.6 %. ^{1}H NMR (δ in $CDCl_3$, 400 MHz, ppm): 4.16-4.21 ppm (q, J=7.12 Hz, 2H, CH$_3$C*H*$_2$COO-); 3.54-3.66 ppm (m, 10H, -C*H*$_2$OC*H*$_2$C*H*$_2$OC*H*$_2$C*H*$_2$OCH$_3$); 3.44 ppm (s, 2H, -NHC*H*$_2$COO-); 3.38 ppm (s, 3H, -OC*H*$_3$); 2.80-2.83 ppm (t, 2H, -C*H*$_2$NHCH$_2$COO-); 2.09 ppm (bs, 1H, -N*H*-); 1.26-.1.29 ppm (t, 3H, -COOCH$_2$C*H*$_3$). ^{13}C {^{1}H} NMR (δ in $CDCl_3$, 125 MHz, ppm): 172.2 ppm (-*C*OO-); 70.3-71.9 ppm (-*C*H$_2$*C*H$_2$O*C*H$_2$*C*H$_2$OCH$_2$CH$_2$NHCH$_2$COO*C*H$_2$-); 59.0-60.7 ppm (-*C*H$_2$CH$_2$NH*C*H$_2$-); 48.8-50.9 ppm (*C*H$_3$OCH$_2$CH$_2$OCH$_2$CH$_2$OCH$_2$*C*H$_2$-); 14.2 ppm (-COOCH$_2$*C*H$_3$).

Synthesis of ethyl 2-((2-(2-(2-ethoxyethoxy)ethyl)amino)acetate hydrochloride (10). **10** was synthesized with the same protocol as **2** and **6** in 95.8 %-97.7% yield. ^{1}H NMR (δ in $CDCl_3$, 400 MHz, ppm): 3.28-3.29 ppm (m, 5H, C*H*$_3$OCH$_2$CH$_2$OCH$_2$CH$_2$OCH$_2$C*H*$_2$-); 3.53-3.55 ppm (m, 2H, CH$_3$OCH$_2$CH$_2$OCH$_2$CH$_2$OC*H*$_2$CH$_2$-); 3.61-3.65 ppm (m, 6H, CH$_3$OCH$_2$C*H*$_2$OC*H*$_2$C*H*$_2$-); 3.74-3.75 ppm (m, 2H, CH$_3$OC*H*$_2$-); 3.92 ppm (s, 2H, HOOCC*H*$_2$-). ^{13}C {^{1}H} NMR (δ in $CDCl_3$, 125 MHz, ppm): 46.9-47.2 ppm (*C*H$_3$OCH$_2$CH$_2$OCH$_2$CH$_2$OCH$_2$*C*H$_2$-); 58.0 ppm (CH$_3$OCH$_2$CH$_2$OCH$_2$CH$_2$OCH$_2$CH$_2$-); 65.2 ppm (CH$_3$OCH$_2$CH$_2$OCH$_2$*C*H$_2$-); 69.4-69.5 ppm (CH$_3$O*C*H$_2$*C*H$_2$O*C*H$_2$CH$_2$-); 70.9 ppm (HOOC*C*H$_2$-); 168.9 ppm (HOO*C*CH$_2$-).

Synthesis of 2-(*N*, *N*-tert-butoxycarbonyl-2-(2-(2-ethoxyethoxy)ethyl)amino) acetic acid (11). 11 was synthesized with the same protocol as **3** and **7**. Yield: 80.1%. ^{1}H NMR (δ in

$CDCl_3$, 400 MHz, ppm): 4.00-4.08 ppm (d, 2H, HOOCC*H*$_2$-); 3.47-3.64 ppm (m, 12H, -C*H*$_2$C*H*$_2$OC*H*$_2$C*H*$_2$OC*H*$_2$C*H*$_2$-); 3.39-3.41 ppm (m, 3H, -OC*H*$_3$); 1.44-1.47 ppm (d, 9H, $(CH_3)_3$-). ^{13}C {^{1}H} NMR (δ in $CDCl_3$, 125 MHz, ppm): 28.2-28.3 ppm (-C(*C*H$_3$)$_3$); 48.5-51.3 ppm (*C*H$_3$OCH$_2$CH$_2$OCH$_2$CH$_2$OCH$_2$*C*H$_2$-); 58.9-59.0 ppm (CH$_3$OCH$_2$CH$_2$OCH$_2$*C*H$_2$-); 70.1-70.4 ppm (CH$_3$O*C*H$_2$*C*H$_2$O*C*H$_2$CH$_2$-); 71.6-71.8 ppm (HOOC*C*H$_2$-); 80.7-80.8 ppm (-*C*(CH$_3$)$_3$); 155.1-155.8 ppm (-*C*OOC(CH$_3$)$_3$); 173.9 ppm (-CH$_2$*C*OOH).

Synthesis of Me(OEt)$_2$-NCA (M$_3$). **M$_3$** was synthesized with the same protocol as **M$_1$ and M$_2$**. Yield: 69.9 %). ^{1}H NMR (δ in $CDCl_3$, 400 MHz, ppm): 4.38 ppm (s, 2H, -OOCC*H*$_2$-); 3.71-3.73 ppm (m, 2H, CH$_3$OC*H*$_2$-); 3.59-3.66 ppm (m, 8H, CH$_3$OCH$_2$C*H*$_2$OC*H*$_2$C*H*$_2$OC*H*$_2$-); 3.53-3.56 ppm (m, 2H, CH$_3$OCH$_2$CH$_2$OCH$_2$CH$_2$OCH$_2$C*H*$_2$-); 3.39 ppm (C*H*$_3$O-). ^{13}C {^{1}H} NMR (δ in $CDCl_3$, 125 MHz, ppm): 166.1 ppm (-*C*OOCO-); 152.4 ppm (-COO*C*O-); 69.4-70.5 ppm (*C*H$_3$O*C*H$_2$*C*H$_2$O*C*H$_2$-); 71.9 ppm (-OOC*C*H2-); 59.0 ppm (CH$_3$OCH$_2$CH$_2$OCH$_2$*C*H$_2$-); 50.9 ppm (CH$_3$OCH$_2$CH$_2$OCH$_2$CH$_2$O*C*H$_2$CH$_2$-); 43.5 ppm (CH$_3$OCH$_2$CH$_2$OCH$_2$CH$_2$OCH$_2$*C*H$_2$-).

Representative synthetic procedure for PNMe(OEt)$_3$G. In the glovebox, **M$_3$** (70.7 mg, 0.29 mmol, $[M]_0$ = 1 M) was dissolved in dry THF (160 μL). A volume of $BnNH_2$/THF stock solution (126 μL, 91.2 mM, $[M]_0$: $[BnNH_2]_0$ = 25 : 1) was added to the monomer solution and heated at 50^{o}C for 24 h under nitrogen atmosphere to reach 100 % conversion checked by FT-IR or NMR spectrascopy. The polymerization was quenched by adding excess hexane. The precipitate was collected and washed with hexane, followed by drying under vacuum to obtain a crispy solid. Freeze drying yielded a white fluffy solid (51.2 mg, 86.9 %). ^{1}H NMR (δ in D_2O, 400 MHz, ppm): 7.24-7.32 ppm (benzyl end group); 4.10-4.55 ppm (m, 2H, -COC*H*$_2$-); 3.53-3.59 ppm (m, 12H, -C*H*$_2$C*H*$_2$OC*H*$_2$C*H*$_2$OC*H*$_2$C*H*$_2$OCH$_3$); 3.29 (m, -OC*H*$_3$).

3.2.5 Characterization of PNMe(OEt)$_n$G (n=1-3)

Size exclusion chromatography (SEC) analysis. SEC analysis of the polypeptoids were performed using an Agilent 1200 system (Agilent 1200 series degasser, isocratic pump, auto sampler and column heater) equipped with three Phenomenex 5 μm, 300 × 7.8 mm columns [100 Å, 1000 Å and Linear (2)], a Wyatt OptilabrEX differential refractive index (DRI) detector with a 690 nm light source, and a Wyatt DAWN EOS multiangle light scattering (MALS) detector (GaAs 30mW laser at λ = 690 nm). DMF with 0.1M LiBr was used as the eluent at a flow rate of 0.5 mL·min^{-1}. The column and detector temperature was set at room temperature (20^{o}C). All data analysis was performed using Wyatt Astra V 5.3 software. Polymer molecular weight (MW) and molecular weight distribution (PDI) were obtained by the Zimm model fit of the MALS-DRI data. The absolute polymer molecular weight (M_n) was determined using the measured refractive index increment d*n*/d*c* values. The refractive index increment (d*n*/d*c*) of the polymer was determined using Wyatt's rEX DRI detector and Astra software dn/dc template. The polymer was dissolved in DMF with 0.1 M LiBr to prepare six dilute solutions with known concentrations (0.05-3.00 mg/mL) using volumetric flasks. The solutions were injected to the DRI detector and the corresponding d*n*/d*c* value was determined from the linear fit to a plot of refractive index versus polymer concentration. The d*n*/d*c* values measured for PNMeOEtG$_{106}$, PNMe(OEt)$_2$G$_{102}$ and PNMe(OEt)$_3$G$_{106}$ are 0.0633(4), 0.0686(8) and 0.0563(6) mL/g, respectively.

Thermogravimetric analysis. TGA analysis of the polypeptoids was conducted on a TA TGA 2950 under nitrogen at the heating rate of 10 ^{o}C·min^{-1}. The decomposition temperature (T_d) of the polypeptoids was determined from the onsets of weight loss.

Differential scanning calorimetry (DSC) analysis. DSC analysis of the polypeptoids were conducted on a TA DSC 2920 calorimeter under nitrogen. The polymer (~5 mg) was sealed

into the hermetic aluminum pan and an empty hermetic aluminum pan was used as the reference. The sample containing pans were first heated from -50 ^{o}C to 200 ^{o}C at 10 ^{o}C /min, cooled to -50 ^{o}C at 10 ^{o}C /min and remained at -50^{o}C for 5min, and reheated to 200 ^{o}C at 10 ^{o}C/min. The glass transition temperature (T_g) was determined by the inflection on the slope of heat flow shifting.

Kinetic Studies of $BnNH_2$-initiated ring-opening polymerization of Me $(OEt)_n$-NCA (n=1-3). A predetermined amount of $BnNH_2$ stock solutions in toluene-d_8 were added to a toluene-d_8 solution of Me$(OEt)_n$-NCA (n=1-3) ($[M]_0$ = 0.2 M, $[M]_0$:$[BnNH_2]_0$ = 25:1) at room temperature followed by transferring into a resealable J-Yong NMR tube. ^{1}H NMR spectra were collected every 3 min 44 s at 50^{o}C to determine the conversion of monomers for more than four half-lives. Kinetic experiments were repeated twice for each monomer.

Study of M_n vs polymerization conversion. The polymerization of Me$(OEt)_n$-NCA (n=1-3) was conducted in THF at 50^{o}C ($[M]_0$:$[I]_0$=50:1, $[M]_0$=1 M) and aliquots were taken at different time intervals and analyzed with ^{1}H NMR spectroscopy to determine the conversion. The aliquots taken at different time intervals were further analyzed with MALDI-TOF spectroscopy to obtain the polymer molecular weight (M_n) and molecular weight distribution (PDI). The obtained M_ns were plotted against the corresponding polymerization conversion.

3.2.6 Study of protein-resistant behavior of polypeptoids

Dynamic light scattering analysis. PNMeOEtG (DP_n =106), PEG8000 or lysozyme was dissolved in PBS at 1wt% and filtered through 0.22 μm filters before measurement. All the samples were conducted using Malvern Zetasizer Nano-zs (Zen3600). The He-Ne laser operating at 633 nm was utilized, and scattered light intensity was detected at an external angle of 173^{o}C using non-invasive backscatter (NIBS) technology. Data from three measurement with 12 scans for each

measurement was recorded. The hydrodynamic diameters and PDI of the samples were obtained from cumulant analysis.

Small-angle neutron scattering (SANS). The small angle neutron scattering (SANS) studies were performed at the NIST Center for Neutron Research (NCNR) in Gaithersburg, MD, on the NG7 30 m SANS instrument, using neutrons with wavelength λ = 6 Å and wavelength spread, $\Delta\lambda/\lambda$ = 11%. The temperature was maintained to 20±0.1°C using a circulating bath. A typical SANS data reduction protocol, which consisted of subtracting scattering contributions from the empty cell (2 mm demountable titanium cells), background scattering, and sorting data collected from two different detector distances was used to yield normalized scattering intensities, I(Q) (cm^{-1}) a.k.a. the macroscopic scattering cross-section ($d\Sigma/d\Omega$) as a function of the scattering vector, Q ($Å^{-1}$). Data reduction was conducted employing the NCNR Igor-pro platform. The SANS scattering intensity for our macromolecular solution [48] is modelled as

$$\frac{d\Sigma}{d\Omega} = \phi\Delta\rho^2 VP(Q)S(Q) \qquad (1)$$

Here, ϕ is the volume fraction of the molecules, $\Delta\rho$ and V, are their average scattering contrast and volume, respectively. The single molecular form factor, $P(Q)$, averaged particle scattering over the ensemble of sizes and orientations, is related to the particle structure. The effective structure factor, $S(Q)$, provides information about the intermolecular interaction. For dilute solutions of non-interacting molecules, $S(Q) \approx 1$.

In the current work we have modelled the form factor and the structure for lysozyme molecule using a hard sphere approximation[49-50]. The form factor for the polymer is modelled using the random Gaussian coil[51].

3.2.7 Cytotoxicity study of polypeptoids

The cytotoxicity study was conducted by adapting a reported procedure.[52] The HEp2 cells were plated at 8600 cells per well in a Costar 96-well plate (BD biosciences) and allowed to grow for 48 h. The polypeptoids were dissolved in Eagle's Minimum Essential Medium (EMEM) and diluted to final working concentrations (0, 0.0625, 0.125, 0.25, 0.5, and 1mg/mL). The cells were exposed to the working solutions of polypeptoids up to 1 mg/mL and incubated for 24 h (37^{o}C, 95% humidity, 5% CO_2). The working solution was removed, and the cells were washed with 1X PBS. The medium containing 20% CellTiter Blue (Promega) was added and incubated for 4 h. The viability of cells is measured by reading the fluorescence of the medium at 570/615 nm using a BMG FLUOstar Optima micro-plate reader. In this assay, the indicator dye resazurin is reduced to fluorescent resorufin in viable cells, while non-viable cells are not able to reduce resazurin nor to generate a fluorescent signal. The fluorescence signal of viable (untreated) cells was normalized to 100 %.

3.3 Results and discussion

3.3.1 Synthesis and characterization of Me(OEt)$_n$-NCA and PNMe(OEt)$_n$G

It was the first time to report the synthesis of PEGylated *N*-carboxyanhyride monomers, MeOEt-NCA, Me(OEt)$_2$-NCA and Me(OEt)$_3$-NCA. Me(OEt)$_n$-NCA (n=1-3) were synthesized in moderate overall yields (40.9 -49.7 %) by adapting a reported procedure[53-54] as outlined in Scheme 3.1. The primary amine (2-(2-methoxyethoxy)ethanamine and 2-(2-(2-Methoxyethoxy)ethoxy)ethylamine) used were synthesized in good yields (61.3-67.2%, Scheme 3.2, Figure 3.1 and 3.2) by adapting a reported procedue.[55] The monomer precursors (**3, 7 and 11**) showed rotamers at 25^{o}C in $CDCl_3$ due to restricted rotating of the amide bond, which was supported by the broadening and merged peaks shown in ^{1}H NMR spectra collected at elevated

temperature (50^{o}C) (Figure 3.7, 3.16 and 3.25). The structures of the desired monomers were confirmed by ^{1}H and ^{13}C {^{1}H} NMR spectroscopic analysis (Figure 3.9-3.10, 3.18-3.19 and 3.27-3.28). The polypeptoids bearing oligomeric ethylene oxide side chains (PNMe(OEt)$_n$G, n=1-3) were synthesized by ring-opening polymerizations of their corresponding monomers using benzyl amine as the initiator (Scheme 3.3). All polymerization reactions were conducted in anhydrous THF at 50^{o}C for 24-48 h to reach 100 % conversion at different initial monomer to initiator ratios ([M]$_0$:[I]$_0$). The polymers were purified by precipitation in hexane and collected by filtration followed by drying under vacuum to yield ether crispy white solids (PNMeOEtG) or viscous liquids (PNMe(OEt)$_n$G, n=2-3) in good yields (82.3-87.8%). The number-averaged molecular weight (M_n) and degree of polymerization (DP_n) of the polymer was determined by both the ^{1}H NMR spectroscopy using end-group analysis and by SEC analysis using dn/dc values of the polymers. For example, the DP_n and M_n of PNMeOEtG was determined by the integrations at 4.01-4.52 ppm due to the methylene group in the backbone relative to the integration of signals at 7.3 ppm due to the benzyl end-group (Figure 3.11). The molecular weight of the polymers (M_n) increased as the initial monomer to initiator ratio ([M]$_0$:[I]$_0$) was systematically increased (Table 3.1), as evidenced by ^{1}H NMR and SEC analysis. The polymer molecular weights (M_n) agreed with the theoretically predicated values at low molecular weight range ([M]$_0$:[I]$_0$ < 200:1). However, at high [M]$_0$:[I]$_0$ ratios (200:1 and 400:1), the molecular weight of the polymers (M_n) determined from SEC analysis deviated from the theoretical values probably due to presence of impurities and the impurities were probably also behaved as initiators to react with the monomers. The polymer molecular weight distributions were narrow with low polydispersity indices (PDI) in the 1.03-1.10 range (Table 3.1, Figure 3.30, 3.32 and 3.34) as determined by SEC analysis in 0.1 M LiBr/DMF at room temperature (^{o}C). The structure of low molecular weight PNMe(OEt)$_n$G

(n=1-3) was further confirmed by MALDI-TOF spectroscopic analysis. The spectra showed a symmetric monomodal set of mass ions where m/z equals to integral numbers of the desired repeating unit mass (115.2, 159.7 and 203.3 g/mol) for ($PNMe(OEt)_nG$, n=1-3) plus 22 or 39 for sodium or potassium ion. This is consistent with the targeted polypeptoid structures bearing one benzyl amide and one secondary amine chain end (Scheme 2), in support of controlled polymerization initiated by benzyl amine initiator. (Figure 3.31, 3.33 and 3.35).

Scheme 3.1.Synthetic procedures of $Me(OEt)_n$-NCA (n=1-3).

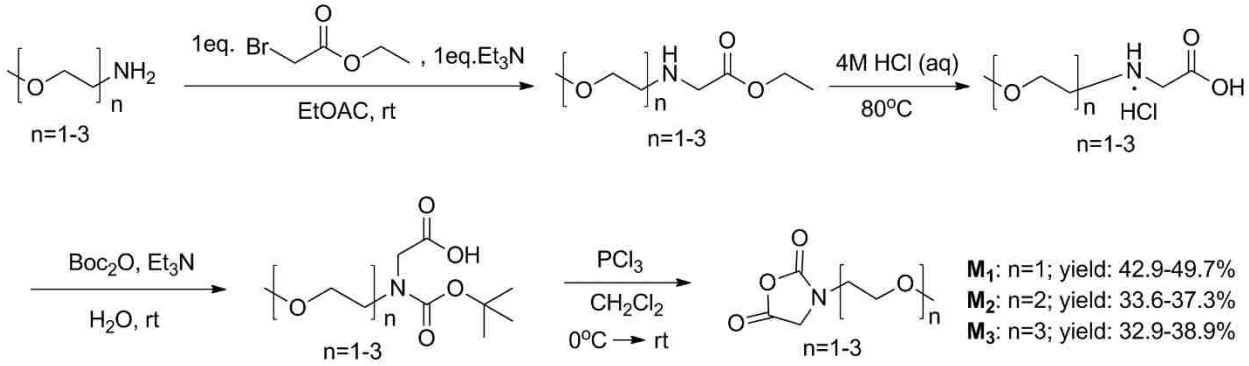

Scheme 3.2. Synthetic procedures of 2-(2-methoxyethoxy)ethanamine and 2-(2-(2-Methoxyethoxy)ethoxy)ethylamine.

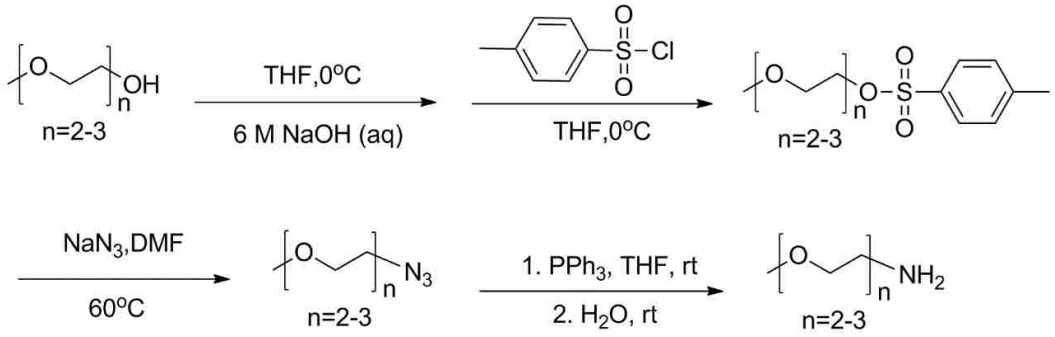

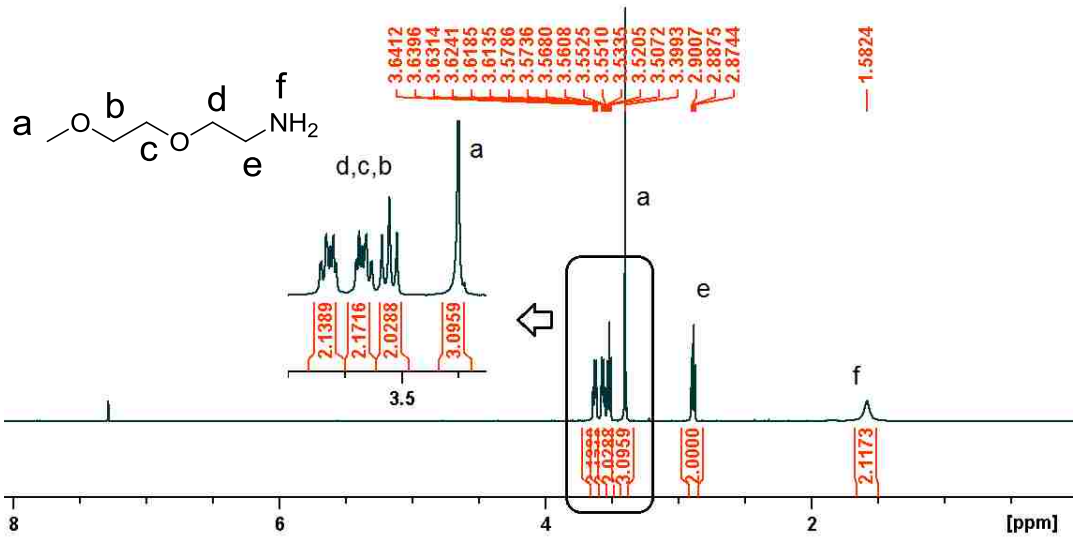

Figure 3.1.[1]H NMR spectrum of 2-(2-methoxyethoxy)ethanamine in $CDCl_3$.

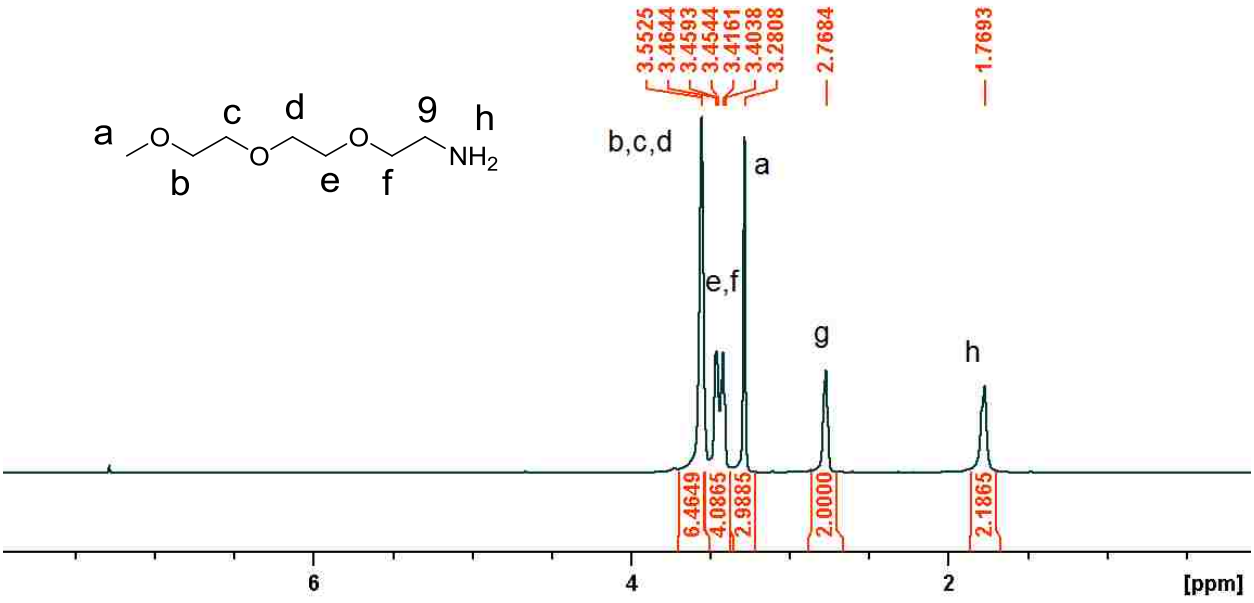

Figure 3.2. [1]H NMR spectrum of 2-(2-(2-Methoxyethoxy)ethoxy)ethylamine.

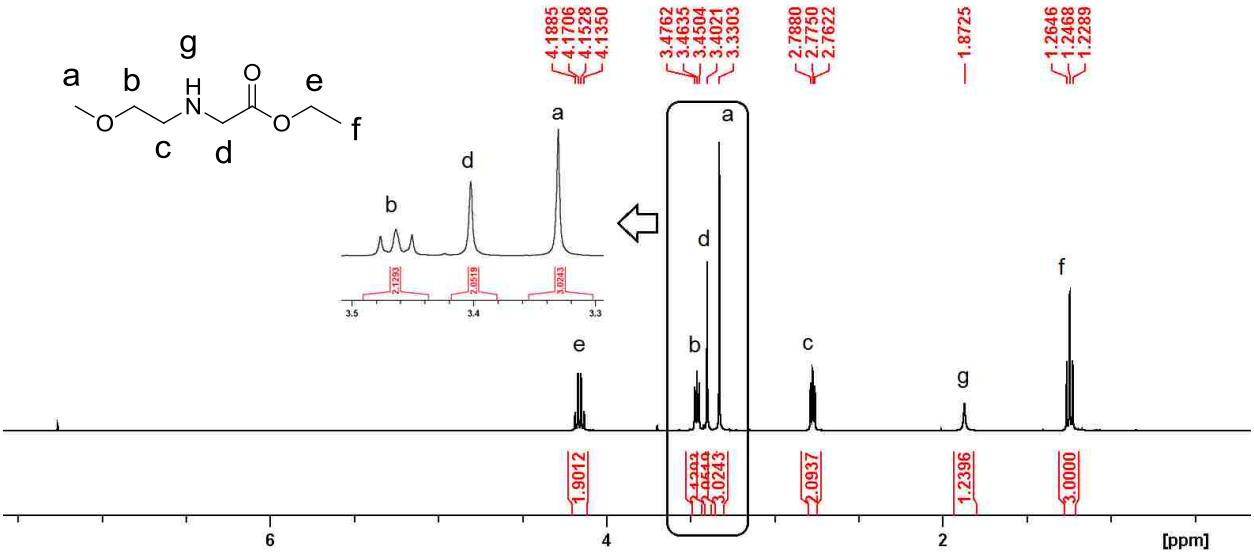

Figure 3.3. ^{1}H NMR spectrum of ethyl 2-((2-methoxyethyl)amino)acetate in $CDCl_3$.

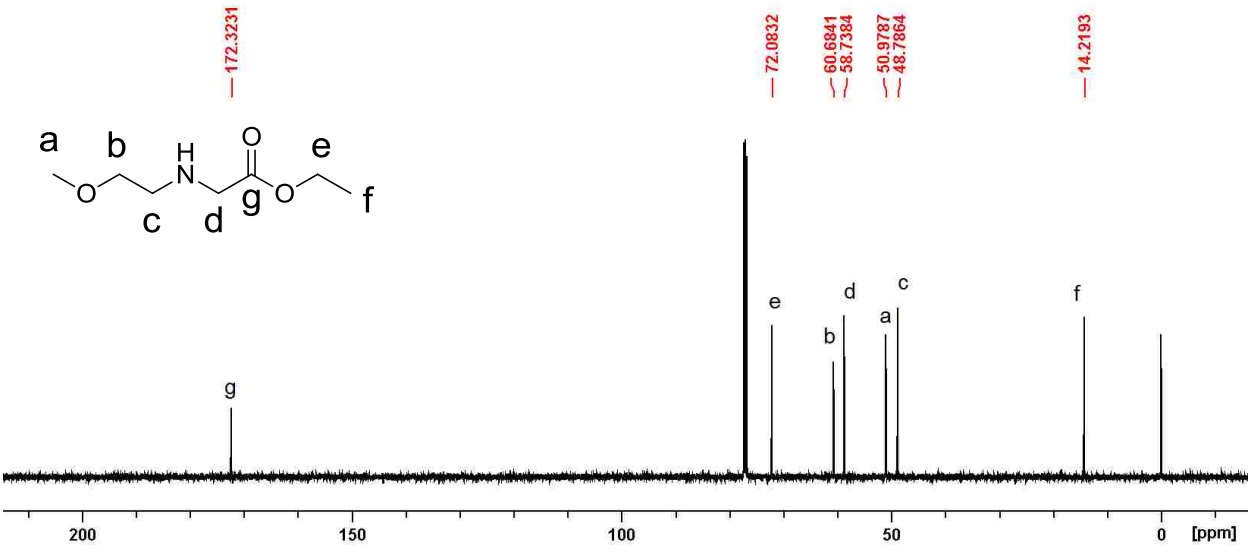

Figure 3.4. ^{13}C {H} NMR spectrum of ethyl 2-((2-methoxyethyl)amino)acetate in $CDCl_3$.

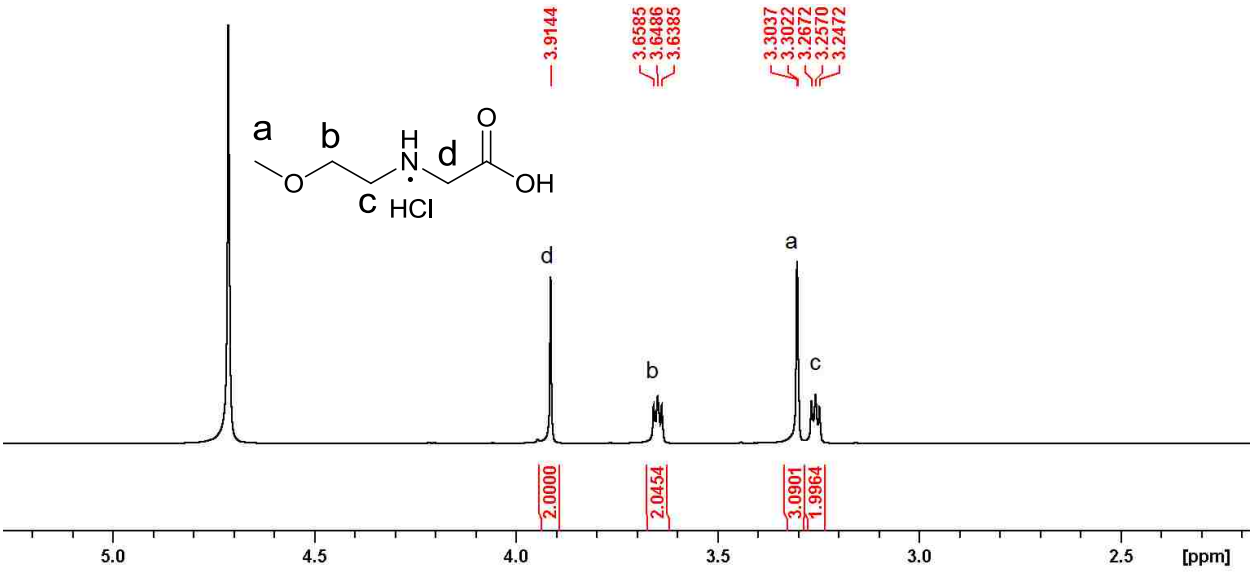

Figure 3.5. ^{1}H NMR spectrum of ethyl 2-((2-methoxyethyl)amino)acetic acid hydrochloride in D_2O.

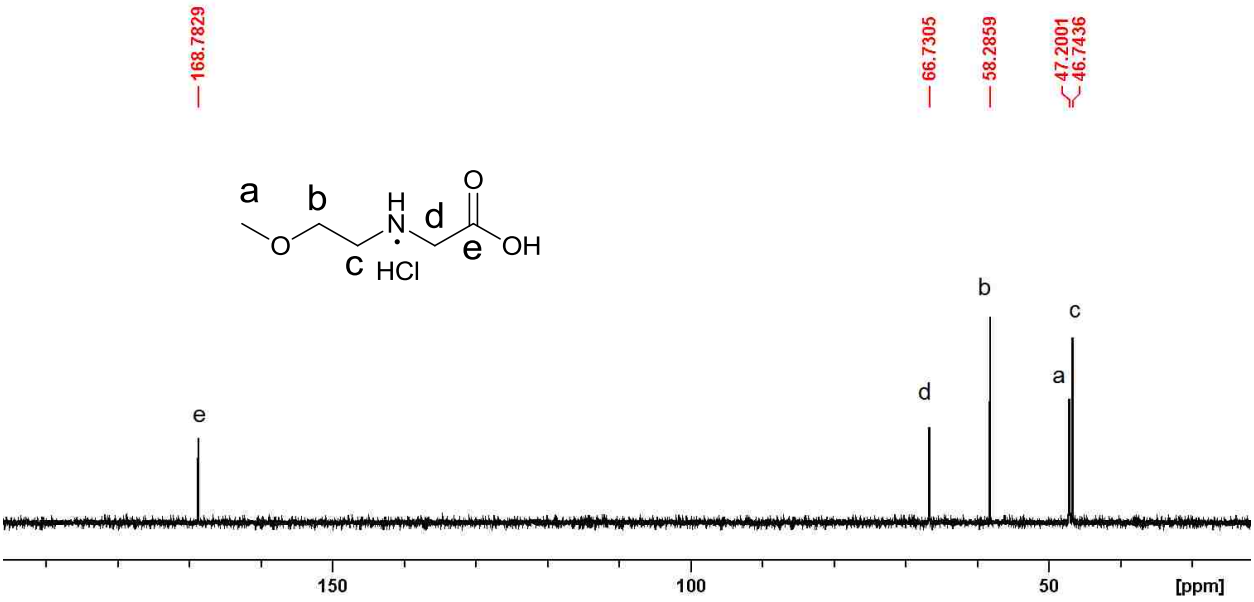

Figure 3.6. ^{13}C {H} NMR spectrum of ethyl 2-((2-methoxyethyl)amino)acetic acid hydrochloride in D_2O.

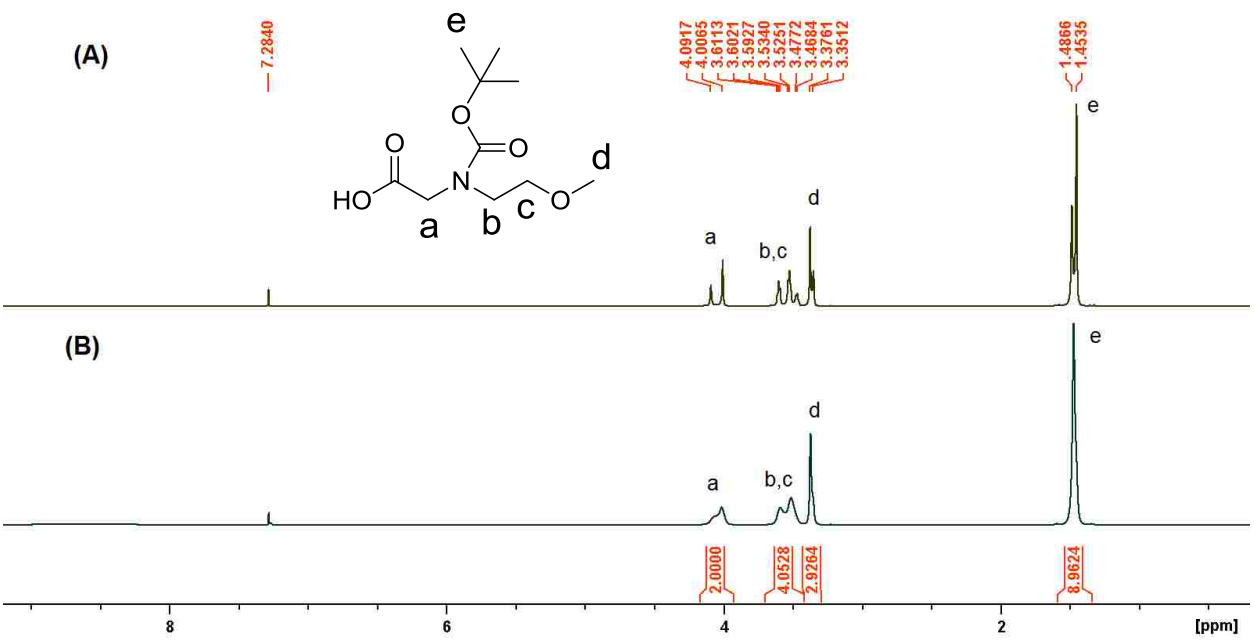

Figure 3.7. ^{1}H NMR spectrum of 2-(*N*, *N*-tert-butoxycarbonyl-2-methoxyamino)acetic acid in $CDCl_3$: (A) at 25 °C and (B) at 50 °C.

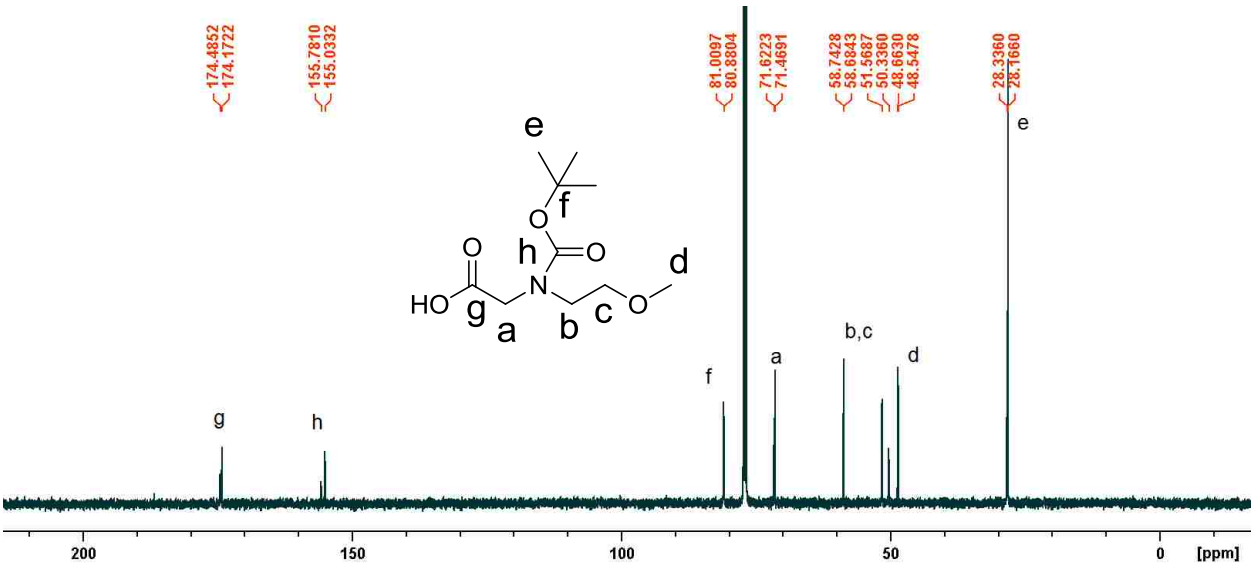

Figure 3.8. ^{13}C {H} NMR spectrum of 2-(*N*, *N*-tert-butoxycarbonyl-2-methoxyamino)acetic acid in $CDCl_3$ at 25 °C.

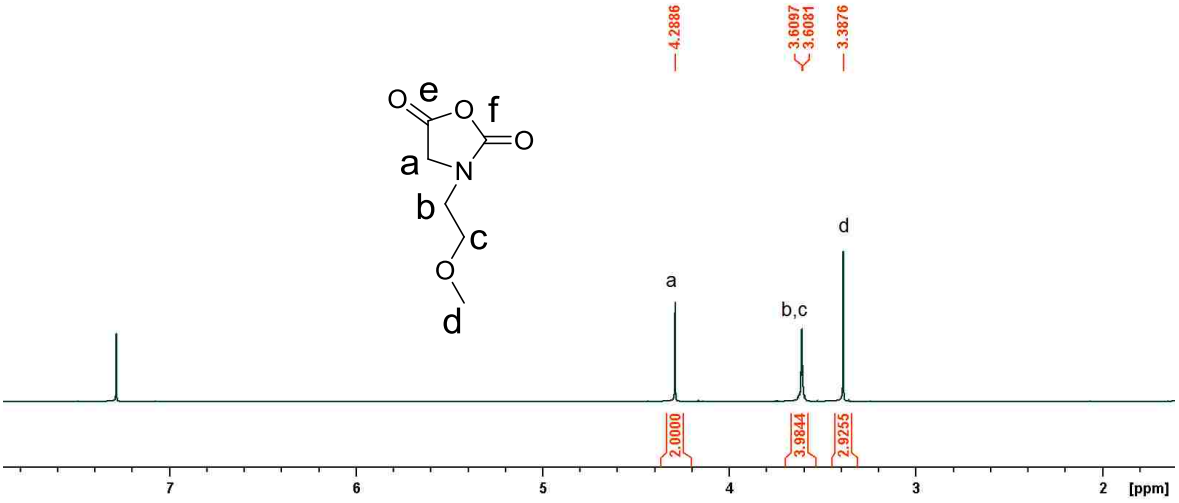

Figure 3.9. ^{1}H NMR spectrum of MeOEt-NCA in $CDCl_3$.

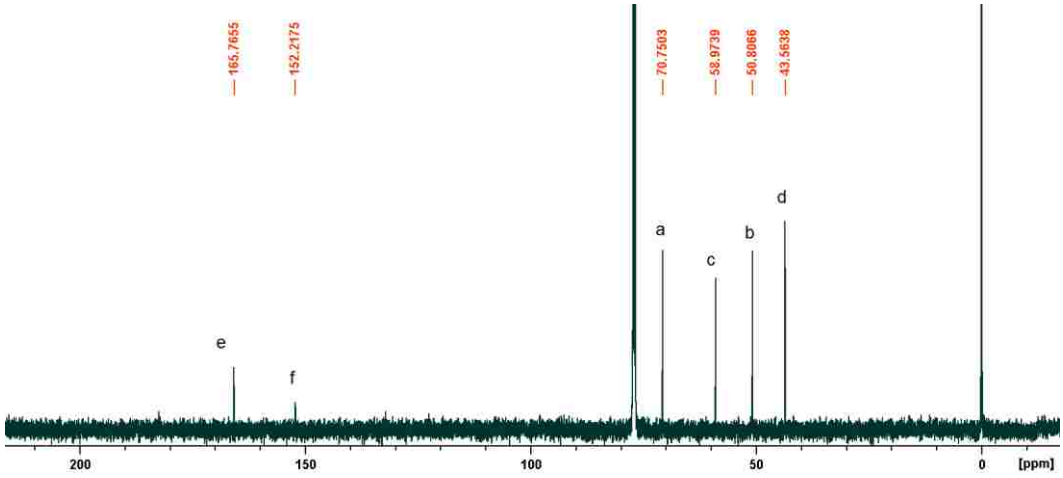

Figure 3.10. ^{13}C {^{1}H} NMR spectrum of MeOEt-NCA in $CDCl_3$.

Scheme 3.3. Benzyl amine-initiated ROP of $Me(OEt)_n$-NCA (n=1-3).

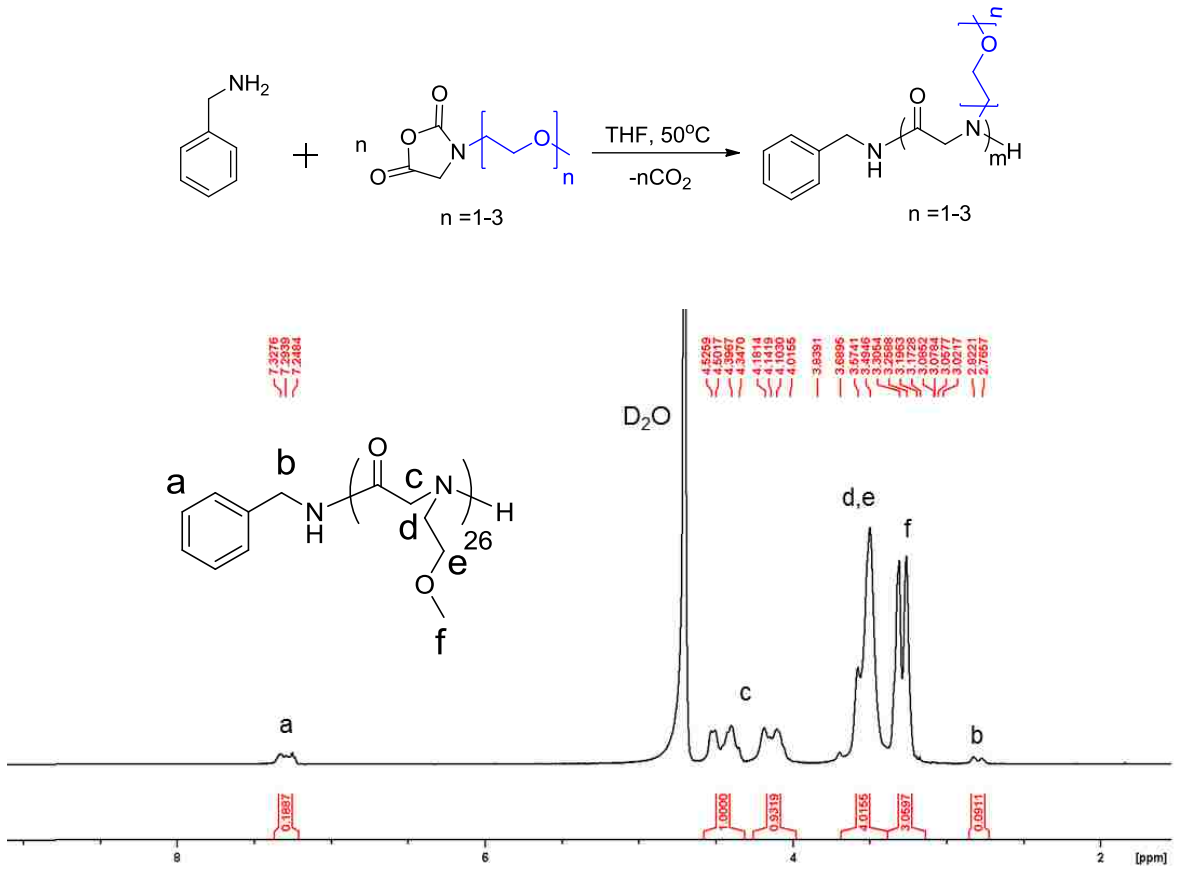

Figure 3.11.[1]H NMR spectrum of PNMeOEtG$_{26}$ in D_2O.

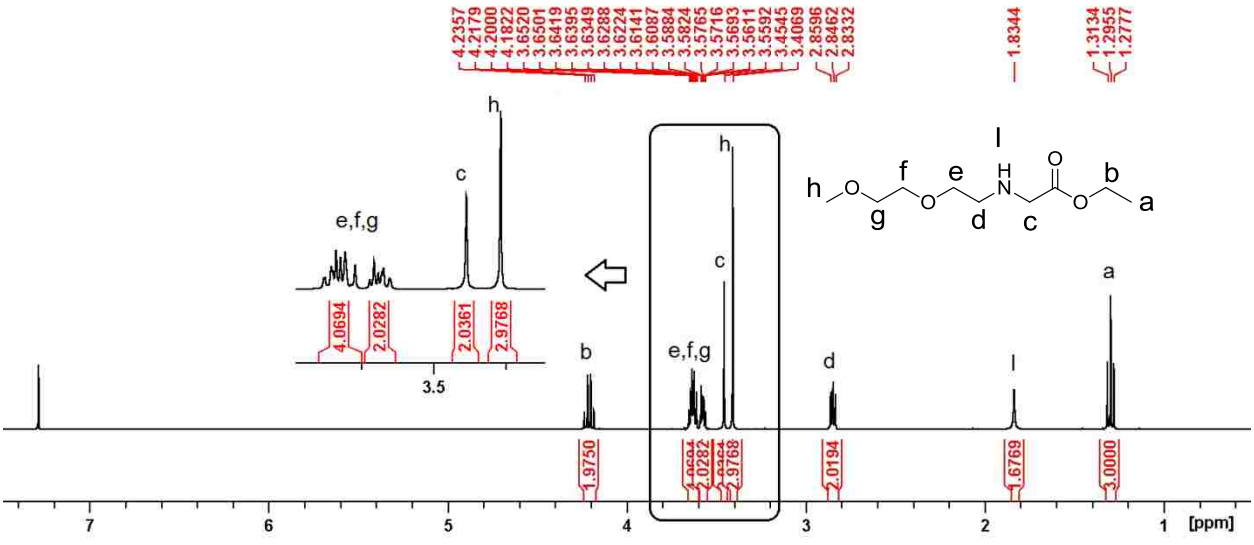

Figure 3.12. [1]H NMR spectrum of ethyl 2-((2-(2-methoxyethoxy)ethyl)amino)acetate in $CDCl_3$.

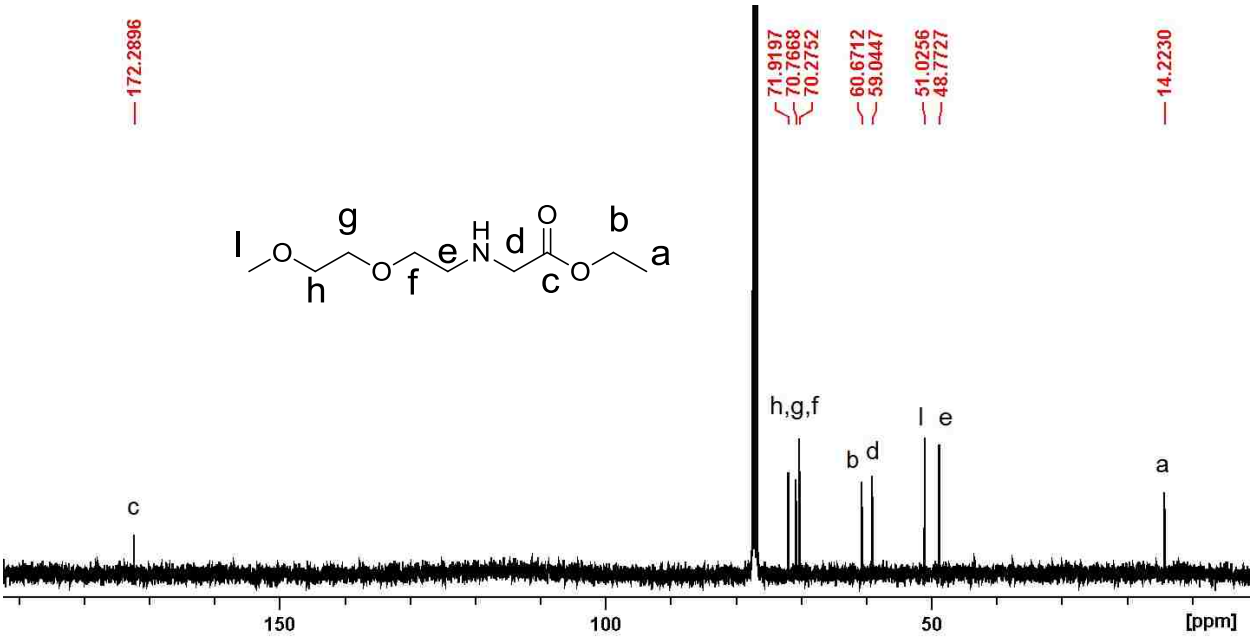

Figure 3.13. ^{13}C {H} NMR spectrum of ethyl 2-((2-(2-methoxyethoxy)ethyl)amino)acetate in $CDCl_3$.

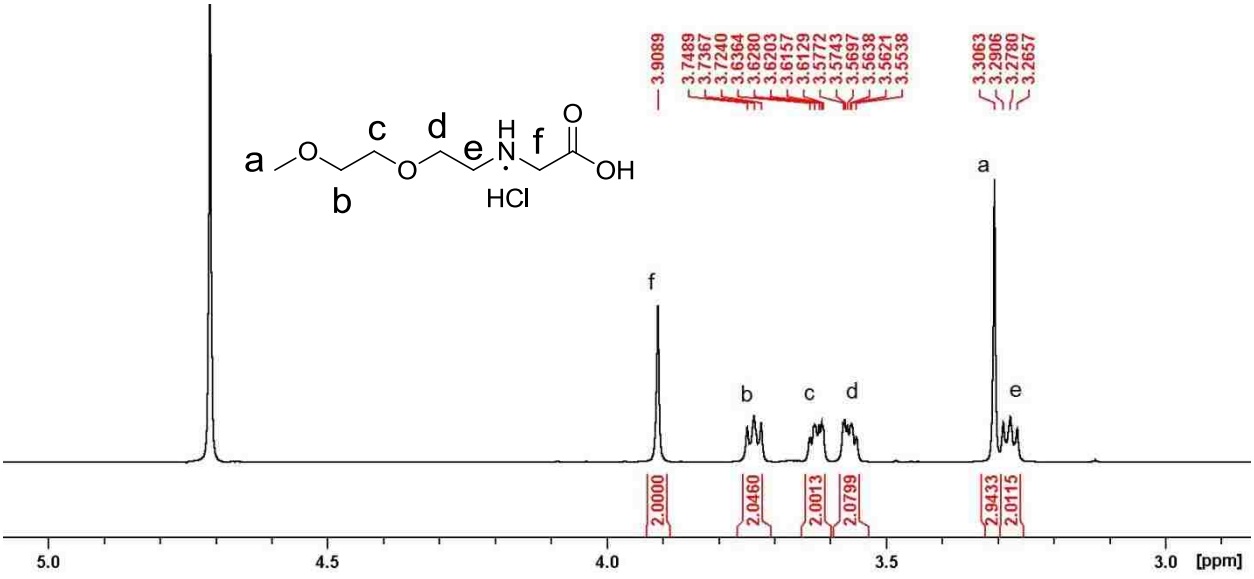

Figure 3.14. ^{1}H NMR spectrum of ethyl 2-((2-(2-methoxyethoxy)ethyl)amino)acetic acid hydrochloride in D_2O.

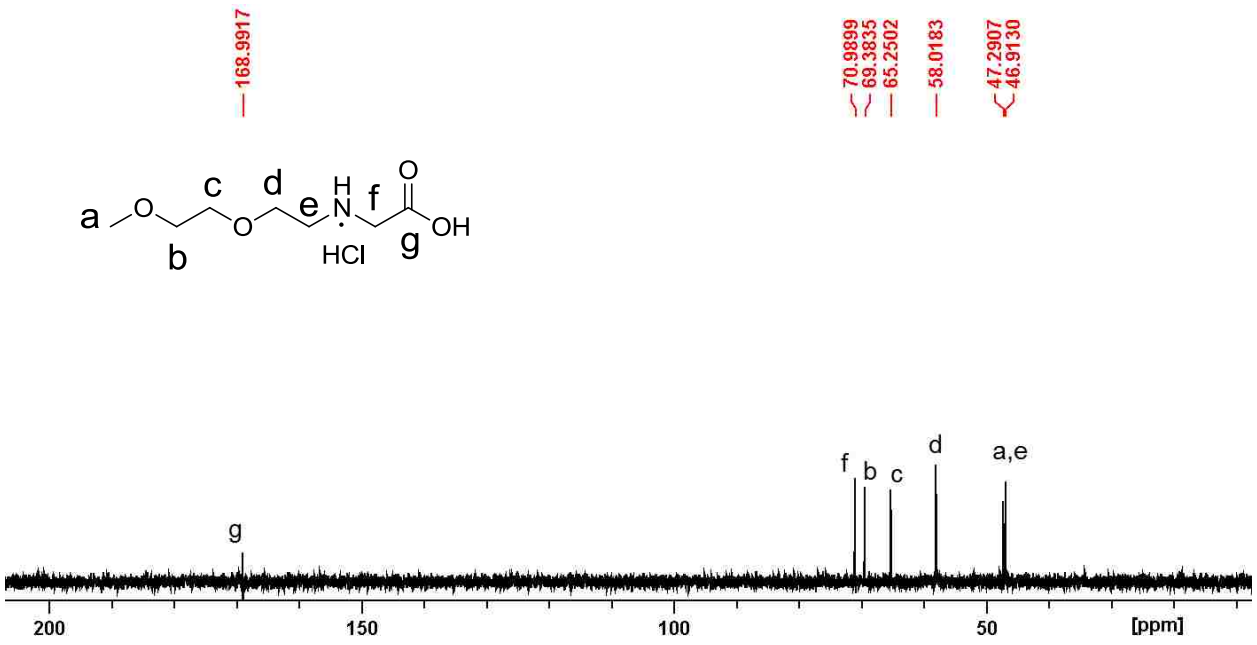

Figure 3.15. ^{13}C {^{1}H} NMR spectrum of ethyl 2-((2-(2-methoxyethoxy)ethyl)amino)acetic acid hydrochloride in D_2O.

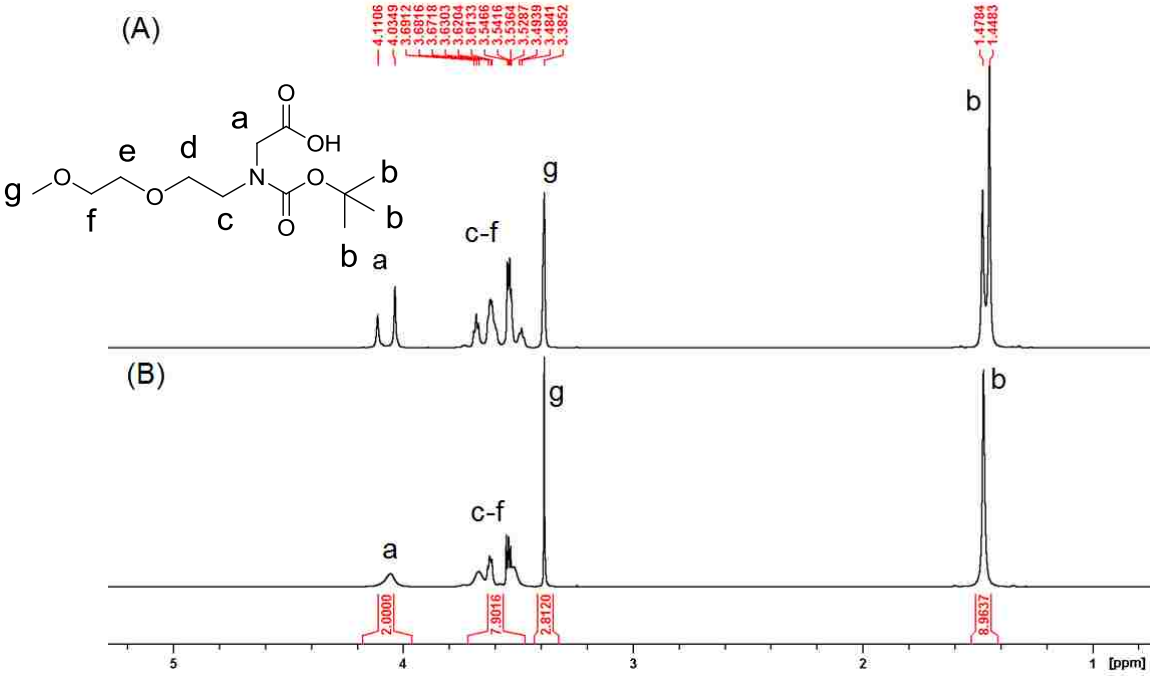

Figure 3.16. ^{1}H NMR spectrum of 2-(N,N-tert-butoxycarbonyl-2-(2-methoxyethoxyethyl)amino)acetic acid in $CDCl_3$: (A) at 25 °C and (B) at 50 °C.

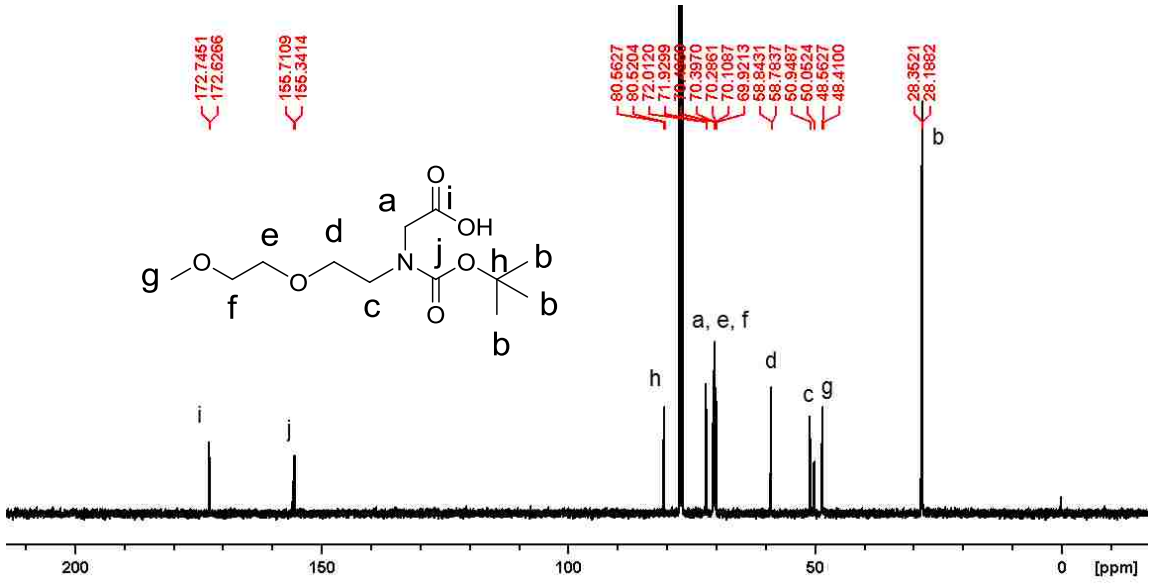

Figure 3.17. ^{13}C {^{1}H} NMR spectrum of 2-(N,N-tert-butoxycarbonyl-2-(2-methoxyethoxyethyl)amino)acetic acid in $CDCl_3$ at 25ºC.

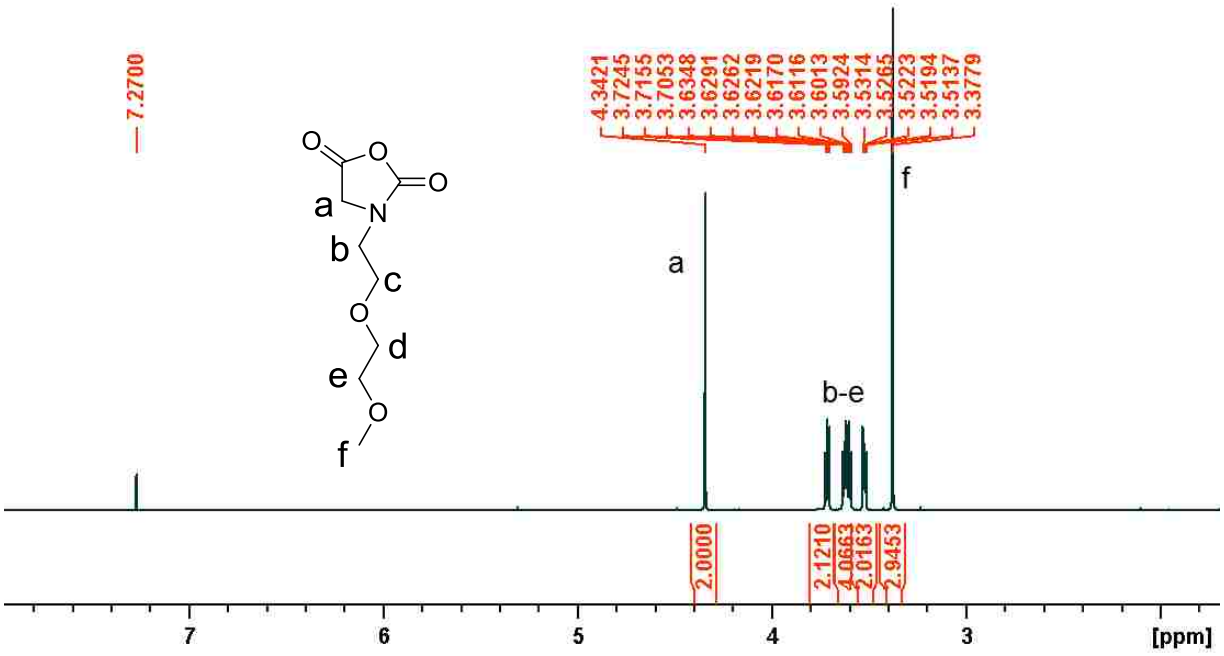

Figure 3.18. ^{1}H NMR spectrum of $Me(OEt)_2$-NCA.

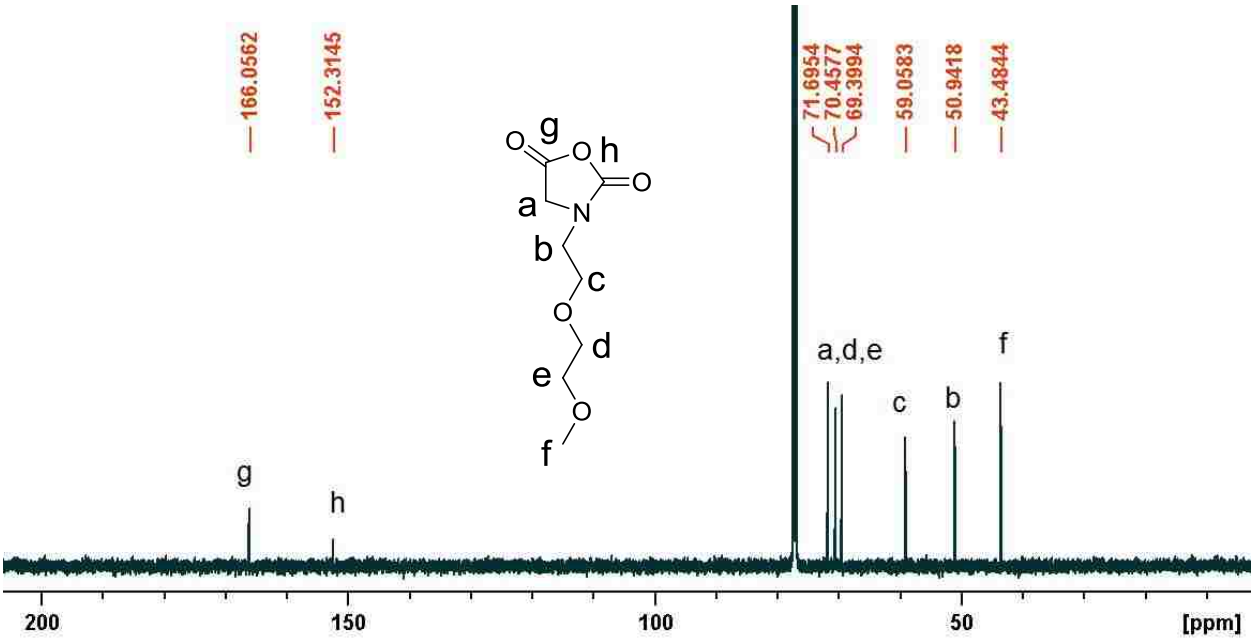

Figure 3.19. ^{13}C {^{1}H} NMR spectrum of $Me(OEt)_2$-NCA.

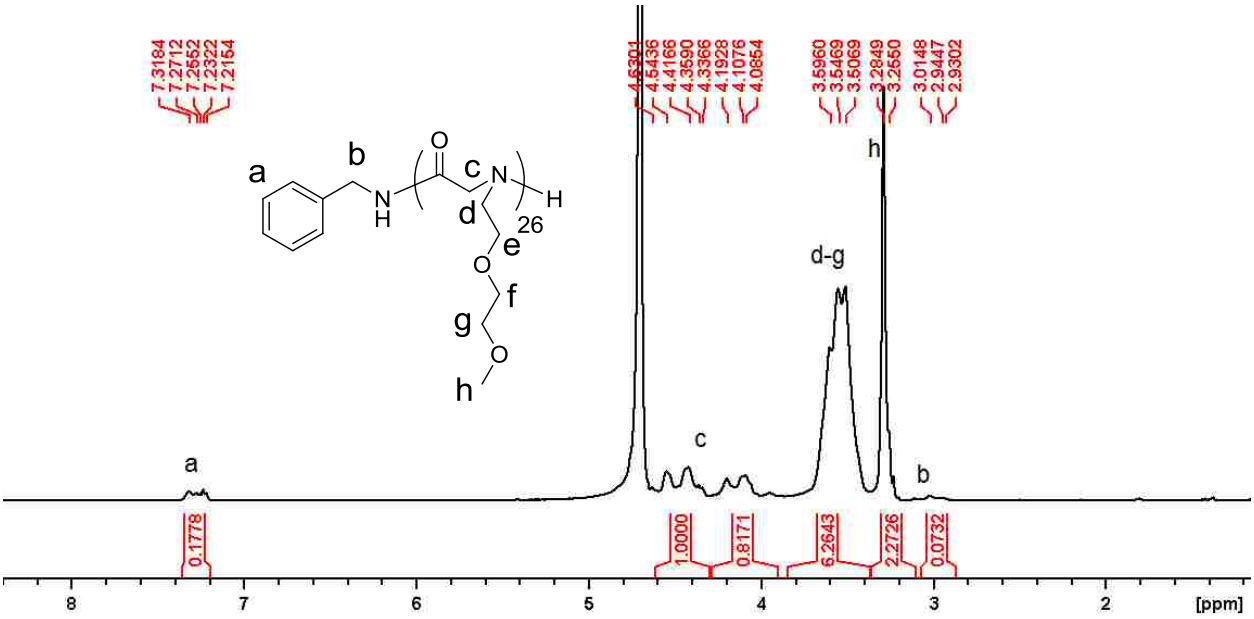

Figure 3.20. ^{1}H NMR spectrum of $PNMe(OEt)_2G$ in D_2O.

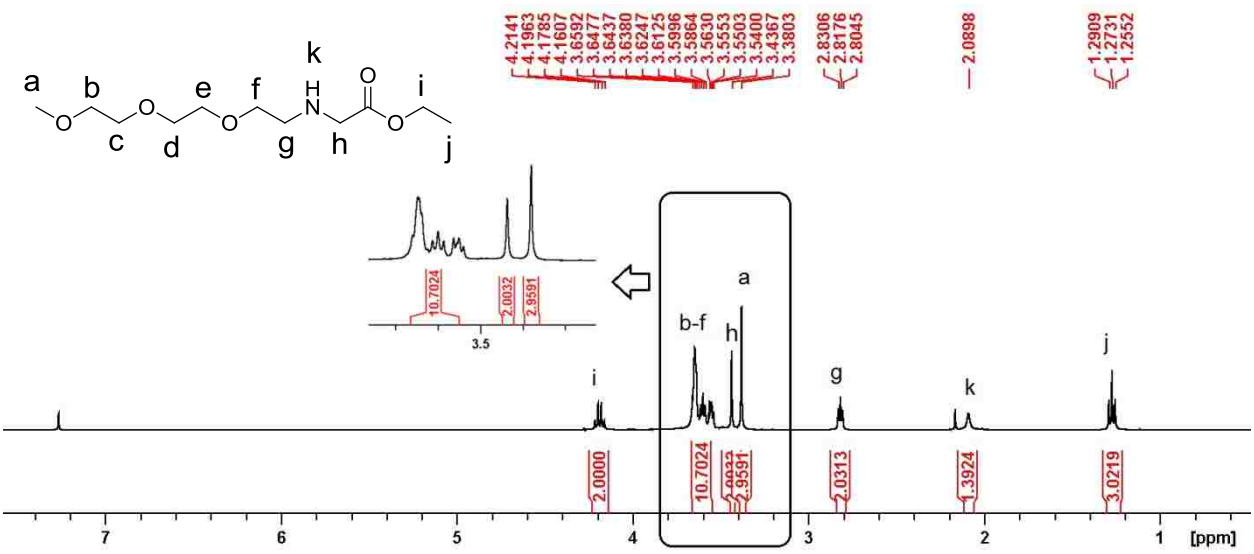

Figure 3.21. ^{1}H NMR spectrum of ethyl 2-((2-(2-(2-ethoxyethoxy)ethyl)amino)acetate in $CDCl_3$.

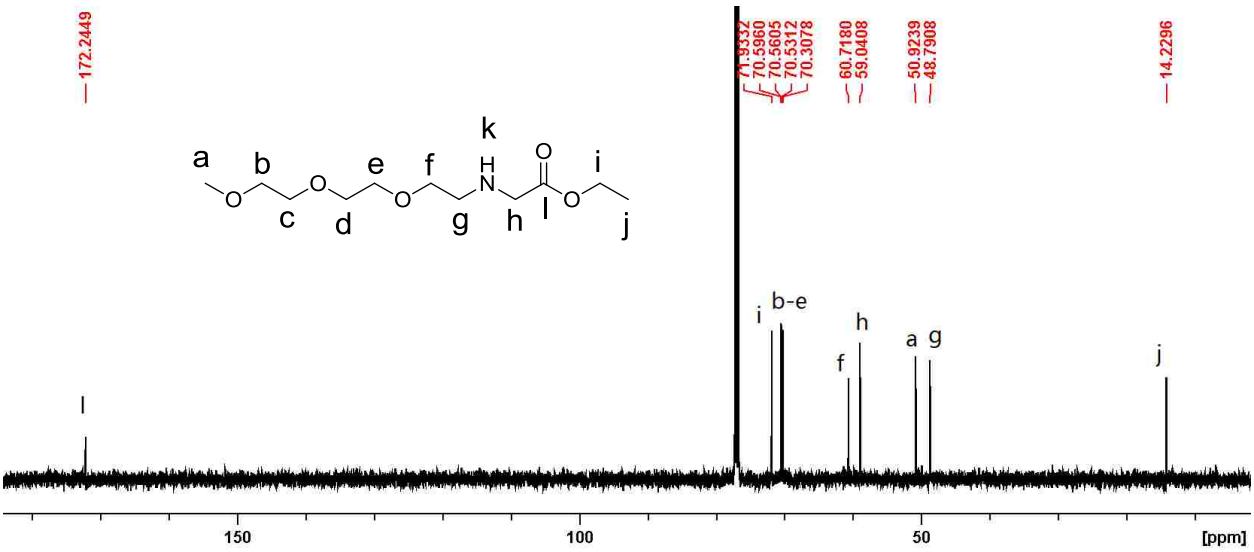

Figure 3.22. ^{13}C {^{1}H} NMR spectrum of ethyl 2-((2-(2-(2-ethoxyethoxy)ethyl)amino)acetate in $CDCl_3$.

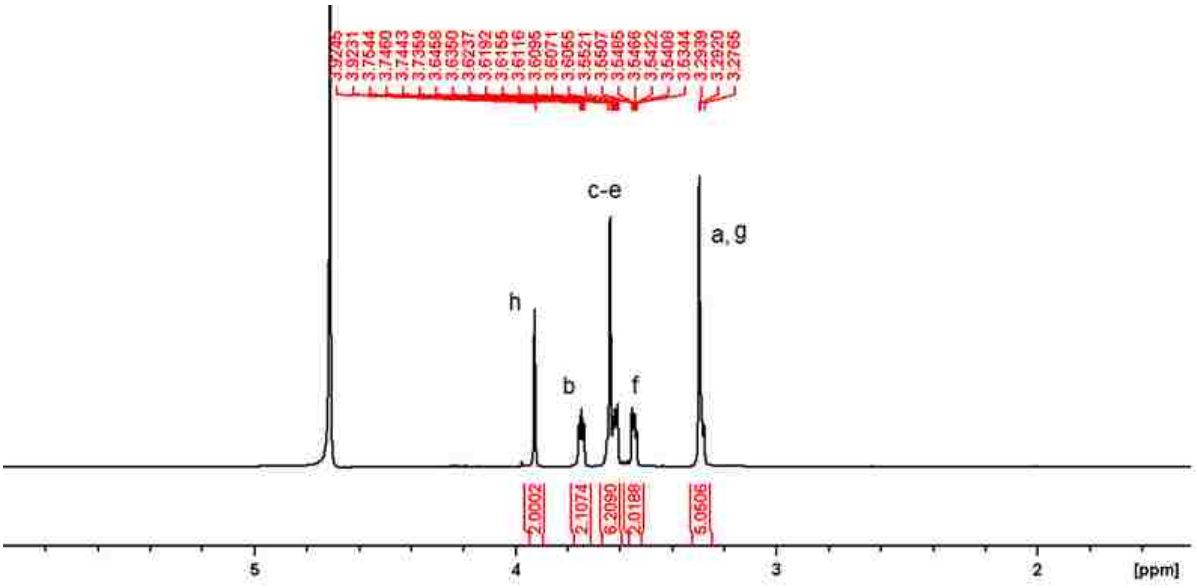

Figure 3.23. ^{1}H NMR spectrum of ethyl 2-((2-(2-(2-ethoxyethoxy)ethyl)amino) acetic acid hydrochloride in D_2O.

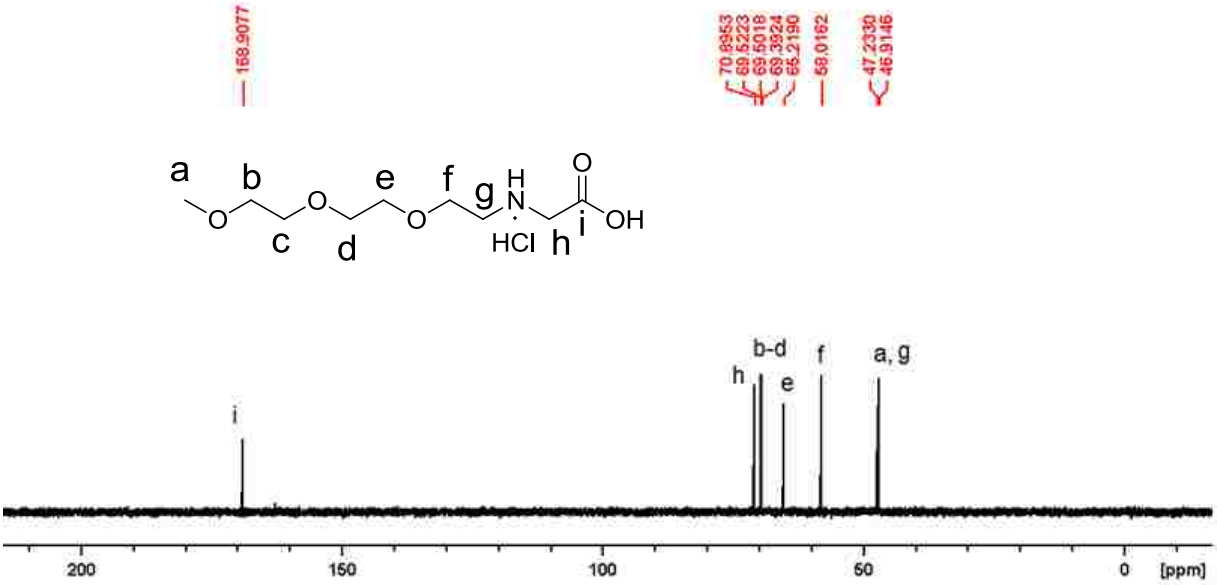

Figure 3.24. ^{13}C {^{1}H} NMR spectrum of ethyl 2-((2-(2-(2-ethoxyethoxy)ethyl)amino) acetic acid hydrochloride in D_2O.

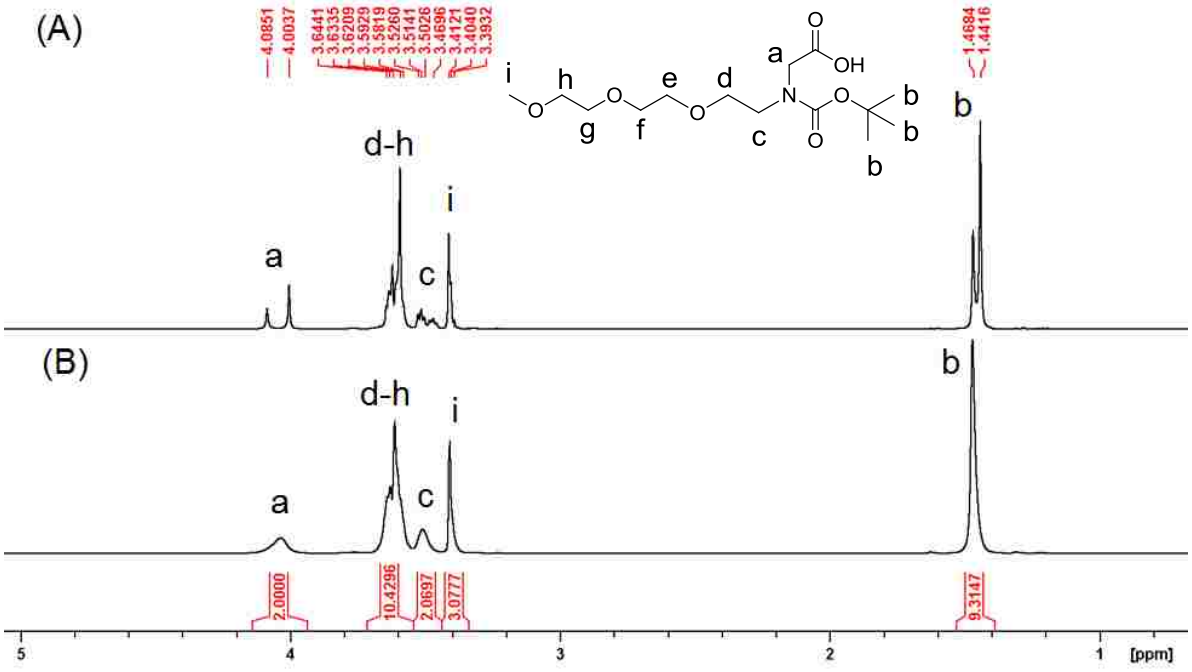

Figure 3.25. ^{1}H NMR spectrum of 2-(*N*,*N*-tert-2-(2-(2-methoxyethoxy) ethoxyethoxycarbonylmethyl)amino) acetic acid in $CDCl_3$: (A) at 25 °C and (B) at 50 °C.

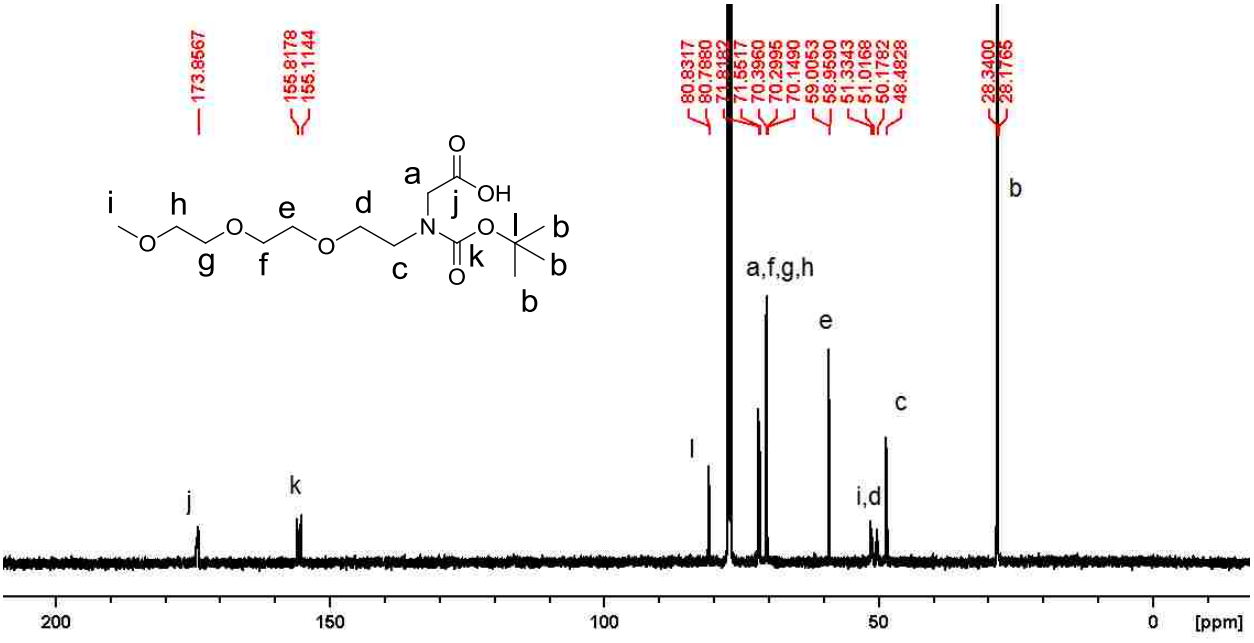

Figure 3.26. ^{13}C {^{1}H} NMR spectrum of 2-(N,N-tert-2-(2-(2-methoxyethoxy) ethoxyethoxycarbonylmethylamino) acetic acid in $CDCl_3$ at 25^{o}C.

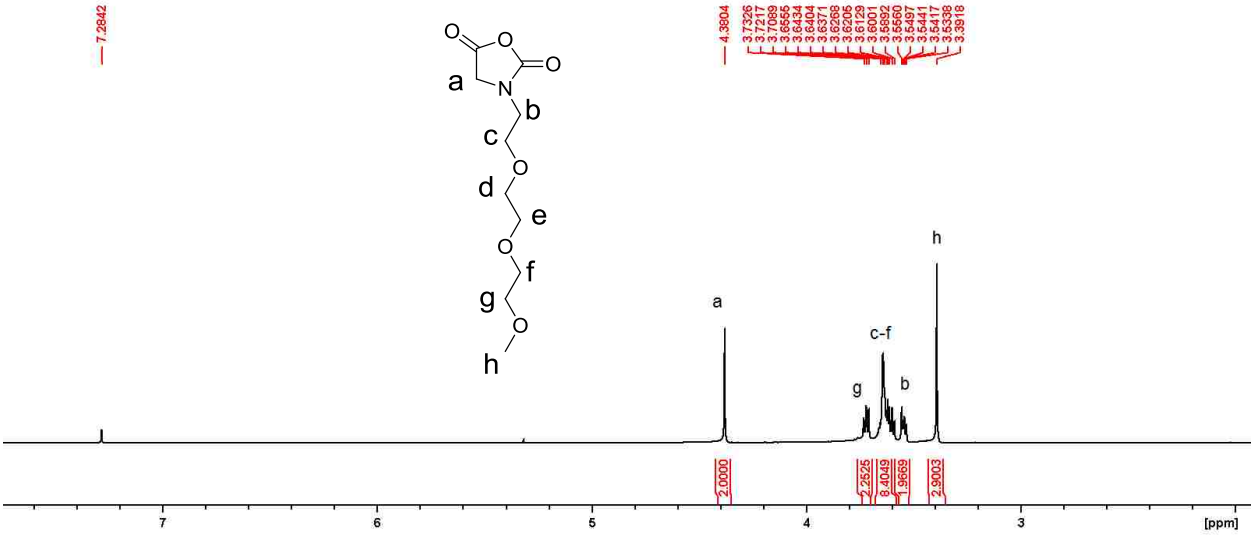

Figure 3.27. ^{1}H NMR spectrum of Me(OEt)$_3$-NCA.

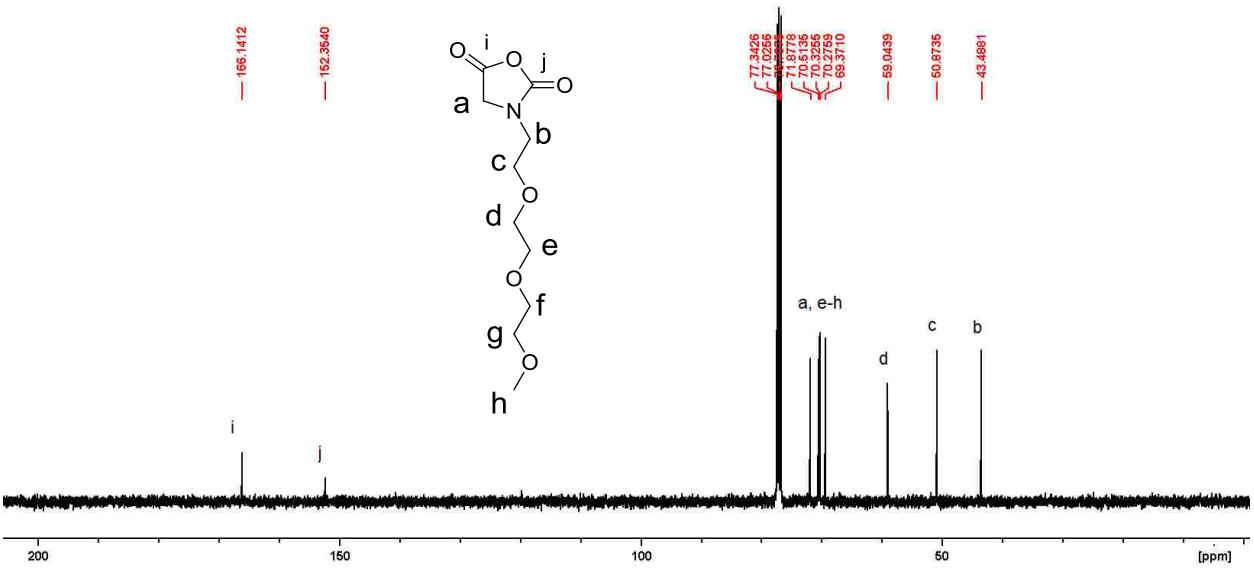

Figure 3.28. ^{13}C {^{1}H} NMR spectrum of Me(OEt)$_3$-NCA.

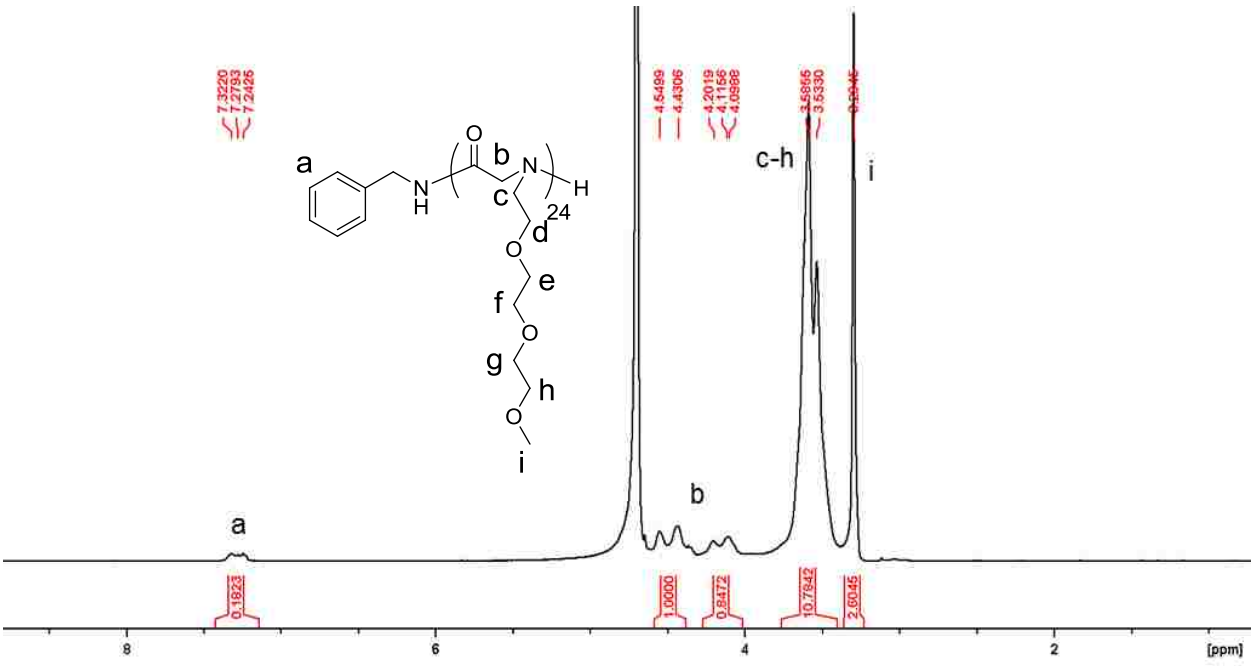

Figure 3.29. ^{1}H NMR spectrum of PNMe(OEt)$_3$G in D_2O.

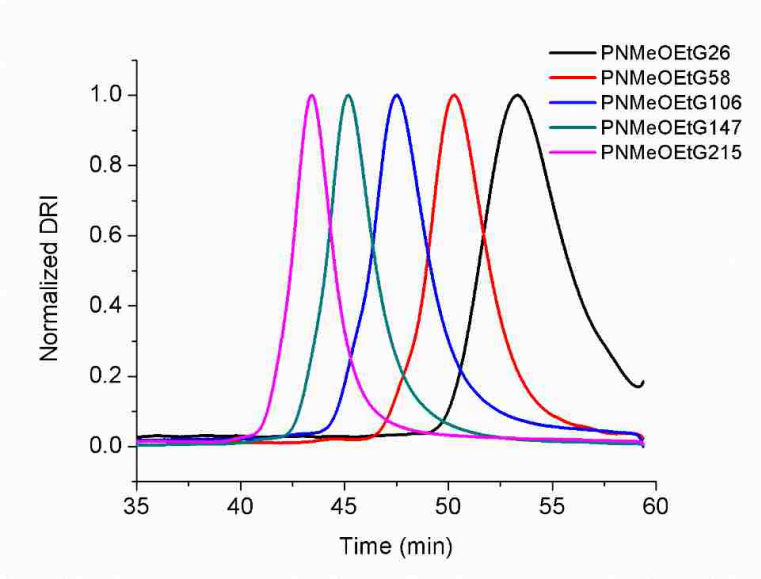

Figure 3.30. SEC chromatograms of PNMeOEtGs prepared from benzyl amine initiated polymerization of MeOEt-NCA (**M$_1$**) ([M$_1$]$_0$:[BnNH$_2$]$_0$ = 25:1 (—), 50:1 (—), 100:1 (—), 200:1 (—), 400:1 (—)). The DPs listed in the figure were determined from the SEC-MALDI-DRI using the dn/dc= 0.0633(4) mL/g (0.1 LiBr/DMF, 20°C) of the polymer.

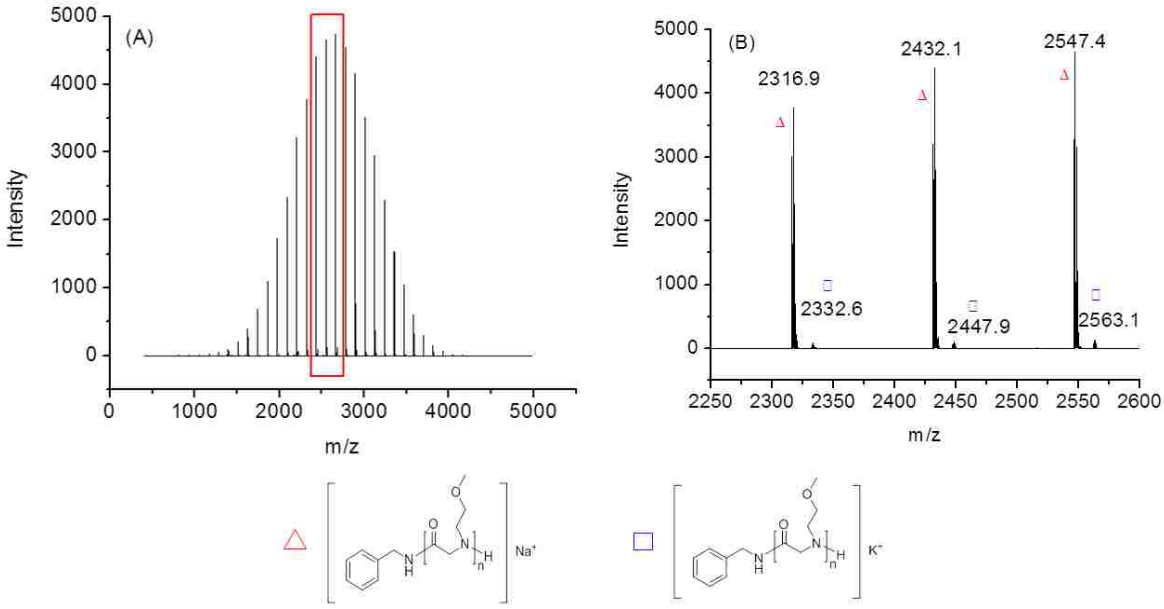

Figure 3.31. (A) Representative full and (B) expanded MALDI-TOF MS spectra of PNMeOEtG (Mn=2.7 kg/mol, PDI=1.03, matrix: CHCA).

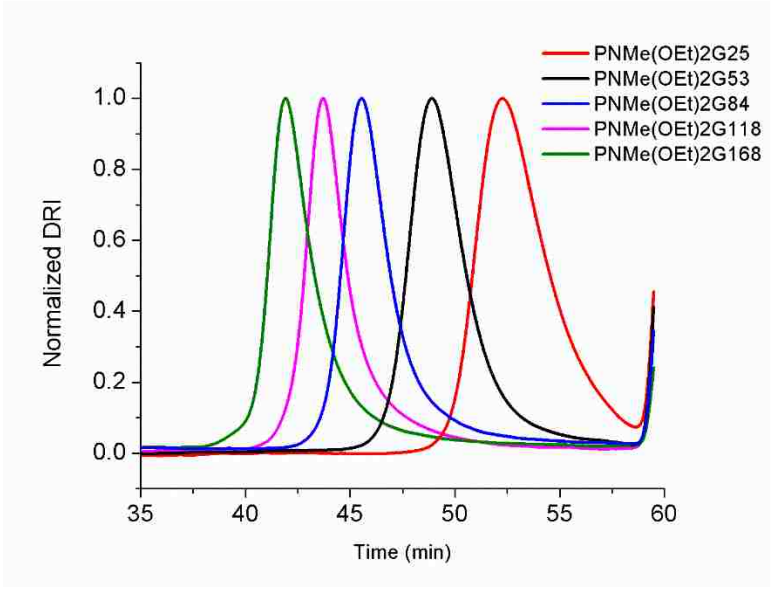

Figure 3.32. SEC chromatograms of PNMe($OEt_)_2$Gs prepared from benzyl amine initiated polymerization of Me$(OEt)_2$-NCA (**M**$_2$) ($[M_1]_0$:$[BnNH_2]_0$ = 25:1 (—), 50:1 (—), 100:1 (—), 200:1 (—), 400:1 (—), Table). The DPs listed in the figure were determined from SEC-MALDI-DRI using the dn/dc= 0.0686(8) mL/g (0.1 LiBr/DMF, 20°C) of the polymer.

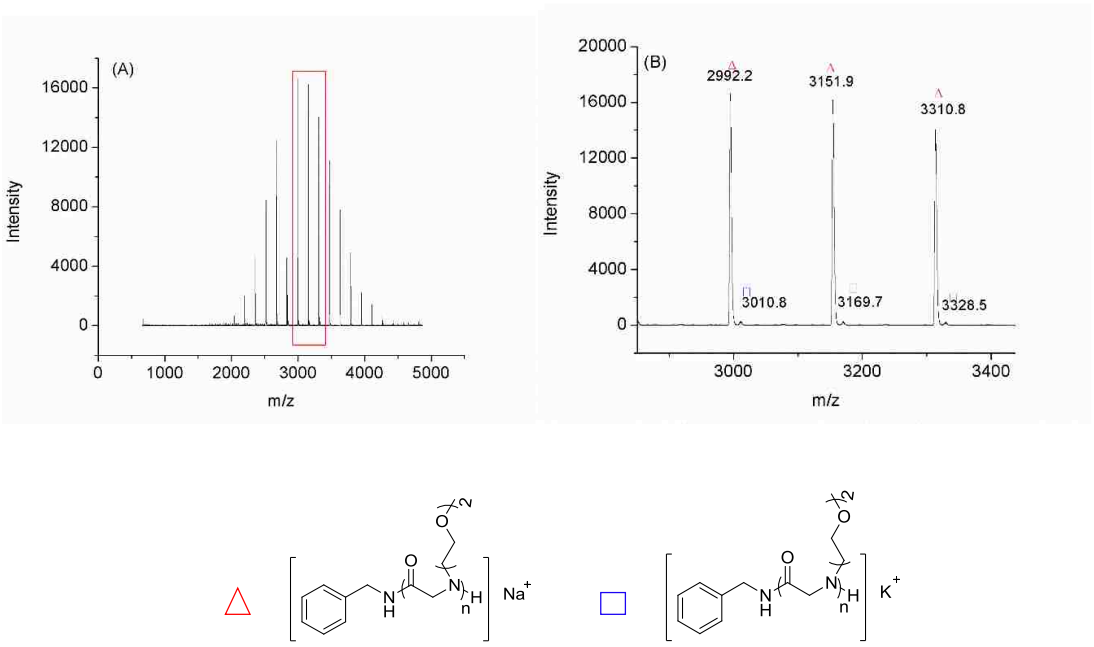

Figure 3.33. (A) Representative full and (B) expanded MALDI-TOF MS spectra of PNMe(OEt)$_2$G (matrix: CHCA).

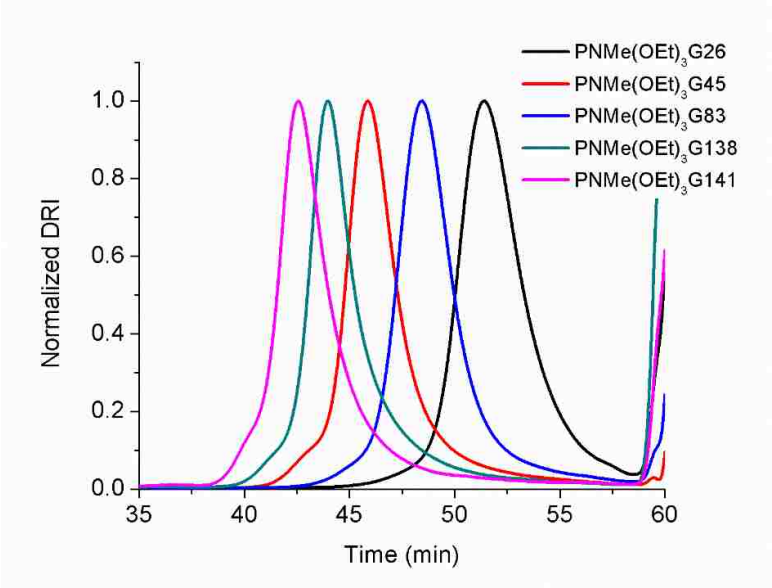

Figure 3.34. SEC chromatograms of PNMe(OEt$_3$Gs prepared from benzyl amine initiated polymerization of Me(OEt)$_3$-NCA (**M$_3$**) ([M$_1$]$_0$:[BnNH$_2$]$_0$ = 25:1 (—), 50:1 (—), 100:1 (—), 200:1 (—), 400:1 (—), Table). The DPs listed in the figure were determined from SEC-MALDI-DRI using the dn/dc= 0.0563(6) mL/g (0.1 LiBr/DMF, 20°C) of the polymer.

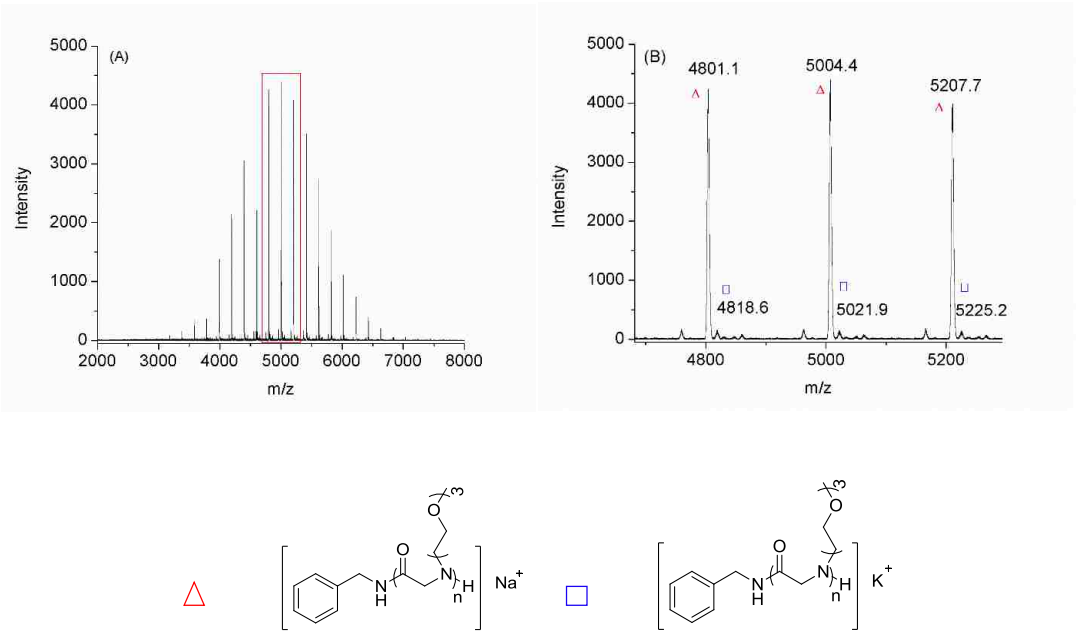

Figure 3.35. (A) Representative full and (B) expanded MALDI-TOF MS spectra of PNMe(OEt)$_3$G (matrix: CHCA).

Polymerization kinetics were investigated at a constant initial monomer to initiator ratio ($[M]_0$:$[BnNH_2]_0$ = 25:1, $[M]_0$ = 0.2 M) in Tolene-d^8 at 50^{o}C in J-Yong NMR tube and the polymerization conversion was determined from the integration of the monomer and corresponding polymer peaks. The polymerizations of the three monomers all exhibited a pseudo-first order dependence on the monomer concentration (*i.e.*, d[M]/dt = k_{obs} [M]), consistent with a living polymerization. As the number of ethylene oxide moiety on the monomer side chain increased from one (MeOEt-NCA) to three (Me(OEt)$_3$-NCA), the observed rate constant (k_{obs}) of the polymerization decreased from 0.01285(±6) to 0.00291(±7) min^{-1} (Figure 3.36C). It was probably due to the higher steric hindrance and more electron-withdrawing effect associated with the increased number of ethylene oxide moiety on the side chain that weakened the nucleophilicity of the secondary amino chain end and thus decreased the propagation rate. In addition, the plot of M_n of the corresponding polymer exhibited a linear relationship as a function of conversion (Figure 3.36-3.37), revealing a constant concentration of propagation species, in agreement with a living

polymerization. The molecular weight distribution (PDI=1.01-1.18) remained relatively narrow during the polymerization.

DSC and TGA analysis of ($PNMe(OEt)_nG$, n=1-3). The PEGylated polypeptoids were characterized by TGA and DSC. The TGA thermograms of $PNMe(OEt)_nG_{50}$ (n=1-3) shown in Figure 3.38 and 3.39 revealed a three-stage decomposition profiles with a slow and gradual mass loss at low temperatures (25 ^oC-100 ^oC) which was attributed to the loss of small amount of water contained in the polymers due to their hydroscopic property, followed by a drastic mass loss occurring at 250-400 ^oC for all three PEGylated polypeptoids and then a gradual decrease of mass loss from 400-500 ^oC. The decomposition temperature (T_d) of the three polymers was higher than 250^oC and thus temperature window (-50^oC-200^oC) was selected for DSC analysis. The respective DSC thermograms of the second heating cycle were showed in Figure 3.38 and 3.39. The absence of melting peak and crystallization exotherm peak revealed that all the three PEGylated polypeptoids (M_n = 3.26-16.9 kg/mol) are amorphous, in agreement with the previously reported oligomeric PEO-mimetic peptoids.[55] The glass transition temperature (T_g) as determined by the inflection on the slope of heat flow shifting are shown in Table 3.2. The T_g values of the PEGylated polypeptoids decreased with increasing the length of ethylene oxide side chains (PNMeOEtG (T_g = 24.5 – 46.4 ^oC) > $PNMe(OEt)_2G$ (T_g = -6.0 – -16.9 ^oC) > $PNMe(OEt)_3G$ (T_g = -34.9 – -41.1 ^oC)), which is consistent with the previously reported observations for oligomers.[55]

The T_g values observed for all the peglated polypeptoids were significantly lower than the amorphous PNMG (127-143^oC) and PNEG (93-114 ^oC) with comparable MW.[56]. The T_g values of the polymer increased with the increase of MW, in consistence with other reported observations,[57] which is attributed to the reduction of free volume due to diminished chain end contents at increasing molecular weight.[58] The T_g of $PNMeOEtG_{20}$ (T_g = 24.5 ^oC, PDI = 1.09)

synthesized by ROP was about 14°C lower than the corresponding 20 mer (T_g = 38.6 °C, PDI < 1.0003) synthesized by solid phase "submonomer" method,[55] probably due to the larger PDI of the former polymer that increased the flexibility of the polymer chains. The discrepancy is presumably resulted from the difference in end-group structures and polydispersity of the samples. As the chains are relative short, end-group structural different will contribute significantly to a difference in free volume and thus T_g. The polymeric sample contains a mixture of chains that are shorter or longer than 20 mer in varying amounts, which will have different T_gs due to free volume difference.

Table 3.1. $BnNH_2$-initiated ROP of MeOEt-NCA (**M_1**), $Me(OEt)_2$-NCA(**M_2**) and $Me(OEt)_2$-NCA(**M_3**).[a]

	Entry	$[M]_0/[I]_0$	Calcd	M_n (Kg/mol)		PDI[b]	Reaction time (h)	Conv.(%)
				SEC[b]	NMR[c]		24	100
PNMeOEtG	1	25:1	2.98	3.26	3.09	1.10	24	100
	2	50:1	5.86	6.26	6.32	1.08	24	100
	3	100:1	11.6	11.1	12.4	1.05	48	100
	4	200:1	23.1	17.0	24.6	1.04	48	100
	5	400:1	46.1	24.8	-	1.04	24	100
$PNMe(OEt)_2G$	1	25:1	4.08	4.03	4.24	1.06	24	100
	2	50:1	8.06	8.57	8.69	1.09	24	100
	3	100:1	16.0	13.5	16.3	1.03	48	100
	4	200:1	31.9	18.9	33.9	1.04	48	100
	5	400:1	63.7	26.8	-	1.05	24	100
$PNMe(OEt)_3G$	1	25:1	5.18	5.29	5.18	1.07	24	100
	2	50:1	10.3	9.34	11.7	1.05	24	100
	3	100:1	20.4	16.9	21.6	1.07	48	100
	4	200:1	40.7	28.2	41.3	1.06	48	100
	5	400:1	81.3	28.6	-	1.08	24	100

[a]All the polymerizations were conducted in THF at 50°C with $[M]_0$=1M. SEC analysis were conducted by directly injecting the polymerization solutions into SEC column after reaching 100% conversion. [b]Determined from a tandem SEC-MALS-DRI system using dn/dc 0.0633(4) mL/g for PNMeOEtG, 0.0686(8) mL/g for $PNMe(OEt)_2G$ and 0.0563(6) mL/g for $PNMe(OEt)_3G$ in 0.1 M LiBr/DMF at room temperature. [c]Determined by ^{1}H NMR end-group analysis. Entry 4: the $BnNH_2$ content is too low to be accurately integrated and therefore the M_n cannot be reliably determined from the end-group analysis.

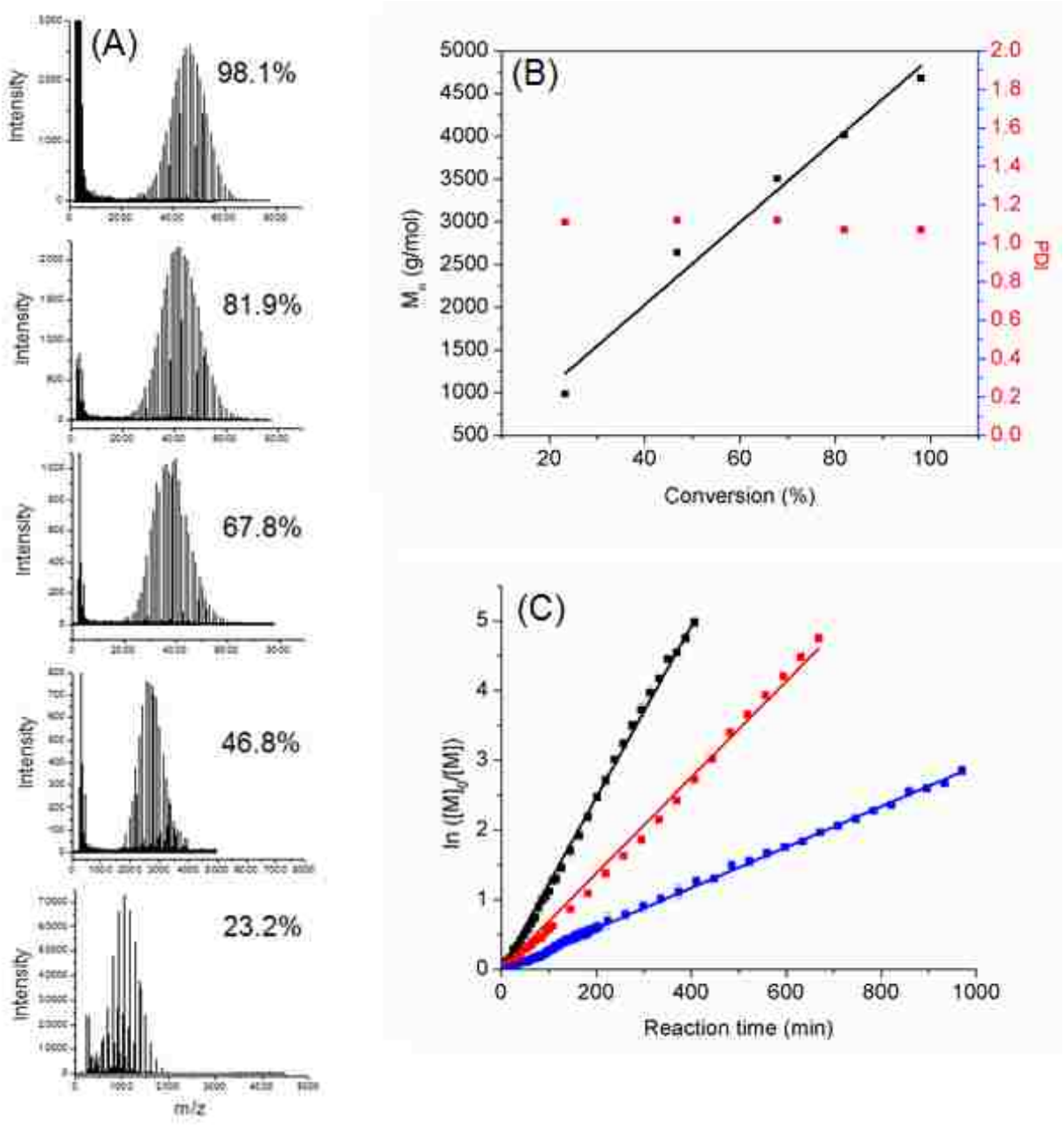

Figure 3.36. (A) MALDI-TOF MS of PNMeOEtG (PDI = 1.07-1.11) at different polymerization conversion. (B) Plots of M_n and PDI verses conversion for $BnNH_2$ initiated polymerization of MeOEt-NCA in THF ($[M]_0$:$[I]_0$=50:1, $[M]_0$ =1 M). (C) Plots of ln ($[M]/[M]_0$) versus the reaction time for $BnNH_2$ initiated polymerization of $Me(OEt)_n$-NCA (n=1-3) ($[M]_0$:$[BnNH_2]$=25:1, $[M]_0$=0.2 M) in toluene-d_8 at 50^{o}C.

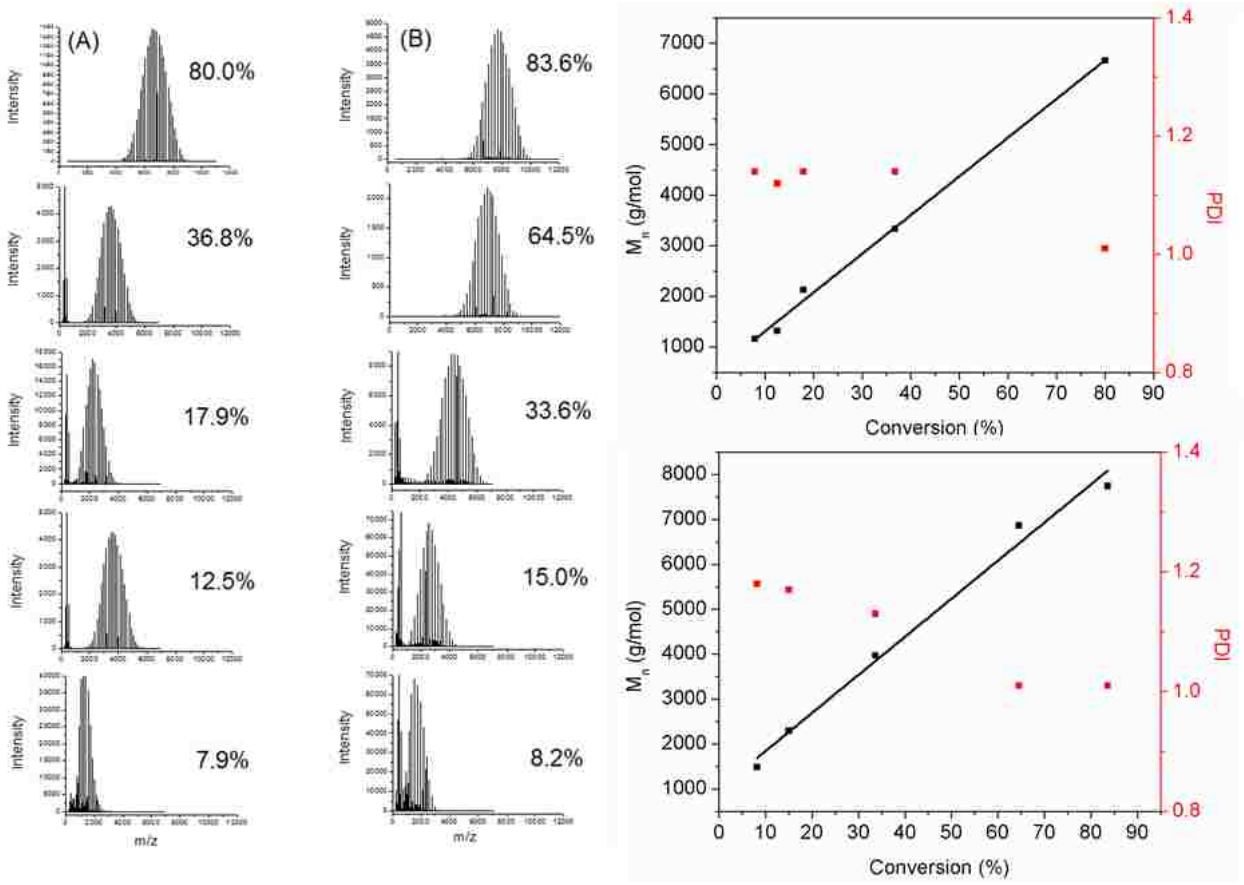

Figure 3.37. (A,B) MALDI-TOF MS of PNMe(OEt)$_n$G (n=2-3) at different polymerization conversion in THF ([M]$_0$:[I]$_0$=50:1, [M]$_0$ =1 M).: (A) PNMe(OEt)$_2$G and (B) PNMe(OEt)$_3$G . (C,D) Plots of M_n and PDI verses conversion for $BnNH_2$ initiated polymerization of Me(OEt)$_n$-NCA (n=2-3): (C) Me(OEt)$_2$-NCA and (D) Me(OEt)$_3$-NCA.

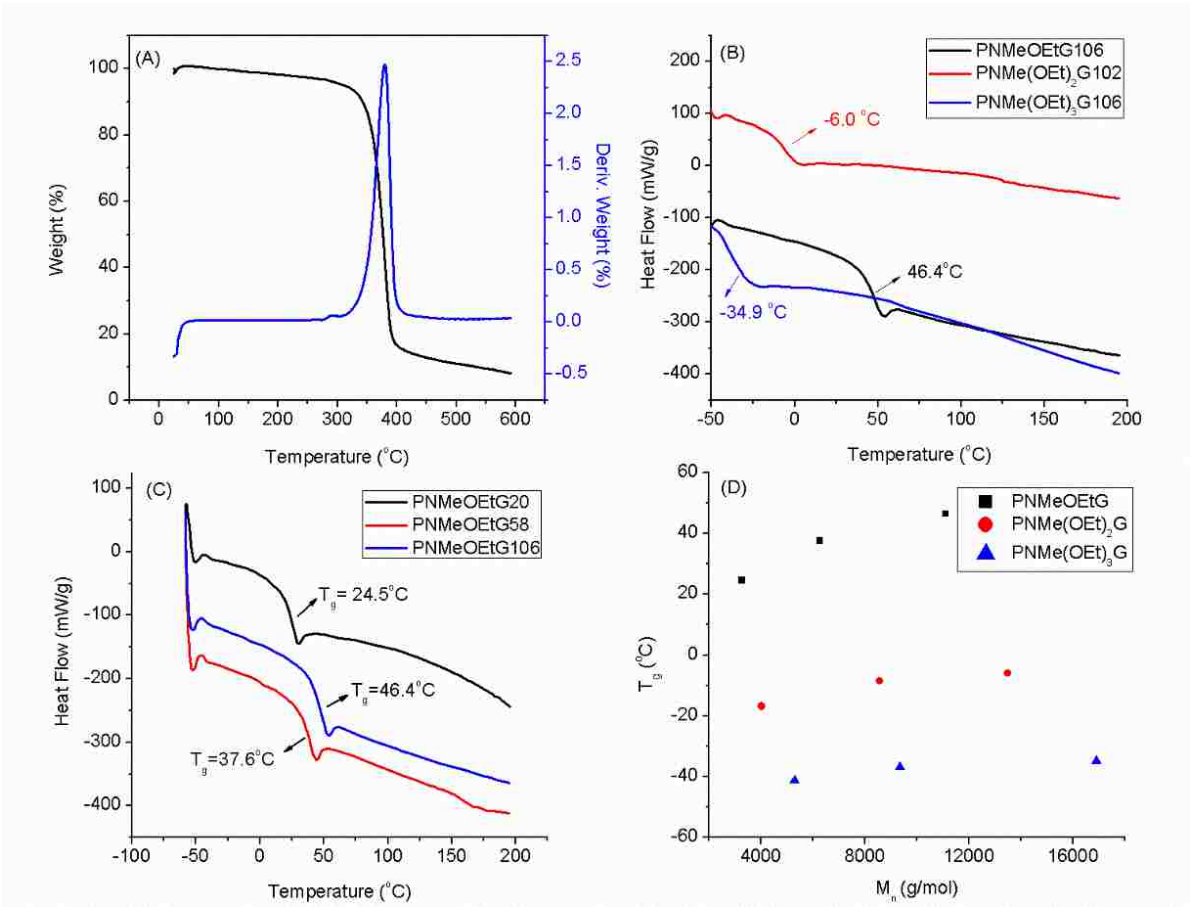

Figure 3.38. (A) Thermogravimetric analysis of PNMeOEtG58. (B) DSC thermograms of PNMe(OEt)$_n$G (n=1-3). (C) DSC thermograms of PNMeOEtG at different MW during the second heating cycle. (D) Plot of T_g verses M_n of PNMe(OEt)$_n$G (n=1-3). The DP_ns listed in the figures were determined from NMR end-group analysis.

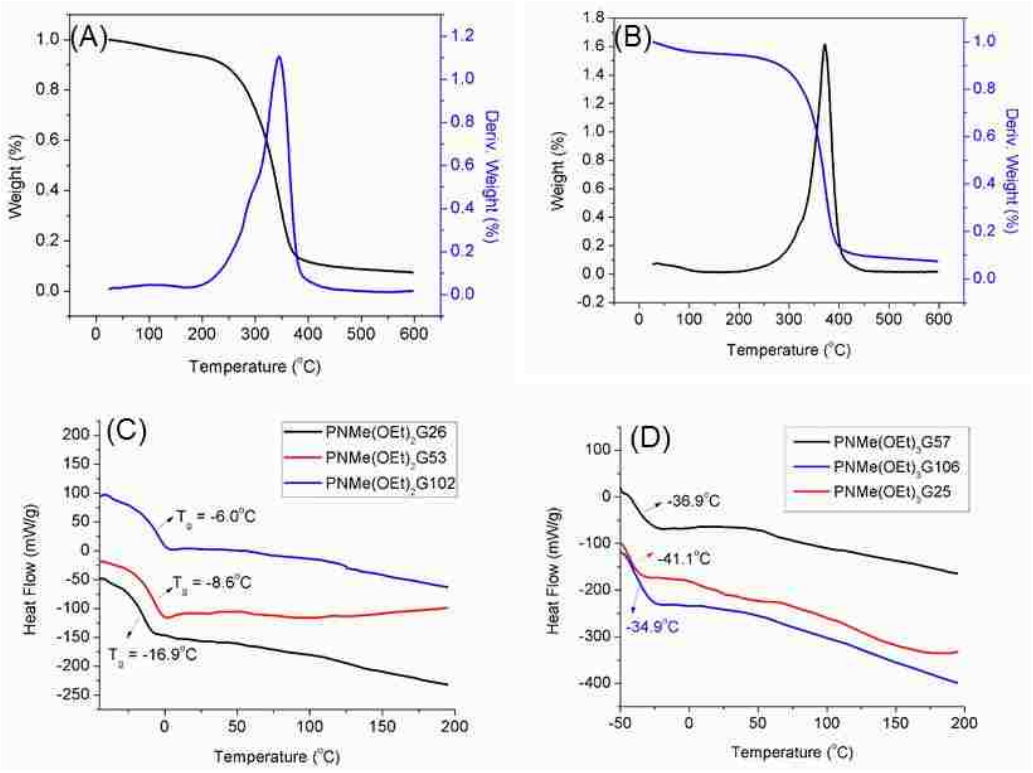

Figure 3.39. Thermogravimetric analysis of PNMe(OEt)$_2$G (A) and PNMe(OEt)$_3$G (B); DSC thermograms of PNMe(OEt)$_2$G (C) and PNMe(OEt)$_3$G (D) at different MW during the second heating cycle.

Table 3.2. T_g of PNMe(OEt)$_n$G (n=1-3) at different MW.

Sample	M_n (kg/mol)	T_g (°C)
PNMeOEtG	3.26	24.5
	6.26	37.6
	11.1	46.4
PNMe(OEt)$_2$G	4.03	-16.9
	8.57	-8.6
	13.5	-6.0
PNMe(OEt)$_3$G	5.29	-41.1
	9.34	-36.9
	16.9	-34.9

3.3.2 Protein adsorption investigation on PNMeOEtG by DLS analysis

As the PEGylated polypeptoids are highly water soluble, charge neutral and have hydrogen bond acceptor both on the backbone and side chains, which fulfill all the criteria of the abovementi-

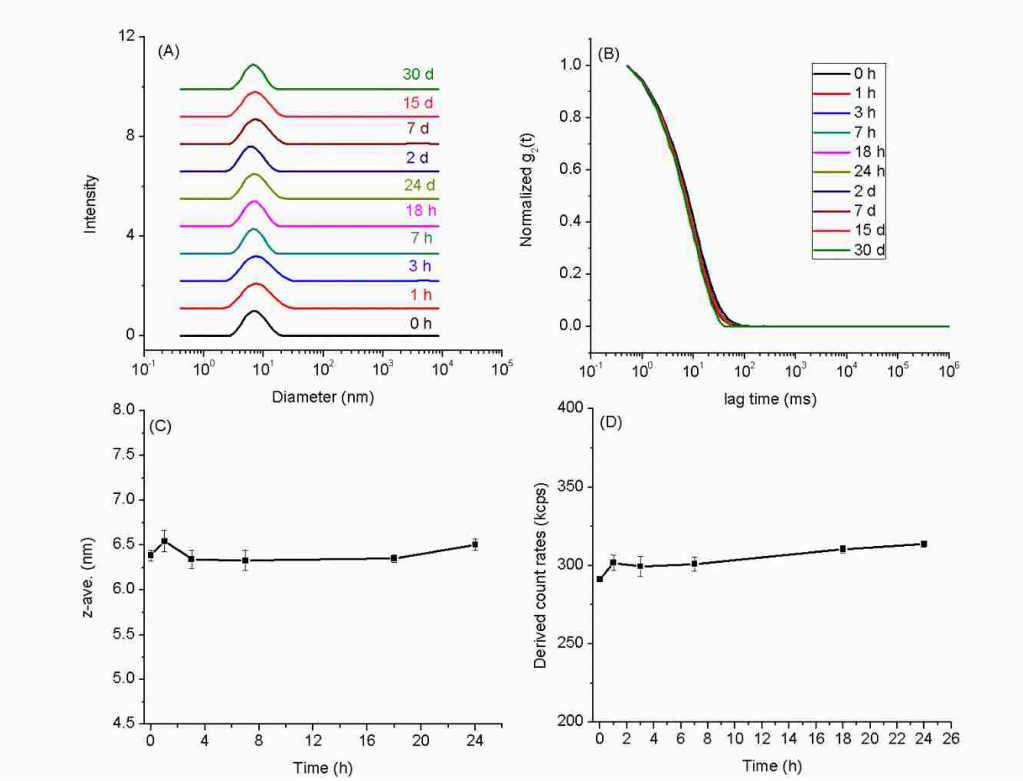

Figure 3.40. DLS analysis of 1wt% PNMeOEtG106 in PBS (A, C) Hydrodynamic size distribution, (B) correlograms and (D) derived count rates up to 24 h.

oned "whitesides rule" for protein-resistant materials, we hypothesized that the PEGylated polypeptoids may display antifouling property. PNMeOEtG was selected as the model polymer to study the protein resistant characteristics of the PEGylated polypeptoids. DLS was used to monitor the size change of PNMeOEtG, protein (lysozyme) and their mixture in PBS. Lysozyme was selected here as the protein due to their comparable size with PNMeOEtG. Increased hydrodynamic size would be expected for the mixture of lysozyme and PNMeOEtG in PBS if appreciable amount of lysozyme was absorbed to the polymer chains. Both the PNMeOEtG and lysozyme at 1wt% in PBS showed no apparent aggregation up to 24 h investigated based on their hydrodynamic size distribution, correlograms and derived count rates (Figure 3.40-3.41). The mixture of 1wt% lysozyme and 1wt% PNMeOEtG in PBS revealed no obvious hydrodynamic size

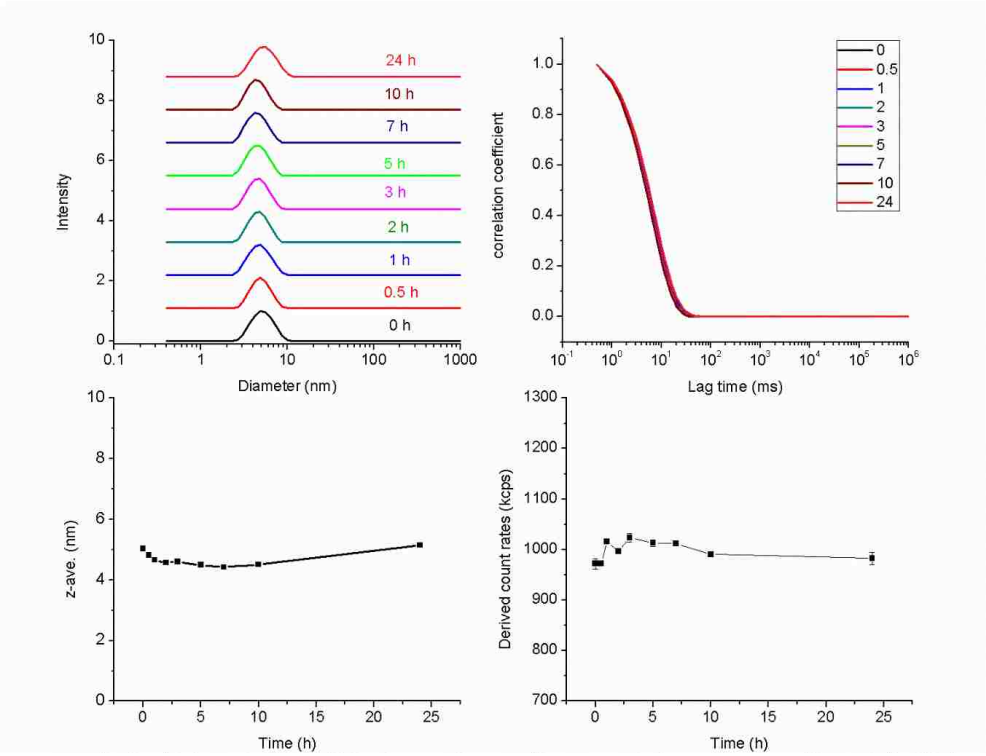

Figure 3.41. DLS analysis of 1wt% lysozyme in PBS (A, C) Hydrodynamic size distribution, (B) correlograms and (D) derived count rates up to 24 h.

increase up to 24 h investigated (Figure 3.42). Furthermore, the hydrodynamic size (dh =5.56 ± 0.16 nm), derived count rates and correlograms of the mixture lies in between that of 1wt% PNMeOEtG (6.39 ± 0.09 nm) and 1wt% lysozyme (4.69 ± 0.25 nm) in PBS, indicating there is no apparent adsorption of lysozyme onto polymer chains (Figure 3.43). For comparison purposes, PEG, a well-known antifouling material, was selected as a positive control to be investigated by DLS analysis. Similarly, the hydrodynamic size (dh = 5.48 ± 0.10 nm), derived count rates and correlograms of the mixture also lies in between that of 1wt% PEG8000 (5.84 ± 0.40 nm) and 1wt% lysozyme (4.69 ± 0.25 nm) in PBS (Figure 3.44), which further supported our hypothesis that no appreciable adsorption of lysozyme was absorbed onto polymer chains.

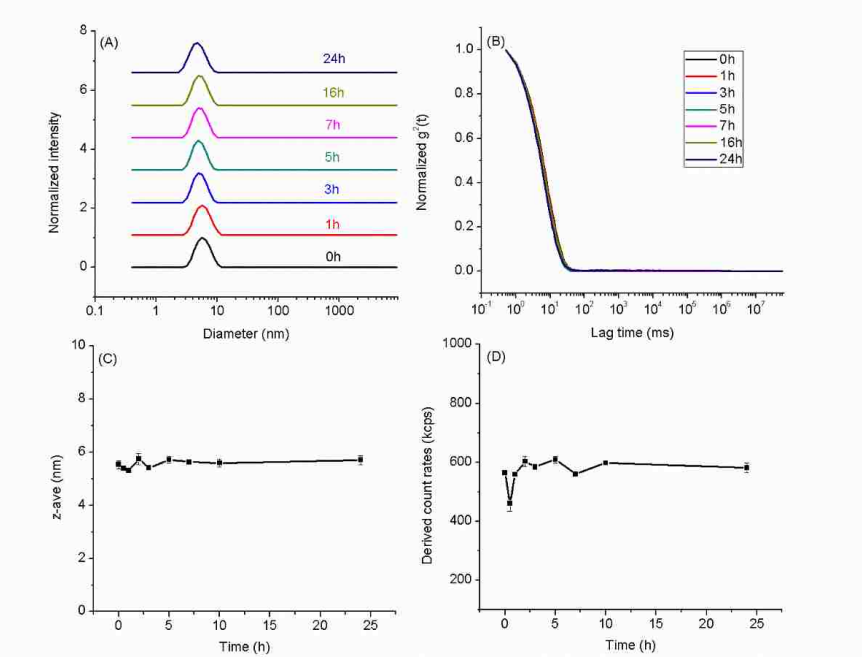

Figure 3.42. DLS analysis of mixture of 1wt% lysozyme and PNMeOEtG106 in PBS: hydrodynamic size distribution (A, C), correlograms (B) and derived count rates (D) up to 24 h.

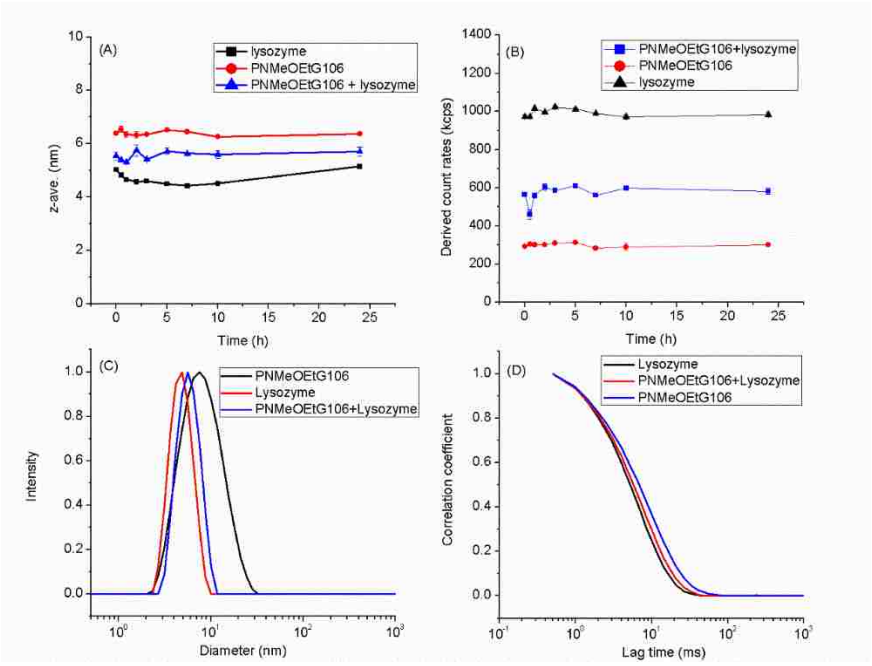

Figure 3.43. DLS analysis of mixture of 1wt% PNMeOEtG106, 1wt% lysozyme, 1wt% lysozyme and 1wt% PNMeOEtG106 in PBS: hydrodynamic size distribution (A) and derived count rates (B) up to 24 h; hydrodynamic size distribution (C) and correlograms (D) at 5h.

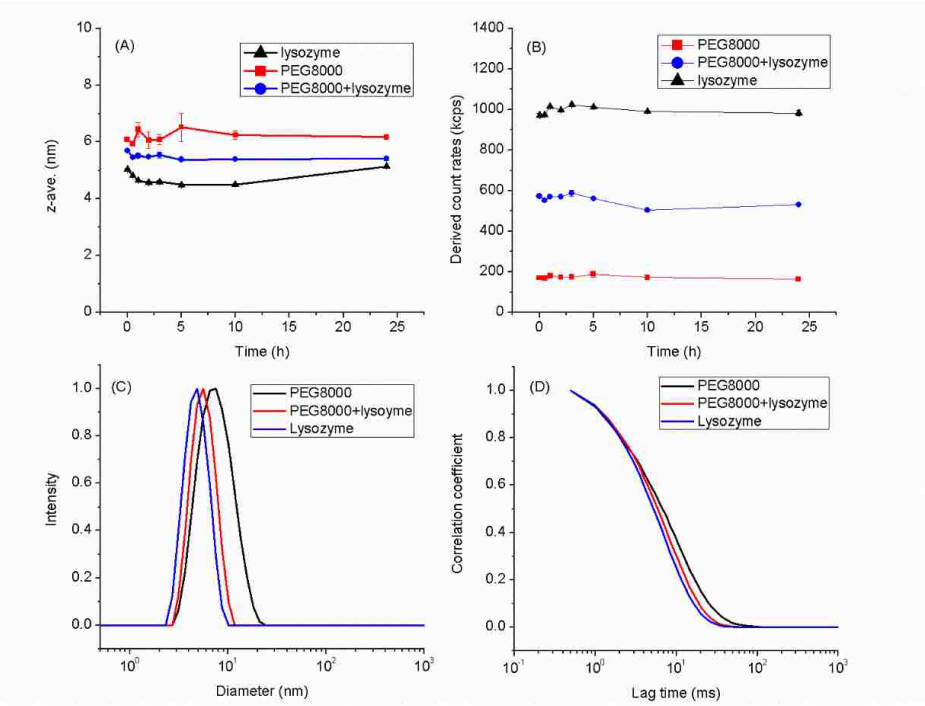

Figure 3.44. DLS analysis of mixture of 1wt% PEG8000, 1wt% lysozyme, 1wt% lysozyme and 1wt% PEG8000 in PBS: hydrodynamic size distribution (A) and derived count rates (B) up to 24 h; hydrodynamic size distribution (C) and correlograms (D) at 5h.

3.3.3 Protein adsorption investigation on PNMeOEtG by SANS analysis

To further support our hypothesis, the interaction between PNMeOEtG and lysozyme was investigated by small angle neutron scattering (SANS) studies in D_2O. The data presented in Figure 3.45 is after background subtraction of the buffer solvent in D_2O.

Figure 3.45(a) represents the SANS diffraction data for the Lysozyme at pH 7.0 and 7.4. The structure factor at low Q, $S(Q = 0)$, is proportional to the osmotic compressibility and it decreases with increase in concentration (ϕ). In addition, $S(Q)$ shows a peak at small angles that is related to the average distance between the neighbouring molecules.

Interestingly we saw the evolution of the structure factor with lowering of the pH value. Following equation (1) at pH 7.4 the data was modelled using a hard sphere form factor ($S(Q) = 1$)[59], whereas the data at pH 7.0 was modelled using a hard sphere (HS) form factor and a structure

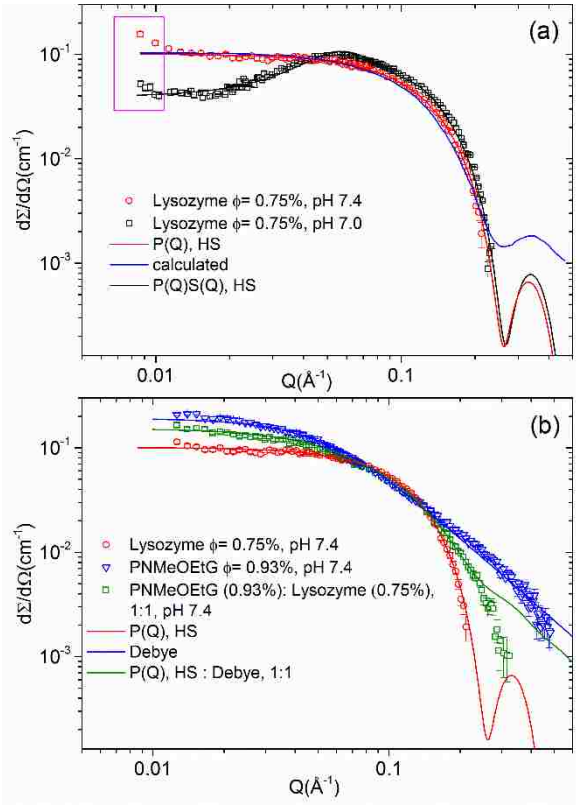

Figure 3.45. SANS diffraction pattern: (a) lysozyme in buffer for different pH values (b) comparison of the scattering pattern among lysozyme, polymer (PNMeOEtG) and 1:1 lysozyme – polymer mixture. The solid lines are the fits using equation (1) as explained in the text.

factor (Percuss Yevick approximation)[49-50]. The solid blue line is the calculated form factor from the atomic coordinates of the lysozyme[60-61]. It should be noted that the modelled form factor is in good agreement with that calculated from the atomic coordinates of the lysozyme. The small discrepancy is attributed to the concentration effect. The HS form factor for the lysozyme yields a radius of, R_L = 1.75±0.01 nm which is in agreement with that obtained from the literature [62]. However we do not find difference in size while modelling with an ellipsoidal form factor [60]. The contrast in water is calculated, $\Delta\rho \sim 2.6 \times 10^{10}$ cm^{-2}, for the density of 1.32 g/cm^3 [63]. In Figure 3.45 (a) the highlighted box shows an increase in scattering, that illustrates the formation of clusters or aggregates. It results from the attractive interaction between the lysozyme molecules. However, the HS S(Q) interaction radius yields, R_C = 4.85±0.02 nm, which is ~ 2.8 times larger than R_L.

This point towards the fact that the formation of equilibrium clusters as a result of lowering of the pH value (from 7.4 to 7.0) is responsible for the structure factor peak in Figure 3.45 (a). Formation of dynamic clusters was also reported by Shukla *et al.* [60] where the S(Q) peak position was found to be independent of concentration for lysozyme molecules. The strong repulsive interaction between the clusters causes a sharp decrease in the overall forward scattering, $\frac{d\Sigma}{d\Omega}(Q \to 0)$, that is manifested as a structure factor (interaction) peak. The interaction peak reveals the distance between the clusters (~ $2R_C$) but not the individual lysozyme molecules. Our studies also point to the fact that formation of such clusters might be related to the change in the pH or the surface charge density of the lysozyme molecules.

In Figure 3.45 (b) a comparison of the SANS diffraction pattern for a mixture of lysozyme and PNMeOEtG polymer is presented. For the pure polymer the form factor was modelled using a Debye function that resembles a random Gaussian coil [51] in equation (1) for, $S(Q) = 1$. It yields a radius of gyration, R_g = 2.62±0.02 nm. The corresponding open square data, represents 1:1 mixture of the polymer and the lysozyme in a pH 7.4 buffer solution. We can model the data simply by calculating 1:1 ratio of the scattering pattern obtained from the Debye function for the polymer and the HS form factor for the lysozyme. This univocally point out the fact that there is no interaction between the polymer and the lysozyme. The resulting scattering curve is a mere sum of the individual scattering pattern. The small discrepancy of the modelled line for the mixture at high Q (> 0.26 $Å^{-1}$) is due to the absence of correct resolution data for the lysozyme solution. It should be noted that these are in contrast to the previous study on hemoglobin protein interaction with polyethylene oxide (PEO), where a marked increase in interaction was observed[64].

3.3.4 Cytotoxicity

The cytotoxicity study was investigated in HEp2 cells, and the result was shown in Figure 3.46. PEG (8000 Da), a gold standard for antifouling material, is used as a positive control. The PNMeOEtG of different molecular weight (3.26-11.1 kg/mol) showed minimal toxicity (cell viability > 90 %) towards HEp2 cells up to concentration of 1mg/mL investigated, which is critical for them to be used as biomaterials in biomedical and biotechnological fields.

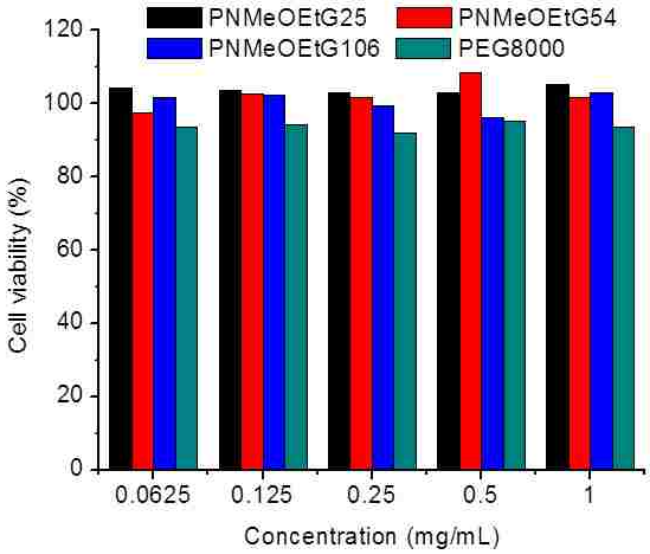

Figure 3.46. Cell viability study of PNMeOEtG polypeptoids compared to PEG (8000 Da).

3.4 Conclusions

N substituted *N*-carboxyanhydride monomers bearing oligomeric ethylene glycol side chains (Me(OEt)$_n$-NCA, for the first time, were successfully synthesized with moderate yields. PEGylated polypeptoids (PNMe(OEt)$_3$G, n=1-3) were successfully synthesized by BnNH$_2$-initiated ring-opening polymerization of the corresponding monomers with controlled molecular weight ([M]$_0$:[I]$_0$ < 200:1) and narrow molecular distribution (PDI=1.03-1.10). Kinetic studies revealed a pseudo-first order dependence on the monomer concentration (i.e., d[M]/dt = k_{obs} [M]), consistent with a living polymerization. The resulting PEGylated polypeptoids are hydrophilic

both on the polymer backbone and side chain with good water solubility (>200 mg/ml). Similarly to the previously reported PEO-mimetic oligomers (20 mer), the PEGylated polypeptoids are amorphous and the glass transition temperature (T_g) is increased with decreasing side chain length: $PNMe(OEt)_3G$ (T_g = -34.9 – -41.1 ^oC) < $PNMe(OEt)_2G$ (T_g = -6.0 – -16.9 ^oC) <PNMeOEtG (T_g = 24.5 – 46.4^oC). The glass transition temperature (T_g) of the PEGylated polypeptoids is also increased with increasing of molecular weight investigated. The preliminary DLS results showed that the PNMeOEtG remained fully hydrated without apparent aggregation in PBS buffer for more than one month and no obvious hydrodynamic size increase was observed for the mixture of lysozyme and PNMeOEtG up to 24 h based on dynamic light scattering (DLS) analysis. The preliminary small angle neutron scattering (SANS) analysis of lysozyme, PNMeOEtG, and mixture of lysozyme and PNMeOEtG in D_2O revealed no appreciable interaction between lysozyme and PNMeOEtG, indicating minimum adsorption of lysozyme to PNMeOEtG. The SANS structure factor analysis has pointed out a sharp increase in repulsive interaction with the change in pH content of the buffer that results in equilibrium cluster formation. In addition, the polypeptoids at different MW showed minimum cytotoxicity towards HEp2 cells. All of these results suggest the PEGylated polypeptoids a potential antifouling material for the biomedical and biotechnological application.

3.5 Reference

1. Meyers, S. R.; Grinstaff, M. W. Biocompatible and Bioactive Surface Modifications for Prolonged In Vivo Efficacy. *Chem. Rev.* **2012,** *112* (3), 1615-1632.

2. Horbett, T. A., Protein Adsorption on Biomaterials. In *Biomaterials: Interfacial Phenomena and Applications*, AMERICAN CHEMICAL SOCIETY: 1982; Vol. 199, pp 233-244.

3. Mojtaba, B.; Maryam, K.; Larry, D. U., Poly(ethylene glycol) and Poly(carboxy betaine) Based Nonfouling Architectures: Review and Current Efforts. In *Proteins at Interfaces III State of the Art*, American Chemical Society: 2012; Vol. 1120, pp 621-643.

4. Wei, Q.; Becherer, T.; Angioletti-Uberti, S.; Dzubiella, J.; Wischke, C.; Neffe, A. T.; Lendlein, A.; Ballauff, M.; Haag, R. Protein Interactions with Polymer Coatings and Biomaterials. *Angew. Chem. Int. Ed.* **2014,** *53* (31), 8004-8031.

5. Pertsin, A. J.; Grunze, M. Computer Simulation of Water near the Surface of Oligo(ethylene glycol)-Terminated Alkanethiol Self-Assembled Monolayers. *Langmuir* **2000,** *16* (23), 8829-8841.

6. Chapman, R. G.; Ostuni, E.; Takayama, S.; Holmlin, R. E.; Yan, L.; Whitesides, G. M. Surveying for Surfaces that Resist the Adsorption of Proteins. *J. Am. Chem. Soc.* **2000,** *122* (34), 8303-8304.

7. Ostuni, E.; Chapman, R. G.; Holmlin, R. E.; Takayama, S.; Whitesides, G. M. A Survey of Structure−Property Relationships of Surfaces that Resist the Adsorption of Protein. *Langmuir* **2001,** *17* (18), 5605-5620.

8. Knop, K.; Hoogenboom, R.; Fischer, D.; Schubert, U. S. Poly(ethylene glycol) in Drug Delivery: Pros and Cons as Well as Potential Alternatives. *Angew. Chem. Int. Ed.* **2010,** *49* (36), 6288-6308.

9. Romberg, B.; Metselaar, J. M.; Baranyi, L.; Snel, C. J.; Bünger, R.; Hennink, W. E.; Szebeni, J.; Storm, G. Poly(amino acid)s: Promising enzymatically degradable stealth coatings for liposomes. *Int. J. Pharm.* **2007,** *331* (2), 186-189.

10. Chelmowski, R.; Köster, S. D.; Kerstan, A.; Prekelt, A.; Grunwald, C.; Winkler, T.; Metzler-Nolte, N.; Terfort, A.; Wöll, C. Peptide-Based SAMs that Resist the Adsorption of Proteins. *J. Am. Chem. Soc.* **2008,** *130* (45), 14952-14953.

11. Engler, A. C.; Ke, X.; Gao, S.; Chan, J. M. W.; Coady, D. J.; Ono, R. J.; Lubbers, R.; Nelson, A.; Yang, Y. Y.; Hedrick, J. L. Hydrophilic Polycarbonates: Promising Degradable Alternatives to Poly(ethylene glycol)-Based Stealth Materials. *Macromolecules* **2015,** *48* (6), 1673-1678.

12. Konradi, R.; Pidhatika, B.; Mühlebach, A.; Textor, M. Poly-2-methyl-2-oxazoline: A Peptide-like Polymer for Protein-Repellent Surfaces. *Langmuir* **2008,** *24* (3), 613-616.

13. Pidhatika, B.; Möller, J.; Benetti, E. M.; Konradi, R.; Rakhmatullina, E.; Mühlebach, A.; Zimmermann, R.; Werner, C.; Vogel, V.; Textor, M. The role of the interplay between polymer architecture and bacterial surface properties on the microbial adhesion to polyoxazoline-based ultrathin films. *Biomaterials* **2010,** *31* (36), 9462-9472.

14. Hoogenboom, R. Poly(2-oxazoline)s: A Polymer Class with Numerous Potential Applications. *Angew. Chem. Int. Ed.* **2009,** *48* (43), 7978-7994.

15. Teare, D. O. H.; Schofield, W. C. E.; Garrod, R. P.; Badyal, J. P. S. Poly(N-acryloylsarcosine methyl ester) Protein-Resistant Surfaces. *J. Phys. Chem. B* **2005,** *109* (44), 20923-20928.

16. Huber, D. L.; Manginell, R. P.; Samara, M. A.; Kim, B.-I.; Bunker, B. C. Programmed Adsorption and Release of Proteins in a Microfluidic Device. *Science* **2003,** *301* (5631), 352-354.

17. Chan, J. M. W.; Ke, X.; Sardon, H.; Engler, A. C.; Yang, Y. Y.; Hedrick, J. L. Chemically modifiable N-heterocycle-functionalized polycarbonates as a platform for diverse smart biomimetic nanomaterials. *Chem. Sci.* **2014,** *5* (8), 3294-3300.

18. Jeong, J. H.; Song, S. H.; Lim, D. W.; Lee, H.; Park, T. G. DNA transfection using linear poly(ethylenimine) prepared by controlled acid hydrolysis of poly(2-ethyl-2-oxazoline). *J. Controlled Release* **2001,** *73* (2–3), 391-399.

19. Wang, C.-H.; Fan, K.-R.; Hsiue, G.-H. Enzymatic degradation of PLLA-PEOz-PLLA triblock copolymers. *Biomaterials* **2005,** *26* (16), 2803-2811.

20. Duracher, D.; Veyret, R.; Elaïssari, A.; Pichot, C. Adsorption of bovine serum albumin protein onto amino-containing thermosensitive core-shell latexes. *Polym. Int.* **2004,** *53* (5), 618-626.

21. Miller, S. M.; Simon, R. J.; Ng, S.; Zuckermann, R. N.; Kerr, J. M.; Moos, W. H. Proteolytic studies of homologous peptide and N-substituted glycine peptoid oligomers. *Biorg. Med. Chem. Lett.* **1994,** *4* (22), 2657-2662.

22. Miller, S. M.; Simon, R. J.; Ng, S.; Zuckermann, R. N.; Kerr, J. M.; Moos, W. H. Comparison of the proteolytic susceptibilities of homologous L-amino acid, D-amino acid, and N-substituted glycine peptide and peptoid oligomers. *Drug Dev. Res.* **1995,** *35* (1), 20-32.

23. Patch, J. A.; Barron, A. E. Mimicry of bioactive peptides via non-natural, sequence-specific peptidomimetic oligomers. *Curr. Opin. Chem. Biol.* **2002,** *6* (6), 872-877.

24. Latham, P. W. Therapeutic peptides revisited. *Nat Biotech* **1999,** *17* (8), 755-757.

25. Hardesty, J. O.; Cascão-Pereira, L.; Kellis, J. T.; Robertson, C. R.; Frank, C. W. Enzymatic Proteolysis of a Surface-Bound α-Helical Polypeptide. *Langmuir* **2008,** *24* (24), 13944-13956.

26. De Marre, A.; Hoste, K.; Bruneel, D.; Schacht, E.; De Schryver, F. Synthesis, Characterization, and in Vitro Biodegradation of Poly(Ethylene Glycol) Modified Poly[5N-(2-Hydroxyethyl-L-Glutamine]. *J. Bioact. Compatible Polym.* **1996,** *11* (2), 85-99.

27. Gabizon, A. P., D. Liposome formulations with prolonged circulation time in blood and enhanced uptake by tumors. *Proc. Natl. Acad. Sci. U.S.A.* **1988,** *85* (18), 6949-6953.

28. Friend, D. R.; Pangburn, S. Site-specific drug delivery. *Med. Res. Rev.* **1987,** *7* (1), 53-106.

29. Tempelaar, S.; Mespouille, L.; Coulembier, O.; Dubois, P.; Dove, A. P. Synthesis and post-polymerisation modifications of aliphatic poly(carbonate)s prepared by ring-opening polymerisation. *Chem. Soc. Rev.* **2013,** *42* (3), 1312-1336.

30. Pascual, A.; Tan, J. P. K.; Yuen, A.; Chan, J. M. W.; Coady, D. J.; Mecerreyes, D.; Hedrick, J. L.; Yang, Y. Y.; Sardon, H. Broad-Spectrum Antimicrobial Polycarbonate Hydrogels with Fast Degradability. *Biomacromolecules* **2015,** *16* (4), 1169-1178.

31. Wang, H.-F.; Su, W.; Zhang, C.; Luo, X.-h.; Feng, J. Biocatalytic Fabrication of Fast-Degradable, Water-Soluble Polycarbonate Functionalized with Tertiary Amine Groups in Backbone. *Biomacromolecules* **2010,** *11* (10), 2550-2557.

32. Zhang, Z.; Kuijer, R.; Bulstra, S. K.; Grijpma, D. W.; Feijen, J. The in vivo and in vitro degradation behavior of poly(trimethylene carbonate). *Biomaterials* **2006,** *27* (9), 1741-1748.

33. Zhang, D.; Lahasky, S. H.; Guo, L.; Lee, C.-U.; Lavan, M. Polypeptoid Materials: Current Status and Future Perspectives. *Macromolecules* **2012,** *45* (15), 5833-5841.

34. Barron, A. E.; Zuckerman, R. N. Bioinspired polymeric materials: in-between proteins and plastics. *Curr. Opin. Chem. Biol.* **1999,** *3* (6), 681-687.

35. Lahasky, S. H.; Hu, X.; Zhang, D. Thermoresponsive Poly(α-peptoid)s: Tuning the Cloud Point Temperatures by Composition and Architecture. *ACS Macro Letters* **2012,** *1* (5), 580-584.

36. Fetsch, C.; Flecks, S.; Gieseler, D.; Marschelke, C.; Ulbricht, J.; van Pée, K.-H.; Luxenhofer, R. Self-Assembly of Amphiphilic Block Copolypeptoids with C2-C5 Side Chains in Aqueous Solution. *Macromol. Chem. Phys.* **2015,** *216* (5), 547-560.

37. Xuan, S.; Lee, C.-U.; Chen, C.; Doyle, A. B.; Zhang, Y.; Guo, L.; John, V. T.; Hayes, D.; Zhang, D. Thermoreversible and Injectable ABC Polypeptoid Hydrogels: Controlling the Hydrogel Properties through Molecular Design. *Chem. Mater.* **2016,** *28* (3), 727-737.

38. Li, A.; Zhang, D. Synthesis and Characterization of Cleavable Core-Cross-Linked Micelles Based on Amphiphilic Block Copolypeptoids as Smart Drug Carriers. *Biomacromolecules* **2016,** *17* (3), 852-861.

39. Ulbricht, J.; Jordan, R.; Luxenhofer, R. On the biodegradability of polyethylene glycol, polypeptoids and poly(2-oxazoline)s. *Biomaterials* **2014,** *35* (17), 4848-4861.

40. Sun, J.; Zuckermann, R. N. Peptoid Polymers: A Highly Designable Bioinspired Material. *ACS Nano* **2013,** *7* (6), 4715-4732.

41. Luxenhofer, R.; Fetsch, C.; Grossmann, A. Polypeptoids: A perfect match for molecular definition and macromolecular engineering? *J. Polym. Sci., Part A: Polym. Chem.* **2013,** *51* (13), 2731-2752.

42. Zuckermann, R. N. Peptoid origins. *Peptide Science* **2011,** *96* (5), 545-555.

43. Secker, C.; Brosnan, S. M.; Luxenhofer, R.; Schlaad, H. Poly(α-Peptoid)s Revisited: Synthesis, Properties, and Use as Biomaterial. *Macromol. Biosci.* **2015,** *15* (7), 881-891.

44. Lau, K. H. A.; Ren, C.; Sileika, T. S.; Park, S. H.; Szleifer, I.; Messersmith, P. B. Surface-Grafted Polysarcosine as a Peptoid Antifouling Polymer Brush. *Langmuir* **2012,** *28* (46), 16099-16107.

45. Lau, K. H. A.; Ren, C.; Park, S. H.; Szleifer, I.; Messersmith, P. B. An Experimental–Theoretical Analysis of Protein Adsorption on Peptidomimetic Polymer Brushes. *Langmuir* **2011,** *28* (4), 2288-2298.

46. Statz, A. R.; Barron, A. E.; Messersmith, P. B. Protein, cell and bacterial fouling resistance of polypeptoid-modified surfaces: effect of side-chain chemistry. *Soft Matter* **2008,** *4* (1), 131-139.

47. Schneider, M.; Fetsch, C.; Amin, I.; Jordan, R.; Luxenhofer, R. Polypeptoid Brushes by Surface-Initiated Polymerization of N-Substituted Glycine N-Carboxyanhydrides. *Langmuir* **2013,** *29* (23), 6983-6988.

48. Gupta, S.; Camargo, M.; Stellbrink, J.; Allgaier, J.; Radulescu, A.; Lindner, P.; Zaccarelli, E.; Likos, C. N.; Richter, D. Dynamic phase diagram of soft nanocolloids. *Nanoscale* **2015,** *7* (33), 13924-34.

49. Percus, J. K.; Yevick, G. J. Analysis of Classical Statistical Mechanics by Means of Collective Coordinates. *Physical Review* **1958,** *110* (1), 1-13.

50. Kinning, D. J.; Thomas, E. L. Hard-Sphere Interactions between Spherical Domains in Diblock Copolymers. *Macromolecules* **1984,** *17* (9), 1712-1718.

51. Debye, P. Molecular-weight Determination by Light Scattering. *The Journal of Physical and Colloid Chemistry* **1947,** *51* (1), 18-32.

52. Xuan, S.; Zhao, N.; Zhou, Z.; Fronczek, F. R.; Vicente, M. G. H. Synthesis and in Vitro Studies of a Series of Carborane-Containing Boron Dipyrromethenes (BODIPYs). *J. Med. Chem.* **2016,** *59* (5), 2109-2117.

53. Robinson, J. W.; Secker, C.; Weidner, S.; Schlaad, H. Thermoresponsive Poly(N-C3 glycine)s. *Macromolecules* **2013,** *46* (3), 580-587.

54. Guo, L.; Zhang, D. Cyclic Poly(α-peptoid)s and Their Block Copolymers from N-Heterocyclic Carbene-Mediated Ring-Opening Polymerizations of N-Substituted N-Carboxylanhydrides. *J. Am. Chem. Soc.* **2009,** *131* (50), 18072-18074.

55. Sun, J.; Stone, G. M.; Balsara, N. P.; Zuckermann, R. N. Structure–Conductivity Relationship for Peptoid-Based PEO–Mimetic Polymer Electrolytes. *Macromolecules* **2012,** *45* (12), 5151-5156.

56. Fetsch, C.; Luxenhofer, R. Thermal Properties of Aliphatic Polypeptoids. *Polymers* **2013,** *5* (1), 112.

57. Biswas, C. S.; Patel, V. K.; Vishwakarma, N. K.; Tiwari, V. K.; Maiti, B.; Maiti, P.; Kamigaito, M.; Okamoto, Y.; Ray, B. Effects of Tacticity and Molecular Weight of Poly(N-isopropylacrylamide) on Its Glass Transition Temperature. *Macromolecules* **2011,** *44* (14), 5822-5824.

58. Lin, Y. H. Entanglement and the molecular weight dependence of polymer glass transition temperature. *Macromolecules* **1990,** *23* (25), 5292-5294.

59. Gupta, S.; Fischer, J. K. H.; Lunkenheimer, P.; Loidl, A.; Novak, E.; Jalarvo, N.; Ohl, M. Effect of adding nanometre-sized heterogeneities on the structural dynamics and the excess wing of a molecular glass former. *Scientific Reports* **2016,** *6*, 35034.

60. Shukla, A.; Mylonas, E.; Di Cola, E.; Finet, S.; Timmins, P.; Narayanan, T.; Svergun, D. I. Absence of equilibrium cluster phase in concentrated lysozyme solutions. *Proc Natl Acad Sci U S A* **2008,** *105* (13), 5075-80.

61. Diamond, R. Real-space refinement of the structure of hen egg-white lysozyme. *J Mol Biol* **1974,** *82* (3), 371-91.

62. Stradner, A.; Sedgwick, H.; Cardinaux, F.; Poon, W. C.; Egelhaaf, S. U.; Schurtenberger, P. Equilibrium cluster formation in concentrated protein solutions and colloids. *Nature* **2004,** *432* (7016), 492-5.

63. Narayanan, J.; Liu, X. Y. Protein interactions in undersaturated and supersaturated solutions: A study using light and x-ray scattering. *Biophysical Journal* **2003,** *84* (1), 523-532.

64. Gupta, S.; Biehl, R.; Sill, C.; Allgaier, J.; Sharp, M.; Ohl, M.; Richter, D. Protein Entrapment in Polymeric Mesh: Diffusion in Crowded Environment with Fast Process on Short Scales. *Macromolecules* **2016,** *49* (5), 1941-1949.

CHAPTER 4 : SOLUTION SELF-ASSEMBLY OF COIL-CRYSTALLINE DIBLOCK COPOLYPEPTOIDS (PNMG-b-PNDG)

4.1 Introduction

The solution self-assembly of amphiphilic coil-crystalline AB diblock copolymers has attracted growing interest recently; however, the theoretical and experimental studies on their solution equilibrium morphologies are limited so far. Studies have shown that a variety of unconventional micellar morphologies (*e.g.*, cylindrical[1-2], discal[3], tape-like[4], platelet micelles[5-6]) can be obtained by the solution self-assembly of amphiphilic coil-crystalline AB diblock copolymers. Recently, we have shown that both linear and cyclic diblock copolypeptoids (*c*/*l*-PNMG-b-PNDG) self-assembled into spherical micelles that reorganized into long cylindrical micelles with uniform diameter in methanol, which was driven by the crystallization of the crystalline PNDG domain (section 1.3.3).[7] At higher concentrations in methanol (5-10 wt%), both cyclic and linear diblock copolyeptoids (*c*/*l*-PNMG-b-PNDG) were shown to form free-standing gels consisting of entangled fibrils at room temperature.[8]

Following our previous studies, we have synthesized a series of linear amphiphilic crystalline-coil diblock copolypeptoids (*i.e.*, *l*-PNMG-*b*-PNDG and *l*-PNMG-*b*-PNBG) having well-controlled degree of polymerization but different compositions by sequential benzyl amine-initiated ROPs of the corresponding *N*-substituted *N*-carboxyanhydrides (Me-NCA, De-NCA and Bu-NCA).The preliminary study of the copolypeptoid composition effect on their solution morphologies was conducted.

4.2 Experimental

4.2.1 Synthesis and characterization of diblock copolymers

All the crystalline-coil AB diblock copolypeptoids were synthesized by primary amine-initiated ring-opening polymerization of the corresponding *N*-substituted *N*-carboxyanhydrides (R-NCAs) in a sequential manner. A representative procedure for the synthesis of *l*-PNMG-b-PNDG was presented. In the glovebox, Me-NCA ($[M_1]$) (87.2 mg, 0.76 mmol, $[M_1]_0$=0.4 M) was dissolved in anhydrous acetonitrile. Stock solution of benzyl amine in acetonitle (82 µL, 92.7 mM, $[M_1]$: $[BnNH_2]_0$=100:1) was added. The reaction mixture was stirred at room temperature for 16 h to reach a complete conversion of polymerization. Acetonitrile solution of De-NCA ($[M_2]$) (189 µL, 0.4 M, 0.076 mmol, $[M_1]_0$:$[M_2]_0$: $[BnNH_2]_0$=100:10:1) was added to the above mixture and allowed to stir at 50^{o}C for another 24 h to reach a full conversion. The polymer solution was dried under vaccume and re-dissolved in DCM followed by addition of excess hexane to precipitate out the polymer. The polymer was collected by filtration and washed with ample hexane followed by drying under vacuum to afford white solid (55.8 mg) in 81.2% yield. The molecular weights (M_ns) were determined by end-group analysis using ^{1}H NMR spectroscopy.

4.2.2 Self-assembly of diblock copolypeptoids

The diluted solutions of diblock copolypeptoids (*l*-$PNMG_{130}$-b-$PNDG_{70}$, *l*-$PNMG_{114}$-b-$PNDG_{89}$, *l*-$PNMG_{125}$-b-$PNDG_{117}$, $PNMG_{105}$-b-$PNBG_{115}$) were prepared by dialysis method due to their limited solubility in MeOH: the diblock polymers were dissolved in DCM at 1.0 mg/mL concentration followed by dialysis against MeOH for 7days. The resulting solutions were heated at 70-80^{o}C, above the side chain melting point of PNDG, for 1h and slowly cooled down to room temperature. All the dilute solutions of other diblock copoypeptoids were prepared by directly dissolving in MeOH at 1.0 mg/ml and heated at 70^{o}C for 1h followed by slowly cooling down to

room temperature. The prepared dilute solutions of diblock copolypeptoids were characterized by DLS and TEM analysis at different time intervals.

4.2.3 DLS measurement of dilute polymer solutions

Polymer solution in MeOH (1.0 mg/mL) was filtered through a 0.22 µm filter and heated at 70-80 ^{o}C for 1 h followed by slowly cooling down to room temperature. The polymer solution was characterized by DLS at different time intervals. All the DLS measurements were conducted using Malvern Zetasizer Nano-zs (Zen3600). The He-Ne laser operating at 633 nm was utilized, and scattered light intensity was detected at an external angle of 173 ^{o}C using non-invasive backscatter (NIBS) technology. Data from three measurements with 12 scans for each measurement was recorded. At each temperature, the sample was equilibrated for 3 min.

4.2.4 TEM/cryo-TEM analysis of dilute polymer solutions

Polymer solution in MeOH (1.0 mg/mL) was filtered through a 0.22 µm filter and heated at 70-80 ^{o}C for 1 h followed by slowly cooling down to room temperature. The polymer solution was stored at room temperature for 3 d. FEI Vitrobot was used for the sample preparation of cryo-TEM experiment. 5 µL of the above polymer solution in MeOH (1 mg/mL) was applied to a 300 mesh lacey carbon coated TEM grid. Double side blotting to the grid for 2 seconds leaves a thin film on the grid. The grid then was quickly plunged into liquid ethane chilled by liquid nitrogen. The vitrified sample grid was loaded in a single tilt liquid nitrogen cryo transfer holder, and was then inserted to FEI G2 F30 Tecnal TEM operated at 120keV, with a FEI digital camera and analyzed using FEI Digital Micrograph software. The grids for the regular TEM was prepared by adding 5 µL of the above polymer solution in MeOH (1mg/mL) onto the 300 mesh carbon grid followed by blotting with a filter paper and drying at room temperature. The grids then were stained with uranyl acetate for 1 min.

4.3 Results and discussion

4.3.1 Synthesis and characterization of AB diblock copolypeptoids

A series of linear AB diblock copolypeptoids (*l*-PNMG-b-PNDG and *l*-PNMG-*b*-PNBG) have been synthesized by benzyl amine-initiated ROP of the corresponding R-NCAs in a sequential manner (Scheme 4.1). The compositions of the AB diblock copolypeptoids were determined by ^{1}H NMR spectroscopy (Table 4.1, Figure 4.1 and 4.2). For example, the number-averaged degree of polymerization (DP_n) of *l*-PNMG-b-PNDG (*l*-AB) was determined by the integrations at 2.89-3.04 ppm and 0.91 ppm due to the methyl protons in the PNMG block and the methyl protons in the PNDG block relative to the integration of the benzyl end-group signals at 7.31 ppm. The compositions of the AB diblock copolypeptoids can be well tuned by controlling the initial monomer to initiator ratio ($[M]_0$:$[BnNH_2]_0$). The volume fraction of the PNDG block was systematically varied in the 0.27-0.79 range. The *l*-PNMG-b-PNDG diblock copolymers were not suitable for size exclusion chromatographic (SEC) analysis using LiBr/DMF and THF due to their limited solubility in these solvents. The molecular weights (M_ns) determined by ^{1}H NMR spectroscopy were comparable to the theoretically predicted values, as shown in table 4.1.

Scheme 4.1. Synthesis of diblock copolypeptoids (*l*-PNMG-b-PNDG and *l*-PNMG-*b*-PNBG).

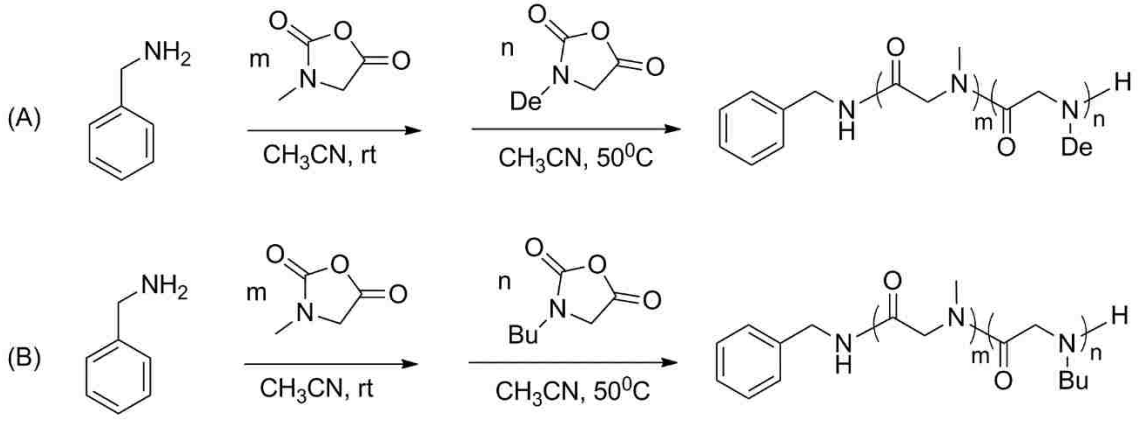

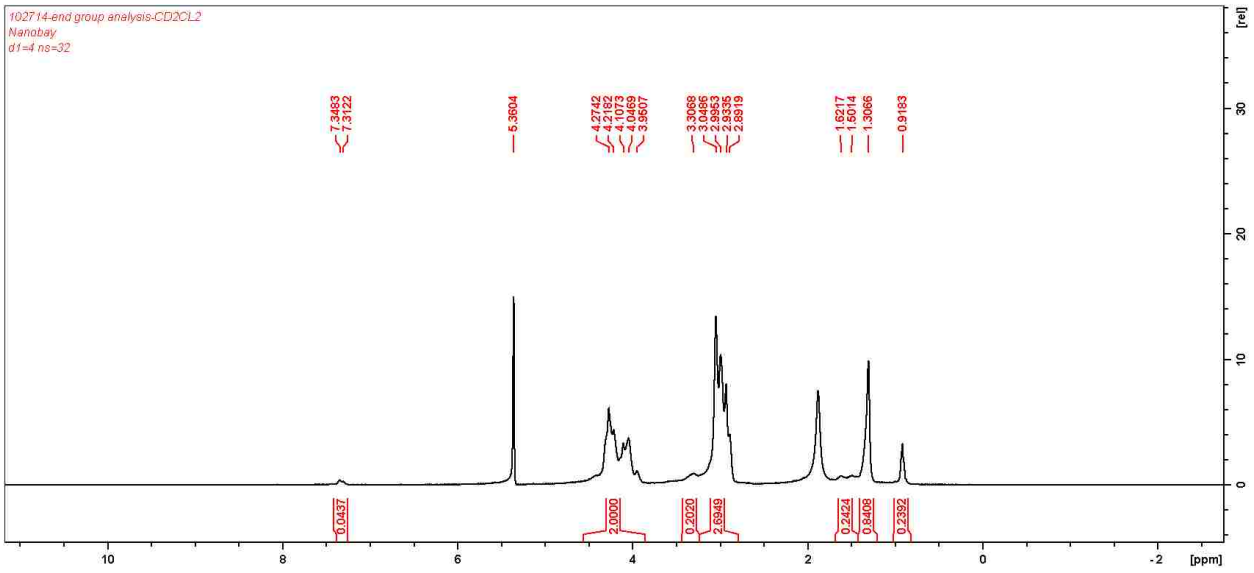

Figure 4.1.[1]H NMR spectrum of *l*-PNMG$_{99}$-b-PNDG$_9$ in CD_2Cl_2.

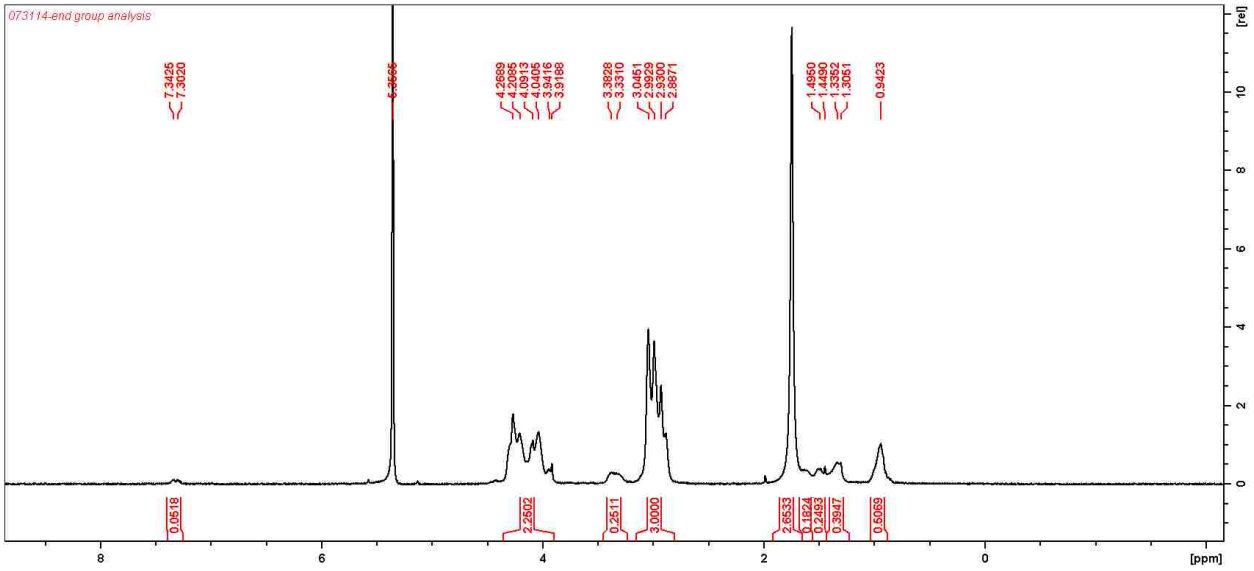

Figure 4.2. [1]H NMR spectrum of *l*-PNMG$_{96}$-b-PNBG$_{12}$ in CD_2Cl_2.

Table 4.1. Molecular parameters of AB diblock copolytoids.

Entry	[a]Sample	[b]$[M]_1$:$[M]_2$:$[I]_0$	Φ PNDG		[e]Micelle Sturcture	[f]Diameter (nm)
			[c]Calcd	[d]NMR		
1	*l*-PNMG$_{99}$-b-PNDG$_9$	100:10:1	0.29	0.27	Cylindrical	12.6±0.8
2	*l*-PNMG$_{90}$-b-PNDG$_{17}$	100:20:1	0.45	0.44	Cylindrical	10.9±1.2
3	*l*-PNMG$_{92}$-b-PNDG$_{37}$	100:40:1	0.62	0.62	Cylindrical	13.4 ± 1.8
4	*l*-PNMG$_{168}$-b-PNDG$_{35}$	180:40:1	0.48	0.46	Cylindrical	12.9±1.2
5	*l*-PNMG$_{145}$-b-PNDG$_{52}$	160:60:1	0.61	0.60	Cylindrical	29.0±4.5
6	*l*-PNMG$_{130}$-b-PNDG$_{70}$	140:80:1	0.70	0.69	Cylindrical	21.1±5.8
7	*l*-PNMG$_{114}$-b-PNDG$_{89}$	120:100:1	0.77	0.76	Cylindrical	30.6±6.0
8	*l*-PNMG$_{125}$-b-PNDG$_{117}$	100:120:1	0.83	0.79	Precipitate out	-
9	*l*-PNMG$_{96}$-b-PNBG$_{12}$	100:10:1	-	-	[g]Not Cylindrical	-
10	PNMG$_{105}$-b-PNBG$_{45}$	100:40:40	-	-	Not Cylindrical	-
11	PNMG$_{184}$-b-PNBG$_{16}$	200:20:1	-	-	Not Cylindrical	-
12	PNMG$_{205}$-b-PNBG$_{60}$	180:40:1	-	-	Not Cylindrical	-
13	PNMG$_{163}$-b-PNBG$_{65}$	160:60:1	-	-	Not Cylindrical	-
14	PNMG$_{138}$-b-PNBG$_{84}$	140:80:1	-	-	Not Cylindrical	-
15	PNMG$_{105}$-b-PNBG$_{115}$	100:120:1	-	-	Not Cylindrical	-

[a]The actual DP_n was determined by ^{1}H NMR. [b]Theoretical monomer to initiator ratio [c]Theoretical volume fraction of PNDG using the known density of PNMG (1.405 g/cm^3) and PNDG (0.95 g/cm^3). [d]Actual volume fraction of PNDG determined by ^{1}H NMR. [e]Entry 6,7,8 and 15 were prepared by dialysis method and other entries were prepared by direct dissolving method at 1mg/ml in MeOH. [f]Average diameter of more than 30 individual micelles from TEM. The error bar is the standard deviation of the measured diameters. [g]There is no large aggregation formed from DLS results.

4.3.2 Solution self-assembly of AB diblock copolypeptoids

Self-assembly of l-PNMG-b-PNDG in MeOH. To investigate the effect of polymer compositions on the self-assembled morphology of *l*-PNMG-b-PNDG in MeOH, the self-assembly of *l*-PNMG-b-PNDG bearing constant chain length of PNMG block (targeted $DP_n = 100$) while different chain length of PNDG block (Φ PNDG = 0.27-0.62) were investigated by transmission electron microscopy (TEM) using uranyl acetate as the staining reagent, as shown in Figure 4.3 (A-F). At 3 d, cylindrical micelles were observed for all the three samples, *l*-$PNMG_{99}$-b-$PNDG_9$, *l*-$PNMG_{90}$-b-$PNDG_{17}$ and *l*-$PNMG_{92}$-b-$PNDG_{37}$. The cylinder like structures of sample *l*-$PNMG_{92}$-b-$PNDG_{37}$ were also confirmed by cryo-TEM, as shown in Figure 4.3 (G,H). For sample $PNMG_{90}$-b-$PNDG_{17}$ with longer PNDG block length, cylindrical micelles with larger diameters were observed, probably due to the aggregation of individual cylindrical micelles during the TEM preparation process, as evidenced by the cryo-TEM images of the micelles showing no aggregation of individual micelles (Figure 4.4). The diameters of the individual micelles in Figure 4.3 (A-F) (average of at least 50 micelles) were measured for these three samples: d ($PNMG_{99}$-b-$PNDG_9$) = 12.6 ± 0.8 nm, d ($PNMG_{90}$-b-$PNDG_{17}$) = 13.0 ± 0.9 nm and d ($PNMG_{92}$-b-$PNDG_{37}$) = 13.4 ± 1.8 nm. It is interesting that the diameter of the cylindrical micelles formed by $PNMG_{99}$-b-$PNDG_9$ well matched the diameter of a zig-zag conformation of a fully stretched PNDG segment, whereas the diameters of the cylindrical micelles formed by $PNMG_{90}$-b-$PNDG_{17}$ and $PNMG_{92}$-b-$PNDG_{37}$ were much smaller than the theoretically predicated diameter assuming the PNDG was fully stretched, indicating that the PNDG micellar core adopted a chain folded structure.

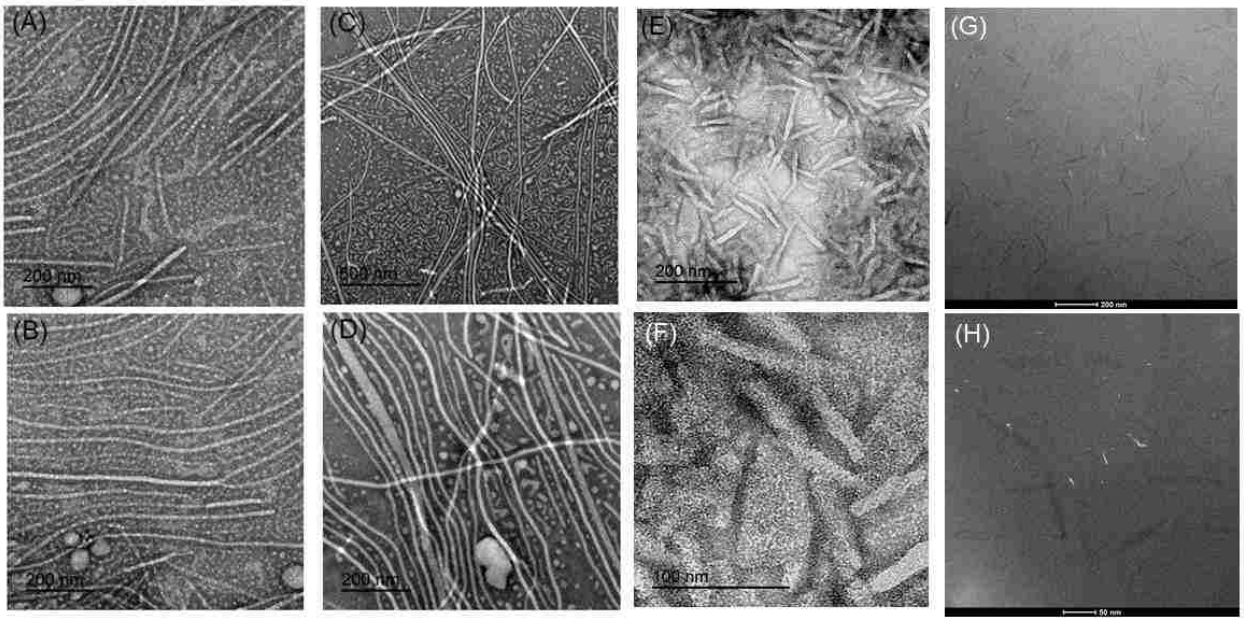

Figure 4.3. TEM images of dilute solutions of *l*-PNMG$_{99}$-b-PNDG$_{9}$ (A, B), *l*-PNMG$_{90}$-b-PNDG$_{17}$ (C, D), and *l*-PNMG$_{92}$-b-PNDG$_{37}$ (E, F) in MeOH after 3 d. The samples were prepared by direct dissolution method and stained with uranyl acetate. Cryo-TEM images of dilute solutions of *l*-PNMG$_{92}$-b-PNDG$_{37}$ (1mg/mL) in MeOH after 3 d (G,H).

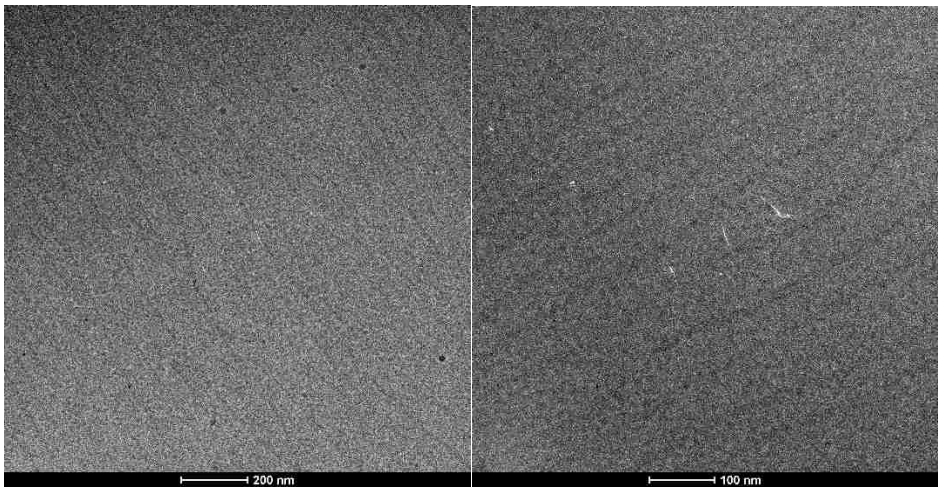

Figure 4.4. Cryo-TEM images of dilute *l*-PNMG$_{90}$-b-PNDG$_{17}$ solution in MeOH at 3 d.

To investigate the effect of different sample preparation method on micelle morphology, solution of *l*-PNMG$_{92}$-b-PNDG$_{37}$ in MeOH (1mg/mL) prepared by dialysis method was also analyzed by TEM. As shown in Figure 4.5, longer cylindrical micelles (d = 12.6 ± 1.0 nm) were

formed by dialysis method compared to that formed by direct dissolution method (Figure 4.3 G,H), probably due to the slow diffusion of MeOH in the dialysis method that allow the micelles to crystallize slowly.

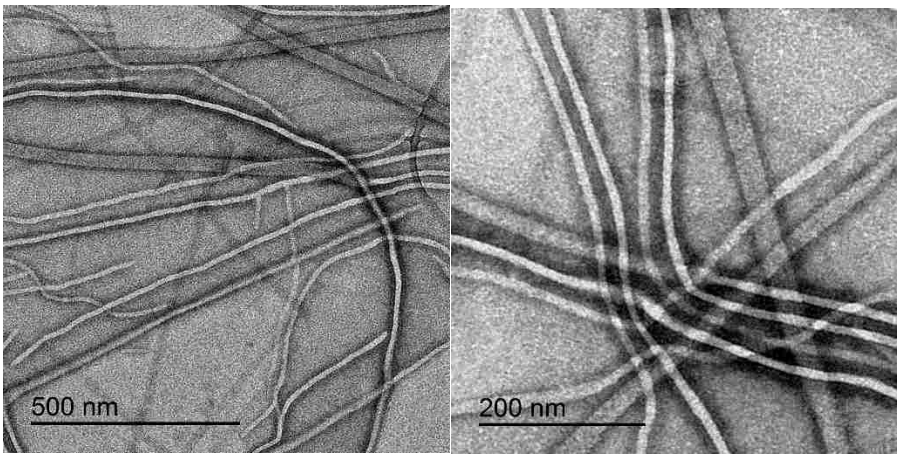

Figure 4.5. TEM images of dilute solutions of *l*-PNMG$_{92}$-b-PNDG$_{37}$ in MeOH prepared by dialysis method. The sample was stained with uranyl acetate prior to TEM imaging.

The self-assembly of the diblock copolypeptoids (*l*-PNMG-b-PNDG) with constant total chain length (targeted DP_n = 220) while different volume fraction ratio of PNMG and PNDG (Φ PNDG = 0.46-0.79), were also investigated in MeOH. Miceller solutions of *l*-PNMG$_{168}$-b-PNDG$_{35}$ and *l*-PNMG$_{145}$-b-PNDG$_{52}$ were prepared by direct dissolution in MeOH, whereas miceller solutions of *l*-PNMG$_{130}$-b-PNDG$_{70}$, *l*-PNMG$_{114}$-b-PNDG$_{89}$ and *l*-PNMG$_{125}$-b-PNDG$_{117}$ were prepared by dialysis method due to their higher hydrophobicity and limited solubility in methanol. All the samples formed cylinder-like structures in MeOH at 3 d (Figure 4.5). The core of the cylindrical micelles were more likely to adopt a chain folded structure, as evidenced by the average diameters of the individual cylindrical micelles (d = 12.9 ± 1.0 – 29.0 ± 4.5 nm) which were much smaller than the theoretically predicated value assuming the PNDG core adopted a fully stretched conformation. Sample *l*-PNMG$_{125}$-b-PNDG$_{117}$ was too hydrophobic that precipitation occured

after dialysis against MeOH and sheet-like structure was observed of the suspension under TEM (Figure 4.6).

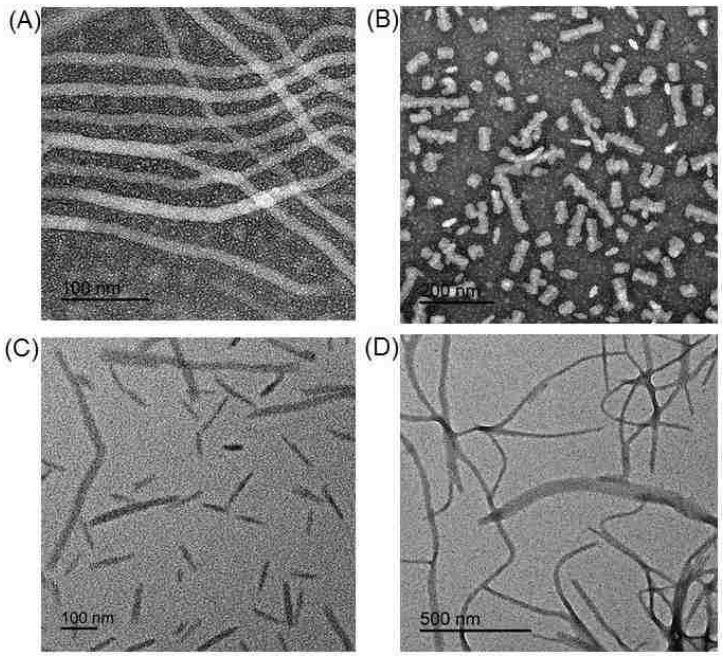

Figure 4.6. TEM images of dilute solutions of *l*-PNMG$_{168}$-b-PNDG$_{35}$ (A), PNMG$_{145}$-b-PNDG$_{52}$ (B), PNMG$_{130}$-b-PNDG$_{70}$ (C) and PNMG$_{114}$-b-PNDG$_{89}$ (D). (A) and (B) were stained with uranyl acetate, whereas (C) and (D) were not.

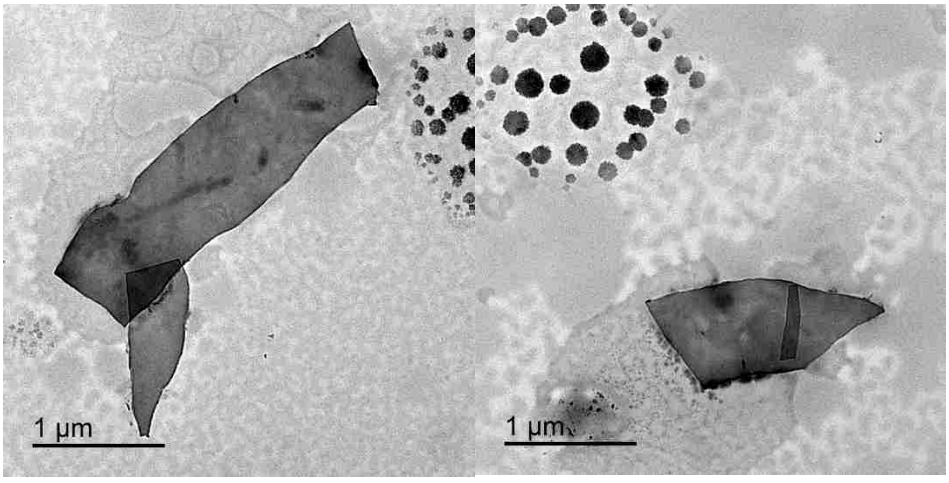

Figure 4.7. TEM images of *l*-PNMG$_{125}$-b-PNDG117 in MeOH stained with uranyl acetate.

The self-assembly of the polymers was also monitored by DLS for *l*-PNMG$_{168}$-b-PNDG$_{35}$ and *l*-PNMG$_{145}$-b-PNDG$_{52}$.in dilute methanol solution (1.0 mg/mL) at room temperature. For

sample *l*-PNMG$_{168}$-b-PNDG$_{35}$ (Figure 4.7 A), two size distribution peaks were observed after immediately dissolution in MeOH, which was tentatively attributed to the spherical micelles and short cylinders formed at the beginning. The peaks shifted to larger size with increasing time, indicating the formation of longer cylinders, consistent with the TEM results (Figure 4.5). For sample *l*-PNMG$_{145}$-b-PNDG$_{52}$ of higher PNDG volume fraction (Φ PNDG = 0.60), monomodel size distribution was observed at all time investigated (from t=0 to t=10d) (Figure 4.7B), probably due to the "freezed morphology" of short cylinders as shown in TEM (Figure 4.5).

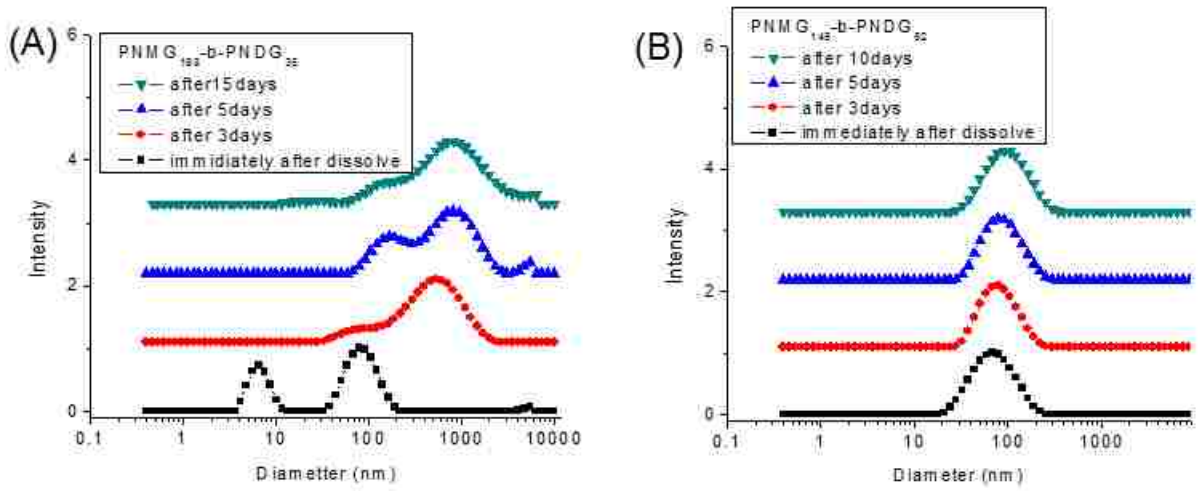

Figure 4.8. DLS-determined hydrodynamic size distribution of 1.0 mg/mL PNMG$_{168}$-b-PNDG$_{35}$ and 1.0 mg/mL PNMG$_{145}$-b-PNDG$_{52}$ in methanol at room temperature.

Self-assembly of l-PNMG-b-PNBG in MeOH. Cylindrical micelles were observed in MeOH under TEM in a wide composition window (Table 4.1 and Figure 4.8). The crystallization of the solvophobic PNDG block including both main chain and side chain crystallization, was expected to drive the formation of cylindrical micelles. To support our hypothesis, *l*-PNMG-*b*-PNBG polymers where the PNBG blocks only undergo main chain crystallization were synthesized and their solution self-assembly in MeOH was compared with that of *l*-PNMG-*b*-PNDG. As expected, no evidence of cylindrical micelle formation for *l*-PNMG-*b*-PNBG polymers at the entire compositions range, as indicated by the lack of large particle formation over time from

DLS analysis. Representative DLS measurement (Figure 4.9A and B) indicated that diameters of micelles formed by $PNMG_{205}$-b-$PNBG_{60}$ and $PNMG_{163}$-b-$PNBG_{65}$ remained almost constant (< 10 nm) over time, indicating no large aggregates formed. No cylindrical micelles were observed under TEM for sample $PNMG_{105}$-b-$PNBG_{115}$ with the highest volume fraction of PNBG block in room temperature MeOH at 1.0 mg/mL (Figure 4.9C). The results were consistent with the observation that no gel was formed for $PNMG_{105}$-b-$PNBG_{45}$ at 20 wt% in MeOH at room temperature over a period of two months.

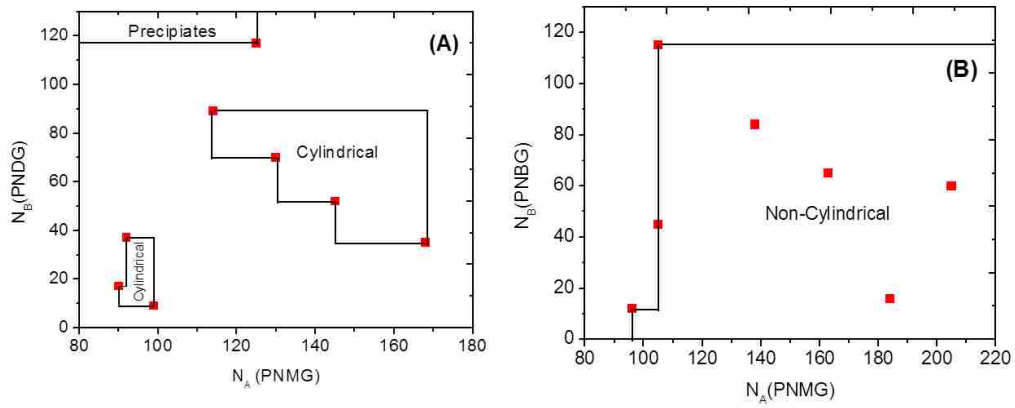

Figure 4.9. Composition-solution morphology diagrams for (A) *l*-PNDG-*b*-PNMG and (B) *l*-PNBG-*b*-PNMG in 1.0 mg/mL MeOH solution at room temperature. N_A: DP_n of PNMG; N_B: DP_n of PNDG or PNBG. The non-cylindrical region in (B) is determined by DLS analysis.

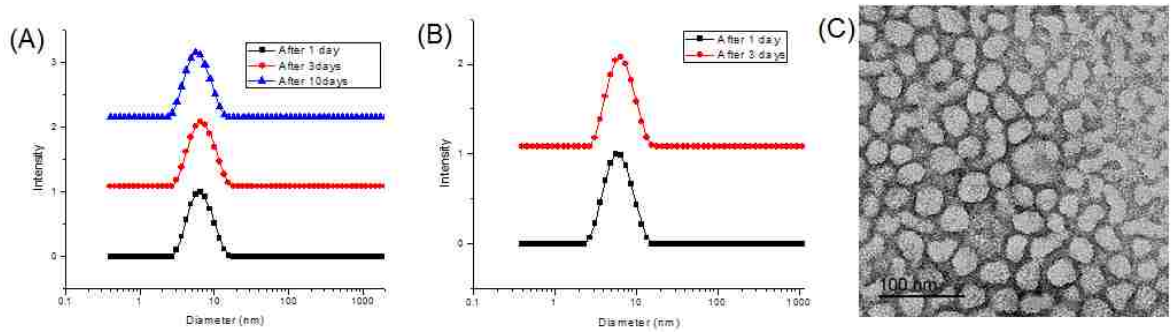

Figure 4.10. DLS-determined hydrodynamic size distribution of (A) $PNMG_{205}$-b-$PNBG_{60}$ and (B) $PNMG_{163}$-b-$PNBG_{65}$ in MeOH at room temperature. (C) TEM images of dilute solution of $PNMG_{105}$-b-$PNBG_{115}$ in MeOH stained with uranyl acetate.

4.4 Conclusion and future work

A series of amiphiphilic coil-crystalline *l*-PNMG-*b*-PNDG and *l*-PNMG-*b*-PNBG diblock copolypeptoids were synthesized by ROP of the corresponding monomers. *l*-PNMG-*b*-PNDG formed cylindrical micelles in MeOH in a wide composition window (Φ PNDG = 0.27-0.79). By contrast, *l*-PNMG-*b*-PNBG bearing shorter alkyl side chains in the solvophobic segment than that in *l*-PNMG-*b*-PNDG showed no evidence of cylindrical micelle formation based on DLS and TEM analysis. TEM analysis revealed that the cylindrical micelles formed by *l*-$PNMG_{99}$-*b*-$PNDG_9$ with short PNDG block (Φ PNDG = 0.27) appears to adopt a core of fully stretched PNDG chains, while the micellar core of all other *l*-PNMG-*b*-PNDG polymers were likely to adopt a chain folded conformation. To further investigate the driving force of the cylindrical micelle formation of the coil-crystalline diblock copolypeptoids (*l*-PNMG-*b*-PNDG) in methanol, *l*-PNMG-*b*-PNEHG with the hydrophobic block PNEHG having no side chain crystallization will be synthesized and its solution self-assembly in methanol will be investigated. A systematic study on how the polymer composition, architecture and crystalline packing affect the morphology of crystalline-coil block copolymers in dilute solution is currently in progress. The solution morphologies will be fully characterized by, TEM/crto-TEM, S/WAXS, and SANS methods to determine the micellar structure and the crystalline packing in the micellar core.

4.5 Reference

1. Wang, X.; Guerin, G.; Wang, H.; Wang, Y.; Manners, I.; Winnik, M. A. Cylindrical Block Copolymer Micelles and Co-Micelles of Controlled Length and Architecture. *Science* **2007,** *317* (5838), 644-647.

2. Gilroy, J. B.; Gädt, T.; Whittell, G. R.; Chabanne, L.; Mitchels, J. M.; Richardson, R. M.; Winnik, M. A.; Manners, I. Monodisperse cylindrical micelles by crystallization-driven living self-assembly. *Nat. Chem.* **2010,** *2* (7), 566-570.

3. Yin, L.; Hillmyer, M. A. Disklike Micelles in Water from Polyethylene-Containing Diblock Copolymers. *Macromolecules* **2011,** *44* (8), 3021-3028.

4. Cao, L.; Manners, I.; Winnik, M. A. Influence of the Interplay of Crystallization and Chain Stretching on Micellar Morphologies: Solution Self-Assembly of Coil−Crystalline Poly(isoprene-block-ferrocenylsilane). *Macromolecules* **2002,** *35* (22), 8258-8260.

5. Lotz, B.; Kovacs, A. J.; Bassett, G. A.; Keller, A. Properties of copolymers composed of one poly-ethylene-oxide and one polystyrene block. *Kolloid-Zeitschrift und Zeitschrift für Polymere* **1966,** *209* (2), 115-128.

6. Gast, A. P.; Vinson, P. K.; Cogan-Farinas, K. A. An intriguing morphology in crystallizable block copolymers. *Macromolecules* **1993,** *26* (7), 1774-1776.

7. Lee, C.-U.; Smart, T. P.; Guo, L.; Epps, T. H.; Zhang, D. Synthesis and Characterization of Amphiphilic Cyclic Diblock Copolypeptoids from N-Heterocyclic Carbene-Mediated Zwitterionic Polymerization of N-Substituted N-Carboxyanhydride. *Macromolecules* **2011,** *44* (24), 9574-9585.

8. Lee, C.-U.; Lu, L.; Chen, J.; Garno, J. C.; Zhang, D. Crystallization-Driven Thermoreversible Gelation of Coil-Crystalline Cyclic and Linear Diblock Copolypeptoids. *ACS Macro Letters* **2013,** *2* (5), 436-440.

CHAPTER 5 : INTRODUCTION TO DIPYRROMETHENES (BODIPYS) AND BORON NEUTRON CAPTURE THERAPHY (BNCT)

5.1 Introduction to BODIPYs

5.1.1 Synthetic methodologies of BODIPYS

Boron dipyrromethene (4,4-difluoro-4-bora-3a,4a-diaza-s-indacene), abbreviated as BODIPY (Figure 5.1), has been considered as a versatile fluorophore dye in the last three decades.[1] BODIPY is formed by boron complexation of a dipyrromethene with boron trifluoride diethyl etherate ($BF_3O(CH_2CH_3)_2$), leading to a rigid tricyclic system usually associated with narrow absorption and emission spectra and high fluorescence quantum yields.[2]

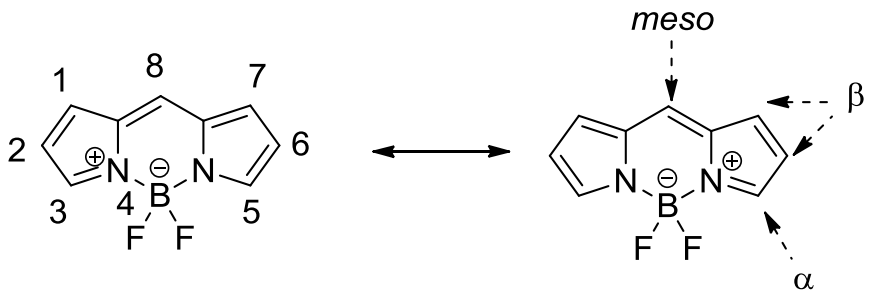

Figure 5.1. Structure of BODIPY fluorophore and its IUPAC numbering system.

Since the first BODIPY reported by Treibs and Kreuzer in 1968[3], numerous BODIPYs have been synthesized using several following strategies. The first synthetic approach (Scheme 5.1), which usually is used to build symmetrical BODIPYs, involves the acid-catalyzed condensation between α-free pyrroles (**1**) and various aldehydes (**2**)[4]. The resulting dipyrromethanes (**5**) were further oxidized to corresponding dipyrromethenes (**6**) using dichloro-5,6-dicyano-1,4-benzoquinone (DDQ) followed by complexation with boron trifluoride diethyl etherate ($BF_3{\cdot}OEt_2$) under basic conditions to afford the desired BODIPYs (**7**). Additionally, the condensation can also be achieved between α-free pyrroles (**1**) and acyl chloride (**3**)[5], or anhydride (**4**)[6] to directly yield the dipyrromethene (**6**) followed by deprotonation with base (*e.g.*, triethylamine) and boron complexation to afford the symmetrical BODIPYs (**7**). As shown in Scheme 5.2, the second method[7], which generally is used to approach both

symmetrical and unsymmetrical BODIPYs, involves the acid catalyzed condensation of 2-acetyl pyrroles (**8**) and an α-free pyrroles (**9**) followed by oxidation with DDQ to provide the corresponding dipyrromethenes (**11**). Subsequent complexation of **11** with $BF_3 \cdot OEt_2$ provides symmetrical or unsymmetrical BODIPYs (**12**). The third method (Scheme 5.3)[8] is usually used to synthesize *meso*-unsubstituted symmetrical BODIPYs. It involves the condensation between two identical α-formylpyrroles (**13**) catalyzed by $POCl_3$ to produce the corresponding dipyrromethenes (**14**), followed by boron complexation to afford desired BODIPYs (**15**). One advantage of this method is that it can afford higher yields in comparison with the first method.

A new synthetic method (Method 4, Scheme 5.4), using dipyrro (thio) ketone, to synthesize symmetrical or unsymmetrical BODIPYs, has been developed and investigated in recent years.[9-15] The dipyrrothioketone precursors can be obtained from the condensation between α-free pyrroles (**16**) and thiophosgene ($CSCl_2$), further treated with CH_3I, organic base, and $BF_3 \cdot OEt_2$ to obtain *meso*-thioester BODIPYs (**18**), or treated with KOH/H_2O_2 to yield dipyrroketones (**19**).[9] Alternatively, dipyrroketones (**19)** can also be synthesized using $Pb(OAc)_4/PbO_2$ oxidation of dipyrromethanes, which can be prepared by condensation of readily available 2-methyl pyrroles (**21**) in the presence of bromine, followed by DDQ oxidation.[11] Another alternative way to synthesize both symmetrical (**19)** or unsymmetrical dipyrroketones (**25**) is via a reaction between α-(*N*,*N*-dimethyl-amido) pyrroles (**24**) in the presence of $POCl_3$, followed by hydrolysis with aqueous sodium acetate.[13-15] Oxidative halogenation using POX_3 (X = Cl or Br) or phosgene ($COCl_2$) of the dipyrroketones (**19** and **25**), followed by deprotonation with base and complexation with $BF_3 \cdot OEt_2$ yields the corresponding symmetrical (**20**, **23**) or unsymmetrical (**26**) *meso*-halo-BODIPYs.

Scheme 5.1. The first synthetic method of symmetric BODIPYs.

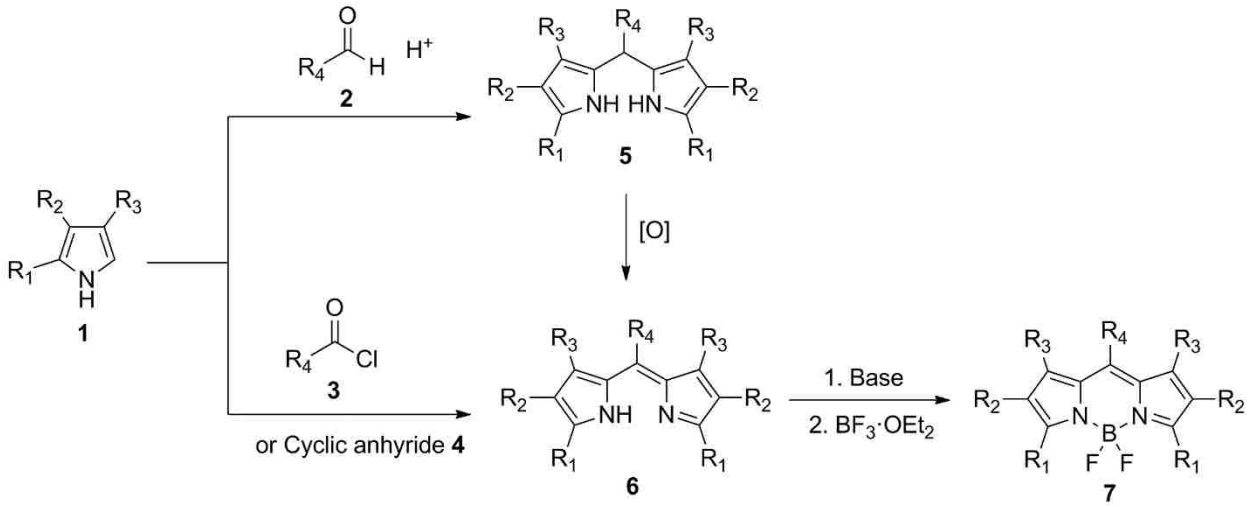

Scheme 5.2. The second synthetic method of symmetrical or unsymmetrical BODIPYs.

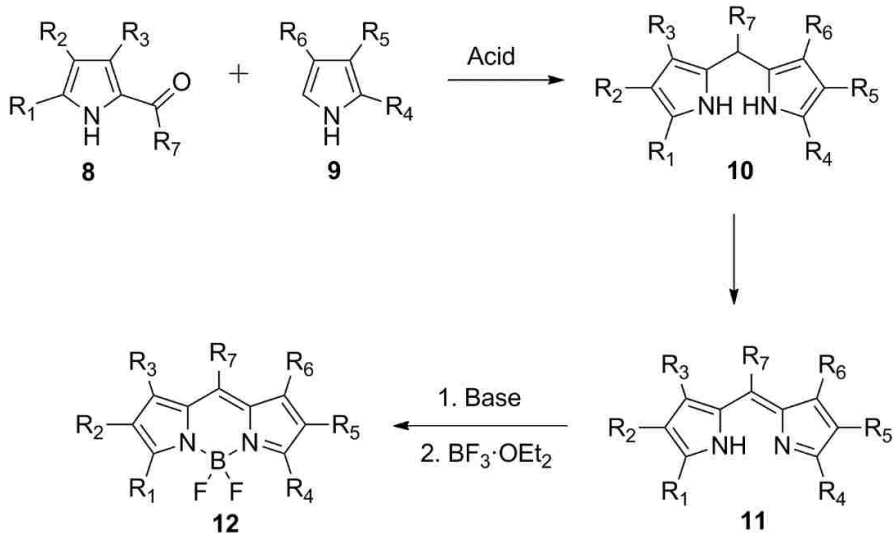

Scheme 5.3. The third synthetic method of symmetrical BODIPYs with meso position unsubstituted.

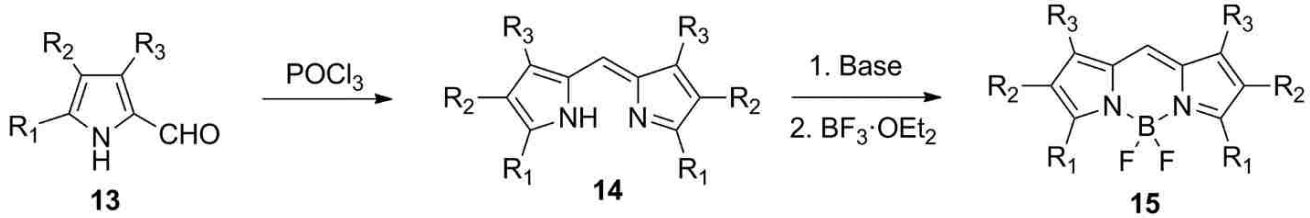

Scheme 5.4. The fourth synthetic method of symmetrical and unsymmetrical BODIPYs.

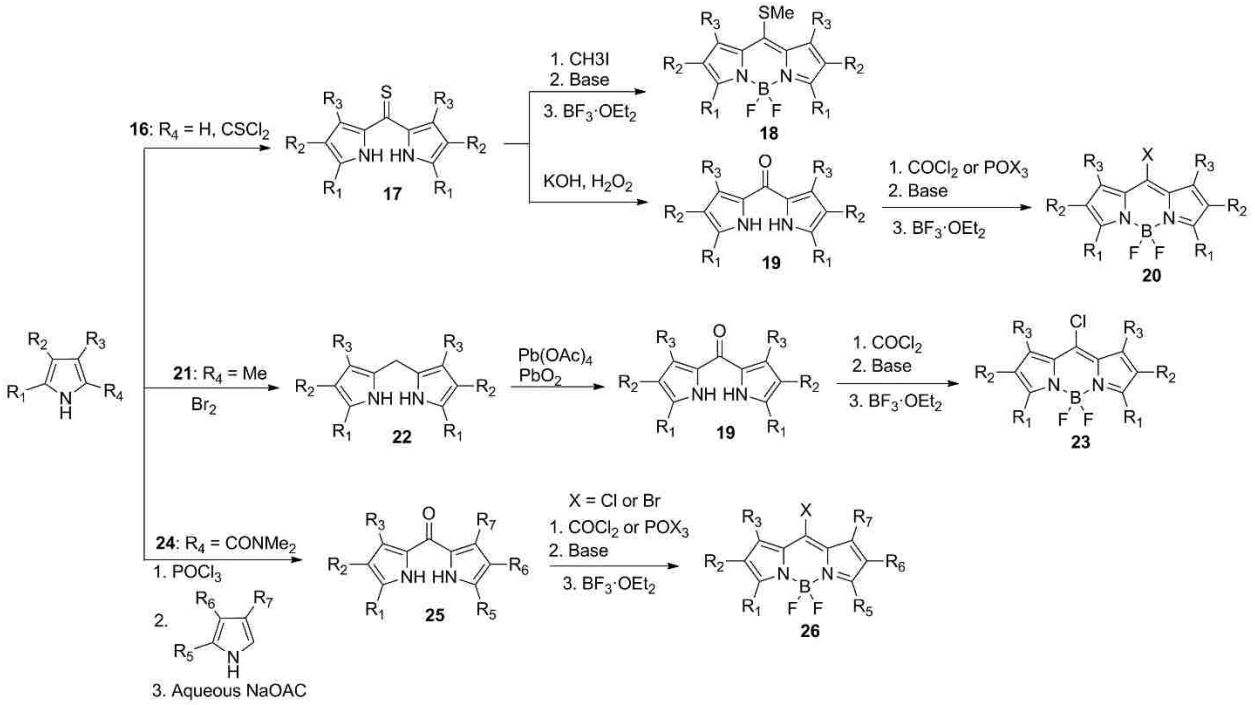

5.1.2 Functionalization of BODIPYs

To synthesize versatile BODIPYs for different applications, different methodologies have been developed to introduce various functional substituents to the BODIPY skeleton. The convention method, the so-called pre-functionalization, is to develop various pyrrole precursors for the synthesis of BODIPYs as shown in Scheme 5.1-5.4. For example, five- or six-member ring cyclic anhydride can be used as the carbonyl source in Method 1 to introduce carboxylic acids at the *meso* position of BODIPYs.[6] The carboxylic acid group can be activated with *N*-hydroxysuccinimide (NHS) and *N*,*N*′-dicyclohexylcarbodiimide (DCC) for further conjugation with peptides or proteins.

Scheme 5.5. Resonance structures of BODIPY.

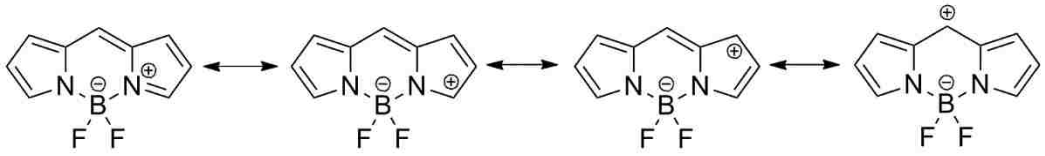

As outlined in Scheme 5.5, the BODIPY skeleton have different resonance structures with carbons 1, 3, 5, 7 and 8 bearing more positive charge character, therefore is more electrophilic than carbons 2 and 6. Post-functionalization of BODIPYs can be realized by taking advantage of the different electrophilicity at different carbon positions to introduce different functional groups to BODIPYs.[14]

Halogenated BODIPYs have emerged as a versatile platform for the post-functionalization of BODIPYs to introduce a variety of functionalities to the BODIPY core by both metal-catalyzed cross-coupling (*e.g.*, Suzuki, Stille, Heck, and Sonogashira)[16-17] and nucleophilic substitution reactions[18-20].

Halogenated BODIPYs can be prepared from halogenated precursor including halogenated pyrroles, dipyrromethanes and dipyrroketones, as shown in Scheme 5.4. Another alternative strategy to synthesize halogenated BODIPYs is to employ direct electrophilic substitution reactions at different positions of BODIPYs. As shown in Scheme 5.6. mono-, di-, tetra, hexabromo-BODIPYs were synthesized via regioselective electrophilic bromination of pyrrolic-unsubstituted BODIPYs using bromine.[21] The step-wise bromination first took place at 2,6-, then at 3,5-, and eventually at 1,7-positions, as confirmed by NMR and X-ray analysis. These polybrominated BODIPYs showed regioselectivity towards the nucleophilic aromatic substitution (S_NAr) reaction and exhibited a decreasing reactivity order as followed: 3,5-bromo > 1,7-bromo > 2,6-bromo. On the other hand, tetrabromo BODIPY exhibited a high reactivity towards Suzuki coupling reactions, while the regioselectivity of different bromo groups was not investigated.

Scheme 5.6. Bromination of BODIPY.

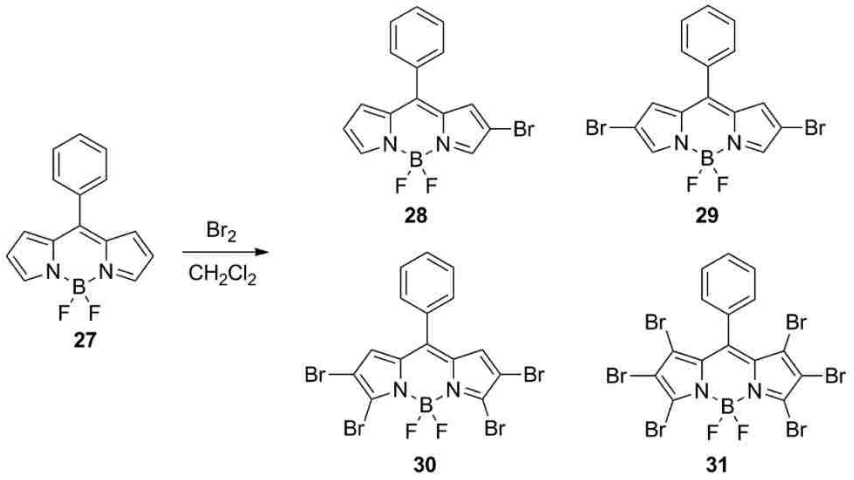

To increase the regioselectivity of the post-functionalization of halogenated BODIPYs, a pentachloro-BODIPY synthesized from *meso*-chloro-BODIPY (**32**) using TCCA/AcOH was reported recently (Scheme 5.7A).[14] The regioselective chlorination reaction produced di-, tri-, tetra-, and pentachloro-BODIPYs in moderate to good yields. In this work, the pentachloro-BODIPY **36** was shown to undergo regioselective Pd (0)-catalyzed Suzuki and Stille cross-coupling reactions, first at the 8-position, followed by the 3,5- and then the 2,6-positions. The similar reactivity trend was also observed for the nuceophilic substitution reactions. To illustrate the versatility of BODIPY **36**, multifunctionalization was performed on this BODIPY. 4-Methoxylphenyl group was selectively introduced at the 8-position via a Suzuki coupling reaction, followed by a Stille coupling reaction to introduce the phenylethynyl groups at the 3,5-positions. The second Stille coupling reaction catalyzed by $Pd(PCy_3)G2$ introduced the thienyl group at the 2,6-positions to provide penta-coupled BODIPY **37** that absorbs and emits in the NIR region, as shown in Scheme 5.7B.

Scheme 5.7. Chlorination of meso-Cl-BODIPY (A) and multifunctionalization of penta-Cl-BODIPY (B)

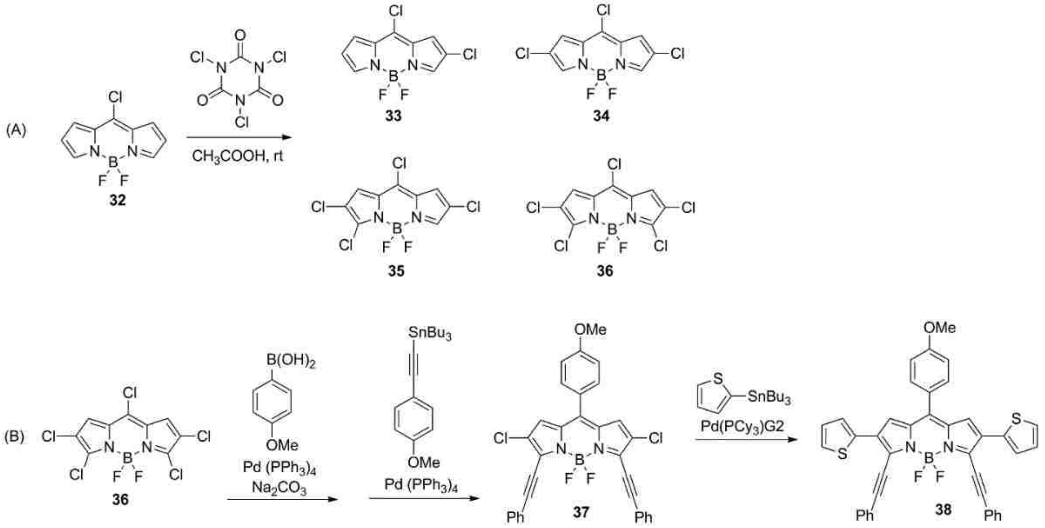

Extending the above work, three-perhalogenated BODIPYs (**40-1**, **40-2**, **40-3**), bearing chloro and bromo groups at all carbon positions of the BODIPYs were synthesized recently from the corresponding chloro-BODIPYs (**39-1**, **39-2**, **39-3**) using bromine (Scheme 5.8). The regioselectivity of the BODIPY **40-3** was investigated at all carbon positions by using Stille cross-coupling reactions and boron substitution reactions.[15] The reactivity order of the halogens under these conditions is: 8-Cl ≈ 1,7-Br > 3,5-Cl > 2,6-Cl > 4,4'-F. It was also the first time to report the nona-functionalized BODIPYs.

Scheme 5.8. Synthesis of perhalogenated BODIPYs.

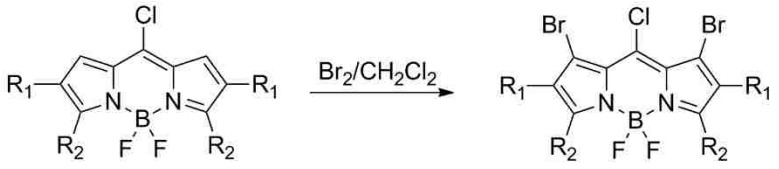

39-1: $R_1 = R_2 = H$
39-2: $R_1 = Cl$, $R_2 = H$
39-3: $R_1 = R_2 = Cl$

40-1: $R_1 = R_2 = Br$
40-2: $R_1 = Cl$, $R_2 = Br$
40-3: $R_1 = R_2 = Cl$

5.1.3 Application of BODIPYs

BODIPYs, featuring strong UV-vis absorbance and sharp fluorescence with high quantum yields, are relatively stable in the physiological environment, and also have high photostability. Moreover, the functionalizability of the halogen-BODIPYs in section 5.1.2 render them high tunability to approach various BODIPYs for different applications. Therefore, BODIPYs have shown growing interest in various applications such as biological imaging, biological labeling, drug delivery, and sensing.[1, 22-24] For example, the 2,6-diiodo BODIPYs, were shown to be efficient photodynamic (PDT) sensitizers due to the enhanced quantum yield of singlet oxygen induced by the heavy atom effect.[25] Also, a variety of fluorescent probes for Pd^{2+},[26] and Cu^{2+},[27] could be prepared by substitution reactions between dihalo-BODIPYs and nuleophiles (*e.g.*, azacrown) in high yields.

5.2 Introduction to BNCT

5.2.1 Mechanisms of BNCT

BNCT is a promising binary anticancer therapy that selectively targets and destroys malignant tumor cells, while spare the damage to healthy normal cells.[28-32] BNCT involves the irradiation of non-radioactive ^{10}B-containing tumors with low-energy thermal or epithermal neutrons, produces excited ^{11}B nuclei which spontaneously fission to give cytotoxic high linear energy transfer (high-LET) α and recoiling ^{7}Li particles, along with γ radiation, and approximately 2.4 MeV of kinetic energy (Figure 5.2). Low-energy epithermal neutrons are able to penetrate 8 cm into tissues to reach deep-located tumors. The generated high-LET particles have short path lengths of 5-9 μM in tissue (about the diameter of a single cell), restricting the damage to ^{10}B-containing tumor cells. The biologically abundant nuclei ^{12}C (0.0034 barn), ^{1}H (0.33 barn), and

^{14}N (1.8 barn) show negligible interference with the ^{10}B (n,α)^{7}Li neutron capture reaction due to their much smaller nuclear cross sections in comparison with ^{10}B.

$$^{10}_{5}B + {}^{1}n \longrightarrow {}^{11}_{5}B \longrightarrow {}^{7}Li^{3+} + {}^{4}He^{2+} + \gamma + 2.4\ MeV$$

Figure 5.2. The $^{10}B(n, \alpha)^{7}Li$ neutron capture and fission reactions

BNCT has been used clinically for several decades in the treatment of various types of tumors including head and neck cancers, primary and metastatic melanomas, and high-grade brain tumors (*e.g.*, glioblastoma multiforme, GBM).[31, 33-34]

5.2.2 General criteria for BNCT agents

Generally, an effective boron delivery drug for BNCT should display the following characteristics:[28-32] 1) deliver therapeutic amounts of ^{10}B to tumor, estimated to be at least 20 μg/g tumor or approximately 10^{9} atoms/cell), 2) high tumor-to-normal tissue and tumor-to-blood concentration ratios (> 5), 3) low systemic toxicity, 4) rapid clearance from blood and normal tissues while persisting in tumor during the irradiation treatment, and 5) easy quantification of tissue-localized boron. In addition, for brain tumor treatment, the BNCT drugs should be able to permeate across the blood-brain barrier (BBB), either by passive transmembrane diffusion or through targeting of transporters and receptors that are expressed at the BBB.[35] The passive diffusion of compounds across cellular membranes and the BBB depends on various factors, including the compound's lipophilicity, molecular weight, electrical charge, degree of ionization, hydrogen bonding ability, and intermolecular interactions.[35-37] In general, low molecular weight (< 500 Da) boron delivery agents with favorable lipophilicity (octanol−water partition coefficient, log P <5) show enhanced passive diffusion across cellular membranes and the BBB.[36-39] However, a major challenge in drug development for BNCT has been the selective delivery of therapeutic amounts of boron to tumor cells, with minimal toxicity to normal tissues. Another challenge in the

treatment of brain tumors is the often inefficient BBB permeability of the BNCT drugs. Over the last few decades, thousands of boron carriers for BNCT have been designed and synthesized, but only a few have been tested in pre-clinical trials. Among these, many are able to deliver higher amount of boron to tumors relative to the surrounding normal tissue, due to the so-called "enhanced permeability and retention (EPR) effect". However, the selectivity of boron accumulation is often low, which can cause undesired toxic effects to healthy tissues. In order to improve the tumor selectivity of BNCT agents, their encapsulation into delivery agents, such as liposomes, and/or association with tumor-targeting moieties (*e.g*. peptides, folic acid, antibodies) has been explored. In addition, several administration methodologies and combination therapies have also been investigated. One very promising methodology that bypasses the BBB and enhances boron tumor uptake is convection-enhanced delivery (CED), a method for local drug infusion directly into brain. CED bypasses the BBB and is able to delivery high amounts of boron (>100 μg/g tumor) to intracerebral tumors, with very high tumor-to-blood and tumor-to-normal brain ratios.[32, 40] More recently, another tumor treatment strategy designated magnetic drug targeting (MDT) has also been introduced.[41] MDT uses an external magnetic field to direct boron-containing magnetic nanoparticles, administrated intraarterially, to tumor tissues. The MTD strategy is independent from molecular and biological recognition or passive accumulation, and allows selective accumulation of the drug.

5.2.3 Main categories of BNCT agents

The two clinically used boron-containing drugs are the sodium salt of sulfhydryl boron hydride $Na_2B_{12}H_{11}SH$ (BSH) and the amino acid (*L*)-4-dihydroxyborylphenylalanine (BPA) (Figure 5.3, 41-42).[31, 33-34, 42-45] Although BSH and BPA show low toxicity and have recorded efficacy in clinical BNCT trials, they have only low selectivity for tumors, and low retention

times.[32, 45-46] Other promising classes of boronated compounds, including boronated amino acids, peptides, monoclonal antibodies (MAb), nucleosides, lipids, carbohydrates, liposomes, porphyrin derivatives, BODIPYs, and nanoparticles, have been synthesized and investigated as potential BNCT agents.[30, 32, 40, 47] The preferred boron sources in these compounds are the neutral isomeric carboranes *ortho*-, *meta*-, and *para*-$C_2B_{10}H_{12}$, negatively charged *closo*-$B_{12}H_{12}^{2-}$, *closo*-$CB_{11}H_{12}^{-}$, the open cage *nido*-$C_2B_9H_{12}^{-}$, and metallo-bis(dicarbollides) such as $[3,3'\text{-}Co(1,2\text{-}\ C_2B_9H_{11})_2]^{-}$ (Figure 5.3, 43-49) as a result of their remarkable properties that include: 1) high boron content, 2) amphiphilicity, 3) high photochemical, kinetic, and hydrolytic stabilities, and 4) ease of functionalization and attachment to targeting molecules.[40, 48] Several reviews have been published on compound development for BNCT.[29-30, 32, 40, 47-57] Among the different classes of boron delivery agents, nucleosides, amino acids, porphyrin derivatives and tumor-targeted compounds that recognize a tumor-associated epitope, are amongst the most promising BNCT agents due to their generally lower toxicity and increased tumor specificity and uptake. Porphyrin derivatives and boron dipyrromethenes (BODIPYs) have attracted considerable interest as potential BNCT drugs due to their fluorescent characteristic which facilitate the quantification of tissue-localized boron.

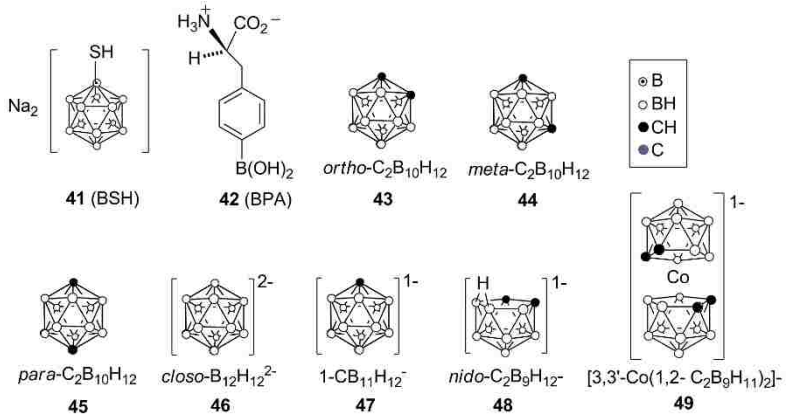

Figure 5.3. Structures of BSH, BPA and common boron clusters currently used in BNCT drug development.

Taking advantage of the synthetic development of BODIPYs and the attractive properties of BODIPYs including strong absorbance and fluorescence with high quantum yields, high stability in physiological environment, and high photostability, as mentioned in section 5.1, a series of carborane-containing BODIPYs were synthesized and their *in vitro* biological studies were investigated. Detailed information was included in Chapter 6. In Chapter 7, a series of push-pull BODIPYs were synthesized and their photophysical and electrochemical properties were compared.

5.3 Reference

1. Lu, H.; Mack, J.; Yang, Y.; Shen, Z. Structural modification strategies for the rational design of red/NIR region BODIPYs. *Chem. Soc. Rev.* **2014,** *43* (13), 4778-4823.

2. Descalzo, A. B.; Xu, H.-J.; Shen, Z.; Rurack, K. Red/Near-infrared Boron–Dipyrromethene Dyes as Strongly Emitting Fluorophores. *Ann. N. Y. Acad. Sci.* **2008,** *1130* (1), 164-171.

3. Treibs, A.; Kreuzer, F.-H. Difluorboryl-Komplexe von Di- und Tripyrrylmethenen. *Justus Liebigs Ann. Chem.* **1968,** *718* (1), 208-223.

4. Lee, C.-H.; S. Lindsey, J. One-flask synthesis of meso-substituted dipyrromethanes and their application in the synthesis of trans-substituted porphyrin building blocks. *Tetrahedron* **1994,** *50* (39), 11427-11440.

5. Ulrich, G.; Ziessel, R. Convenient and Efficient Synthesis of Functionalized Oligopyridine Ligands Bearing Accessory Pyrromethene-BF2 Fluorophores. *J. Org. Chem.* **2004,** *69* (6), 2070-2083.

6. Wang, D.; Fan, J.; Gao, X.; Wang, B.; Sun, S.; Peng, X. Carboxyl BODIPY Dyes from Bicarboxylic Anhydrides: One-Pot Preparation, Spectral Properties, Photostability, and Biolabeling. *J. Org. Chem.* **2009,** *74* (20), 7675-7683.

7. Wood, T. E.; Thompson, A. Advances in the Chemistry of Dipyrrins and Their Complexes. *Chem. Rev.* **2007,** *107* (5), 1831-1861.

8. Wu, L.; Burgess, K. A new synthesis of symmetric boraindacene (BODIPY) dyes. *Chem. Commun.* **2008,** (40), 4933-4935.

9. Goud, T. V.; Tutar, A.; Biellmann, J.-F. Synthesis of 8-heteroatom-substituted 4,4-difluoro-4-bora-3a,4a-diaza-s-indacene dyes (BODIPY). *Tetrahedron* **2006,** *62* (21), 5084-5091.

10. Leen, V.; Yuan, P.; Wang, L.; Boens, N.; Dehaen, W. Synthesis of Meso-Halogenated BODIPYs and Access to Meso-Substituted Analogues. *Org. Lett.* **2012,** *14* (24), 6150-6153.

11. Wang, H.; Fronczek, F. R.; Vicente, M. G. H.; Smith, K. M. Functionalization of 3,5,8-Trichlorinated BODIPY Dyes. *J. Org. Chem.* **2014,** *79* (21), 10342-10352.

12. Wang, H.; Vicente, M. G. H.; Fronczek, F. R.; Smith, K. M. Synthesis and Transformations of 5-Chloro-2,2′ -Dipyrrins and Their Boron Complexes, 8-Chloro-BODIPYs. *Chem. Eur. J.* **2014,** *20* (17), 5064-5074.

13. Zhao, N.; Vicente, M. G. H.; Fronczek, F. R.; Smith, K. M. Synthesis of 3,8-Dichloro-6-ethyl-1,2,5,7-tetramethyl–BODIPY from an Asymmetric Dipyrroketone and Reactivity Studies at the 3,5,8-Positions. *Chem. Eur. J.* **2015,** *21* (16), 6181-6192.

14. Zhao, N.; Xuan, S.; Fronczek, F. R.; Smith, K. M.; Vicente, M. G. H. Stepwise Polychlorination of 8-Chloro-BODIPY and Regioselective Functionalization of 2,3,5,6,8-Pentachloro-BODIPY. *J. Org. Chem.* **2015,** *80* (16), 8377-8383.

15. Zhao, N.; Xuan, S.; Byrd, B.; Fronczek, F. R.; Smith, K. M.; Vicente, M. G. H. Synthesis and regioselective functionalization of perhalogenated BODIPYs. *Org. Biomol. Chem.* **2016,** *14* (26), 6184-6188.

16. Rohand, T.; Qin, W.; Boens, N.; Dehaen, W. Palladium-Catalyzed Coupling Reactions for the Functionalization of BODIPY Dyes with Fluorescence Spanning the Visible Spectrum. *Eur. J. Org. Chem.* **2006,** *2006* (20), 4658-4663.

17. Leen, V.; Braeken, E.; Luckermans, K.; Jackers, C.; Van der Auweraer, M.; Boens, N.; Dehaen, W. A versatile, modular synthesis of monofunctionalized BODIPY dyes. *Chem. Commun.* **2009,** (30), 4515-4517.

18. Rohand, T.; Baruah, M.; Qin, W.; Boens, N.; Dehaen, W. Functionalisation of fluorescent BODIPY dyes by nucleophilic substitution. *Chem. Commun.* **2006,** (3), 266-268.

19. Li, L.; Nguyen, B.; Burgess, K. Functionalization of the 4,4-difluoro-4-bora-3a,4a-diaza-s-indacene (BODIPY) core. *Biorg. Med. Chem. Lett.* **2008,** *18* (10), 3112-3116.

20. Leen, V.; Leemans, T.; Boens, N.; Dehaen, W. 2- and 3-Monohalogenated BODIPY Dyes and Their Functionalized Analogues: Synthesis and Spectroscopy. *Eur. J. Org. Chem.* **2011,** *2011* (23), 4386-4396.

21. Jiao, L.; Pang, W.; Zhou, J.; Wei, Y.; Mu, X.; Bai, G.; Hao, E. Regioselective Stepwise Bromination of Boron Dipyrromethene (BODIPY) Dyes. *J. Org. Chem.* **2011,** *76* (24), 9988-9996.

22. Kowada, T.; Maeda, H.; Kikuchi, K. BODIPY-based probes for the fluorescence imaging of biomolecules in living cells. *Chem. Soc. Rev.* **2015,** *44* (14), 4953-4972.

23. Yuan, L.; Lin, W.; Zheng, K.; He, L.; Huang, W. Far-red to near infrared analyte-responsive fluorescent probes based on organic fluorophore platforms for fluorescence imaging. *Chem. Soc. Rev.* **2013,** *42* (2), 622-661.

24. Boens, N.; Leen, V.; Dehaen, W. Fluorescent indicators based on BODIPY. *Chem. Soc. Rev.* **2012,** *41* (3), 1130-1172.

25. Yogo, T.; Urano, Y.; Ishitsuka, Y.; Maniwa, F.; Nagano, T. Highly Efficient and Photostable Photosensitizer Based on BODIPY Chromophore. *J. Am. Chem. Soc.* **2005,** *127* (35), 12162-12163.

26. Móczár, I.; Huszthy, P.; Maidics, Z.; Kádár, M.; Klára, T. Synthesis and optical characterization of novel enantiopure BODIPY linked azacrown ethers as potential fluorescent chemosensors. *Tetrahedron* **2009,** *65* (39), 8250-8258.

27. Yang, C.; Gong, D.; Wang, X.; Iqbal, A.; Deng, M.; Guo, Y.; Tang, X.; Liu, W.; Qin, W. A new highly copper-selective fluorescence enhancement chemosensor based on BODIPY excitable with visible light and its imaging in living cells. *Sensors Actuators B: Chem.* **2016,** *224*, 110-117.

28. Hawthorne, M. F. The Role of Chemistry in the Development of Boron Neutron Capture Therapy of Cancer. *Angew. Chem. Int. Ed.* **1993,** *32* (7), 950-984.

29. Soloway, A. H.; Tjarks, W.; Barnum, B. A.; Rong, F.-G.; Barth, R. F.; Codogni, I. M.; Wilson, J. G. The Chemistry of Neutron Capture Therapy. *Chem. Rev.* **1998,** *98* (4), 1515-1562.

30. Barth, R. F.; Coderre, J. A.; Vicente, M. G. H.; Blue, T. E. Boron Neutron Capture Therapy of Cancer: Current Status and Future Prospects. *Clin. Cancer. Res.* **2005,** *11* (11), 3987-4002.

31. Barth, R. F.; H Vicente, M.; Harling, O. K.; Kiger, W.; Riley, K. J.; Binns, P. J.; Wagner, F. M.; Suzuki, M.; Aihara, T.; Kato, I.; Kawabata, S. Current status of boron neutron capture therapy of high grade gliomas and recurrent head and neck cancer. *Radiat. Oncol.* **2012,** *7* (1), 1-21.

32. Sibrian-Vazquez, M.; Vicente, M. G. H., Boron tumor-delivery for BNCT: Recent Developments and Perspectives. In *Boron Science: New Technologies & Applications*, Hosmane, Narayan S. ed.; CRC Press: Boca Raton, FL, 2011; pp 203-232.

33. Kankaanranta, L.; Seppälä, T.; Koivunoro, H.; Saarilahti, K.; Atula, T.; Collan, J.; Salli, E.; Kortesniemi, M.; Uusi-Simola, J.; Välimäki, P.; Mäkitie, A.; Seppänen, M.; Minn, H.; Revitzer, H.; Kouri, M.; Kotiluoto, P.; Seren, T.; Auterinen, I.; Savolainen, S.; Joensuu, H. Boron Neutron Capture Therapy in the Treatment of Locally Recurred Head-and-Neck Cancer: Final Analysis of a Phase I/II Trial. *Int. J. Radiat. Oncol. Biol. Phys.* **2012,** *82* (1), e67-e75.

34. Hopewell, J. W.; Gorlia, T.; Pellettieri, L.; Giusti, V.; H-Stenstam, B.; Sköld, K. Boron neutron capture therapy for newly diagnosed glioblastoma multiforme: An assessment of clinical potential. *Appl. Radiat. Isot.* **2011,** *69* (12), 1737-1740.

35. Banks, W. A. Characteristics of compounds that cross the blood-brain barrier. *BMC Neurol.* **2009,** *9* (Suppl 1), S3-S3.

36. Habgood, M. D.; Begley, D. J.; Abbott, N. J. Determinants of Passive Drug Entry into the Central Nervous System. *Cell. Mol. Neurobiol.* **2000,** *20* (2), 231-253.

37. Vries, H. E. d.; Kuiper, J.; Boer, A. G. d.; Berkel, T. J. C. V.; Breimer, D. D. The Blood-Brain Barrier in Neuroinflammatory Diseases. *Pharmacol. Rev.* **1997,** *49* (2), 143-156.

38. Pardridge, W. The blood-brain barrier: Bottleneck in brain drug development. *NeuroRx* **2005,** *2* (1), 3-14.

39. Palmer, A. M.; Alavijeh, M. S. Translational CNS medicines research. *Drug Discov. Today* **2012,** *17* (19–20), 1068-1078.

40. Bhupathiraju, N. V. S. D. K.; Vicente, M. G. H., Synthesis of Carborane-Containing Porphyrin Derivatives for the Boron Neutron Capture Therapy of Tumors. In *Applications of Porphyrinoids*; Paolesse, R., Ed. Springer Berlin Heidelberg: Berlin, Heidelberg, 2014; pp. 31-52.

41. Tietze, R.; Unterweger, H.; Dürr, S.; Lyer, S.; Canella, L.; Kudejova, P.; Wagner, F. M.; Petry, W.; Taccardi, N.; Alexiou, C. Boron containing magnetic nanoparticles for neutron capture therapy – an innovative approach for specifically targeting tumors. *Appl. Radiat. Isot.* **2015,** *106*, 151-155.

42. Kawabata, S.; Miyatake, S.-I.; Hiramatsu, R.; Hirota, Y.; Miyata, S.; Takekita, Y.; Kuroiwa, T.; Kirihata, M.; Sakurai, Y.; Maruhashi, A.; Ono, K. Phase II clinical study of boron neutron capture therapy combined with X-ray radiotherapy/temozolomide in patients with newly diagnosed glioblastoma multiforme—Study design and current status report. *Appl. Radiat. Isot.* **2011,** *69* (12), 1796-1799.

43. Kankaanranta, L.; Seppälä, T.; Koivunoro, H.; Välimäki, P.; Beule, A.; Collan, J.; Kortesniemi, M.; Uusi-Simola, J.; Kotiluoto, P.; Auterinen, I.; Serèn, T.; Paetau, A.; Saarilahti, K.; Savolainen, S.; Joensuu, H. l-Boronophenylalanine-Mediated Boron Neutron Capture Therapy for Malignant Glioma Progressing After External Beam Radiation Therapy: A Phase I Study. *Int. J. Radiat. Oncol. Biol. Phys.* **2011,** *80* (2), 369-376.

44. Yamamoto, T.; Nakai, K.; Nariai, T.; Kumada, H.; Okumura, T.; Mizumoto, M.; Tsuboi, K.; Zaboronok, A.; Ishikawa, E.; Aiyama, H.; Endo, K.; Takada, T.; Yoshida, F.; Shibata, Y.; Matsumura, A. The status of Tsukuba BNCT trial: BPA-based boron neutron capture therapy combined with X-ray irradiation. *Appl. Radiat. Isot.* **2011,** *69* (12), 1817-1818.

45. Barth, R. F.; Joensuu, H. Boron neutron capture therapy for the treatment of glioblastomas and extracranial tumours: As effective, more effective or less effective than photon irradiation? *Radiother. Oncol.* **2007,** *82* (2), 119-122.

46. Ichikawa, H.; Taniguchi, E.; Fujimoto, T.; Fukumori, Y. Biodistribution of BPA and BSH after single, repeated and simultaneous administrations for neutron-capture therapy of cancer. *Appl. Radiat. Isot.* **2009,** *67* (7–8, Supplement), S111-S114.

47. Luderer, M. J.; de la Puente, P.; Azab, A. K. Advancements in Tumor Targeting Strategies for Boron Neutron Capture Therapy. *Pharm. Res.* **2015,** *32* (9), 2824-2836.

48. Vicente, M. G. H.; Sibrian-Vazquez, M., Syntheses of Boronated Porphyrins and Their Application in BNCT. In *Handbook of Porphyrin Science: with Applications to Chemistry, Physics, Materials Science, Engineering, Biology and Medicine*, Kadish, K. M.; Smith, K. M.; Guilard, R., Eds. World Scientific: Singapore, 2010; Vol. 4, pp 191-248.

49. Bregadze, V.; Semioshkin, A.; Sivaev, I. Synthesis of conjugates of polyhedral boron compounds with tumor-seeking molecules for neutron capture therapy. *Appl. Radiat. Isot.* **2011,** *69* (12), 1774-1777.

50. Sivaev, I. B.; Bregadze, V. V. Polyhedral Boranes for Medical Applications: Current Status and Perspectives. *Eur. J. Inorg. Chem.* **2009,** *2009* (11), 1433-1450.

51. Hosmane, N. S.; Maguire, J. A.; Zhu, Y.; Takagaki, M., Major Neutron Capture Therapy (NCT) Drug Prototypes. In *Boron and Gadolinium Neutron Capture Therapy for Cancer Treatment*, World Scientific: 2012; pp 41-98. Doi:10.1142/9789814338684_0004.

52. Ban, H. S.; Nakamura, H. Boron-Based Drug Design. *The Chemical Record* **2015,** *15* (3), 616-635.

53. Yinghuai, Z.; Cheng Yan, K.; Maguire, J. A.; Hosmane, N. S. Recent Developments in Boron Neutron Capture Therapy (BNCT) Driven by Nanotechnology. *Curr. Chem. Biol.* **2007,** *1* (2), 141-149.

54. Wang, J.; Wu, W.; Jiang, X. Nanoscaled boron-containing delivery systems and therapeutic agents for cancer treatment. *Nanomedicine* **2015,** *10* (7), 1149-1163.

55. Sumitani, S.; Nagasaki, Y. Boron neutron capture therapy assisted by boron-conjugated nanoparticles. *Polym. J.* **2012,** *44* (6), 522-530.

56. Yinghuai, Z.; Yan, K. C.; Maguire, J. A.; Hosmane, N. S., Boron-Based Hybrid Nanostructures: Novel Applications of Modern Materials. In *Hybrid Nanomaterials*, John Wiley & Sons, Inc.: 2011; pp 181-198. 10.1002/9781118003497.ch6.

57. Nakamura, H., Liposomal Boron Delivery for Neutron Capture Therapy. In *Methods Enzymol.*, Abelson, J. S., Melvin ; Verdine, Gregory; Pyle, Anna, Ed. Academic Press: 2009; Vol. 465, pp 179-208.

CHAPTER 6 : SYNTHESIS AND IN VITRO STUDIES OF A SERIES OF CARBORANE-CONTAINING BORON DIPYRROMETHENES (BODIPY)

6.1 Introduction

Boron neutron capture therapy (BNCT), which can selectively target and destroy malignant cells in the presence of healthy normal cells, is a very promising binary anticancer methodology especially for the treatment of brain tumors[1-3] BNCT involves the irradiation of nonradioactive ^{10}B-containing tumors with low-energy thermal neutrons, causing the excitation of ^{10}B to ^{11}B, which rapidly produces cytotoxic high linear energy transfer (high-LET) α and ^{7}Li particles, γ radiation, and about 2.4 MeV of kinetic energy through a nuclear fission reaction. The generated high-LET particles have short path lengths about the diameter of a single cell (< 10 μm), therefore restricting the damage to ^{10}B-containing tumor cells. In addition, there is little interference with the ^{10}B (n,α)^{7}Li capture reaction due to the very small nuclear cross sections of biologically abundant nuclei including ^{12}C, ^{1}H, and ^{14}N. Another advantage of BNCT is that thermal and epithermal neutrons are able to penetrate deep into tissues to reach deep-seated tumors. However, a relatively high boron tumor concentration of at least 20 μg ^{10}B/g tumor or approximately 10^{9} atoms/cell is required for effective BNCT treatment, and this has driven recent research in the areas of boron drug development and delivery methodologies for BNCT.

BNCT has been used clinically for several decades in the treatment of high-grade brain tumors, such as glioblastoma multiforme (GBM), and other difficult-to-treat malignancies, including primary and metastatic melanomas and recurrent head and neck cancers.[3-5] One major challenge in the BNCT modality for brain tumors is the existence of the blood−brain barrier (BBB)

* Chapter 6 previously appeared as Xuan, S.; Zhao, N.; Zhou, Z.; Fronczek, F. R.; Vicente, M. G. H. Synthesis and in Vitro Studies of a Series of Carborane-Containing Boron Dipyrromethenes (BODIPYs). *J. Med. Chem.* **2016**, *59*, 2109-2117. It is reprinted by permission of ACS Publisher (see page 261).

that prevents most drugs from penetrating into the brain and from reaching the targeted tumor cells.[6-11] In the brain tumor treatment, the prerequisite is that the boron drug should permeate across the BBB, ether by passive transmembrane diffusion or through active transportation of targeting transporters and receptors that are expressed at the BBB.[12] The passive diffusion of boron drugs across the BBB are strongly dependent on the physicochemical properties of the drugs, including their lipophilic character, molecular weight (MW), size, polar surface area, charge, and extent of ionization.[13-15] Among these, the two main characteristics in a small molecule that favor its crossing of cellular membrane and BBB by passive diffusion are (1) molecular weight under 500 Da and (2) high lipophilic character, usually measured by the octanol−water partition coefficient, log P <5.[6, 13-15] Although significant hydrophobicity is important for enhanced permeability across the BBB, BNCT drugs also need to be soluble in aqueous media to enable their systemic administration.[2] Therefore, there is continued need to develop amphiphilic boron drugs with appropriate hydrophilic and lipophilic balance (HLB) and low molecular weight of <500 Da for efficient BBB permeability and tumor cell uptake.

The two boron drugs that have been extensively used in BNCT clinical trials are the sodium salt of the sulfhydryl boron hydride $Na_2B_{12}H_{11}SH$ (BSH) and L-4- dihydroxyborylphenylalanine (BPA).[3-5] Although BSH and BPA have demonstrated efficacy in BNCT clinical trials, they have low selectivity, low tumor retention time and limited BBB permeability,[10, 16] which limit their use in brain tumor treatment. Other boronated compounds have been investigated as potential BNCT drugs, including amino acids, peptides, carbohydrates, nucleosides, liposomes, porphyrins, monoclonal antibodies (mAbs), and nanoparticles.[2-3, 7] the Among these, particularly promising are mAbs due to their very high specificity for a tumor-associated epitope, and porphyrin derivatives due to their ability to transport large amounts of boron within cells. However, these

BNCT agents have limited BBB crossing ability, mainly due to their large size, high molecular weight, and hydrophobicity.[2, 16]

Recently, we have reported the investigation on the BBB crossing ability of a series of carboranylporphyrins conjugated to polyamines, glucose, arginine, and an opioid peptide,[17] but they all exhibited low permeabilities ($Pe < 3.3 \times 10^{-6}$ cm/s) across hCMEC/D3 cell monolayers as the BBB model. In contrast, amphiphilic boron dipyrromethene (BODIPY), referred to as "semi-porphyrins", of low molecular weight displayed enhanced BBB permeability and promise as boron delivery drugs for BNCT.[18] BODIPY dyes have attracted special interest in recent years due to their various applications in biological labeling, drug delivery, imaging, sensing, and theranostics.[19-22] As mentioned in Chapter 5, BODIPYs are strongly UV−vis absorbing and generally emit sharp fluorescence with high quantum yields, which can facilitate detection and quantification of tissue-localized boron in BNCT. BODIPYs have also shown negligible sensitivity toward solvent polarity and solution pH, high permeability across cellular membranes, and relatively high stability under physiological conditions.

BODIPYs functionalized with carborane clusters have been prepared using Suzuki[18] and Sonogashira[23] cross-coupling reactions of the corresponding 2,6-diiodo-substituted BODIPYs. Alternatively, carboranes can be introduced onto the BODIPY at the 3(5)- and/or 8-positions through substitution reactions of the corresponding chlorinated derivatives.[18, 24-25] Herein we report the synthesis of a series of seven carboranyl-BODIPYs from the corresponding chloro-BODIPY derivatives, with molecular weights in the range 366−527 Da and log P in the range 1.5−2.7. The cytotoxicity and uptake of the BODIPYs in human glioma T98G cells, as well as their permeability across the BBB using hCMEC/D3 cells, were investigated and compared.

6.2 Experimental

6.2.1 General considerations

All the chemicals and reagents were purchased from Sigma-Aldrich and Fisher Scientific and used as received. 1-Mercapto-1,2-carborane was purchased from Katchem. Reactions were monitored by analytical thin-layer chromatography (TLC) performed on precoated plates (polyester-back, 60 Å, 0.2 mm, Sorbent Technologies). Purifications were conducted by column chromatography on silica gel (230−400 mesh, 60 Å, Sorbent Technologies) or preparative TLC plates (f254, VWR). ^{1}H and ^{13}C {^{1}H} NMR spectra were obtained using a Bruker AV-400 NanoBay (400 MHz for ^{1}H NMR and 100 MHz for ^{13}C NMR) and a Bruker AV-500 spectrometer (125 MHz for ^{13}C NMR) at room temperature. ^{11}B NMR was obtained on a Bruker AV-400 III (128 MHz), using $BF_3 \cdot OEt_2$ as reference. Chemical shifts (δ) are given in parts per million (ppm) in $CDCl_3$ (7.27 ppm for 1H NMR, 77.0 ppm for ^{13}C NMR); coupling constants (J) are given in Hz. High resolution mass spectrometry (HRMS) spectra were obtained using a 6210 ESI-TOF mass spectrometer (Agilent Technologies). 4-(1-Methyl-1,2-carborane)-methylphenylboronic acid[26] and BODIPYs 1a,[27] 3a,[24] 3b,[18] 6a,[25]and 7[25] were synthesized as previously reported.

6.2.2 General procedure for synthesis of BODIPYs via nucleophilic substitution reaction

The starting chloro-BODIPY (0.05 mmol) was dissolved in 2 mL of THF. 1-Mercapto-1,2-carborane (0.055 mmol) and K_2CO_3 (0.5 mmol) were added, and the final mixture was stirred at room temperature. TLC was used to monitor the reaction until completion (2−5 h). The crude solid product was filtered and purified by column chromatography or preparative TLC using CH_2Cl_2/hexanes or ethyl acetate/hexanes for elution.

8-(1,2-Carboranyl-1-thio)-BODIPY 1b. 16.1 mg (88%), mp 213-215 °C. ^{1}H NMR ($CDCl_3$, 400 MHz): δ 8.01 (2H, s), 7.36 (2H, s), 6.64 (2H, s), 3.77 (1H, s), 1.8−3.5 (10H, br). ^{13}C

NMR ($CDCl_3$, 100 Hz): δ 148.6, 139.4, 133.3, 132.2, 120.4, 72.2, 65.0. ^{11}B NMR ($CDCl_3$, 128 MHz): δ −0.08 (1B, t, ^1J(B,F) = 27.8 Hz), −12.97 to - −1.57 (10B, m). HRMS (ESI-TOF) m/z calcd for $C_{11}H_{17}B_{11}F_1N_2S$ $[M - F]^+$ 347.2199; found 347.2200.

8-(1,2-Carboranyl-1-thio)-1,3-dimethyl-BODIPY 2b. 18.7 mg (95%). ^1H NMR ($CDCl_3$, 400 MHz): δ 7.71 (1H, s), 7.10 (1H, s), 6.49 (1H, s), 6.29 (1H, s) 3.79 (1H, s), 2.65 (1H, s), 2.55 (1H, s), 1.8-3.5 (10h, br); ^{13}C NMR ($CDCl_3$, 100 Hz): δ 166.9, 148.6, 141.4, 138.3, 137.2, 130.0, 127.0, 126.0, 117.4, 73.3, 65.1, 16.7, 15.7; ^{11}B NMR (CDCl3, 128 MHz): δ 0.14 (1B, t, $^1J_{(B,F)}$= 29.8 Hz), -12.97-(-1.60) (10B, m); HRMS (ESI-TOF) m/z calcd for $C_{13}H_{22}B_{11}F_2N_2S$ $[M+H]^+$ 395.2576; found 395.2566.

BODIPY 5b. 20.9 mg (93%). ^1H NMR ($CDCl_3$, 400 MHz): δ 7.44 (1H, s), 3.70 (2H, s), 2.58 (3H, s), 2.44-2.45 (8H, overlap, m), 2.02 (3H, s), 1.8-3.5 (10h, br), 1.05-1.09 (3H, t, $^3J_{(H,H)}$= 7.4 Hz); ^{13}C NMR ($CDCl_3$, 100 Hz): δ 162.7, 141.5, 141.1, 137.8, 137.2, 134.1, 130.1, 128.4, 74.9, 64.1, 17.3, 14.5, 14.2, 14.0, 13.4, 10.2; ^{11}B NMR (CDCl3, 128 MHz): δ -0.06 (1B, t, $^1J_{(B,F)}$= 30.0 Hz), -11.89-(-1.64) (10B, m); HRMS (ESI-TOF) m/z calcd for $C_{17}H_{30}B_{11}F_2N_2S$ $[M+H]^+$ 451.3204; found 451.3195.

BODIPY 6b. 17.9 mg (74%). ^1H NMR ($CDCl_3$, 400 MHz): δ 3.69 (1H, s), 2.60 (3H, s), 2.44 (8H, overlap, m), 2.00 (3H, s), 1.8-3.5 (10h, br), 1.06-1.10 (3H, t, $^3J_{(H,H)}$= 7.6 Hz); ^{13}C NMR ($CDCl_3$, 125 Hz): δ 163.1, 141.3, 141.2, 137.8, 137.7, 137.6, 132.7, 128.5, 126.4, 74.9, 64.1, 17.3, 14.8, 14.6, 14.1, 13.5, 9.1; ^{11}B NMR ($CDCl_3$, 128 MHz): δ 0.08 (1B, t, $^1J_{(B,F)}$ = 30.0 Hz), -12.94-(-1.45) (10B, m); HRMS (ESI-TOF) m/z calcd for $C_{17}H_{29}B_{11}ClF_2N_2S$ $[M+H]^+$ 485.2818; found 485.2824.

BODIPY 4. BODIPY **1a** (11.3 mg, o.o5 mmol) was dissolved in toluene (4 ml). 1M Na_2CO_3 (aq) (1 ml), $Pd(PPh_3)_4$ (5% mol), and 4-(1-methyl-*ortho*-carborane)methylphenyl boronic

acid (29.2 mg, 0.1 mmol) were added and the final mixture was refluxed overnight. The mixture was poured into water (10 ml) and extracted with dichloromethane (10 ml × 3). The organic layers were collected, washed with H_2O and brine, and dried over anhydrous Na_2SO_4. The solvents were removed by rotary evaporation to give the crude products. The further purification was performed by column chromatography (ethyl acetate/hexanes as the eluent) to provide the titled product (10.6 mg), in 45% yield. ^{1}H NMR ($CDCl_3$, 400 MHz): δ 8.0 (2H, s), 7.56-7.58 (2H, m), 7.37-7.39 (2H, m), 6.92 (2H, s), 6.58 (2H, s), 3.57 (2H, s), 2.22 (3H, s), 1.8-3.5 (10h, br); ^{13}C NMR ($CDCl_3$, 100 Hz): δ 146.4, 144.5, 137.7, 134.9, 133.6, 131.5, 130.7, 130.4, 118.7, 75.0, 40.9, 23.8; ^{11}B NMR ($CDCl_3$, 128 MHz): δ 0.18 (1B, t, $^1J_{(B,F)}$= 28.6 Hz), −10.74- −3.16) (10B, m); HRMS (ESI-TOF) m/z calcd for $C_{19}H_{25}B_{11}FN_2$ $[M-F]^+$ 419.3108; found 419.3111.

6.2.3 HPLC analysis of BODIPYs

Normal-phase HPLC was performed on a Dionex system including a P680 pump and UVD 340 detector connected to a Dynamax axial compression column packed with Rainin 60 Å irregular silica gel. The flow rate of 1 mL/min was used. For compound 1b, a stepwise gradient of 50% B (ethyl acetate) and 50% A (hexane) in the first 3 min to 80% B and 20% A during the next 18 min to 50% B and 50% A for the next 6 min was used. For all other compounds, a stepwise gradient of 10% B and 90% A in the first 5 min to 70% B and 30% A during the next 10 min to 10% B and 90% A for the next 10 min was used.

6.2.4 Spectroscopic studies

UV−visible and fluorescence spectra were collected on a PerkinElmer Lambda 35 UV/vis spectrometer and PerkinElmer LS 55 luminescence spectrometer at room temperature. Quartz cuvettes (10 mm path length) and spectroscopic grade solvents were used for both measurements. Optical density (ε) was determined by using the solutions with absorbance at λ_{max} (0.5−1).

Quantum yields were determined by using the dilute solutions with absorbance (0.04−0.06) at the particular excitation wavelength. Cresyl violet perchlorate (0.54 in methanol) and rhodamine 6G in ethanol (0.95) were used as external standards for the carboranyl BODIPYs 5b, 6b, and 1b−3b, 4, 7, respectively. The relative fluorescence quantum yields (Φ_f) were determined by calculations using the following equation,[28]

$$\Phi_X = \Phi_R \times (F_X/F_R)\times(A_R/A_X)\times(n_X/n_R)^2$$

where Φ stands for fluorescence quantum yields; n stands for refractive indexes; *F* stands for the areas under the emission peaks; A stands for absorbance at the particular excitation wavelength, subscripts X and R refer to the tested samples and standard sample, respectively.

6.2.5 Crystallography

X-ray data for **2b** and **5b** were collected at 90 K with Mo Kα radiation (λ = 0.71073 Å) on a Bruker Kappa Apex-II DUO diffractometer. For BODIPY **2b**, $C_{13}H_{21}B_{11}F_2N_2S$, monoclinic space group $P2_1/c$, *a* = 10.7729(5), *b* = 15.7487(7), *c* = 12.5738(6) Å, β = 104.222(2)°, *V* = 2067.88(17) Å^3, *Z* = 4,22,855 measured data. Final *R* = 0.040, *Rw* = 0.106 for 264 refined parameters and 7883 independent reflections having θ_{max} = 33.2°. For BODIPY **5b,** $C_{17}H_{29}B_{11}F_2N_2S$, monoclinic space group $P2_1/c$, *a* = 13.688(2), *b* = 12.1938(17), *c* = 15.488(2) Å, β=113.231(6)^0, *V* = 2375.3(6) Å^3, *Z* = 4,47,866 measured data. Final *R* = 0.040, *Rw* = 0.110 for 303 refined parameters and 8658 independent reflections having θ_{max} = 32.6°. The CIFs have been deposited at the Cambridge Crystallographic Data Centre (CCDC 1426277-1426278).

6.2.6 Octanol-water partition coefficients

The partition coefficients (Log *P*) were measured by adapting a reported procedure.[29] 1-Octanol and Milli-Q water were mutually saturated and the two phases were separated. A 64 μM stock solution was prepared by dissolving the BODIPY into water-saturated 1-octanol. 2 mL of

the stock solution was added to 6 mL Milli-Q water in a 15 mL volumetric tube and the mixture was intensively vortexed for 10 min. After complete separation of the two phases, an aliquot from the 1-octanol layer was diluted with water-saturated 1-octanol and its absorbance was recorded with a Varian Cary 50 Bio UV-Vis spectrophotometer with a 10 mm path length quartz cuvette. The Log *P* values were calculated as follows:

$$LogP = Log(\frac{A_{oct}}{A_0 - A_{oct}} \cdot \frac{V_W}{V_O})$$

where A_0 and A_{oct} are the absorbance of the compound in the water-saturated octanol before and after partitioning; V_w and V_o are the water and 1-octanol volumes, respectively.

6.2.7 Cell studies of BODIPYs

The T98G cell line used in this study was purchased from ATCC and cultured in ATCC-formulated Eagle's Minimum Essential Medium containing 10% FBS and 1% antibiotic (Penicillin-streptomycin). The hCMEC/D3 cells were obtained from Dr. Pierre-Olivier Couraud from Institut COCHIN in Paris (France). All other reagents were purchased from Life Technologies.

Dark Cytotoxicity. A 32 mM compound stock solution wasprepared by dissolving the BODIPY in 100% DMSO. The stock solution was diluted into final working concentrations (0, 6.25, 12.5, 25, 50, and 100 μM). Human glioma T98G cells were plated at 15 000 cells per well in a Costar 96-well plate (BD biosciences) and allowed to grow for 24 h. The cells were exposed to the working solutions of compounds up to 100 μM and incubated overnight (37 °C, 95% humidity, 5% CO_2). The working solution was removed, and the cells were washed with 1× PBS. The medium containing 20% CellTiter Blue (Promega) was added and incubated for 4 h. The viability of cells is measured by reading the fluorescence of the medium at 570/615 nm using a BMG

FLUOstar Optima microplate reader. This fast, sensitive, and popular assay uses the indicator dye resazurin which is reduced to fluorescent resorufin in viable cells, while nonviable cells are not able to reduce resazuin or to generate a fluorescent signal. The fluorescence signal of the untreated cells was normalized to 100%.

Phototoxicity. Human glioma T98G cells were prepared as described above. The cells were incubated with compound concentrations of 100, 50, 25, 12.5, 6.25, 3.125, and 0 μM for 24 h. The loading medium was removed, and the cells were washed with 1×PBS buffer and then refilled with fresh media. The cells were exposed to a 600 W halogen lamp light source filtered with a water filter (transmits radiation 250−950 nm) and a beam turning mirror with 200 nm to 30 μm spectral range (Newport), for 20 min. The total light dose was approximately 1.5 J/cm^2. After light exposure, the cells were returned to the incubator for 24 h and assayed for cell viability as described above.

Time-dependent cellular uptake. Human T98G cells were prepared as described above. The cells were exposed to 10 μM of each compound solution for 0, 1, 2, 4, 8, and 24 h. The loading medium was removed at the end of each incubation period, and the cells were washed with 1× PBS and solubilized by adding 0.25% Triton X-100 in 1× PBS. Standard curves using 10, 5, 2.5, 1.25, 0.625, and 0.3125 μM concentrations were obtained by diluting 400 μM of each BODIPY solution with 0.25% Triton X-100 (Sigma-Aldrich) in 1× PBS. A cell standard curve was prepared using 10^4, 2×10^4, 4×10^4, 6×10^4, 8×10^4, and 10^5 cells per well. The cell number was quantified using a CyQuant cell proliferation assay (Life Technologies). The compound concentration in cells at each time period was determined using a BMG FLUOstar Optima microplate reader at 485/590 nm. Cellular uptake is expressed in terms of compound concentration (nM) per cell.

Microscopy. Human HEp2 cells were incubated in a six-well plate (MatTek) and allowed to grow overnight. The cells were exposed to 10 μMof each BODIPY and incubated for 6 h (37 °C, 95% humidity, 5% CO_2), followed by the addition of organelle tracers obtained from Invitrogen. The organelle tracers were used at the following concentrations: LysoSensor Green, 50 nM; MitoTracker Green, 250 nM; ER Tracker Blue/White, 100 nM; and BODIPY FL C5 Ceramide, 50 nM. The cells were incubated with the BODIPY and tracers for 30 min and washed with PBS three times before imaging. The images were acquired using a Leica DMRXA2 upright microscope with a water immersion objective and DAPI, GFP, and Texas Red filter cubes (Chroma Technologies).

hCMEC/D3 cell line (BBB model) (Figure 6.1).

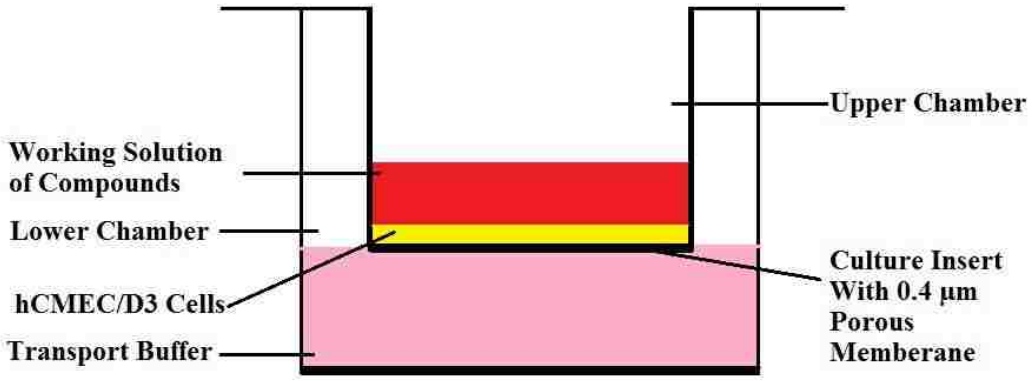

Figure 6.1. The blood-brain mimic for experimental in vitro BBB study. The upper chamber mimics the blood compartment, the lower chamber mimics the cerebral compartment, and the hCMEC/D3 cell monolayer represents the BBB.

The BBB permeabilities were determined following a pulished procedure.[30-31] Specifically, the hCMEC/D3 cells were incubated in a six-well, 0.4 μm porosity PET Transwell plate (Corning) for 48 h, allowing the formation of a model brain capillary endothelial monolayer (checked by microscopy). EBM-2 medium containing 5% FBS, 1% penicillin/streptomycin, hydrocortisone, ascorbic acid, chemically defined lipid concentrate (1/100), HEPES, and bFGF was used as the

growth medium. The coated PET Transwell plates with and without endothelial cells were transferred into six-well plates. The measurements were performed in triplicate for each compound, using three PET Transwell plates with cells and three without cells. The time points of the treatment were 0, 10, 25, and 45 min. At time 0, a 0.5 mL sample of each BODIPY or standard Lucifer yellow (LY) at 50 μM concentration in transport buffer was added to the upper chamber (mimicking the blood), and 1.5 mL of transport buffer was added to the lower chamber (mimicking the BBB); see Figure S24 in the Supporting Information. The transport buffer was prepared by adding 5 mL of HEPES (1 M) and 5 mL of sodium pyruvate (100 μM) to 400 mL of HBSS. The plates were incubated at 37 °C, 95% humidity, and 5% CO_2. At time 10 and 25 min, each upper PET Transwell was transferred to the corresponding prepared six-well plate containing 1.5 mL of transport buffer: the so-called "25 min" first and then the "45 min". At each time point, solution in the lower chamber was added into a 96-well plate with 100 μL for each well (five wells). The fluorescence intensity of the solution was measured by using a BMG FLUOstar plate reader at 485/590 nm and 425/538 nm (excitation/emission) for BODIPYs and LY, respectively, and the concentrations were determined from the corresponding standard curves. The calculations of permeability coefficients (Pe, in cm/s) were performed following the clearance principle as described in the equations below (eqs 1 and 2), where X is the amount of sample in the lower chamber and Cd is the concentration of sample in the upper chamber at each time point. The total cleared volume at each time point is calculated by summing the incremental cleared volumes up to the given time point.

$$\text{clearance (mL)} = X/Cd \quad (1)$$

The cleared volume is plotted vs time, and a linear fit is applied.

$$P_e\,(\text{cm/s}) = \left(\frac{1}{PSt} - \frac{1}{PSf}\right)/(A \times 60) \quad (2)$$

where PSt is the slope of the clearance curve for the culture, PSf is the slope of the clearance curve with the control Transwell plate without cells, and A is the surface area of the PET Transwell plate.

6.3 Results and discussion

6.3.1 Synthesis and characterization

Synthesis of carboranyl BODIPYs. A series of seven carboranyl-BODIPYs **1b**, **2b**, **3b**,[18] **4**, **5b**, **6b**, and **7**,[25] were synthesized as shown in Scheme 6.1. The ortho-carborane cluster was chosen as the boron source because of its high boron content, high hydrophobicity, high stability under physiologic conditions, and low toxicity.[7, 11] The key chloro-BODIPY starting materials were synthesized from the corresponding dipyrroketones, as previously reported.[24-25, 27] 8-Chloro-BODIPYs **1a**−**3a** and **5a** were converted into their corresponding 8-carboranylthio-BODIPYs by reaction with 1.1 equiv of 1-mercapto-o-carborane in THF at room temperature, in yields ranging from 88% to 95%. We have previously reported that 3,8-dichloro-BODIPY **6a** undergoes highly regioselective substitutions at the 8-position in the presence of N- and O-centered nucleophiles.[25] Using more reactive S-nucleophiles, the 8- vs 3-substitution regioselectivity tends to decrease. However, due to the electron-withdrawing nature of the carborane cluster, BODIPY **6a** reacted smoothly with 1.1 equiv of 1-mercapto-o-carborane, affording **6b** with high regioselectvity in 74% yield. On the other hand, BODIPY **7** was prepared from **6a** via two successive regioselective reactions, a Stille cross-coupling at the 8-position using 1 equiv of tributylphenylstannane and $Pd(PPh_3)_4$, followed by substitution using an excess of 1-mercapto-o-carborane, as we have previously reported.[25] The Suzuki cross-coupling reaction of BODIPY **1a** with 1.5 equiv of 4-(1-methyl-o-carborane)-methylphenylboronic acid in toluene and in the presence of $Pd(PPh_3)_4$ and 1 M Na_2CO_3(aq) produced BODIPY **4** in 45% isolated yield.

Scheme 6.1. Synthesis of carborane-containing BODIPYs.

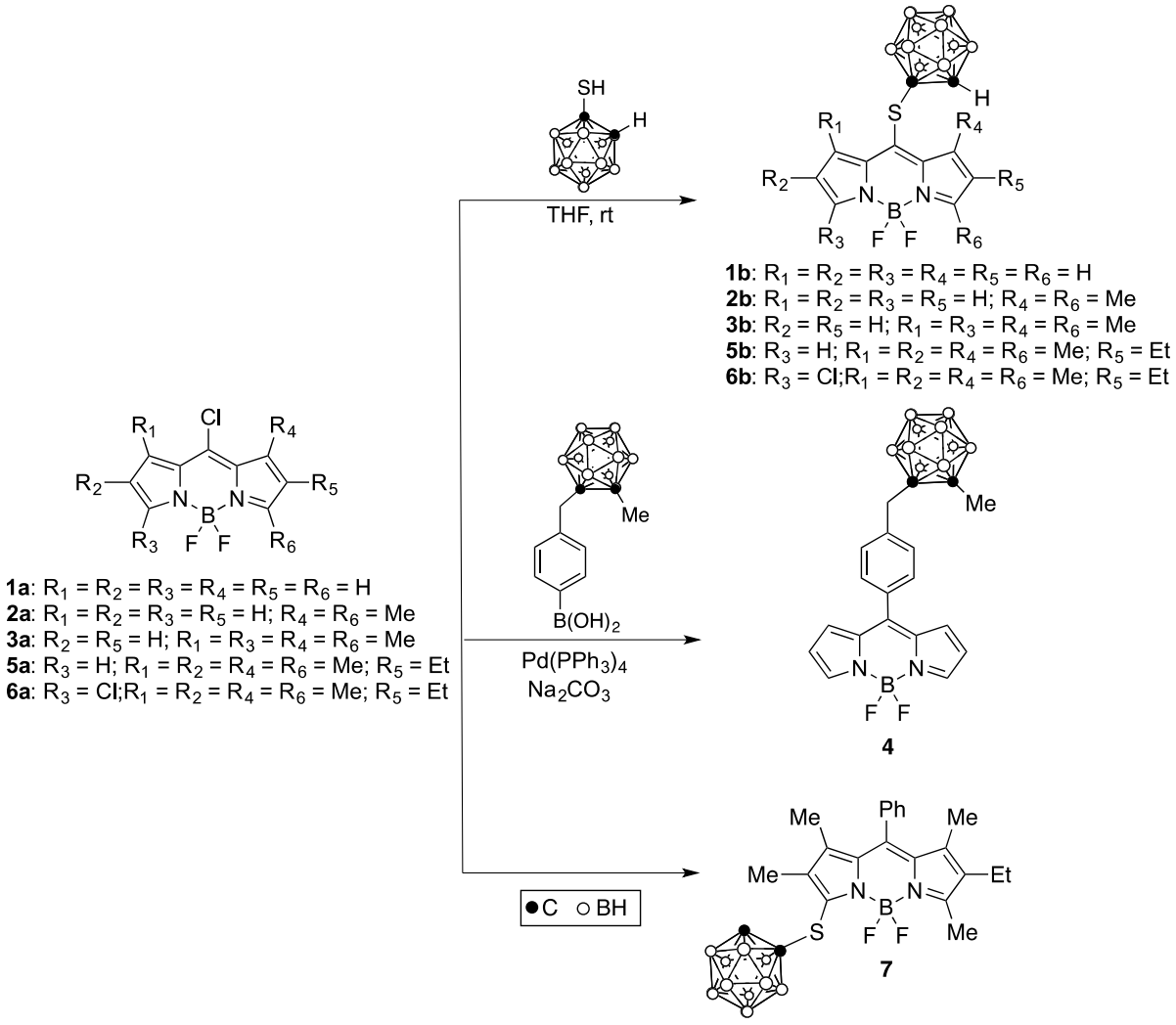

HPLC, NMR and X-ray analysis. All compounds were of ≥95% purity, as determined by HPLC (Figures 6.2-6.8). The commercially available LY standard is of 97% purity, as provided by Life Technologies. The structures of the new BODIPYs **1b**, **2b**, **5b**, **6b** and **4** were confirmed by ^{1}H-, ^{13}C- (Figures 6.9-6.18) and ^{11}B-NMR (Figures 6.19-6.24), HRMS, and in the case of **2b** and **5b** by X-ray crystallography (Figure 6.25). The X-ray structures of **3b**[20] and **7**.[27] have been previously reported. Crystals of BODIPYs **2b** and **5b** suitable for X-ray analysis were obtained by slow diffusion of hexanes into chloroform. In **2b**, the B atom of the central C_3N_2B ring lies slightly (0.214 Å) out of the plane of the other five atoms, which are fairly coplanar, having a mean

deviation of 0.013 Å. The carborane lies on the bisector of this plane, with C-C-S-C torsion angle 93.9°. In **5b**, the central ring is slightly more planar, with the meso C atom lying 0.098 Å out of the C_2N_2B plane. The S atom lies 0.319 Å out of this plane, and as in **2b**, the carborane lies on the bisector, with C-S-C-C torsion angle 94.1°. The ethyl group is also approximately perpendicular to the ring system, with C-C-CH_2-CH_3 torsion angle 83.7°.

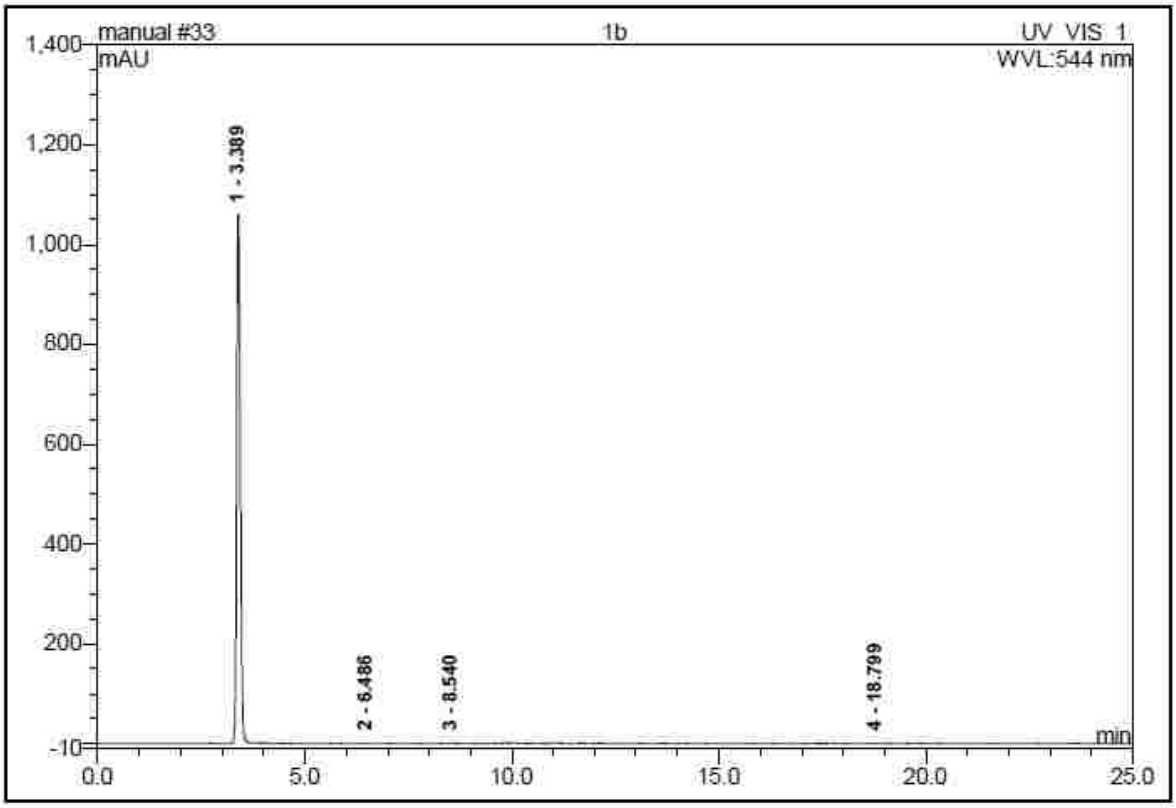

No.	Ret.Time min	Peak Name	Height mAU	Area mAU*min	Rel.Area %	Pos.	Type
1	3.39	n.a.	1058.790	108.247	99.90	n.a.	BMB
2	6.49	n.a.	0.378	0.033	0.03	n.a.	BMB
3	8.54	n.a.	0.390	0.032	0.03	n.a.	BMB
4	18.80	n.a.	0.316	0.041	0.04	n.a.	BMB
Total:			1059.874	108.353	100.00	0.000	

Figure 6.2. HPLC trace for BODIPY **1b**.

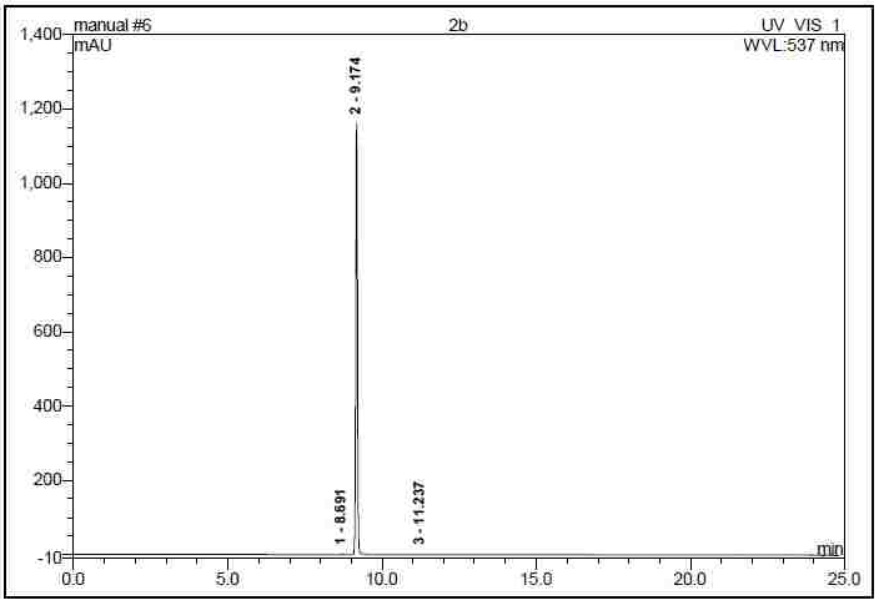

No.	Ret.Time min	Peak Name	Height mAU	Area mAU*min	Rel.Area %	Pos.	Type
1	8.69	n.a.	1.781	0.145	0.20	n.a.	BMB
2	9.17	n.a.	1158.645	72.917	99.75	n.a.	BMB
3	11.24	n.a.	0.276	0.041	0.06	n.a.	BMB
Total:			1160.702	73.103	100.00	0.000	

Figure 6.3. HPLC trace for BODIPY **2b**.

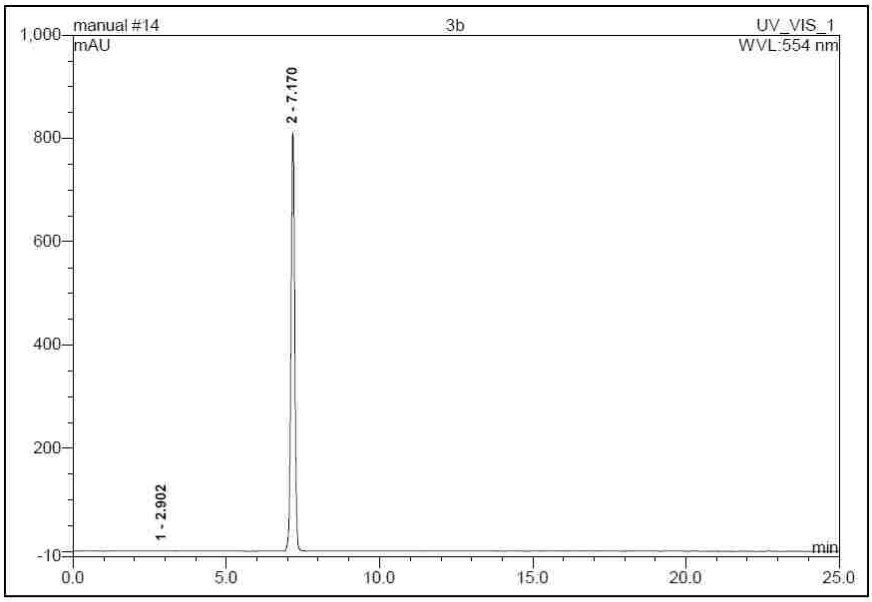

No.	Ret.Time min	Peak Name	Height mAU	Area mAU*min	Rel.Area %	Pos.	Type
1	2.90	n.a.	0.840	0.076	0.07	n.a.	BMB
2	7.17	n.a.	808.123	113.015	99.93	n.a.	BMB
Total:			808.964	113.090	100.00	0.000	

Figure 6.4. HPLC trace for BODIPY **3b**.

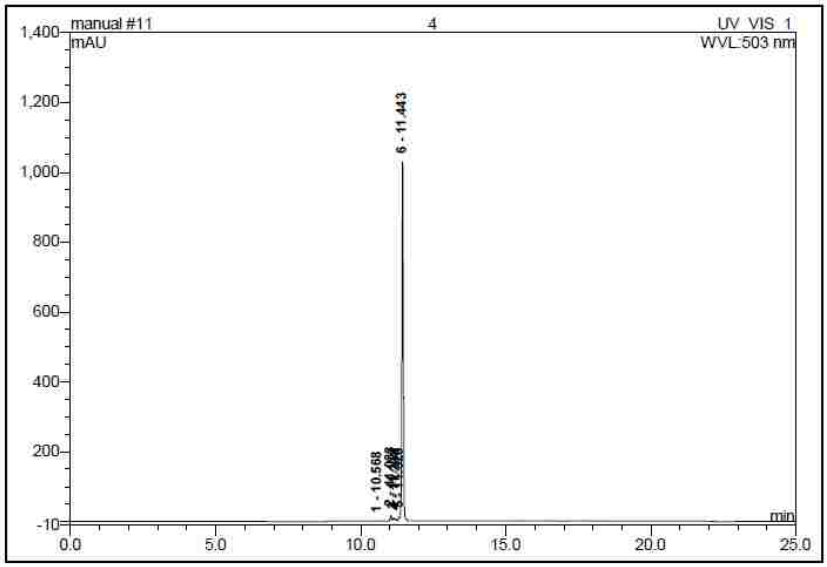

No.	Ret.Time min	Peak Name	Height mAU	Area mAU*min	Rel.Area %	Pos.	Type
1	10.57	n.a.	0.474	0.042	0.07	n.a.	BMB
2	11.03	n.a.	14.449	0.798	1.34	n.a.	BM
3	11.13	n.a.	7.880	0.421	0.71	n.a.	M
4	11.21	n.a.	4.142	0.193	0.33	n.a.	MB
5	11.32	n.a.	8.984	0.413	0.69	n.a.	BM
6	11.44	n.a.	1023.704	57.500	96.86	n.a.	MB
Total:			1059.633	59.367	100.00	0.000	

Figure 6.5. HPLC trace for BODIPY **4**.

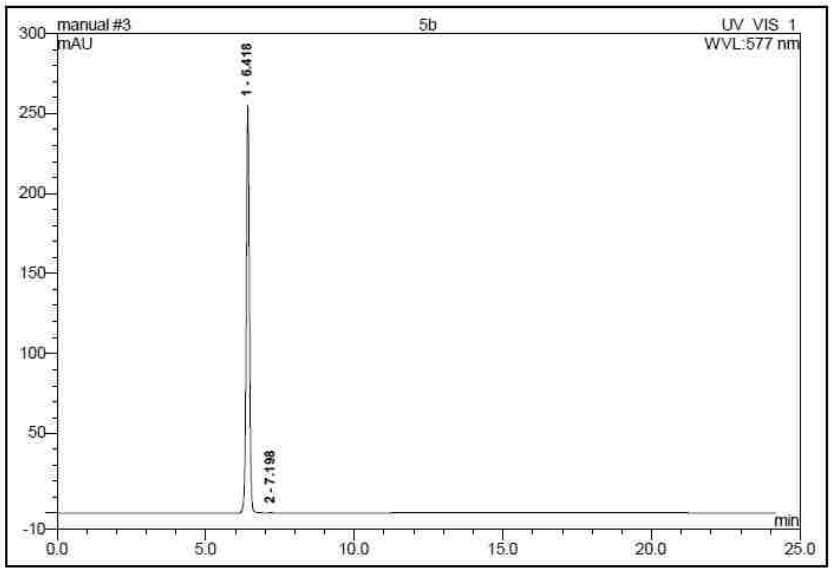

No.	Ret.Time min	Peak Name	Height mAU	Area mAU*min	Rel.Area %	Pos.	Type
1	6.42	n.a.	254.054	31.278	99.90	n.a.	BMB
2	7.20	n.a.	0.187	0.031	0.10	n.a.	BMB
Total:			254.242	31.309	100.00	0.000	

Figure 6.6. HPLC trace for BODIPY **5b**.

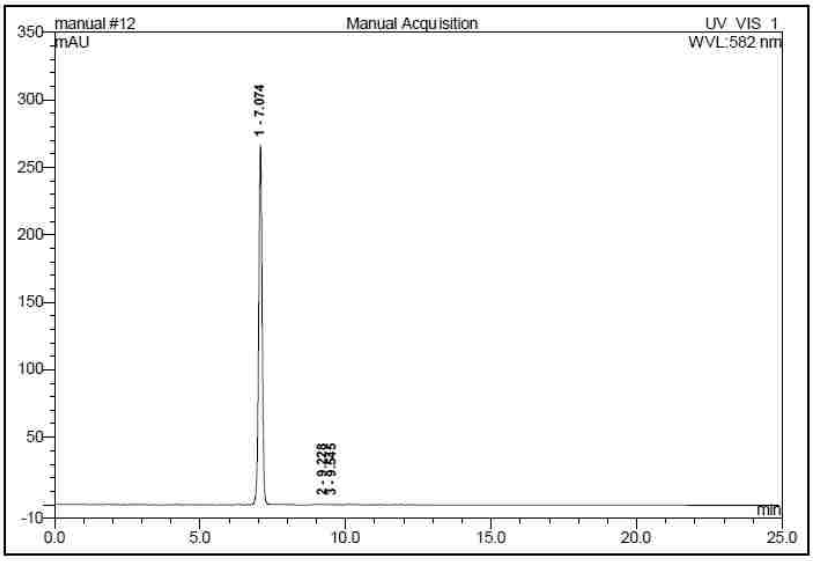

No.	Ret.Time min	Peak Name	Height mAU	Area mAU*min	Rel.Area %	Pos.	Type
1	7.07	n.a.	266.472	36.392	99.62	n.a.	BMB
2	9.23	n.a.	0.176	0.101	0.28	n.a.	BM
3	9.55	n.a.	0.206	0.037	0.10	n.a.	MB
Total:			266.854	36.530	100.00	0.000	

Figure 6.7. HPLC trace for BODIPY **6b**.

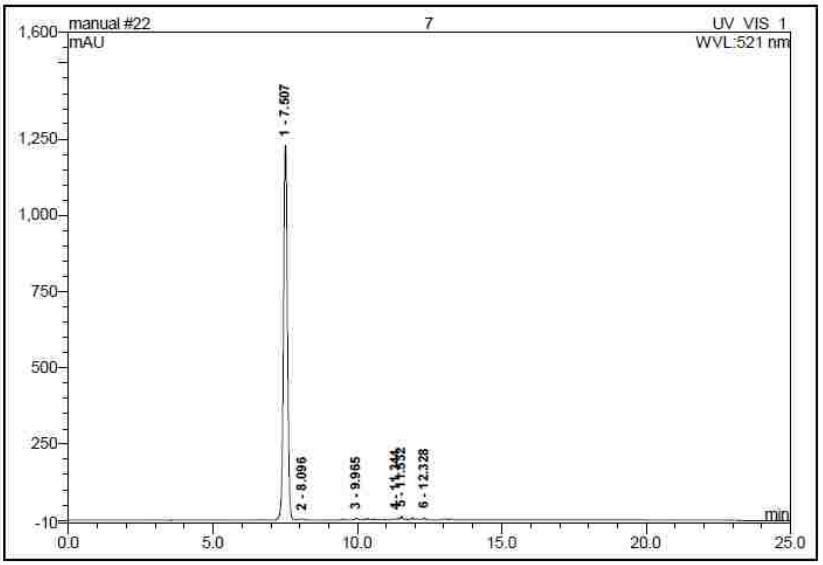

No.	Ret.Time min	Peak Name	Height mAU	Area mAU*min	Rel.Area %	Pos.	Type
1	7.51	n.a.	1225.251	192.805	98.91	n.a.	BMB
2	8.10	n.a.	2.630	0.400	0.21	n.a.	BMB
3	9.97	n.a.	4.524	0.416	0.21	n.a.	BMB
4	11.34	n.a.	1.855	0.084	0.04	n.a.	Ru
5	11.53	n.a.	10.341	0.918	0.47	n.a.	BMB
6	12.33	n.a.	5.302	0.316	0.16	n.a.	BMB
Total:			1249.902	194.938	100.00	0.000	

Figure 6.8. HPLC trace for BODIPY **7**.

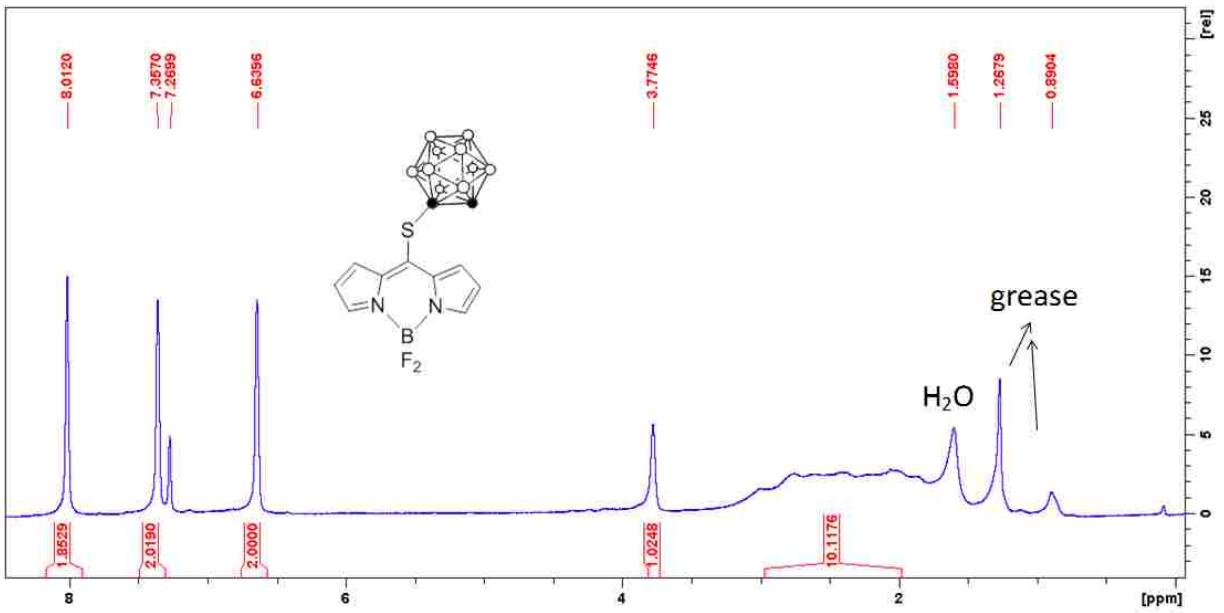

Figure 6.9. ^{1}H NMR spectrum of BODIPY**1b**.

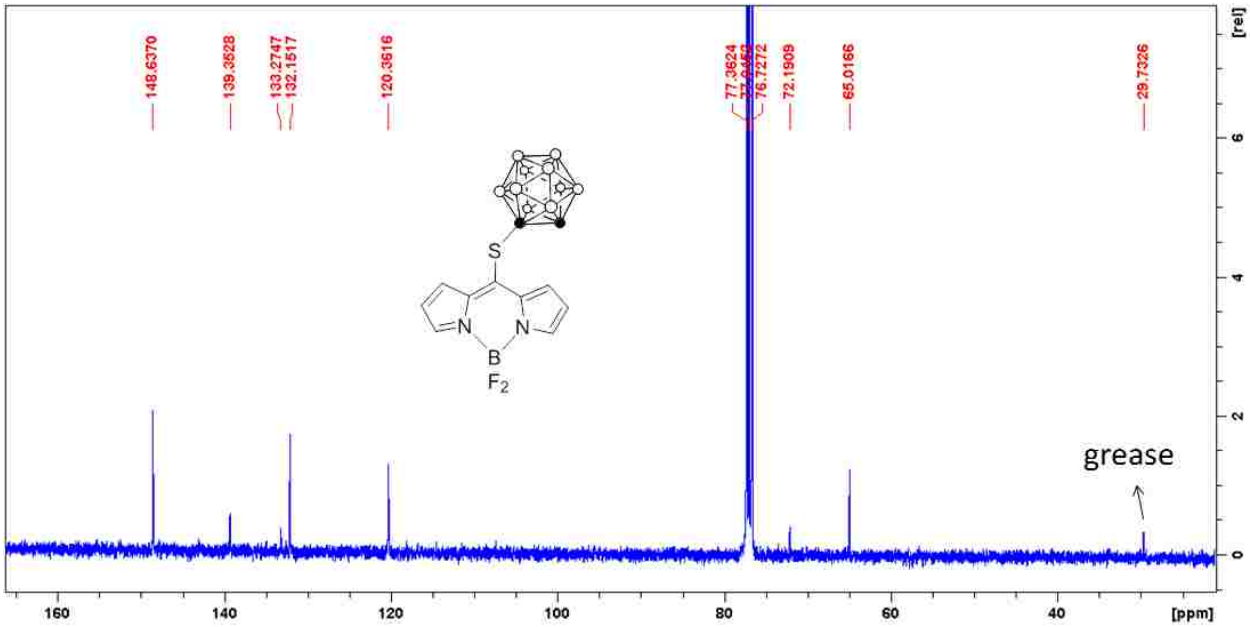

Figure 6.10. ^{13}C {^{1}H} NMR spectrum of BODIPY**1b**.

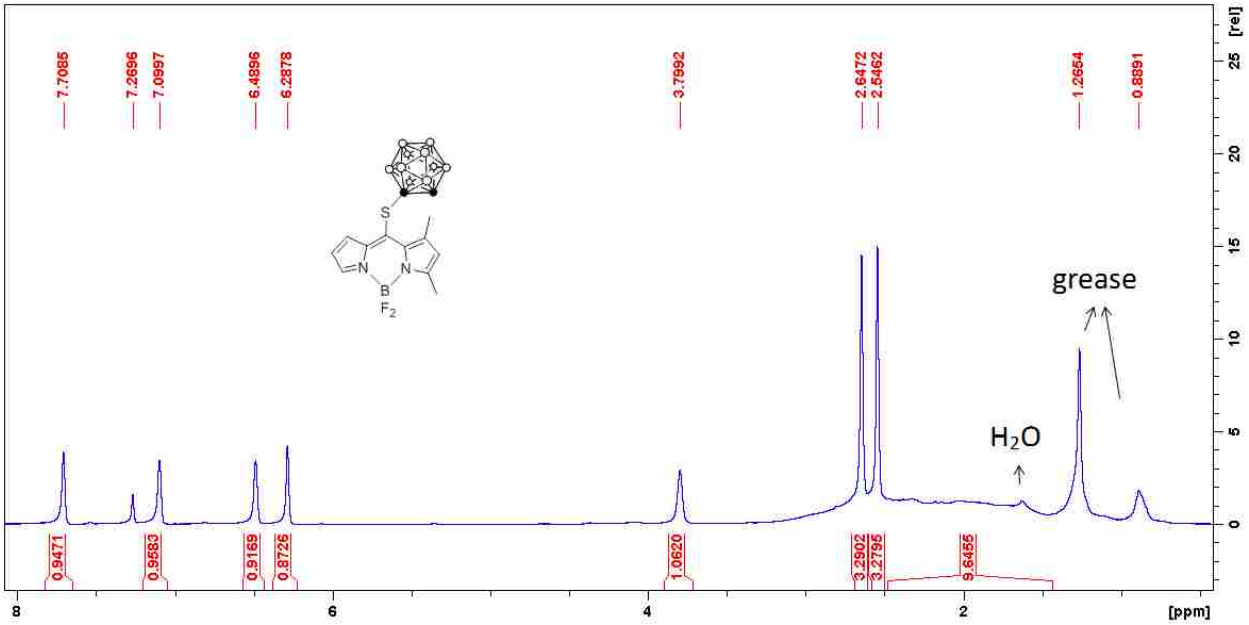

Figure 6.11. ^{1}H NMR spectrum of BODIPY**2b**.

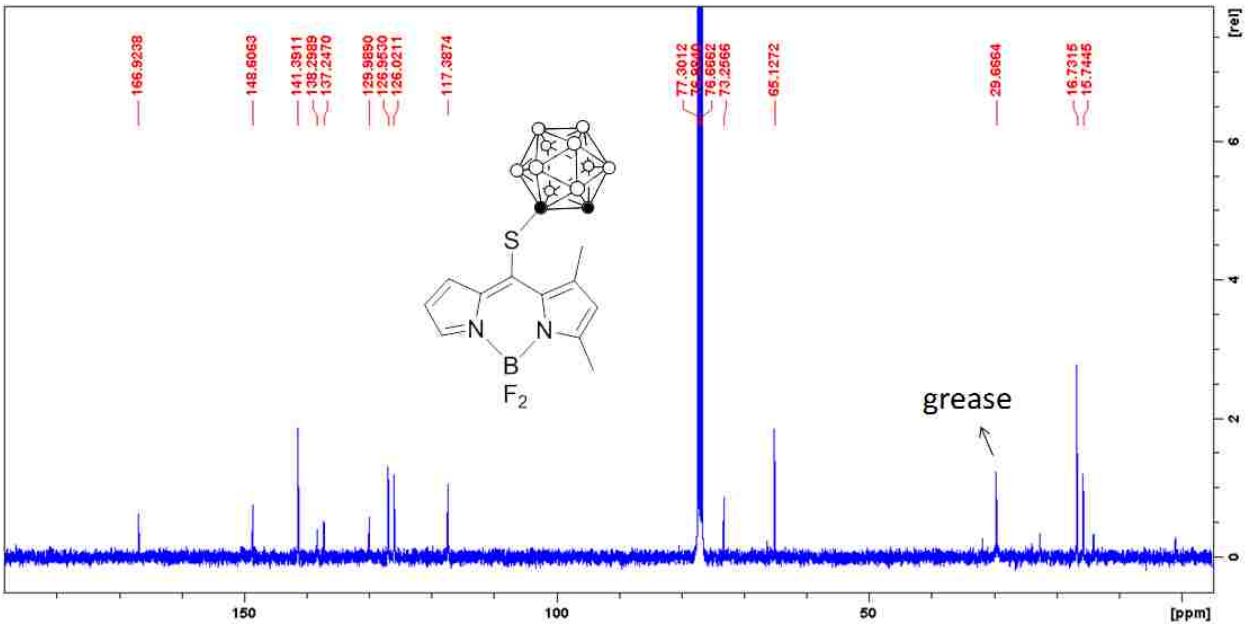

Figure 6.12. ^{13}C {^{1}H} NMR spectrum of BODIPY**2b**.

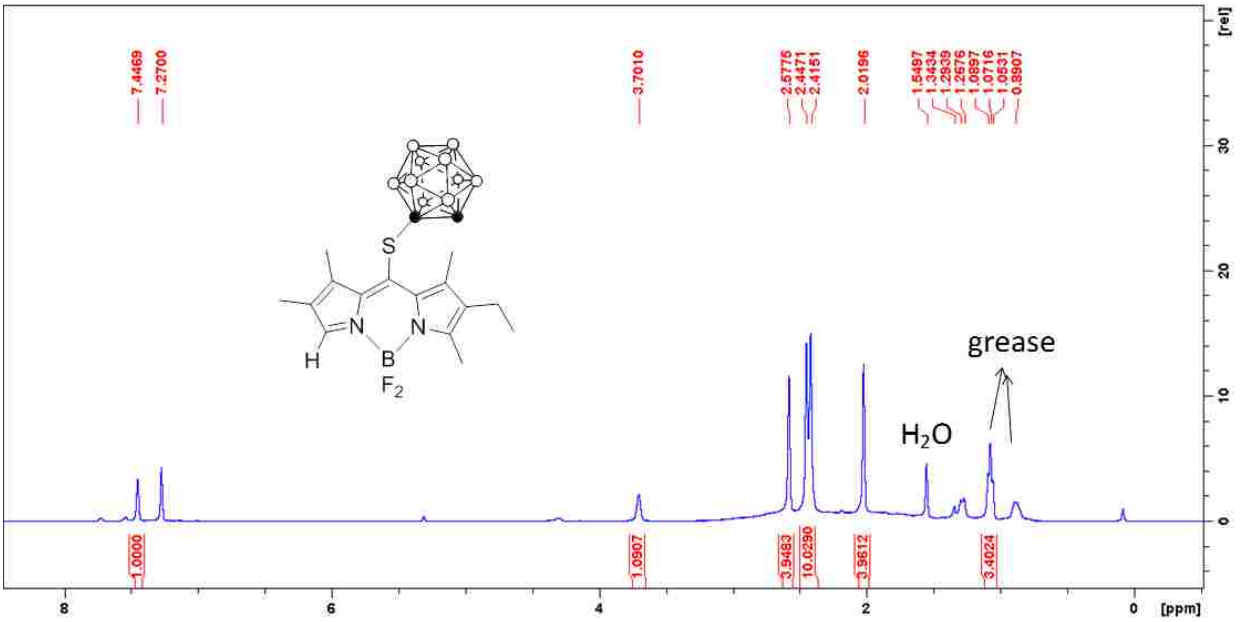

Figure 6.13.[1]H NMR spectrum of BODIPY **5b**.

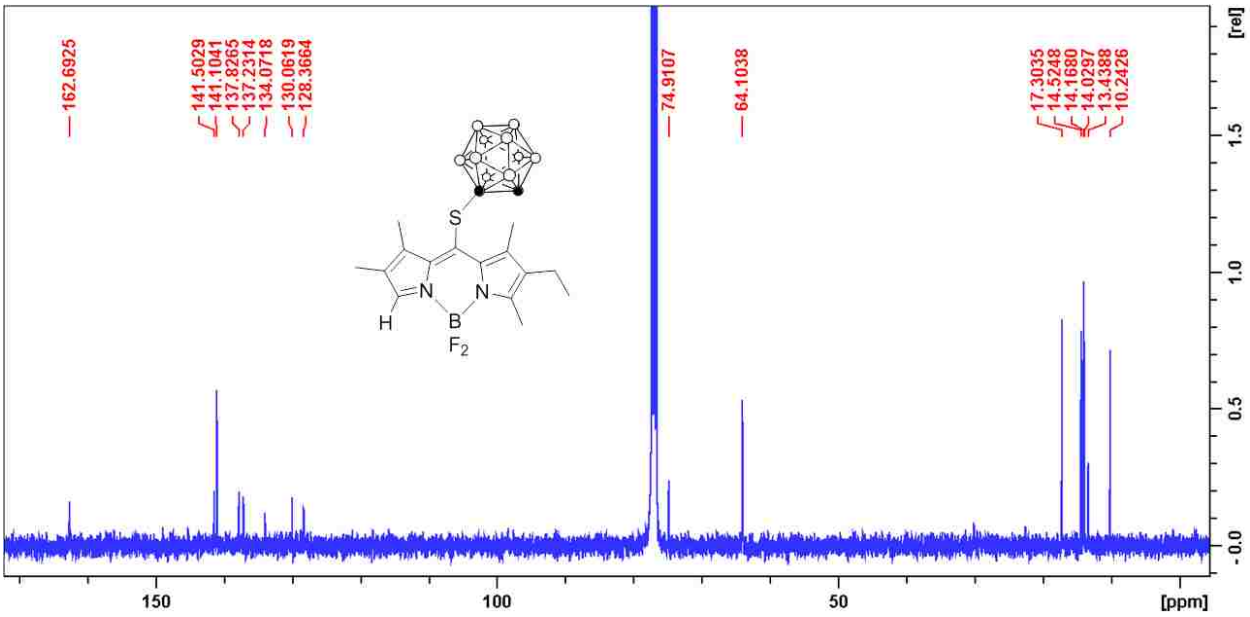

Figure 6.14. ^{13}C {^{1}H} NMR spectrum of BODIPY**5b**.

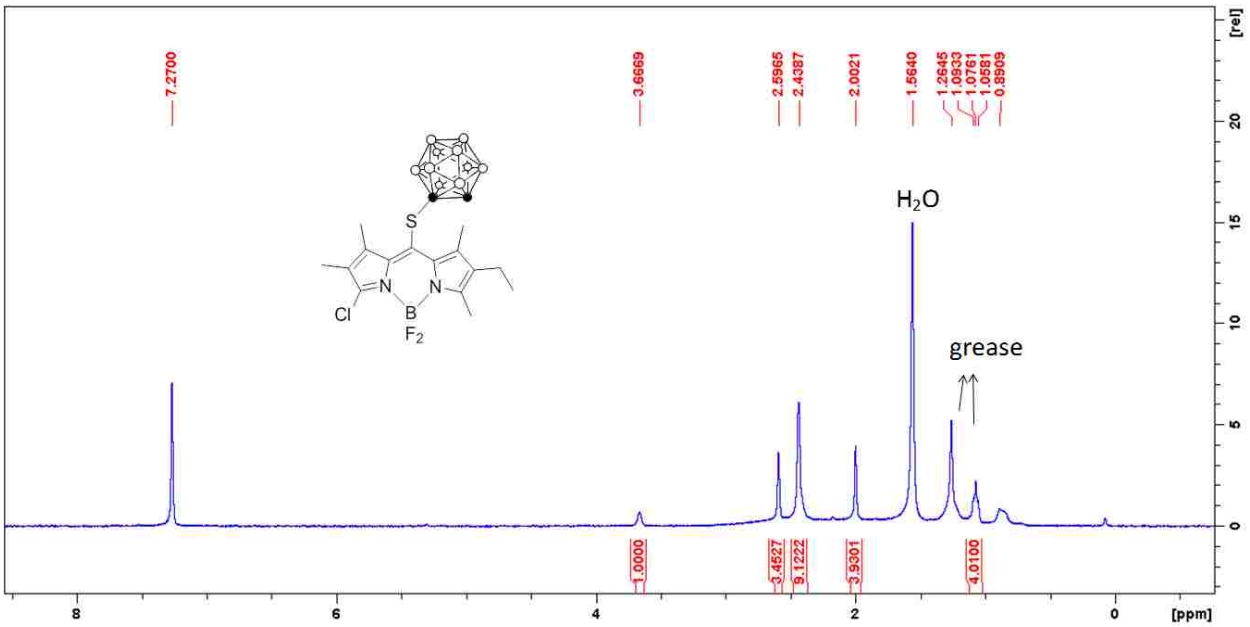

Figure 6.15. ^{1}H NMR spectrum of BODIPY**6b**.

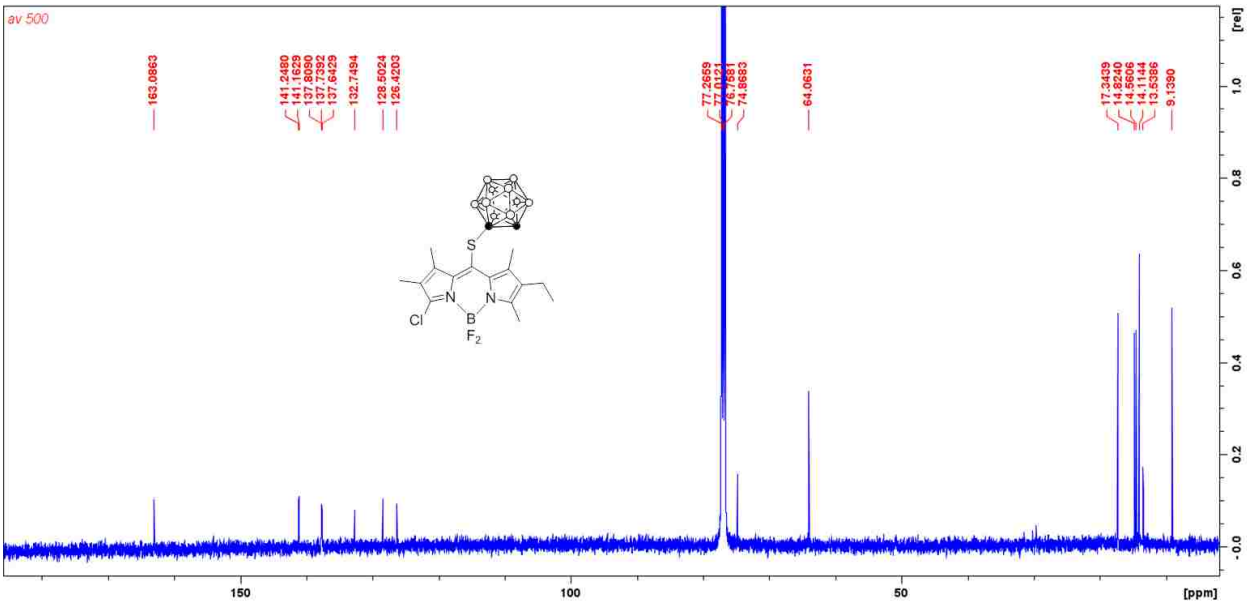

Figure 6.16. ^{13}C {^{1}H} NMR spectrum of BODIPY**6b**.

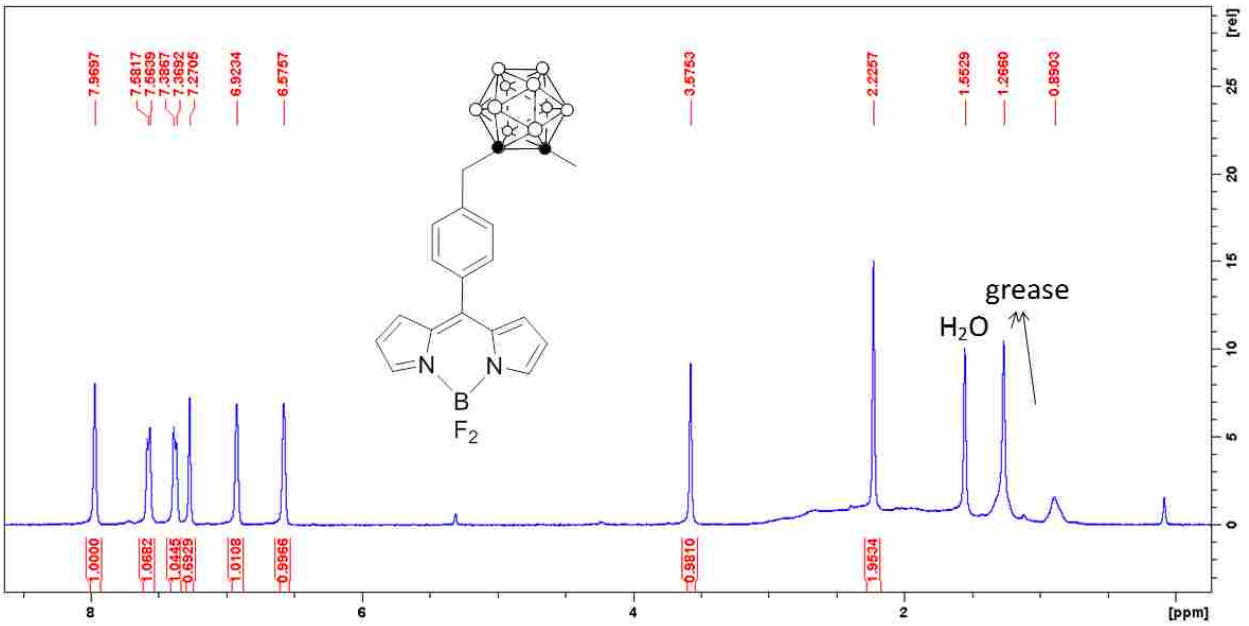

Figure 6.17. ^{1}H NMR spectrum of BODIPY**4.**

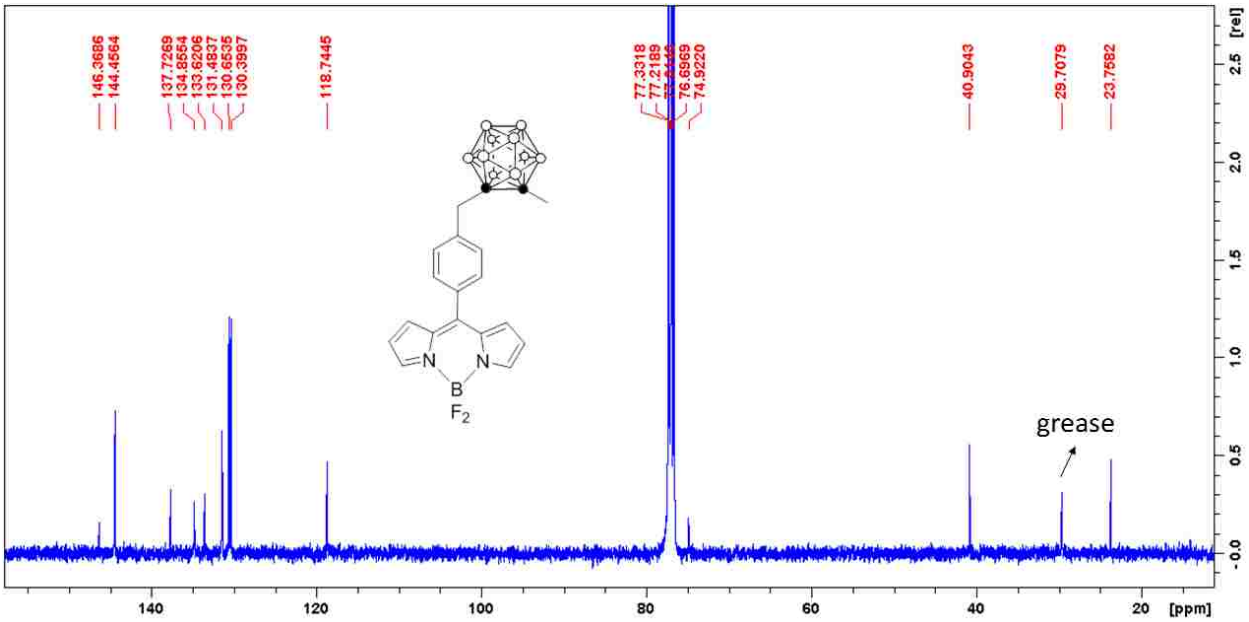

Figure 6.18. ^{13}C {^{1}H} NMR spectrum of BODIPY**4**.

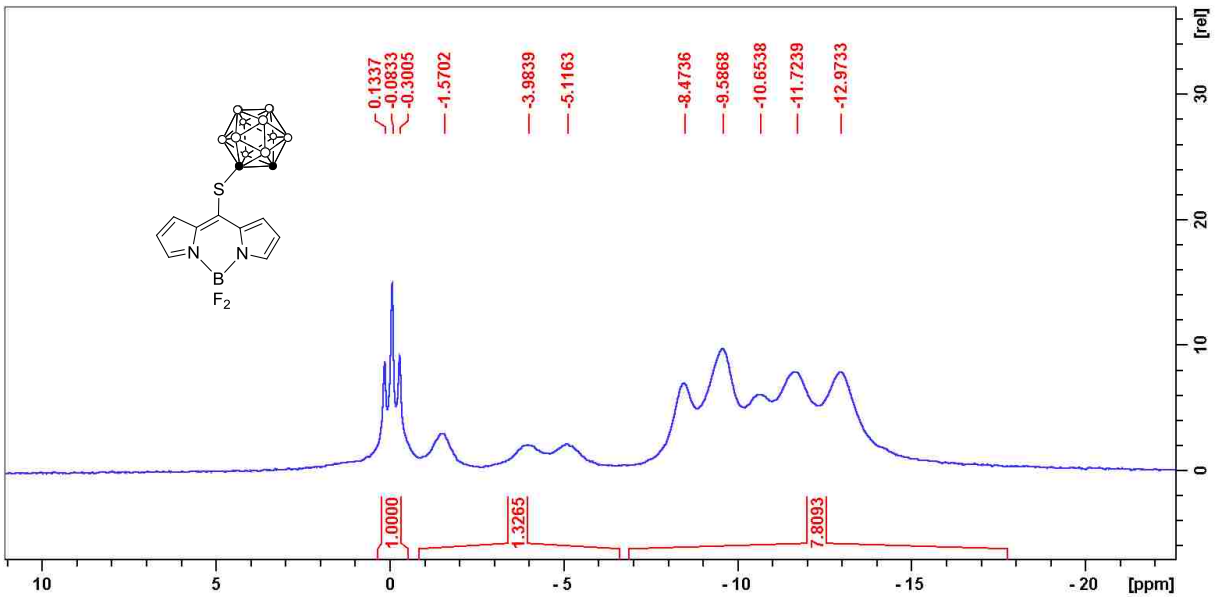

Figure 6.19. ^{11}B NMR spectrum of BODIPY **1b**.

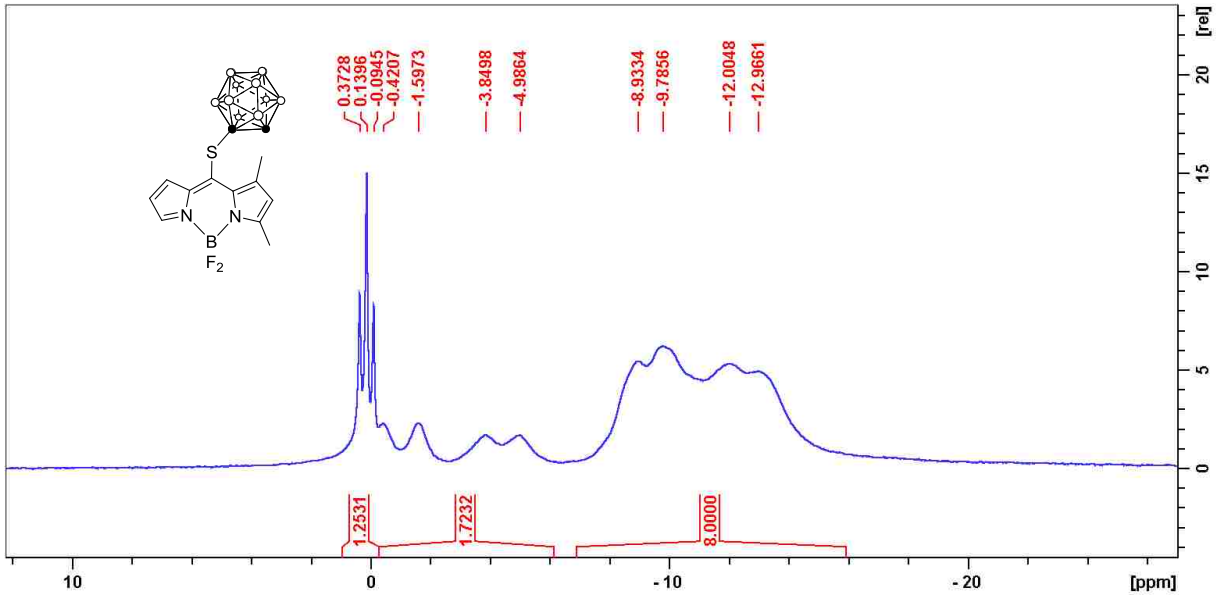

Figure 6.20. ^{11}B NMR spectrum of BODIPY **2b**.

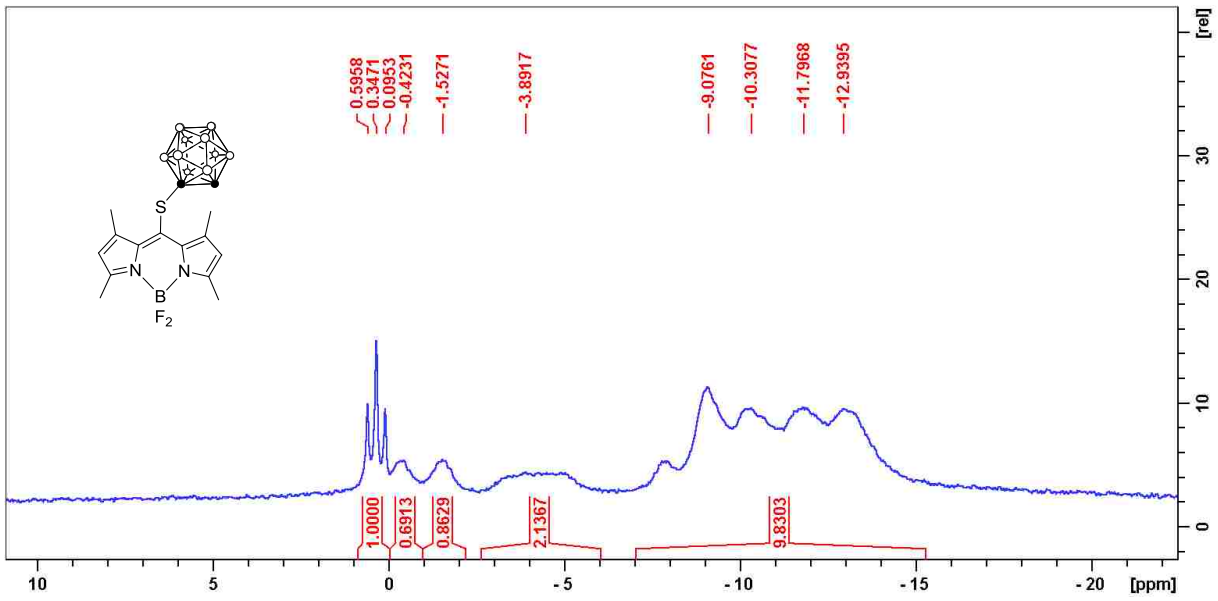

Figure 6.21. ^{11}B NMR spectrum of BODIPY**3b**.

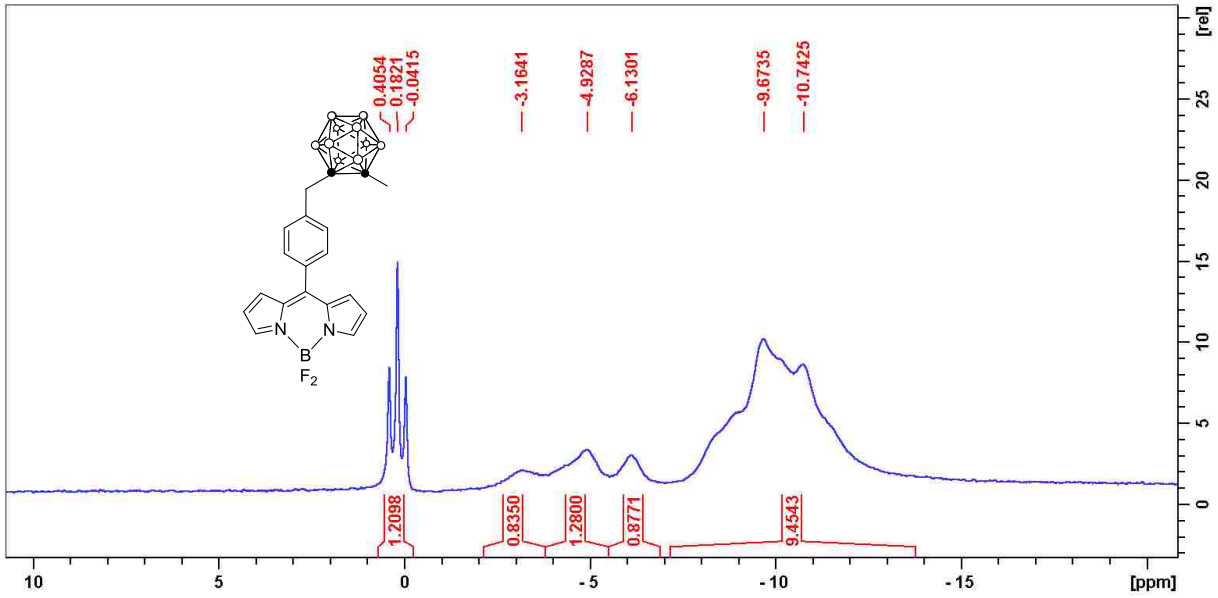

Figure 6.22. ^{11}B NMR spectrum of BODIPY **4**.

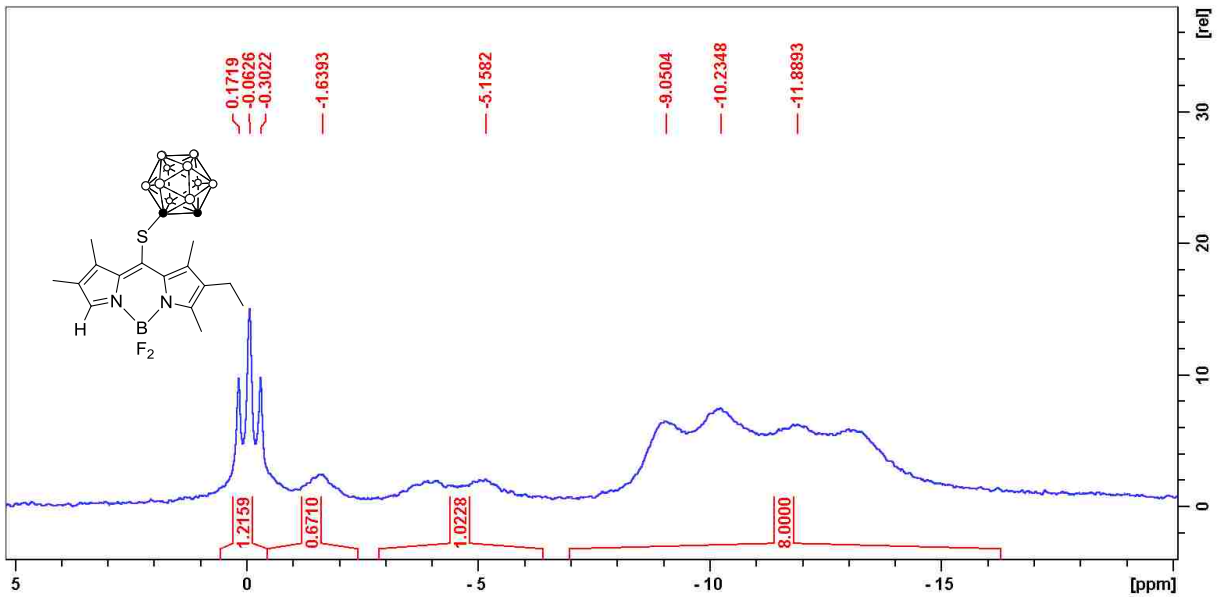

Figure 6.23. ^{11}B NMR spectrum of BODIPY **5b**.

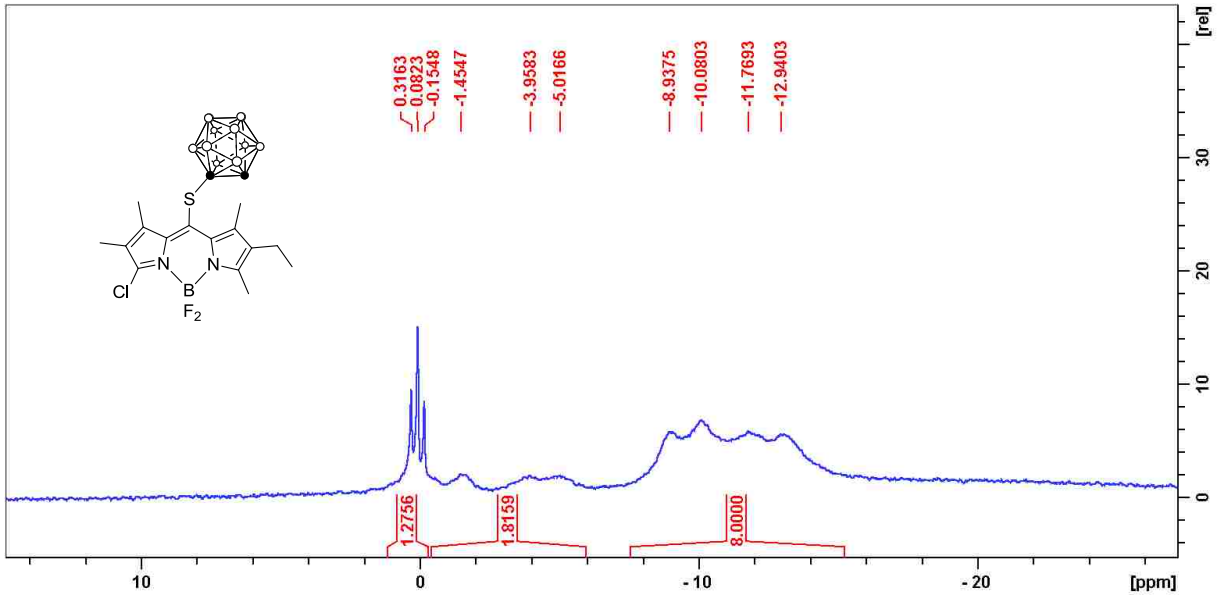

Figure 6.24. ^{11}B NMR spectrum of BODIPY **6b**.

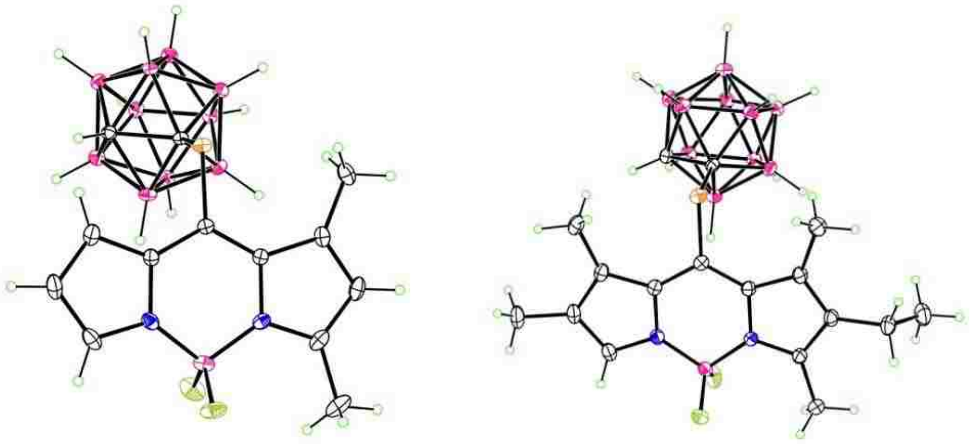

Figure 6.25. X-ray crystal structure of **2b** (left) and **5b** (right).

Spectroscopic analysis. The spectroscopic properties of all BODIPYs in dichloromethane solution were investigated and the results are summarized in Table 1 (see also Figures 6.26-6.27). The absorption spectra of all BODIPYs followed the Lambert-Beer law, indicating there is no appreciable aggregation in this solvent at the concentrations investigated. The introduction of an *ortho*-carboranylthio group at the 8-position in BODIPYs **1b-3b**, **5b** and **6b**, caused large red-shifts on the maximum absorption (up to 57 nm) and emission (up to 73 nm) bands (Figure 6.26). This is probably due to the stabilization of the LUMO by this group, which decreases the HOMO-LUMO gap.[34] On the other hand, introduction of the same group at the 3-position, as in BODIPY **7**, induced a slight blue-shift (ca. 5 nm) relative to the starting BODIPY **6a**.[27] Arylation at the 8-position, as in BODIPY **4**, also produced a slight blue-shift compared with the starting 8-chloro-BODIPY **1a** probably due to a large dihedral angle between the aryl group and the BODIPY core. The fluorescence quantum yields were higher for BODIPY **1b**, suggesting low rotational freedom for the 8-carboranylthio group, and it decreased with increasing alkyl substitution for **2b**, **3b** and **5b**. This is attributed to increased energy lost to non-radiative deactivation processes.[27,34] On the

other hand, BODIPY **4** shows much lower quantum yield than **7**, probably due to the higher rotation of the 8-aryl group in the absence of 1,7-methyl groups.

Table 6.1. Spectroscopic properties of BODIPYs in dichloromethane at room temperature.

BODIPY	Absorption λ_{max} (nm)	log ε ($M^{-1}cm^{-1}$)	Emission, λ_{max} (nm)	Φ_f[a]	Stokes shift (nm)
1b	544	4.42	556	0.52	12
2b	537	4.54	553	0.29	16
3b	554	4.45	576	0.065	22
4	502	4.50	517	0.034	15
5b	577	4.29	608	0.060	31
6b	582	4.16	609	0.090	27
7	521	4.18	540	0.58	19

[a]Rhodamine 6G in ethanol (0.95) was used as standard for all compounds except for **5b** and **6b**, which used crystal violet perchlorate in methanol (0.54) as the standard.

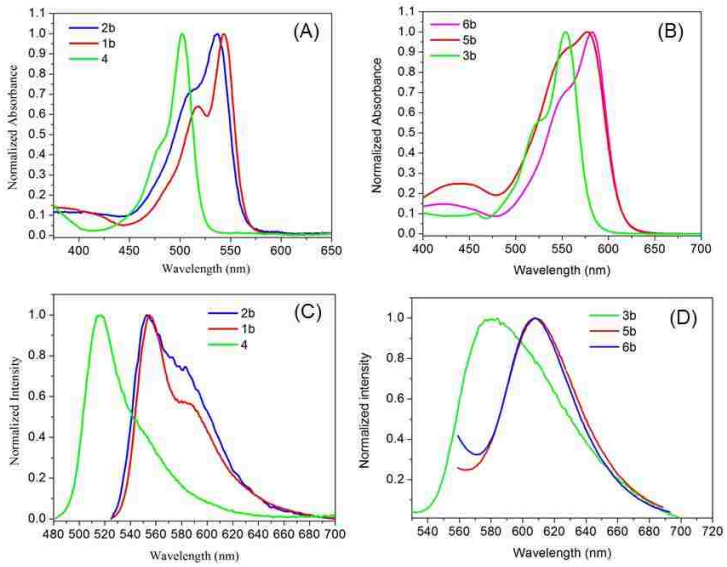

Figure 6.26. (A, B) Normalized UV/Vis spectra of BODIPYs **1b**, **2b**, **4**, **3b**, **5b** and **6b**; (C, D) Normalized fluorescence spectra of BODIPYs **1b**, **2b**, **4**, **3b**, **5b** and **6b** in dichloromethane at room temperature.

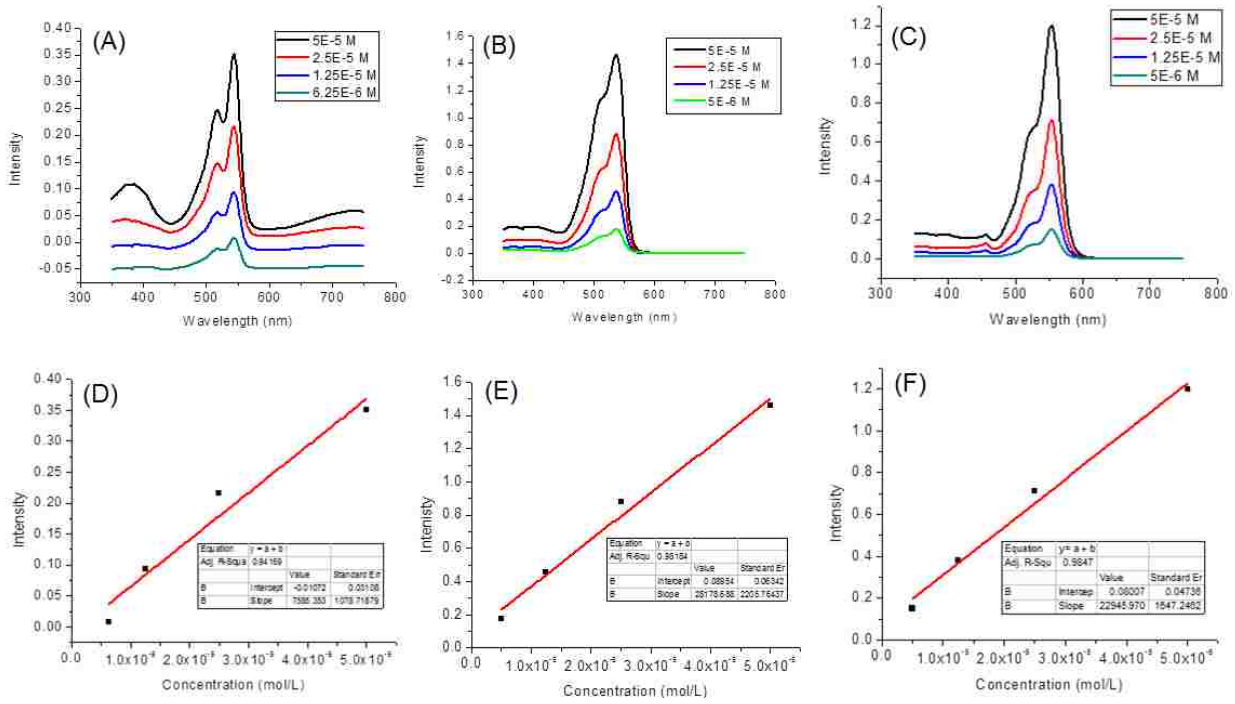

Figure 6.27. (A-C) Absorption spectra of BODIPY **1b**, **2b** and **3b** at different concentrations in dichloromethane; (E-F) Plot of absorbance intensity of BODIPY **1b**, **2b** and **3b** vs. concentration in dichloromethane.

6.2.2 Cytotoxicity and uptake in T98G Cells

This is the first report on the cytotoxicity and cellular uptake of carborane-containing BODIPYs. The cytotoxicity (dark and light, using 1.5 J/cm^2 light dose) and time-dependent uptake of all carboranyl-BODIPYs were investigated in human glioma T98G cells and the results are summarized in Table 6.2 and Figures 6.28-6.29. The IC_{50} values were calculated from dose−response curves.

None of the BODIPYs, with the exception of **5b**, showed any toxicity in the dark at concentrations up to 100 μM investigated, as shown in Figure 6.28A. Upon irradiation with light, all the BODIPYs, with exception of **3b** (IC_{50} = 80 μM) and **5b** (IC_{50} = 40 μM), exhibited minimal photocytotoxicity (IC_{50} > 98 μM) (Figure 6.28B). The higher phototoxicity observed for **5b** (IC_{50} = 40 μM) might be a result of its higher uptake by T98G cells, which was evidenced by the cellular

uptake study showing **5b** accumulated the most within cells at all the time points investigated. BODIPY **7** accumulated the least, among this series of BODIPYs, which was probably due to its poor aqueous solubility. The lipophilic character of this series of BODIPYs was evaluated by determining their distribution between 1-octanol and water, and the values obtained for the partition coefficients (log P) are given in Table 6.2. The extent of cellular uptake did not correlate with the hydrophobic character of the BODIPYs, which increased in the order **1b** < **2b** < **3b** < **5b** ~ **6b** < **4** ≪ **7**.

Table 6.2. Dark, photocytotoxicity (1.5 J/cm^2) and uptake plateau concentration of BODIPYs in human glioma T98G cells. Permeabilty coefficients (P_e) of BODIPYs and lucifer yellow (LY) in human endothelial hCMEC/D3 cells. Octanol-water partition coefficients (log *P*) of BODIPYs.

Comp.	MW (g/mol)	log *P*	Darktoxicity IC_{50} (μM)	Phototoxicity IC_{50} (μM)	Cellular uptake at 24 h (nM/cell)	Major sites of localization	$P_e \times 10^{-5}$ (cm/s)
LY	457.24	-	-	-	-	-	2.2±0.8
1b	366.25	1.50	>100	>100	0.23±0.05	Lyso, Mito, Golgi, ER	16.4±3.3
2b	394.31	1.69	>100	>98	0.36±0.03	Lyso, Mito, Golgi, ER	6.0±1.0
3b	422.36	1.73	>100	>80	0.11±0.02	Lyso, Mito, Golgi, ER	4.4±0.5
4[a]	438.33	2.11	>100	>100	0.41±0.03	Lyso, Mito, Golgi, ER	-
5b	450.41	1.95	>100	>40	1.5±0.05	Lyso, Mito, Golgi, ER	2.6±0.9
6b	484.85	1.93	>100	>100	0.46±0.06	Lyso, Mito, Golgi, ER	5.4±0.6
7[a]	526.50	2.70	>100	>100	0.0034±0.0004	Lyso, Mito, Golgi, ER	-

[a]The Pe values were not determined for these compounds due to their limited solubility in buffer.

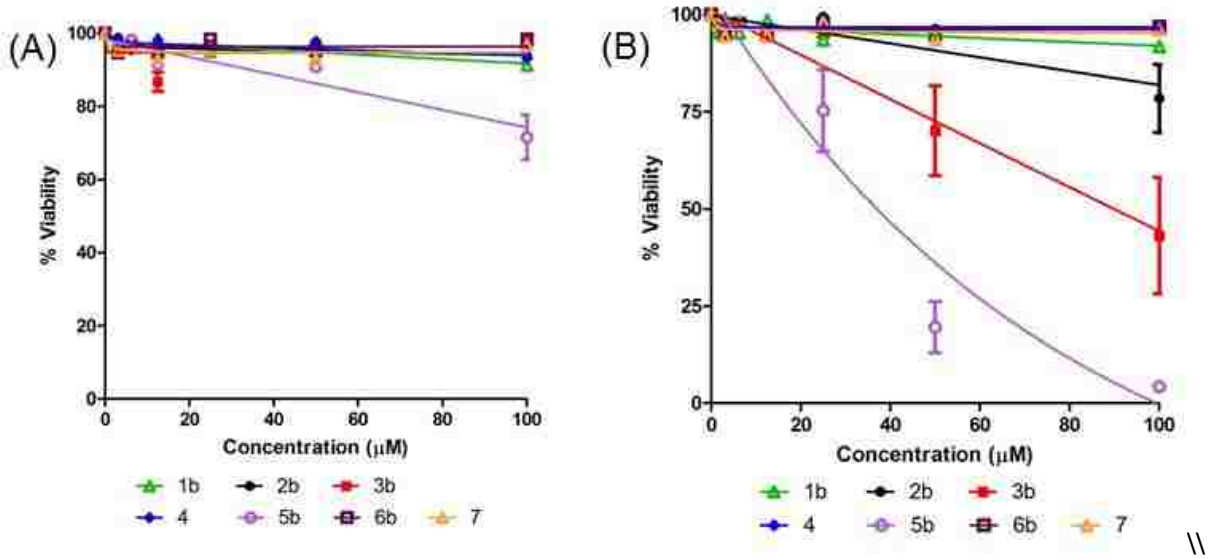

Figure 6.28. Dark cytotoxicity (A) and Phototoxicity (B) of 1b-7 using human glioma T98G cells.

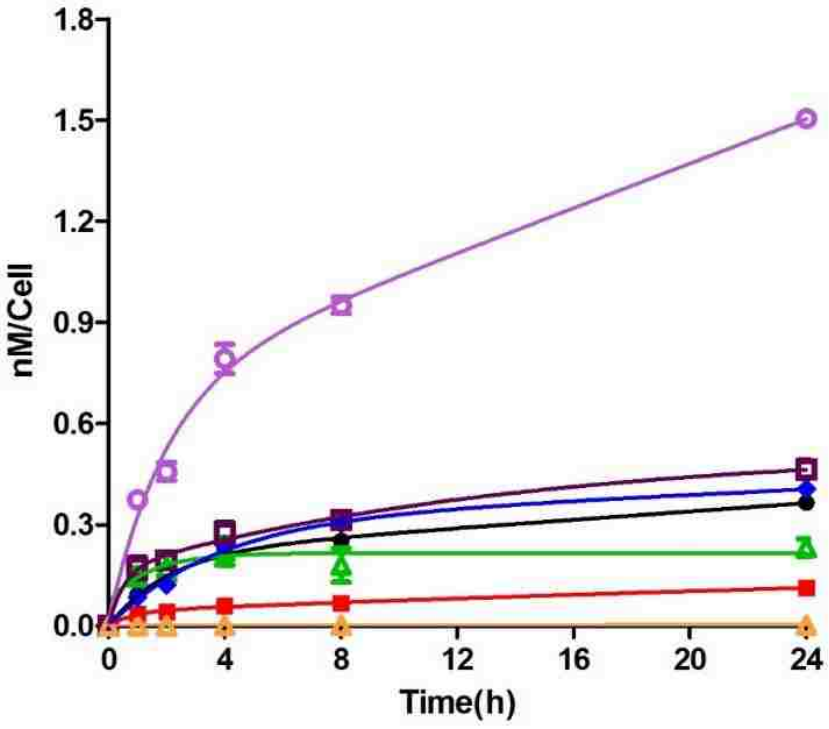

Figure 6.29. Time-dependent uptake of BODIPYs **1b** (green), **2b** (black), **3b** (red), **4** (blue), **5b** (purple), **6b** (dark red) and **7** (orange) at 10 μM in human glioma T98G cells.

All compounds, with the exception of **7**, were taken up rapidly in the first 2 h after which slower uptake was observed for all compounds except for 1b where a plateau was reached. After 24h, the amount of compound accumulated within cells varied considerably (Table 6.2); compound **5b** showed the highest uptake, about 436-fold higher than **7**, followed by **6b** (135-fold higher than **7**), **4** (118-fold higher than **7**), **2b** (106-fold higher than **7**), **1b** (67-fold higher than **7**), and **3b** (33-fold higher than **7**). These results indicate that among this series of compounds, BODIPY **5b** could deliver the largest and therapeutic amount of boron within glioma cells, with very low dark toxicity.

To investigate the sites of subcellular localization of the carboranyl-BODIPYs, HEp2 rather than T98G cells were used for fluorescence microscopy, as the HEp2 cells facilitate imaging by nicely spreading on the surface of the six-well plate. This work was done in collaboration with Ms. Zehua Zhou. The organelle-specific probes BODIPYCeramide (Golgi), LysoSensor Green (lysosomes), MitoTracker Green (mitochondria), and ER Tracker Blue/White (endoplasmic reticulum) were used in the overlay experiments. The results are shown in Figures 6.30-6.33 for BODIPYs **1b-7**. All carboranyl-BODIPYs localized preferentially in the cell ER, as shown in Figures 6.30-6.33. In addition, the BODIPYs were also observed, but to a smaller extent, in the lysosomes, mitochondria, and Golgi apparatus. These results are in agreement with previous studies showing preferential ER-localization for BODIPY molecules.

6.2.3 BBB permeability

The *in vitro* BBB model, as shown in Figure1, was used for the evaluation of BBB permeability of the carboranyl BODIPYs. The hCMEC/D3 cell line is a useful model for studies of BBB permeability because it retains many of the morphological and functional characteristics

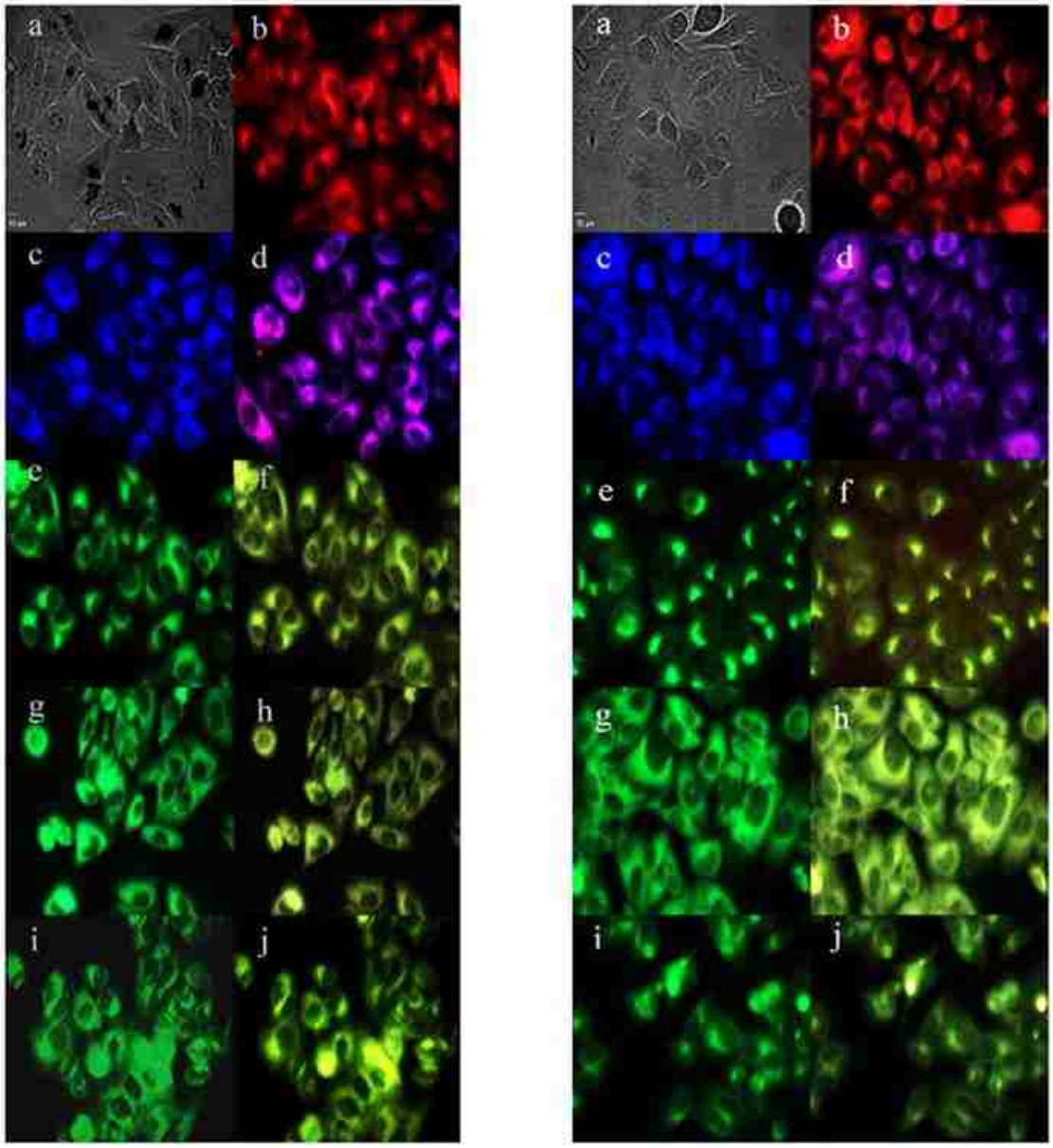

Figure 6.30.Subcellular localization of **1b** (left) and **5b** (right) in HEp2 cells at 10 μM for 6 h: (a) phase contrast, (b) overlay of BODIPY and phase contrast, (c) ERTracker Blue/White, (d) overlay of BODIPY and ER Tracker, (e) BODIPY ceramide, (f) overlay of BODIPY and BODIPY ceramide, (g) MitoTracker Green, (h) overlay of BODIPY and MitoTracker, (i) LysoSensor Green, (j) overlay of BODIPY and LysoSensor. Scale bar: 10 μm.

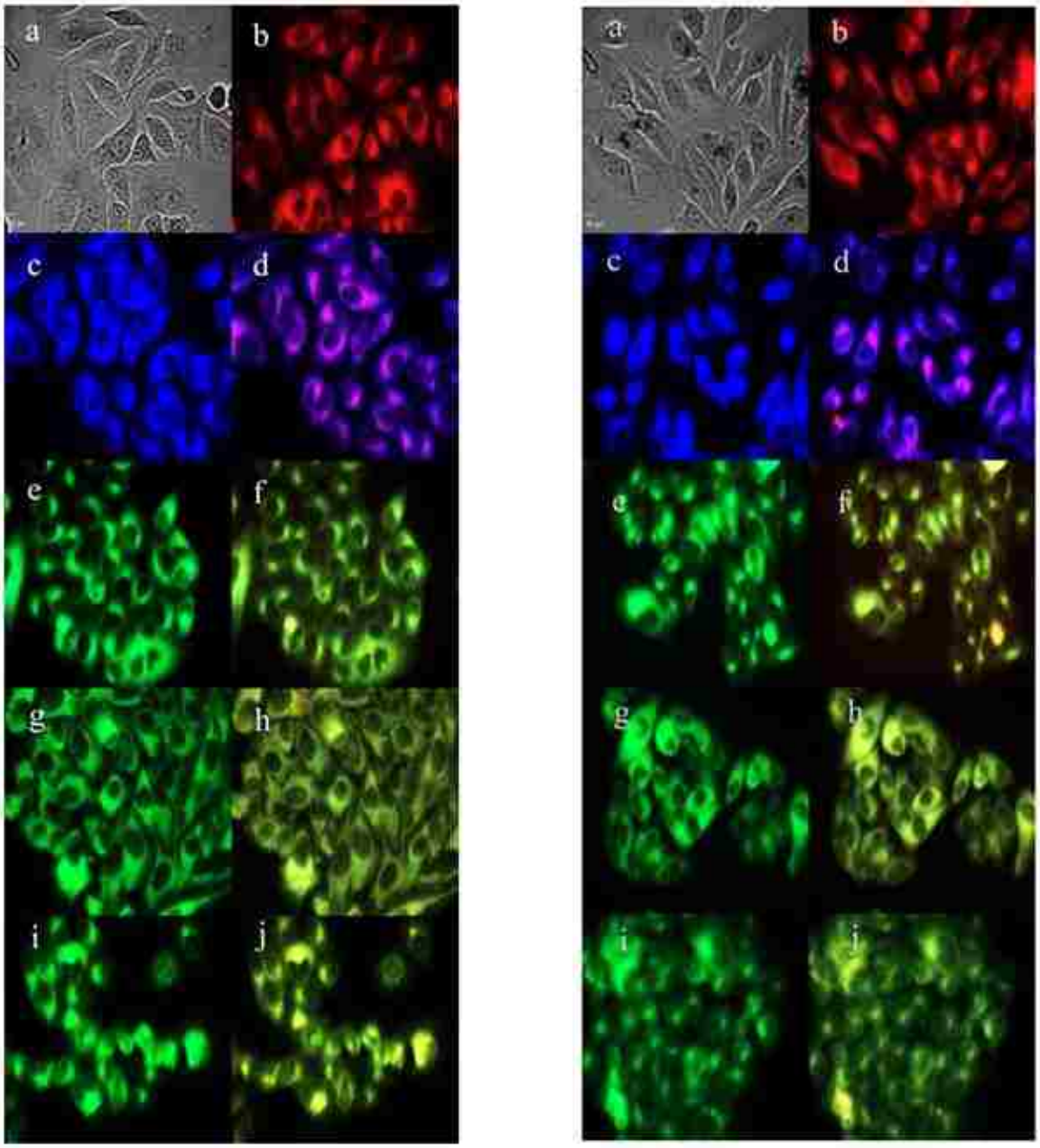

Figure 6.31. Subcellular localization of **2b** (left) and **3b** (right) in HEp2 cells at 10 μM for 6 h: (a) phase contrast, (b) overlay of BODIPY and phase contrast, (c) ERTracker Blue/White, (d) overlay of BODIPY and ER Tracker, (e) BODIPY ceramide, (f) overlay of BODIPY and BODIPY ceramide, (g) MitoTracker Green, (h) overlay of BODIPY and MitoTracker, (i) LysoSensor Green, (j) overlay of BODIPY and LysoSensor. Scale bar: 10 μm.

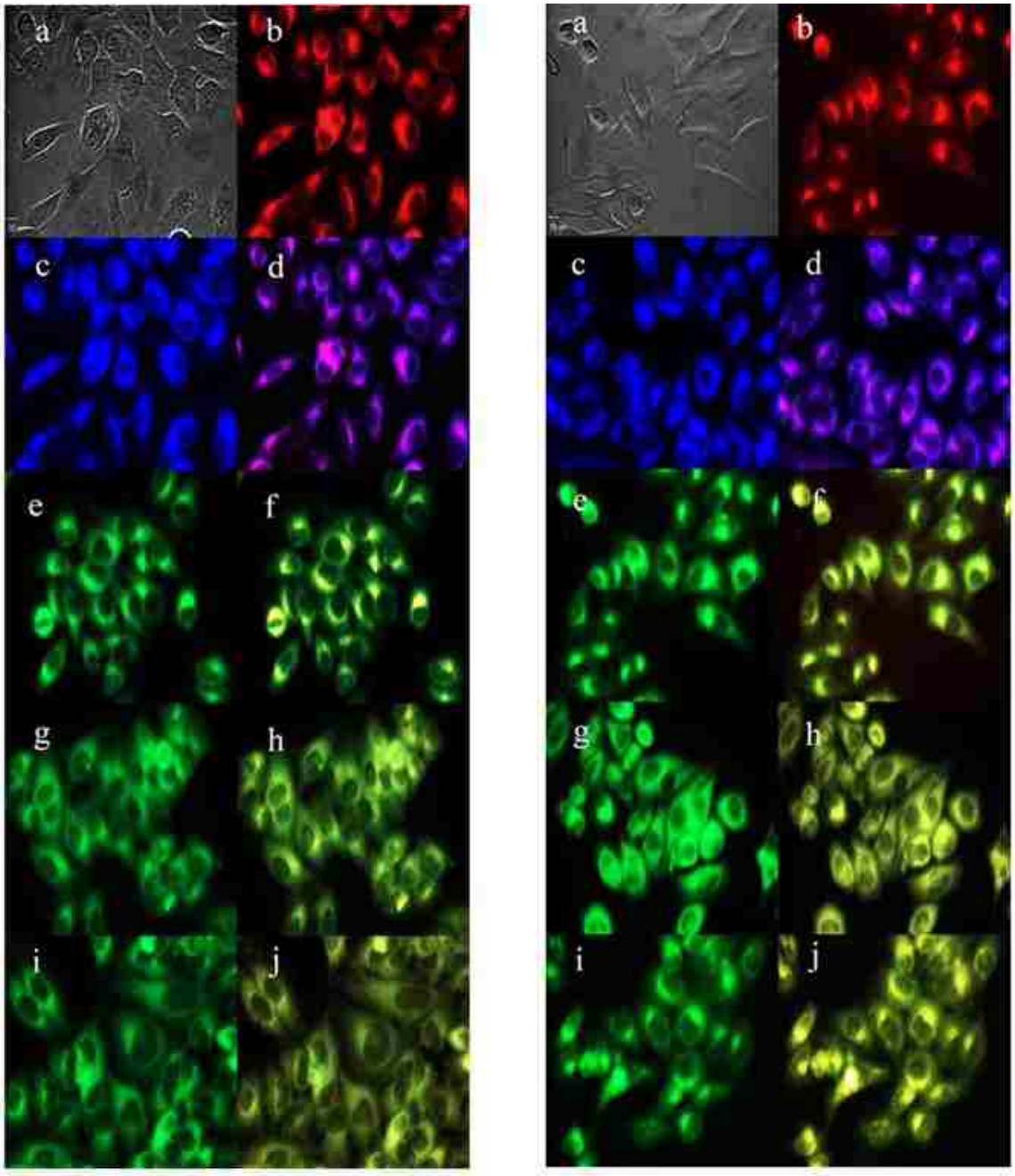

Figure 6.32. Subcellular localization of **4** (left) and **6b** (right) in HEp2 cells at 10 μM for 6 h: (a) phase contrast, (b) overlay of BODIPY and phase contrast, (c) ERTracker Blue/White, (d) overlay of BODIPY and ER Tracker, (e) BODIPY ceramide, (f) overlay of BODIPY and BODIPY ceramide, (g) MitoTracker Green, (h) overlay of BODIPY and MitoTracker, (i) LysoSensor Green, (j) overlay of BODIPY and LysoSensor. Scale bar: 10 μm.

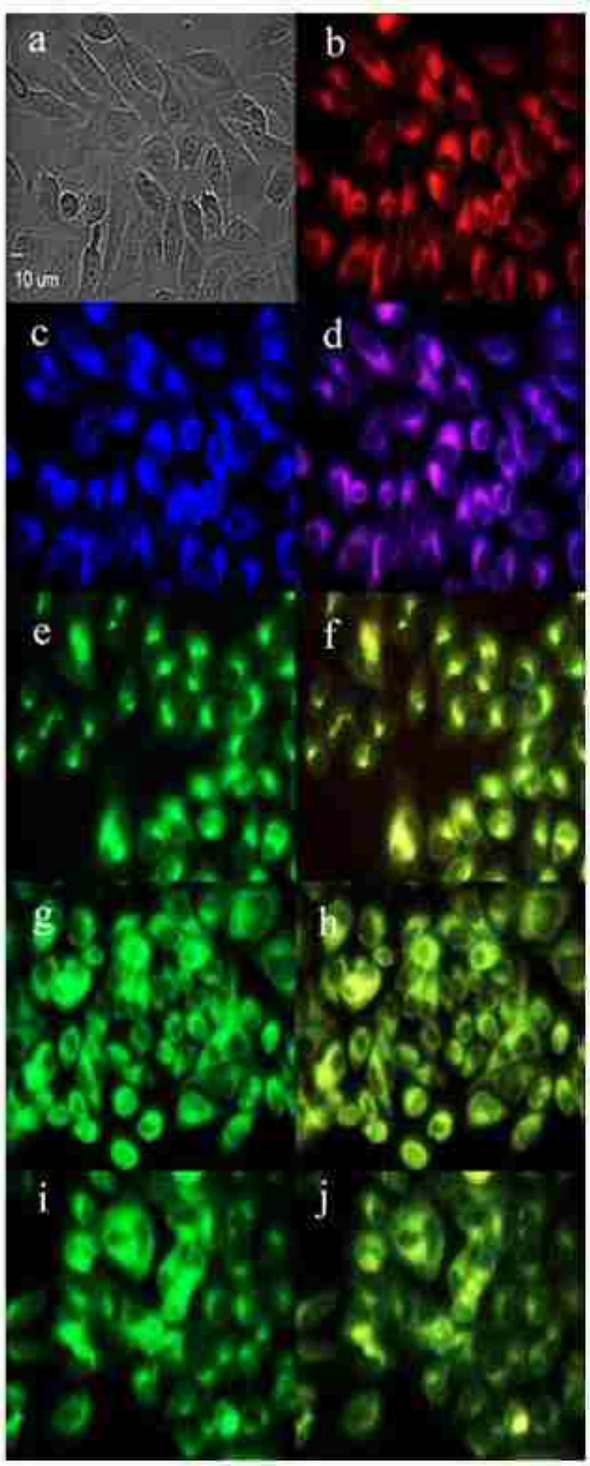

Figure 6.33. Subcellular localization of **7** in HEp2 cells at 10 μM for 6 h: (a) phase contrast, (b) overlay of BODIPY and phase contrast, (c) ERTracker Blue/White, (d) overlay of BODIPY and ER Tracker, (e) BODIPY ceramide, (f) overlay of BODIPY and BODIPY ceramide, (g) MitoTracker Green, (h) overlay of BODIPY and MitoTracker, (i) LysoSensor Green, (j) overlay of BODIPY and LysoSensor. Scale bar: 10 μm.

of human brain endothelial cells.[31-33] Recently, the BBB permeability of a series of carboranyl porphyrins[17] and BODIPYs[18] have been investigated using this model. All the carboranyl porphyrins and BODIPYs tested showed low permeability values ($P_e < 3 \times 10^{-6}$ cm/s) with the exception of BODIPY **3b** which showed higher permeability ($P_e = 4 \times 10^{-5}$ cm/s) than LY. This was attributed to its smaller MW and lower hydrophobic character among the compounds tested. To investigate the effect of MW and lipophilicity of compounds on their ability to cross the BBB, a new series of derivatives of 3b (MW = 422, log P = 1.7), with MW and hydrophobic character (log P) in the ranges 366−527 Da and 1.5−2.7, respectively, were evaluated. For comparison purposes and for evaluation of the cell monolayer integrity, the BBB permeability of LY, a polar fluorescent molecule with MW in the same range (457.24 Da) as the BODIPYs, was also determined. The results obtained are shown in Table 6.2. The P_e values could not be determined for **4** and **7**, due to the precipitation of these compounds in buffer associated with their high lipophilicity and poor water solubility. All carboranyl-BODIPYs tested showed higher BBB permeability compared with LY, a marker for low BBB permeability. Among this series of compounds, **1b** showed the highest P_e value (7-fold higher than LY), probably due to its lower MW (366 Da) and favorable hydrophobic character (log P = 1.50), conferring it the highest solubility in buffer as well as lipophilicity. Compound **2b**, of similar MW (394 Da) and hydrophobicity (log P = 1.69) to **1b**, showed the second highest P_e value. The other BODIPYs, including **3b**, with increased alkyl and/or aryl substitution, MW > 400 Da, and log P > 1.7, showed lower P_e values although still higher than that determined for LY. Compound **5b** showed the lowest P_e value among this series of BODIPYs, slightly higher than LY, and therefore is considered to have low BBB permeability, although it was the most efficiently taken up by the T98 glioma cells (Figure 6.29). All other BODIPYs displayed BBB permeabilities higher than that reported for

phenytoin, which has been used as a marker for medium BBB permeability.[31, 34] Among the new BODIPYs, **1b**, **2b**, and **6b** showed higher permeability than **3b**, which displays a slightly higher P_e value than phenytoin. These results show that both the MW and amphiphilicity of the BODIPYs influence their permeability across the BBB and that small amphiphilic carboranyl-BODIPYs of MW < 400 Da and log P < 1.7, such as **1b** and **2b**, are the most efficient at diffusing across the BBB by passive diffusion.

6.4 Conclusions

A series of seven amphiphilic carboranyl-BODIPYs with MW within the range 366−527 Da, including a previously reported BODIPY known to permeate across a BBB model, were synthesized in good yields from the corresponding chloro-BODIPYs by nucleophilic substitution. The structures of the BODIPYs were confirmed by NMR, HRMS and, in the cases of **2b** and **5b**, by X-ray crystallography. The carboranyl-BODIPYs display strong absorption and emission bands in the visible region of the spectrum and quantum yields in dichloromethane in the range 0.6−0.03. All BODIPYs showed low dark toxicity (IC_{50} > 100 μM) in human glioma T98G cells, an important property of potential boron delivery agents because of the high boron concentration requirement in BNCT (>20 μg/g tumor). The BODIPYs also showed low phototoxicity (IC_{50} >80 μM) with the exception of **5b** (IC_{50} =40 μM), probably as a result of its remarkably high uptake into T98G glioma cells. On the other hand, BODIPY **1b** showed the largest permeability across the BBB model consisting of hCMEC/D3 cells. Our results showed that the BODIPYs with MW < 400 Da and log P < 1.7 are the most efficient at crossing the BBB model. The most hydrophobic compound **7** (log P = 2.7) was poorly soluble in aqueous solutions, showed very low uptake into T98G cells, and its precipitation in buffer precluded determination of its BBB permeability. All BODIPYs tested showed higher BBB permeability compared with LY, as well as low dark

cytotoxicity and therefore could potentially be efficient boron delivery agents for BNCT of brain tumors. Among this series, **1b** and **2b** showed the highest BBB permeability while **5b** and **6b** accumulated the most within tumor cells; therefore, these are the most promising BNCT agents.

6.5 Reference

1. Soloway, A. H.; Tjarks, W.; Barnum, B. A.; Rong, F.-G.; Barth, R. F.; Codogni, I. M.; Wilson, J. G. The Chemistry of Neutron Capture Therapy. *Chem. Rev.* **1998,** *98* (4), 1515-1562.

2. Barth, R. F.; Coderre, J. A.; Vicente, M. G. H.; Blue, T. E. Boron Neutron Capture Therapy of Cancer: Current Status and Future Prospects. *Clin. Cancer. Res.* **2005,** *11*, 3987.

3. Barth, R. F.; H Vicente, M.; Harling, O. K.; Kiger, W.; Riley, K. J.; Binns, P. J.; Wagner, F. M.; Suzuki, M.; Aihara, T.; Kato, I.; Kawabata, S. Current status of boron neutron capture therapy of high grade gliomas and recurrent head and neck cancer. *Radiat. Oncol.* **2012,** *7* (1), 1-21.

4. Kankaanranta, L.; Seppälä, T.; Koivunoro, H.; Saarilahti, K.; Atula, T.; Collan, J.; Salli, E.; Kortesniemi, M.; Uusi-Simola, J.; Välimäki, P.; Mäkitie, A.; Seppänen, M.; Minn, H.; Revitzer, H.; Kouri, M.; Kotiluoto, P.; Seren, T.; Auterinen, I.; Savolainen, S.; Joensuu, H. Boron Neutron Capture Therapy in the Treatment of Locally Recurred Head-and-Neck Cancer: Final Analysis of a Phase I/II Trial. *Int. J. Radiat. Oncol. Biol. Phys.* **2012,** *82* (1), e67-e75.

5. Hopewell, J. W.; Gorlia, T.; Pellettieri, L.; Giusti, V.; H-Stenstam, B.; Sköld, K. Boron neutron capture therapy for newly diagnosed glioblastoma multiforme: An assessment of clinical potential. *Appl. Radiat. Isot.* **2011,** *69* (12), 1737-1740.

6. Pardridge, W. The blood-brain barrier: Bottleneck in brain drug development. *NeuroRx* **2005,** *2* (1), 3-14.

7. Sibrian-Vazquez, M.; Vicente, M. G. H., Boron tumor-delivery for BNCT: Recent Developments and Perspectives. In *Boron Science: New Technologies & Applications*, Hosmane, Narayan S. ed.; CRC Press: Boca Raton, FL, 2011; pp 203-232.

8. Deeken, J. F.; Löscher, W. The Blood-Brain Barrier and Cancer: Transporters, Treatment, and Trojan Horses. *Clin. Cancer. Res.* **2007,** *13* (6), 1663-1674.

9. Provenzale, J. M.; Mukundan, S.; Dewhirst, M. The Role of Blood-Brain Barrier Permeability in Brain Tumor Imaging and Therapeutics. *Am. J. Roentgenol.* **2005,** *185* (3), 763-767.

10. Roda, E.; Nion, S.; Bernocchi, G.; Coccini, T. Blood–brain barrier (BBB) toxicity and permeability assessment after L-(4-10Boronophenyl)alanine, a conventional B-containing drug for boron neutron capture therapy, using an in vitro BBB model. *Brain Res.* **2014,** *1583* (0), 34-44.

11. Sivaev, I. B.; Bregadze, V. V. Polyhedral Boranes for Medical Applications: Current Status and Perspectives. *Eur. J. Inorg. Chem.* **2009,** *2009* (11), 1433-1450.

12. Banks, W. A. Characteristics of compounds that cross the blood-brain barrier. *BMC Neurol.* **2009,** *9* (Suppl 1), S3-S3.

13. Vries, H. E. d.; Kuiper, J.; Boer, A. G. d.; Berkel, T. J. C. V.; Breimer, D. D. The Blood-Brain Barrier in Neuroinflammatory Diseases. *Pharmacol. Rev.* **1997,** *49* (2), 143-156.

14. Palmer, A. M.; Alavijeh, M. S. Translational CNS medicines research. *Drug Discov. Today* **2012,** *17* (19–20), 1068-1078.

15. Habgood, M. D.; Begley, D. J.; Abbott, N. J. Determinants of Passive Drug Entry into the Central Nervous System. *Cell. Mol. Neurobiol.* **2000,** *20* (2), 231-253.

16. Coderre, J. A.; Turcotte, J. C.; Riley, K. J.; Binns, P. J.; Harling, O. K.; Kiger, W. S. Boron Neutron Capture Therapy: Cellular Targeting of High Linear Energy Transfer Radiation. *Technol. Cancer Res. Treat.* **2003,** *2* (5), 355-375.

17. Bhupathiraju, N. V. S. D. K.; Hu, X.; Zhou, Z.; Fronczek, F. R.; Couraud, P.-O.; Romero, I. A.; Weksler, B.; Vicente, M. G. H. Synthesis and in Vitro Evaluation of BBB Permeability, Tumor Cell Uptake, and Cytotoxicity of a Series of Carboranylporphyrin Conjugates. *J. Med. Chem.* **2014,** *57* (15), 6718-6728.

18. Gibbs, J. H.; Wang, H.; Bhupathiraju, N. V. S. D. K.; Fronczek, F. R.; Smith, K. M.; Vicente, M. G. H. Synthesis and properties of a series of carboranyl-BODIPYs. *J. Organomet. Chem.* **2015,** *798, Part 1*, 209-213.

19. Loudet, A.; Burgess, K. BODIPY Dyes and Their Derivatives: Syntheses and Spectroscopic Properties. *Chem. Rev.* **2007,** *107* (11), 4891-4932.

20. Boens, N.; Leen, V.; Dehaen, W. Fluorescent indicators based on BODIPY. *Chem. Soc. Rev.* **2012,** *41* (3), 1130-1172.

21. Lu, H.; Mack, J.; Yang, Y.; Shen, Z. Structural modification strategies for the rational design of red/NIR region BODIPYs. *Chem. Soc. Rev.* **2014,** *43* (13), 4778-4823.

22. Kowada, T.; Maeda, H.; Kikuchi, K. BODIPY-based probes for the fluorescence imaging of biomolecules in living cells. *Chem. Soc. Rev.* **2015,** *44* (14), 4953-4972.

23. Godoy, J.; Vives, G.; Tour, J. M. Synthesis of Highly Fluorescent BODIPY-Based Nanocars. *Org. Lett.* **2010,** *12* (7), 1464-1467.

24. Wang, H.; Vicente, M. G. H.; Fronczek, F. R.; Smith, K. M. Synthesis and Transformations of 5-Chloro-2,2′-Dipyrrins and Their Boron Complexes, 8-Chloro-BODIPYs. *Chem. Eur. J.* **2014,** *20* (17), 5064-5074.

25. Zhao, N.; Vicente, M. G. H.; Fronczek, F. R.; Smith, K. M. Synthesis of 3,8-Dichloro-6-ethyl-1,2,5,7-tetramethyl–BODIPY from an Asymmetric Dipyrroketone and Reactivity Studies at the 3,5,8-Positions. *Chem. Eur. J.* **2015,** *21* (16), 6181-6192.

26. Hao, E.; Fabre, B.; Fronczek, F. R.; Vicente, M. G. H. Syntheses and Electropolymerization of Carboranyl-Functionalized Pyrroles and Thiophenes. *Chem. Mater.* **2007,** *19* (25), 6195-6205.

27. Leen, V.; Yuan, P.; Wang, L.; Boens, N.; Dehaen, W. Synthesis of Meso-Halogenated BODIPYs and Access to Meso-Substituted Analogues. *Org. Lett.* **2012,** *14* (24), 6150-6153.

28. Lakowicz, J. R., In *Principles of Fluorescence Spectroscopy*, Springer: New York: 2006.

29. Kraszni, M.; Bányai, I.; Noszál, B. Determination of Conformer-Specific Partition Coefficients in Octanol/Water Systems. *J. Med. Chem.* **2003,** *46* (11), 2241-2245.

30. Siflinger-Birnboim, A.; del Vecchio, P. J.; Cooper, J. A.; Blumenstock, F. A.; Shepard, J. M.; Malik, A. B. Molecular sieving characteristics of the cultured endothelial monolayer. *J. Cell. Physiol.* **1987,** *132* (1), 111-117.

31. Cucullo, L. C., P.-O.; Weksler, B.; Romero, I.-A.; Hossain, M.; Rapp, E.; Janigro, D. Immortalized Human Brain Endothelial Cells and Flow-based Vascular Modeling: a Marriage of Convenience for Rational Neurovascular Studies. *J. Cereb. Blood Flow Metab.* **2008,** *28*, , 312−328.

32. Weksler, B. B.; Subileau, E. A.; Perrière, N.; Charneau, P.; Holloway, K.; Leveque, M.; Tricoire-Leignel, H.; Nicotra, A.; Bourdoulous, S.; Turowski, P.; Male, D. K.; Roux, F.; Greenwood, J.; Romero, I. A.; Couraud, P. O. Blood-brain barrier-specific properties of a human adult brain endothelial cell line. *The FASEB Journal* **2005,** *19* (13), 1872-1874.

33. Weksler, B.; Romero, I. A.; Couraud, P.-O. The hCMEC/D3 cell line as a model of the human blood brain barrier. *Fluids and Barriers of the CNS* **2013,** *10* (1), 16.

34. Ríos Martínez, C. H.; Miller, F.; Ganeshamoorthy, K.; Glacial, F.; Kaiser, M.; de Koning, H. P.; Eze, A. A.; Lagartera, L.; Herraiz, T.; Dardonville, C. A New Nonpolar N-Hydroxy Imidazoline Lead Compound with Improved Activity in a Murine Model of Late-Stage Trypanosoma brucei brucei Infection Is Not Cross-Resistant with Diamidines. *Antimicrob. Agents Chemother.* **2015,** *59* (2), 890-904.

CHAPTER 7 : SYNTHESIS AND OPTOPPHYSICAL INVESTIGATION OF A SERIES OF PUSH-PULL BORON DIPYRROMETHENES (BODIPYS)

7.1 Introduction

Push-pull chromophores with electron donors (D) and electron acceptors (A) attached to a π spacer (D- π -A) have been a subject of interest due to their wide applications in organic light-emitting devices,[1] two photon dyes,[2-3] and dye-sensitized solar cells[4-6]. Porphyrins and phthalocyanines, bearing both electron donors and electron acceptors (D- π -A), have attracted considerable interest in the recent decades to be potentially used as dye-sensitized solar cells.[5, 7-13] Recently, boron dipyrromethanes (BODIPYs), an analogue of porphyrins, featuring excellent optical and electrochemical properties, have emerged as the π spacer of growing interest owing to their potential applications in biological imaging, biological labeling, drug delivery, sensing and in theranostics as well as in photovoltaic field.[14-19] BODIPYs are usually strongly UV-vis absorbing and emit sharp fluorescence peaks with high quantum yields. BODIPYs are also relatively stable in physiological environment and have high photostability. Besides, BODIPYs have high structural tunability which render them easy access to manipulate their properties (*e.g.*, photophysical properties, water solubility, redox potential).

The BODIPY core itself is electron deficient and the installation of electron donating group to the BODIPY endow them the push and pull effect within the molecule.[20-22] In the recent years, to increase the push-pull effect of the BODIPY, electron withdrawing group is also introduced to the BODIPY core to further enhance the pull effect; however, the study of design, characterization and investigation of BODIPYs with both push and pull substituents is limited so far. Currently, the push-pull effect has been studied mainly on three BODIPY platforms with both electron donating (push) and withdrawing (pull) substituents[23-31] (Figure 7.1: I, II and III). The push-pull

investigation on extended dimeric aza-BODIPY dyes was also reported.[32] The attachment of push and pull moieties to the BODIPY skeleton can cause dramatic change in their spectroscopic and electrochemical properties.[24-26, 33] For example, the strong electron donating group (*e.g.*, diphenylaminophenyl) and electron withdrawing group (*e.g.*, 4-carboxylic phenyl) on the BODIPY could lead to enhancement of charge transfer within the molecule for them to be potentially used as dye-sensitized solar cells[27-30] or two photon excitation dyes[2, 31]. The push-pull effects can also red-shift the BODIPYs to the near-infrared (NIR) absorbing region and render them potential use in biological sciences (*e.g.*, biological imaging and sensing).[34] For example, a 66 nm bathochromic shift was caused by introducing electron withdrawing cyano group (-CN) and electron donating methoxy group (-OMe) to the para positions of 1,7-phenyl and 3,5-phenyl substituents of the tetra-phenyl aza BODIPY, respectively.[34]

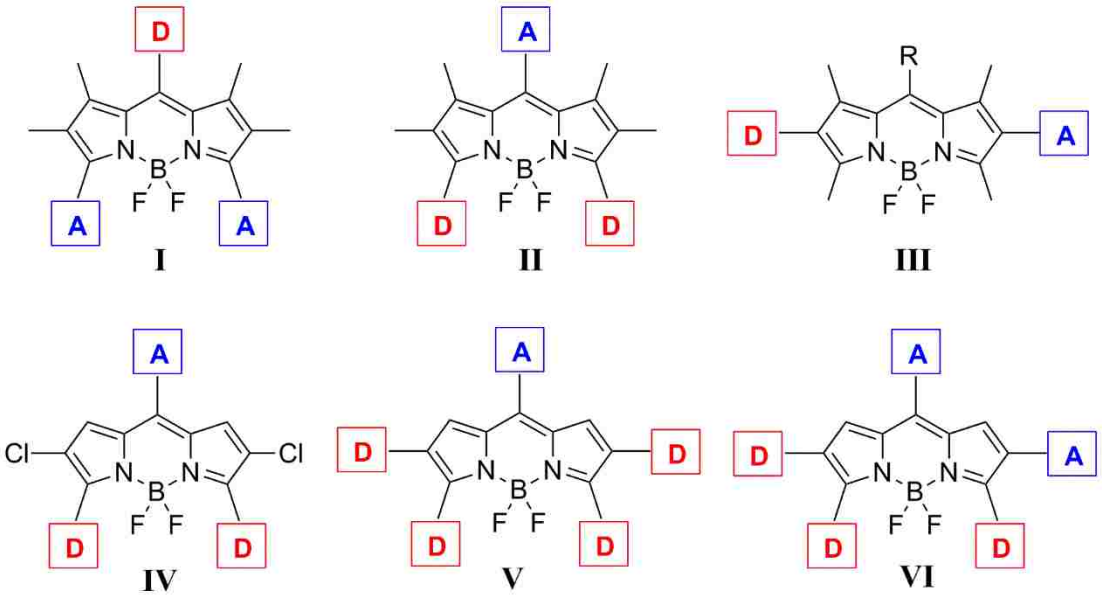

Figure 7.1. Platforms of push-pull BODIPYs.

The reported DFT calculated electronic structure of an unsubstituted model BODIPY showed large electron density of HOMO at 3,5-positions and large electron density of LUMO at

8-position.[16] Therefore, introducing the electron donating group to the 3,5-positions and electron withdrawing group to the 8-positon of the BODIPYs should have effect on their spectroscopic and electrochemical properties by changing the characteristics of HOMO and LUMO (*e.g.*, lower the energy gap between HOMO and LUMO).

Herein, we design and synthesize three new push-pull BODIPY platforms (Figure 7.1: IV, V, VI) with multiple sets of push-pull moieties from the penta-Cl BODIPY using Pd (0)-catalyzed Stille and Suzuki cross-coupling reactions with easily obtained boronic acids and stannane reagents. For all the platforms, electron donating group (-OMe) and electron withdrawing group (-COOBn, -CN) were introduced to para positions of 3,5- and 8- phenyl substituents on the BODIPYs, respectively. As the electron-rich thiophene, especially at the 2 and 6 positions, was shown to cause large bathochromic shift and Stokes shift of BODIPYs,[35-37] two thiophene groups (donor) were additionally installed at 2 and 6 positions to have platform V (Figure 7.1). To investigate how push-pull effect on 2,6 positions affect the spectroscopic and electrochemical properties of BODIPYs, an additional set of push-pull moiety was introduced to 2,6 position to have platform VI (Figure 7.1). Cyclic voltammetry and DFT calculations were conducted on all the BODIPYs and a systematic comparison of these BODIPYs was made to investigate the influence of push-pull effect on their spectroscopic and electrochemical properties. The systematic structure-property investigation exhibit tunability of BODIPY's spectroscopic and electrochemical properties and may provide guidance for the future design of new BODIPYs in different applications.

7.2 Experimental

7.2.1 Synthesis of BODIPYs

All reagents and solvents were purchased from Sigma-Aldrich and Fisher Scientific and used as received. Reactions were monitored by analytical TLC (precoated, polyester backed, 60 Å, 0.2 mm, Sorbent Technologies). Purifications were completed by column chromatography that was performed on silica gel (230-400 mesh, 60 Å, Sorbent Technologies) or preparative TLC plates (f 254 VWR). ^{1}H and ^{13}C $\{^{1}H\}$ NMR spectra were obtained using a Bruker AV-400 Nanobay spectrometer (400 MHz for ^{1}H NMR and 100 MHz for ^{13}C $\{^{1}H\}$ NMR) and a Bruker AV-500 spectrometer (500 MHz for ^{1}H NMR and 125 MHz for ^{13}C $\{^{1}H\}$ NMR) at 298 K. ^{11}B NMR spectra were obtained on a Bruker AV-400 III (128 MHz), using $BF_3 \bullet OEt_2$ as reference. Chemical shifts (δ) are given in parts per million (ppm) in $CDCl_3$ (7.27 ppm for ^{1}H NMR, 77.0 ppm for ^{13}C $\{^{1}H\}$ NMR) and coupling constants (J) are given in Hz. All High resolution mass spectra (HRMS) were obtained using a 6210 ESI-TOF mass spectrometer (Agilent Technologies). Melting points were measured using a MEL-TEMP® capillary melting point apparatus equipped with a FLUKE 51 II thermometer. Crystal structures were determined using data collected at low temperature (90K) on a Bruker Kappa Apex-II DUO diffractometer equipped with a Triumph focusing monochromator for the Mo X-ray beam, a Cu microfocus X-ray source, and an Oxford Cryosystems Cryostream chiller.

General Procedure for Suzuki Cross-Couplings of BODIPYs. The starting BODIPY was added to a 15 mL round-bottomed flask followed by the addition of either 3 mol % of $Pd(PPh_3)_4$ (for **5a**, **5b**) or $Pd(PCy_3)G2$ (for **6a**, **6b** and **8**). The flask was evacuated and refilled with nitrogen three times and toluene (4 mL) and 1M Na_2CO_3 (aq) (1 mL) were added under nitrogen. Boronic acid was added portionwise, and the reaction mixture was stirred and heated

under nitrogen at 90-100ºC. The reaction was monitored by analytical TLC every 30-60 min. After completion, the reaction mixture was added water (20 mL) and extracted with dichloromethane (10 mL × 3). The organic layers were combined, washed with aqueous saturated brine and water, and dried over anhydrous Na_2SO_4. The solvent was removed by rotary evaporator and the obtained reaction residue was purified by column chromatography with dichloromethane/hexanes or ethyl acetate /hexanes as the elution solvents.

8-(4-benzyloxycarbonylphenyl)-2,3,5,6-tetrachloro-BODIPY 5a. The BODIPY **5a** was prepared from BODIPY **1** (20.00 mg, 0.0549mmol) synthesized as previously reported[35] and 2.5 eq of 4-benzyloxycarbonylphenyl boronic acid (70.3 mg, 0.275 mmol), yielding 20.8 mg, 70.0 % of BODIPY **5a** as red solid: mp (185.9-187.5 ºC); ^{1}H NMR ($CDCl_3$, 400 MHz) δ (ppm) = 8.26-8.28 (m, 2H), 7,57-7.59 (m, 2H), 7.42-7.51 (m, 5H), 6.79 (s, 2H), 5.45 (s, 2H); ^{13}C NMR (CDCl3, 125 MHz) δ (ppm) = 166.2, 143.9, 142.2, 135.8, 235.5, 132.9, 131.2, 130.3, 130.1, 128.7, 128.6, 128.3, 127.9, 122.3, 67.4; ^{11}B NMR ($CDCl_3$, 128 MHz) δ (ppm) = -0.24-0.18 (1B, t, $^1J_{(B,F)}$ = 26.4 Hz); HRMS (ESI-TOF): *m/z* calculated for $C_{23}H_{13}BCl_4F_2N_2O_2$: 536.9834; found: 536.9809 [M^-].

8-(4-cyanophenyl)-2,3,5,6-tetrachloro-BODIPY 5b. The BODIPY **5b** was prepared from BODIPY **1** (11.4 mg, 0.0310mmol) and10 eq of 4-cyanophenyl boronic acid (46.0 mg, 0.320 mmol), yielding 6.68 mg, 50.2 % of BODIPY 5b as red solid: mp (280.1-282.2 ºC); ^{1}H NMR ($CDCl_3$, 400 MHz) δ (ppm) = 7.89-7.90 (m, 2H), 7.62-7.64 (m, 2H), 6.76 (s, 2H); ^{13}C {^{1}H} NMR ($CDCl_3$, 125 MHz) δ (ppm) = 144.6, 140.6, 135.9, 132.6, 131.0, 130.8, 127.6, 122.7, 117.4, 115.3; ^{11}B NMR ($CDCl_3$, 128 MHz) δ (ppm) = -0.26-0.15 (1B, t, $^1J_{(B,F)}$ = 26.7 Hz); HRMS (ESI-TOF): *m/z* calcd for $C_{16}H_6BCl_4F_2N_3$: 427.9419; found: 427.9412 [M^-].

8-(4-benzyloxycarbonylphenyl)-3,5-di (4-methoxyphenyl)-2,6-dichloro-BODIPY 6a. The BODIPY **6a** was prepared from BODIPY **5a** (12.9 mg, 0.0239 mmol) and 3 eq of 4-

methoxyphenyl boronic acid (36.3 mg, 0.238 mmol), yielding 9.83 mg, 60.2 % of BODIPY 6a as dark blue solid: mp (233-235 ^{o}C); ^{1}H NMR ($CDCl_3$, 500 MHz) δ (ppm) = 8.28-8.29 (m, 2H), 7.66-7.69 (m, 6H), 7.51-7.53 (m, 2H), 7.41-7.47 (m, 3H), 6.98-6.99 (m, 4H), 6.82 (s, 2H), 3.87 (s, 6H); ^{13}C {^{1}H} NMR ($CDCl_3$, 125 MHz) δ (ppm) = 165.5, 161.0, 155.2, 137.9, 135.7, 132.6, 132.1, 132.0, 130.4, 129.9, 128.7, 128.5, 128.3, 127.8, 123.2, 121.4, 113.6, 67.2, 55.3; ^{11}B NMR ($CDCl_3$, 128 MHz) δ (ppm) = 0.35-0.82 (1B, t, $^{1}J_{(B,F)}$ =30.7 Hz); HRMS (ESI-TOF): *m/z* calcd for $C_{37}H_{27}BCl_2F_2N_2O_4$: 681.1451; found: 681.1450 [M^-].

8-(4-cyanophenyl)-3,5-di(4-methoxyphenyl)-2,6-dichloro-BODIPY 6b. The BODIPY **6b** was prepared from BODIPY **5b** (8.50 mg, 0.0197 mmol) and 3 eq of 4-methoxyphenyl boronic acid (30.0 mg, 0.197 mmol), yielding 7.47 mg, 66.0 % of BODIPY **6b** as dark blue solid: mp (288-290 ^{o}C); ^{1}H NMR ($CDCl_3$, 500 MHz) δ (ppm) = 7.87-7.89 (d, J = 7.7 Hz, 2H), 7.66-7.71 (m, 6H), 6.97-6.98 (d, J = 8.2 Hz, 4H), 6.76 (s, 2H), 3.86 (s, 6H); ^{13}C {^{1}H} NMR ($CDCl_3$, 125 MHz) δ (ppm) = 161.1, 155.7, 139.6, 138.0, 132.3, 132.0, 131.0, 128.0, 127.5, 123.6, 121.2, 117.8, 114.5, 113.6, 55.3; ^{11}B NMR ($CDCl_3$, 128 MHz) δ (ppm) = 0.35-0.82 (1B, t, $^{1}J_{(B,F)}$ =30.6 Hz); HRMS (ESI-TOF): *m/z* calcd for $C_{30}H_{20}BCl_2F_2N_3O_2$: 572.1035; found: 572.1026 [M^-].

8-(4-cyanophenyl)-3,5-di(4-methoxyphenyl)-2-(4-methoxyphenyl)-6-(4-cyanophenyl)-BODIPY 8. The BODIPY **8** was prepared from BODIPY **6b** (8.12 mg, 0.0141), 5 eq of 4-methoxyphenyl boronic acid (10.7 mg, 0.0707 mmol), and 5 eq of 4-cyanophenyl boronic acid (10.4 mg, 0.0707 mmol), yielding 5.43 mg, 54.0 % of BODIPY **8** as dark blue solid: mp (273-275 ^{o}C); ^{1}H NMR ($CDCl_3$, 500 MHz) δ (ppm) = 7.90-7.88 (m, 2H), 7.78-7.80 (m, 2H), 7.44-7.47 (m, 4H), 7.38-7.40 (m, 2H), 7.12-7.10 (M, 2H), 6.93-6.95 (M, 2H), 6.83-6.89 (m, 6H), 6.73-6.75 (m, 2H), 3.84 (s, 3H), 3.83 (s, 3H), 3.77 (s, 3H); ^{13}C {^{1}H} NMR (CDCl3, 125 MHz) δ (ppm) = 160.8, 160.5, 160.0, 159.1, 155.2, 139.4, 138.9, 138.8, 136.5, 134.9, 133.7, 132.3, 132.1, 132.0,

131.9, 131.1, 129.6, 128.7, 128.1, 126.6, 125.7, 123.4, 123.3, 118.9, 118.0, 114.2, 113.8, 113.8, 113.6, 110.2, 55.3, 55.2; ^{11}B NMR ($CDCl_3$, 128 MHz) δ (ppm) = 0.68-1.15 (1B, t, $^{1}J_{(B,F)}$ =30.5 Hz); HRMS (ESI-TOF): *m/z* calcd for $C_{44}H_{31}BF_2N_4O_3$: 711.2499; found: 711.2482 [M^-].

General Procedure for Stille Cross-Couplings of BODIPYs. The starting BODIPY **1** was added to a 15 mL round-bottomed flask followed by the addition of organotin reagent, 3% mol of $Pd(PPh_3)_4$ (for **2**) or $Pd(PCy_3)G2$ (for **3**, **4**, **7**). The flask was evacuated and refilled with nitrogen three times. Toluene (5 mL) was added, and the reaction mixture was stirred and heated at 90-100ºC under nitrogen. Analytical TLC was used to monitor the reaction every 30-60 min. After completion, toluene was removed by rotary evaporator, and the resulting residue was purified by column chromatography with dichloromethane/or ethyl acetate /hexanes as the elution solvents.

The BODIPY **2** was prepared from BODIPY **1** (10.5 mg, 0.0288 mmol) and 10 eq of tributylphenylstannane (106 mg, 0.288 mmol), yielding 8.55 mg, 60.7 % of BODIPY **2** as purple solid: mp (215-217 ºC); ^{1}H NMR ($CDCl_3$, 400 MHz) δ (ppm) = 7.58 – 7.68 (m, 9H), 7.44-7.45 (m, 6H), 6.91 (s, 2H); ^{13}C {^{1}H} NMR ($CDCl_3$, 125 MHz) δ (ppm) = 155.0, 144.6, 133.4, 133.0, 130.9, 130.4, 130.2,130.2, 130.0, 129.2, 128.7, 128.4, 127.9, 123.0, 122.9; ^{11}B NMR ($CDCl_3$, 128 MHz) δ (ppm) = 0.27-0.74 (1B, t, $^{1}J_{(B,F)}$ = 29.9 Hz); HRMS (ESI-TOF): *m/z* calcd for $C_{27}H_{17}BCl_2F_2N_2$: 487.0872; found: 487.0868 [M^-].

3,5,8-triphenyl-2,6-dithiophen-BODIPY 3. The BODIPY **3** was prepared from BODIPY **2** (6.21 mg, 0.0127 mmol) and 10 eq of 2-(tributylstannyl) thiophene (47.4 mg, 0.127 mmol), yielding 4.60 mg, 62.0 % of BODIPY **3** as dark blue solid: mp (178-180 ºC); ^{1}H NMR ($CDCl_3$, 500 MHz) δ (ppm) = 7.72 – 7.70 (m, 2H), 7.68 – 7.62 (m, 3H), 7.54-7.53 (m, 4H), 7.46-7.39 (m, 6H), 7.10-7.09 (dd, J = 5.1, 1.1 Hz, 2H), 7.01 (s, 2H), 6.84-6.82 (dd, J = 5.1, 3.6 Hz, 2H), 6.56-6.55 (dd, J = 3.7, 1.1 Hz, 2H); ^{13}C {^{1}H} NMR ($CDCl_3$, 125 MHz) δ (ppm) = 156.2, 144.27, 135.8,

134.5, 134.1, 131.4, 130.6, 130.5, 130.2, 129.5, 128.6, 128.1, 128.0, 127.2, 126.8, 125.1, 124.7; ^{11}B NMR ($CDCl_3$, 128 MHz) δ (ppm) = 0.44-0.90 (1B, t, $^{1}J_{(B,F)}$ = 29.7 Hz); HRMS (ESI-TOF) *m/z* calcd for $C_{35}H_{23}BFN_2S_2$: 564.1411; found: 564.142 $[M-F]^+$.

2,3,5,6,8-pentaphenyl-BODIPY 4. The BODIPY **4** was prepared from BODIPY **2** (6.51 mg, 0.0133 mmol) and 10 eq of tributylphenylstannane (48.8 mg, 0.133 mmol) with , yielding 3.12 mg, 41.0 % of BODIPY **4** as dark blue solid: mp (273-275 ºC). ^{1}H NMR (CDCl3, 400 MHz) δ (ppm) = 7.71-7.73 (m, 2H), 7.58-7.66 (m, 3H), 7.50-7.52 (m, 4H), 7.32-7.39 (m, 6H), 7.17-7.19 (m, 6H), 7.03 (s, 6H); ^{13}C {^{1}H} NMR ($CDCl_3$, 125 MHz) δ (ppm) = 156.5, 143.9, 134.7, 134.4, 133.9, 131.8, 130.7, 130.4, 130.3, 129.1, 128.6, 128.4, 128.3, 128.2, 127.9, 126.9; ^{11}B NMR ($CDCl_3$, 128 MHz) δ (ppm) = 0.69-1.16 (1B, t, $^{1}J_{(B,F)}$ = 30.4 Hz); HRMS (ESI-TOF): *m/z* calcd for $C_{39}H_{27}BF_2N_2Na$: 594.2164; found: 594.2147 $[M+Na]^+$.

8-(4-cyanophenyl)-3,5-di(4-methoxyphenyl)-2,6-dithiophen-BODIPY 7. The BODIPY **7** was prepared from BODIPY **6b** (4.81 mg, 0.00838 mmol) and 10 eq of 2-(tributylstannyl) thiophene (31.3 mg, 0.0838 mmol), yielding 3.11 mg, 55.4 % of BODIPY 7 as dark blue solid: mp (268-270 ºC); ^{1}H NMR (CDCl3, 500 MHz) δ (ppm) =7.93 (m, 2H), 7.81 (m, 2H), 7.49 – 7.48 (m, 4H), 7.14 (dd, J = 5.1, 1.1 Hz, 2H), 6.94 (m, 4H), 6.87 (dd, J = 5.1, 3.6 Hz, 2H), 6.84 (s, 2H), 6.62 (dd, J = 3.7, 1.2 Hz, 2H), 3.86 (s, 6H); ^{13}C {^{1}H} NMR (CDCl3, 125 MHz) δ (ppm) = 160.7, 157.2, 139.8, 138.7, 135.5, 134.0, 132.3, 131.8, 131.1, 128.7, 127.3, 125.9, 125.4, 125.0, 123.2, 118.1, 114.2, 113.6, 55.2; ^{11}B NMR ($CDCl_3$, 128 MHz) δ (ppm) = 0.47-0.94 (1B, t, $^{1}J_{(B,F)}$ = 29.8 Hz); HRMS (ESI-TOF): *m/z* calcd for $C_{38}H_{26}BFN_3O_2S_2$: 649.1574; found: 649.1546 $[M-F]^+$.

7.2.2 Crystallography

Crystal structures were determined using data collected at T=90K on a Bruker Kappa Apex-II DUO diffractometer. MoKα radiation was used for **2**, **4**, **5a**, **6a**, and **6b**, while CuKα was

used for **7** and **8**. Compound **5a** exhibited a small amount (ca. 10%) of rotational disorder which was evident from partially-populated secondary sites for all the Cl atoms. Compound **6a** was a twin and has two molecules in the asymmetric unit. Compound **7** had both thiophenes disordered into two orientations, with relative occupations 70:30 and 80:20. It also had disordered solvent, which was removed using the SQUEEZE procedure. Compound **8** had one methoxy group disordered into 54:46 orientations and also had disordered solvent removed by SQUEEZE. Crystal Data: **2**, $C_{27}H_{17}BCl_2F_2N_2$, monoclinic, *a* = 15.5375(10), *b* = 6.0426(4), *c* = 23.7983(16) Å, β = 93.080(3)°, space group $P2_1/c$, *Z* = 4, 48,015 reflections measured, θ_{max} = 36.5°, 10,891 unique (R_{int} = 0.052), final R = 0.041 (8237 I>2σ(I) data), w$R(F^2)$ = 0.109 (all data), CCDC 1509815; **4**, $C_{39}H_{27}BF_2N_2$, monoclinic, *a* = 27.801(3), *b* = 8.5828(11), *c* = 25.471(4) Å, β = 105.021(10)°, space group *C*2/c, *Z* = 8, 16,414 reflections measured, θ_{max} = 23.3°, 4177 unique (R_{int} = 0.115), final R = 0.077 (2159 I>2σ(I) data), w$R(F^2)$ = 0.218 (all data) , CCDC 1509816; **5a**, $C_{23}H_{13}BCl_4F_2N_2O_2$, monoclinic, *a* = 13.7912(4), *b* = 10.6546(4), *c* = 15.2354(6) Å, β = 99.863(2)°, space group $P2_1/n$, *Z* = 4, 24,073 reflections measured, θ_{max} = 31.0°, 7034 unique (R_{int} = 0.035), final R = 0.045 (5519 I>2σ(I) data), w$R(F^2)$ = 0.130 (all data) , CCDC 1509817; **6a**, $C_{37}H_{27}BCl_2F_2N_2O_4$, triclinic, *a* = 13.0943(15), *b* = 13.8006(16), *c* = 17.659(2) Å, α = 83.546(7), β = 83.396(7), γ = 80.198(7)°, space group *P*-1, *Z* = 4, 27,197 reflections measured, θ_{max} = 24.0°, 16,564 unique (R_{int} = 0.119), final R = 0.093 (8684 I>2σ(I) data), w$R(F^2)$ = 0.264 (all data), CCDC 1509818; **6b**, $C_{30}H_{20}BCl_2F_2N_3O_2$, triclinic, *a* = 6.4378(3), *b* = 13.1056(7), *c* = 15.3828(8) Å, α = 84.902(2), β = 79.560(2), γ = 84.620(2)°, space group *P*-1, *Z* = 2, 14,444 reflections measured, θ_{max} = 28.3°, 5922 unique (R_{int} = 0.030), final R = 0.038 (4794 I>2σ(I) data), w$R(F^2)$ = 0.092 (all data), CCDC 1509819; **7**, $C_{38}H_{26}BF_2N_3O_2S_2$, triclinic, *a* = 9.8322(8), *b* = 13.3203(11), *c* = 15.0587(12) Å, α =

72.208(6), β = 74.473(6), γ = 81.456(6)°, space group *P*-1, *Z* = 2, 19,146 reflections measured, θ_{max} = 62.8°, 5632 unique (R_{int} = 0.074), final R = 0.062 (3310 I>2σ(I) data), w$R(F^2)$ = 0.170 (all data), CCDC 1509820; **8**, $C_{44}H_{31}BF_2N_4O_3$. $CHCl_3$, triclinic, *a* = 10.3829(9), *b* = 14.3659(14), *c* = 15.0975(14) Å, α = 75.674(7), β = 89.346(7), γ = 78.359(7)°, space group *P*-1, *Z* = 2, 19,963 reflections measured, θ_{max} = 68.4°, 7279 unique (R_{int} = 0.061), final R = 0.105 (5062 I>2σ(I) data), w$R(F^2)$ = 0.341 (all data), CCDC 1509821.

7.2.3 Spectroscopic Studies

All UV-Visible and fluorescence spectra were collected on a Varian Cary 50 spectrometer and Perkin Elmer LS 55 luminescence spectrometer at 298 K, respectively. A 10 mm path length quartz cuvette and spectroscopic solvents were used for all the measurements. Molar absorption coefficient (ε) was determined from the slope of absorbance *vs* concentration of five dilute solutions with absorbance in the range of 0.2-1.0. Quantum yields (Φ_f) were determined by using a series of dilute solutions with absorbance in the range of 0.02-0.06 at particular excitation wavelength. Cresyl violet perchlorate (0.55 in methanol) and methylene blue (0.03 in methanol) were used as external standards for BODIPYs **2**, **6a**, **6b**, **4** and **3**, **7**, **8**, respectively. The relative fluorescence quantum yields (Φ_f) were determined by the following equation[38],

$$\phi_x = \phi_R \left[\frac{Grad_X}{Grad_R} \right] \left[\frac{\eta_X^2}{\eta_R^2} \right]$$

where Φ stands for fluorescence quantum yields; η stands for refractive indexes of solvents; Grad stands for the gradient from the plot of integrated fluorescence intensity *vs* absorbance at λ_{ex}; subscripts X and R stands for the tested sample and standard sample, respectively.

7.2.4 DFT calculations

The DFT calculations were carried out using the Gaussian 09 software package.[39] The ground state geometries of the BODIPYs were optimized by the DFT method with the B3LYP functional and 6-31G (d) basis sets.

7.2.6 Cell studies

The cell studies were conducted by adapting reported procedures.[40] All cell culture media and reagents used in this study were purchased from Invitrogen. The Human HEp2 cells were purchased from ATCC and maintained in a 50 : 50 mixture of DMEM : AMEM supplemented with 5% FBS and 1% penicillin/streptomycin antibiotic. The cells were sub-cultured twice weekly to maintain sub-confluent stocks.

Dark Cytotoxicity: The HEp2 cells were plated at 7500 cells per well in a Costar 96-well plate (BD biosciences) and allowed to grow for 48 h. The stock solution of BODIPY compound (32 mM) was prepared in 100% DMSO and diluted into final working concentrations (0, 6.25, 12.5, 25, 50, and 100 μM). The cells were exposed to the working solutions of compounds up to 200 μM and incubated overnight (37ºC, 95% humidity, 5% CO_2). The working solution was removed, and the cells were washed with 1X PBS. The medium containing 20% CellTiter Blue (Promega) was added and incubated for 4 h. The viability of cells is measured by reading the fluorescence of the medium at 570/615 nm using a BMG FLUOstar Optima micro-plate reader. In this assay, the indicator dye resazurin is reduced to fluorescent resorufin in viable cells, while non-viable cells are not able to reduce resazurin nor to generate a fluorescent signal. The fluorescence signal of viable (untreated) cells was normalized to 100% and non-viable (treated with 0.2% saponin from sigma) cells was normalized to 0%.

Phototoxicity: The human HEp2 cells were prepared as described above and incubated with compound concentrations of 100, 50, 25, 12.5, 6.25, 3.125, and 0 μM for 24 h. The loading solution was removed and the cells were washed with 1 X PBS, and then refilled with fresh medium. The cells were exposed to a 600 W halogen lamp light source filtered with a water filter (transmits radiation 250 - 950 nm) and a beam turning mirror with 200 nm to 30 μm spectral range (Newport), for 20 min. The total light dose provided was approximately 1.5 J/cm^2. After light exposure, the cells were stored in the incubator for 24 h and assayed for cell viability as described above.

Time-Dependent Cellular Uptake: Human HEp2 cells were prepared as described above. The cells were exposed to 10 μM of each compound solution for 0, 1, 2, 4, 8, and 24 h. The loading medium was removed at the end of each incubation period and the cells were washed with 1X PBS, and solubilized by adding 0.25% Triton X-100 in 1X PBS. Each compound solution was diluted to 10, 5, 2.5, 1.25, 0.625 and 0.3125 μM concentrations using 0.25% Triton X-100 (Sigma-Aldrich) in 1X PBS for standard curve. A cell standard curve was prepared using 10^4, 2×10^4, 4×10^4, 6×10^4, 8×10^4, and 10^5 cells per well. The cell number was quantified using a CyQuant Cell Proliferation Assay (Life Technologies). The compound concentration in cells at each time period was determined using a BNM FLUOstar Optima micro-plate reader at 485/590 nm. Cellular uptake is expressed in terms of compound concentration (nM) per cell.

7.3 Results and discussion

7.3.1 Synthesis and structural characterization

A series of BODIPYs **2**, **3**, **4**, **6a**, **6b**, **7**, and **8** were synthesized as shown in Schemes 7.1 and 7.2. The starting penta-chloro-BODIPY (**1**) was synthesized from 8-chloro-BODIPY, as previously reported.[35] Based on the regioselectivity of the penta-chloro-BODIPY (reactivity 8-Cl

> 3,5-Cl > 2,6-Cl) as previously reported,[35] different functional groups can be introduced for the design of versatile push-pull BODIPYs through facile Pd (0) catalyzed cross-coupling reactions. In this initial study, 4-methoxyphenyl boronic acid was chosen as the electron-donating source and 4-Benzyloxycarbonylphenyl and 4-Cyanophenyl boronic acid were chosen as the electron-withdrawing source to endow the BODIPYs push-pull characteristics. 4-Benzyloxycarbonylphenyl boronic acid was synthesized by adapting a reported procedure.[41] The 4-Benzyloxycarbonyl group can be further de-benzylated to carboxylic acid and used for conjugation with peptides. All the compounds were synthesized by ether Suzuki or Stille cross-coupling reactions in fair to good yields. Penta-chloro-BODIPY was treated with 2.5 eq of 4-Benzyloxycarbonylphenyl or 10 eq of 4-Cyanophenyl boronic acid with 3 mol % of $Pd(PPh_3)_4$ and 1M Na_2CO_3 (aq) in refluxing toluene to regioselectively produce BODIPY **5a** and **5b** in 70.0 % and 50.2 % yield, respectively. Subsequently, BODIPY **5a** and **5b** were treated with 3 eq 4-methoxyphenyl boronic acid with 3 mol% of $Pd(PCy_3)G2$ and 1M Na_2CO_3 (aq) in refluxing toluene to regioselectively produce **6a** and **6b** in 60.2 % and 66.0 % yield, respectively.

BODIPY **8** was synthesized by two-step Suzuki-cross coupling reactions using 5 eq of 4-methoxyphenyl boronic acid and 4-cyanophenyl boronic acid, respectively, in overall 54.0 % yield. Compared to catalyst $Pd(PPh_3)_4$, $Pd(PCy_3)G2$ greatly increase the yield of **6a**, **6b** and **8** from around 10 % to nearly 70 %. The increased yields are due to the more reactive complex formed by the more bulky ligands of $Pd(PCy_3)G2$ catalyst.[35, 42] For comparison purpose, BODIPY**2** and **4** with no electron donor and acceptor on the phenyl substituents were synthesized with tributylphenylstannane and 3 mol % of $Pd(PPh_3)_4$ in refluxing toluene, yielding 60.7 % and 41.0 %, respectively. BODIPY **7** was prepared by treating BODIPY **6b** with 2-(tributylstannyl) thiophene and $Pd(PCy_3)G2$ in refluxing toluene in 55.4 % yield.

Scheme 7.1. Synthetic routes of BODIPY **2-4**, **5a**, **5b**, **6a** and **6b**.

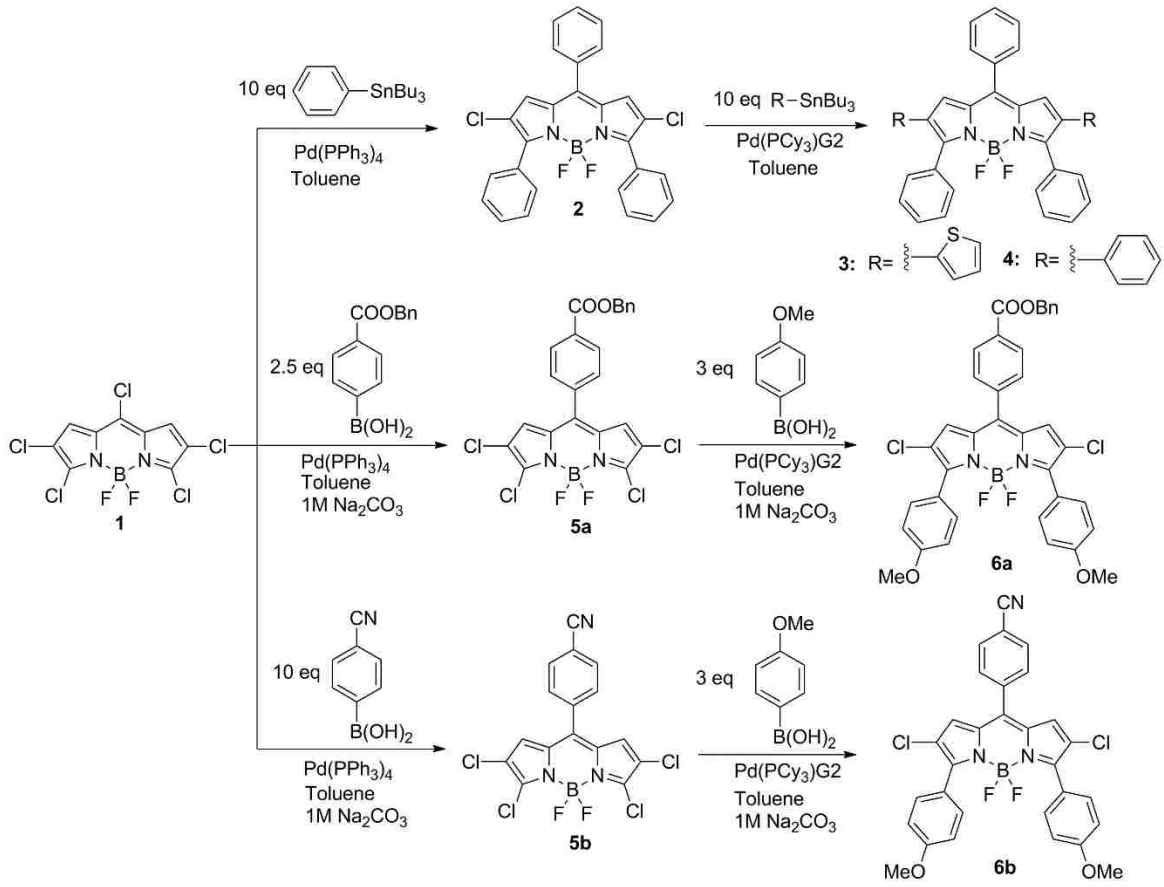

Scheme 7.2. Synthetic routes of BODIPY **7-8**.

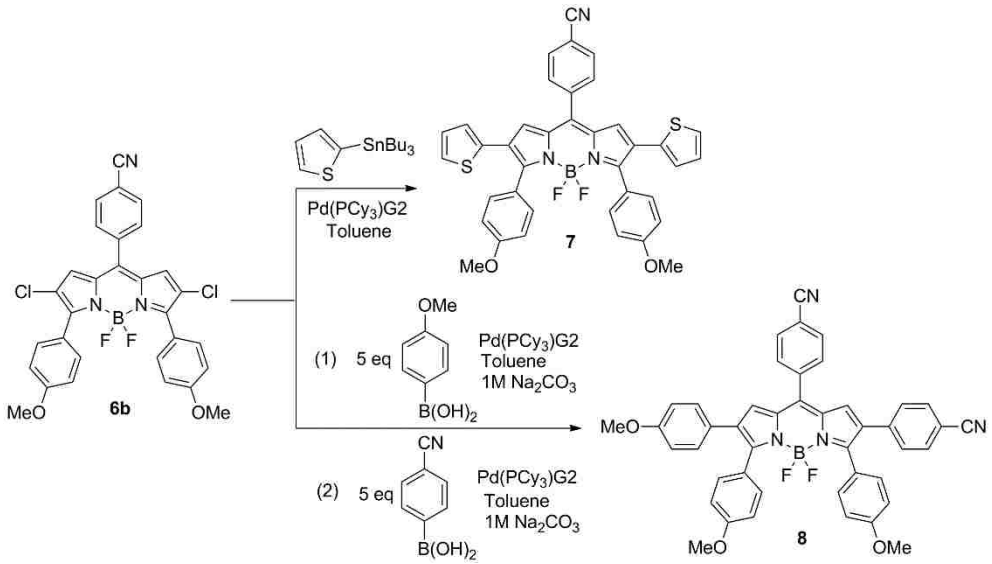

For comparison purpose, BODIPY **3** with no substituents on the phenyl ring were also prepared using the 2-(tributylstannyl) thiophene and $Pd(PCy_3)G2$, yielding 62.0 %. All the compounds were characterized by ^{1}H NMR, ^{13}C NMR, and ^{11}B NMR spectroscopy (Figures 7.2-7.28) as well as HRMS. The structures of BODIPYs **2**, **4**, **5b**, **6b**, **7** and **8** were further confirmed by X-ray crystallography (Figure 7.29).

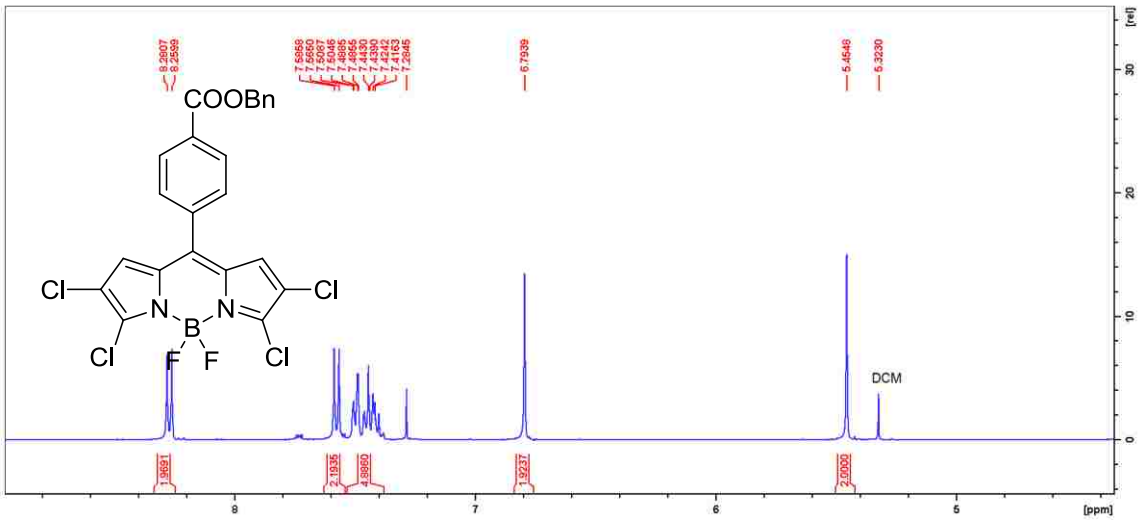

Figure 7.2. ^{1}H NMR spectrum of BODIPY **5a.**

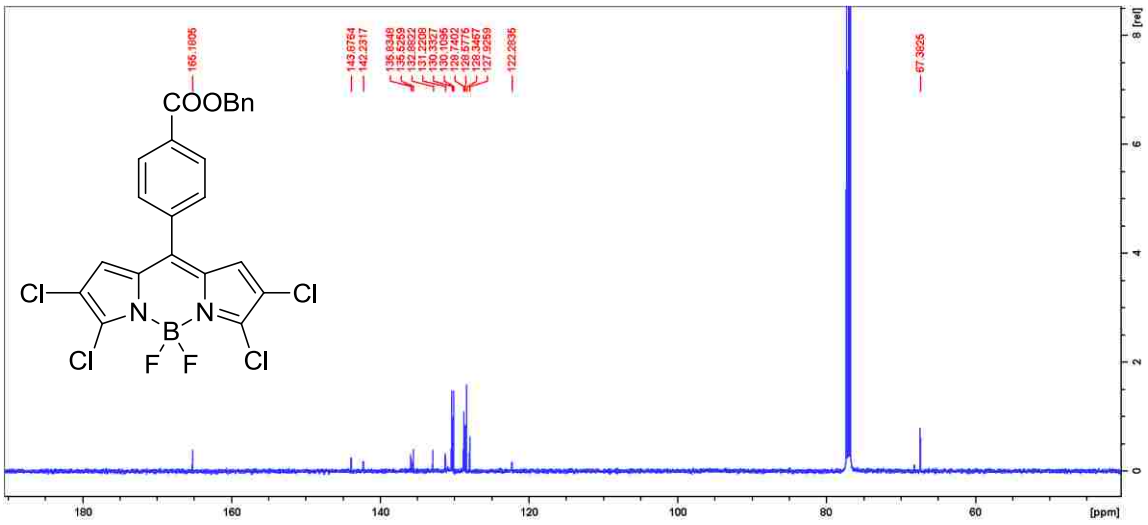

Figure 7.3.^{13}C {^{1}H} NMR spectrum of BODIPY **5a.**

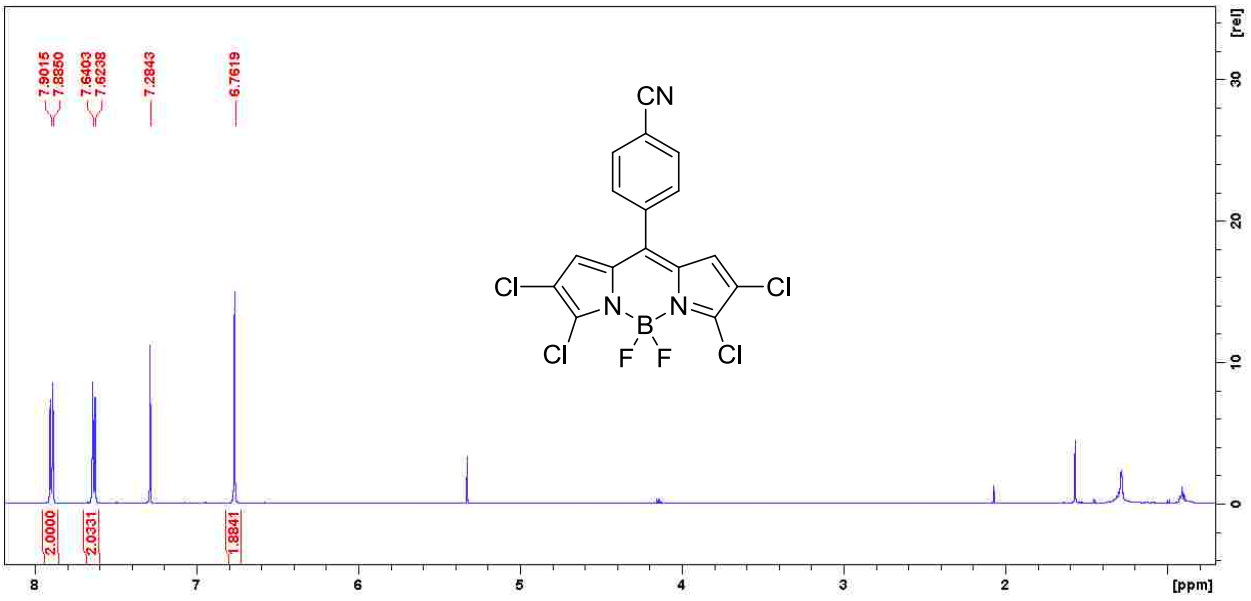

Figure 7.4. ^{1}H NMR spectrum of BODIPY **5b**.

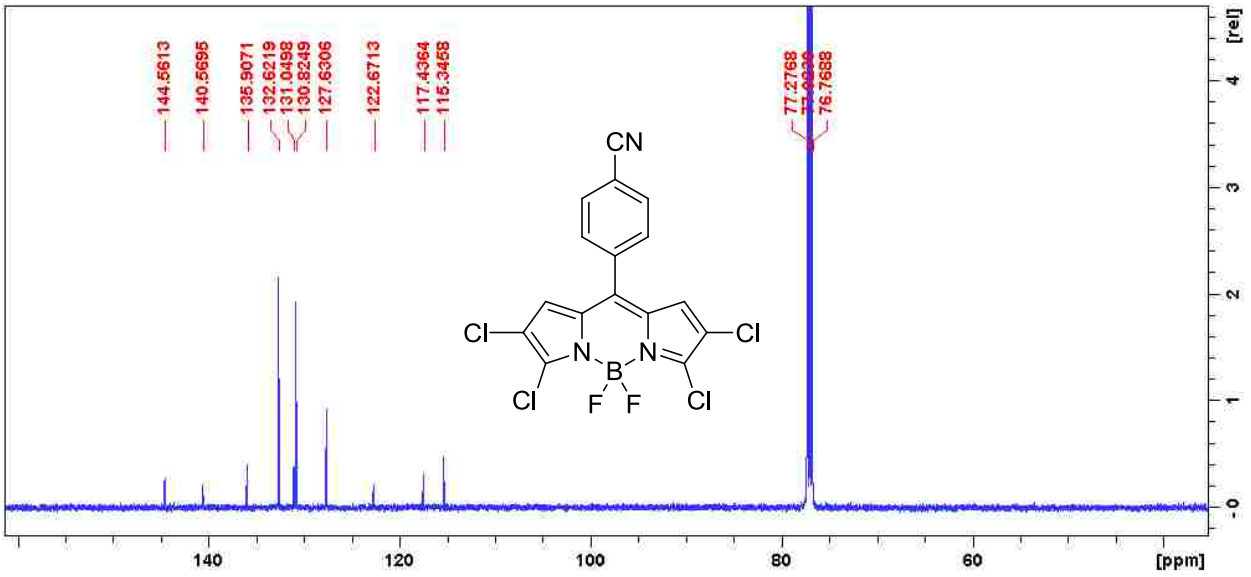

Figure 7.5. ^{13}C {^{1}H} NMR spectrum of BODIPY **5b**.

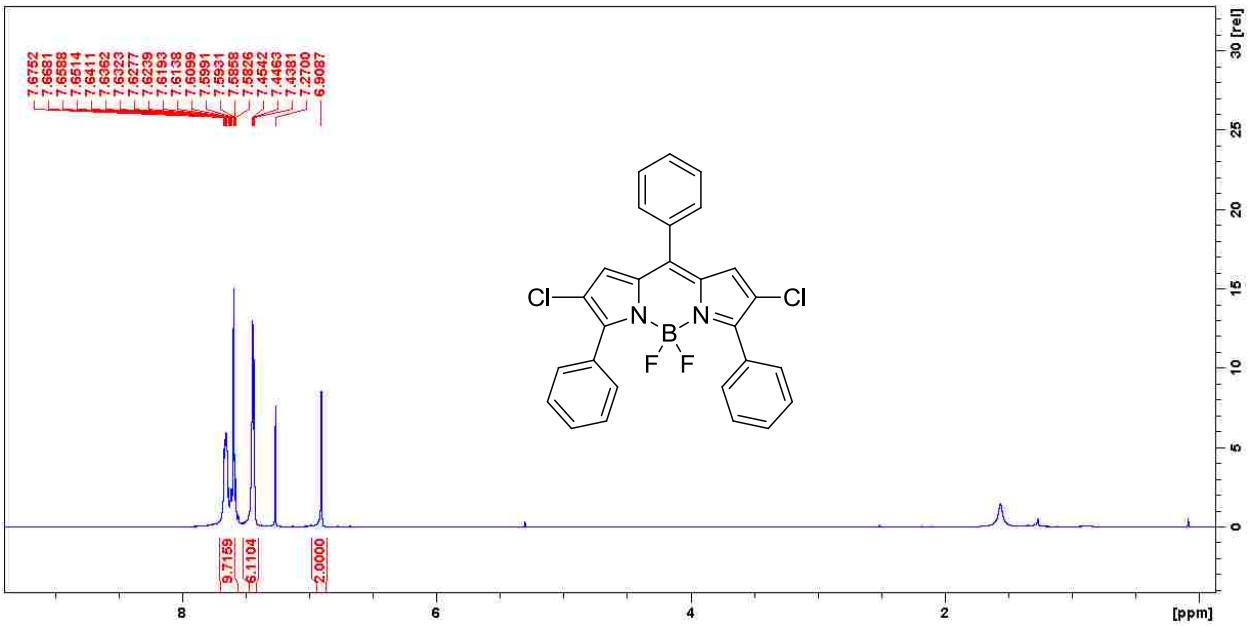

Figure 7.6. ^{1}H NMR spectrum of BODIPY **2**.

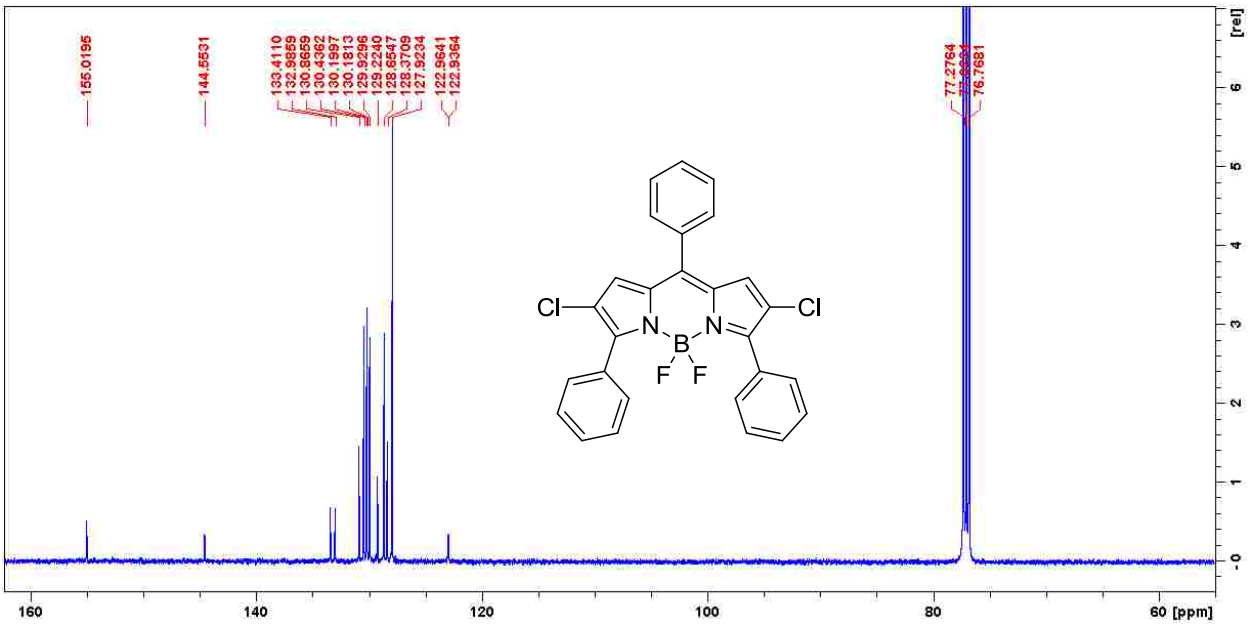

Figure 7.7. ^{13}C {^{1}H} NMR spectrum of BODIPY **2**.

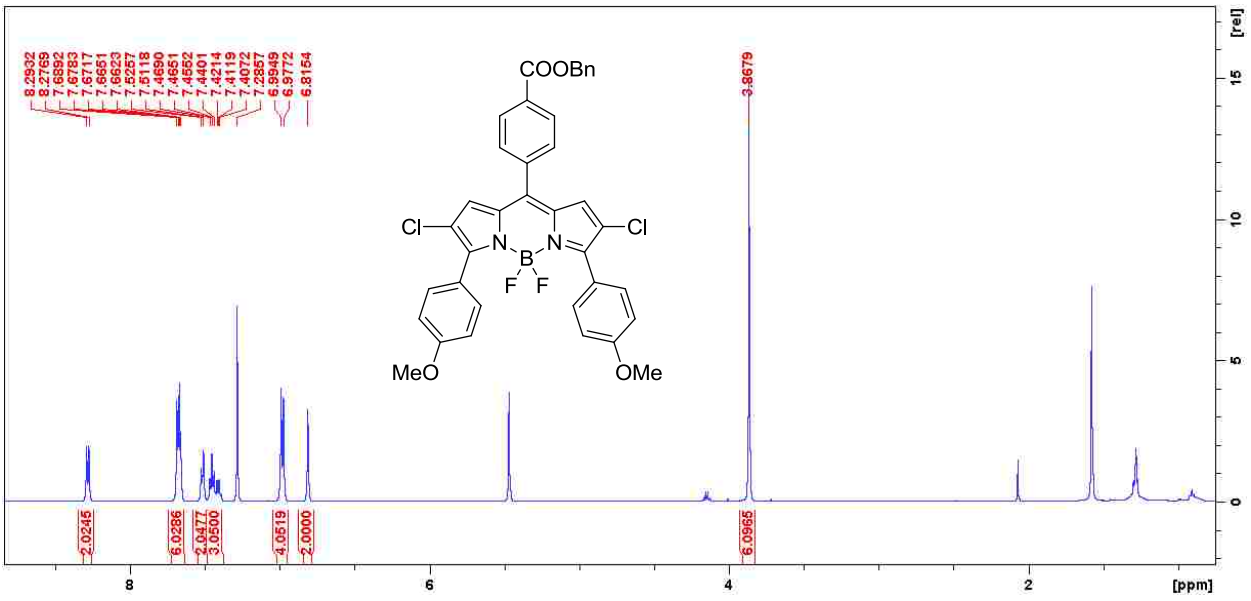

Figure 7.8. ^{1}H NMR spectrum of BODIPY **6a**.

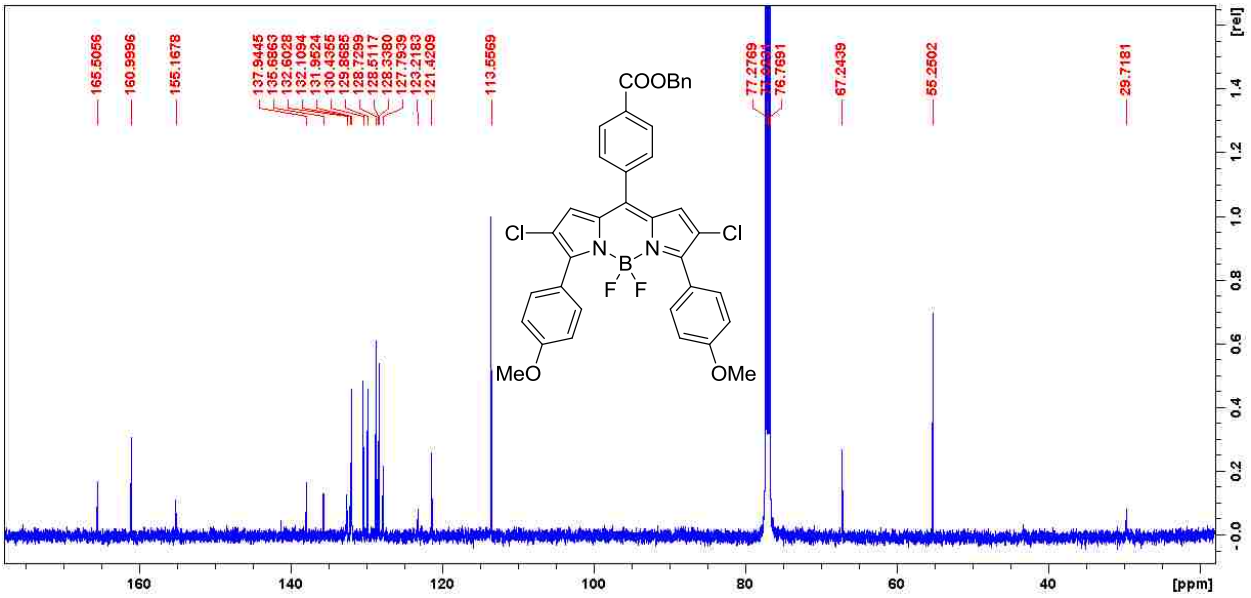

Figure 7.9. ^{13}C {^{1}H} NMR spectrum of BODIPY **6a**.

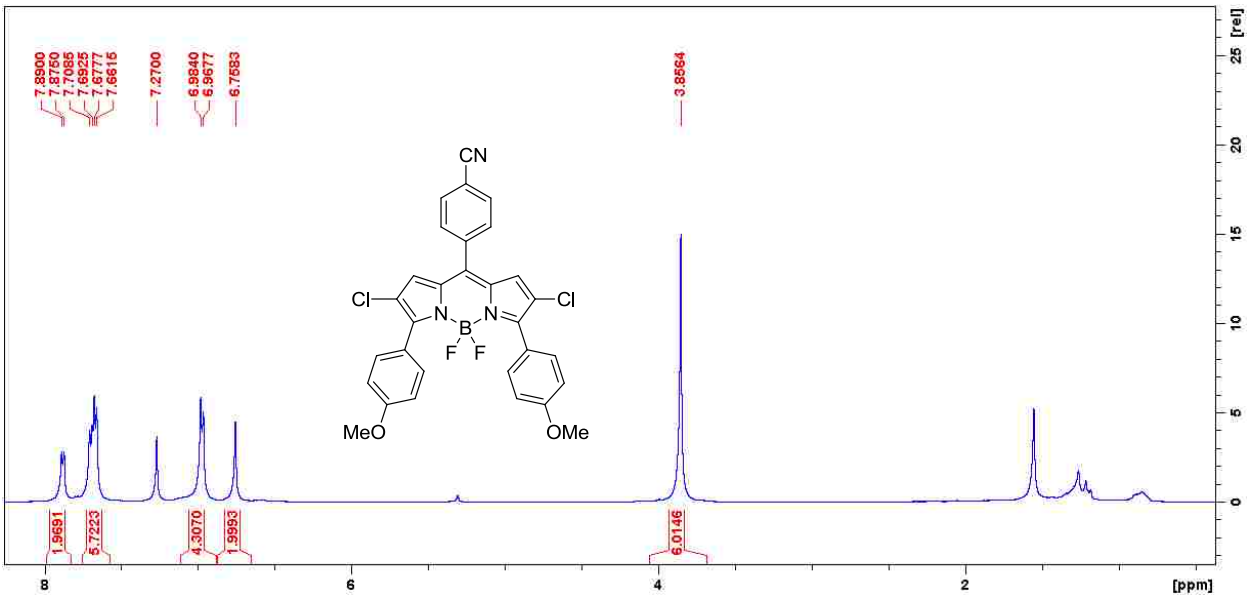

Figure 7.10. ^{1}H NMR spectrum of BODIPY **6b**.

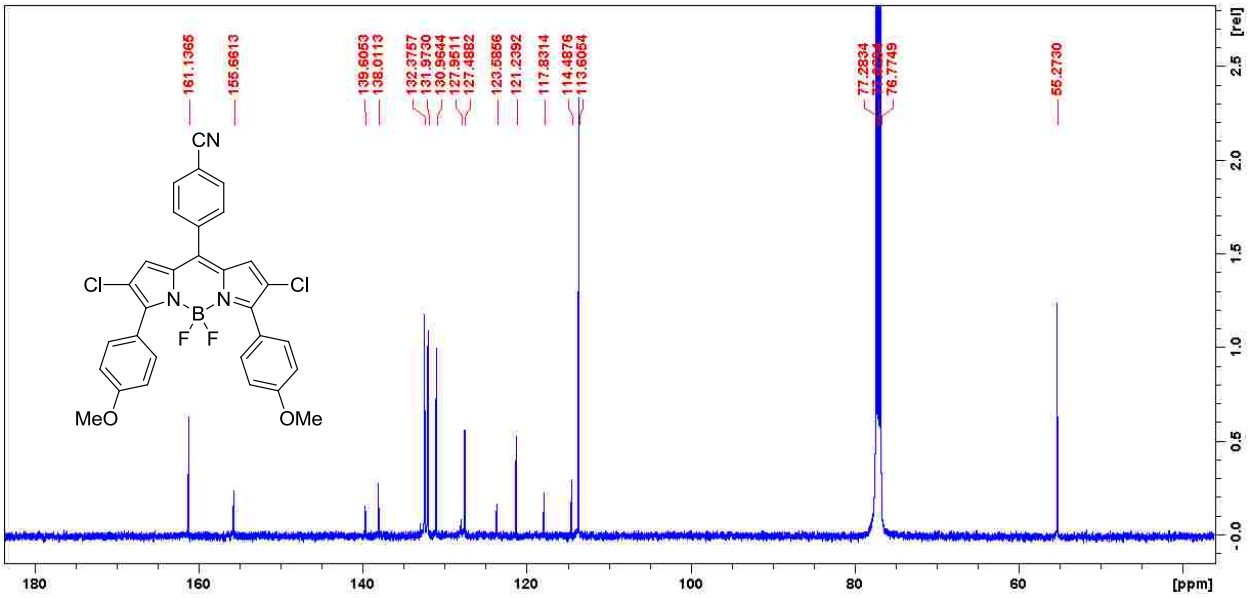

Figure 7.11. ^{13}C {^{1}H} NMR spectrum of BODIPY **6b**.

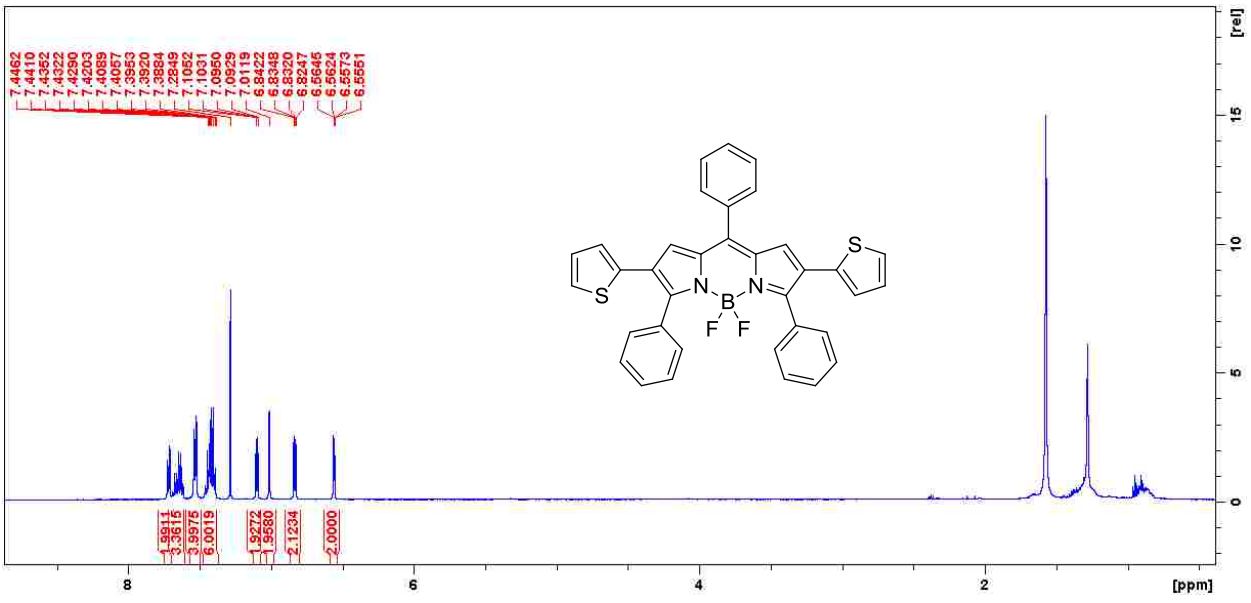

Figure 7.12. ^{1}H NMR spectrum of BODIPY **3**.

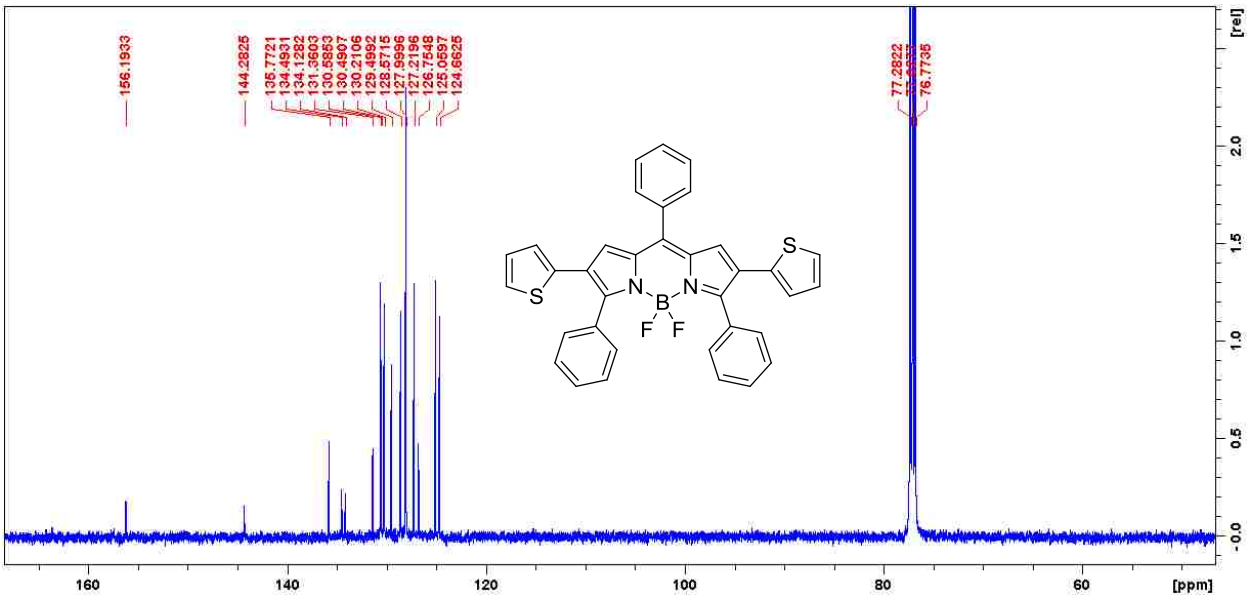

Figure 7.13. ^{13}C {^{1}H} NMR spectrum of BODIPY **3**.

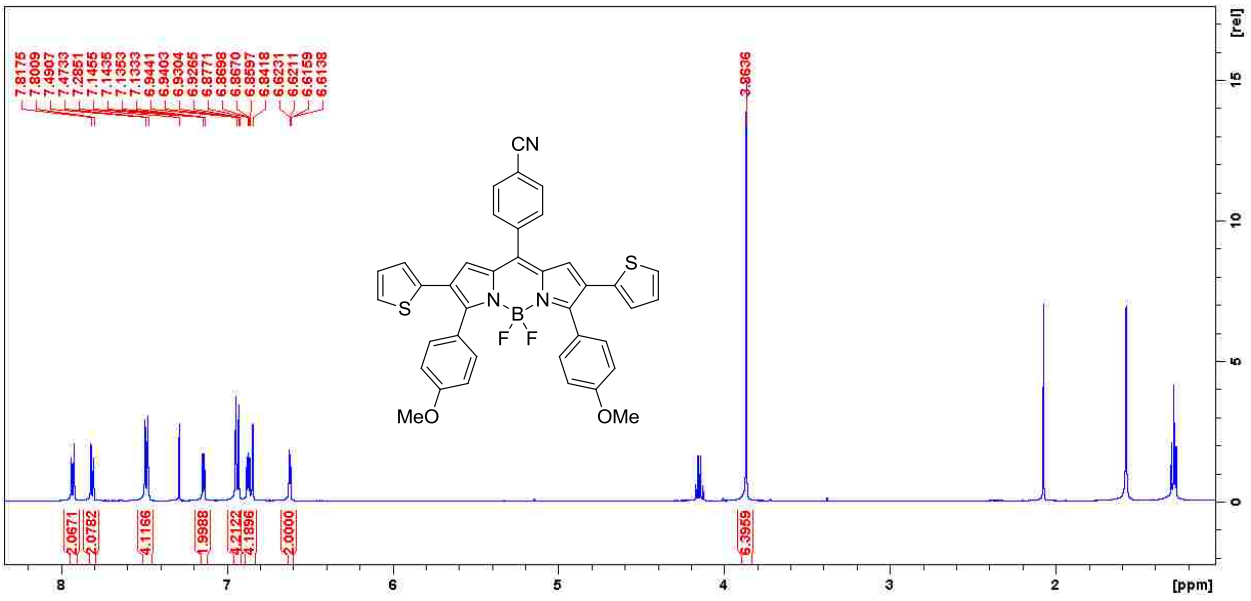

Figure 7.14. ^{1}H NMR spectrum of BODIPY **7**.

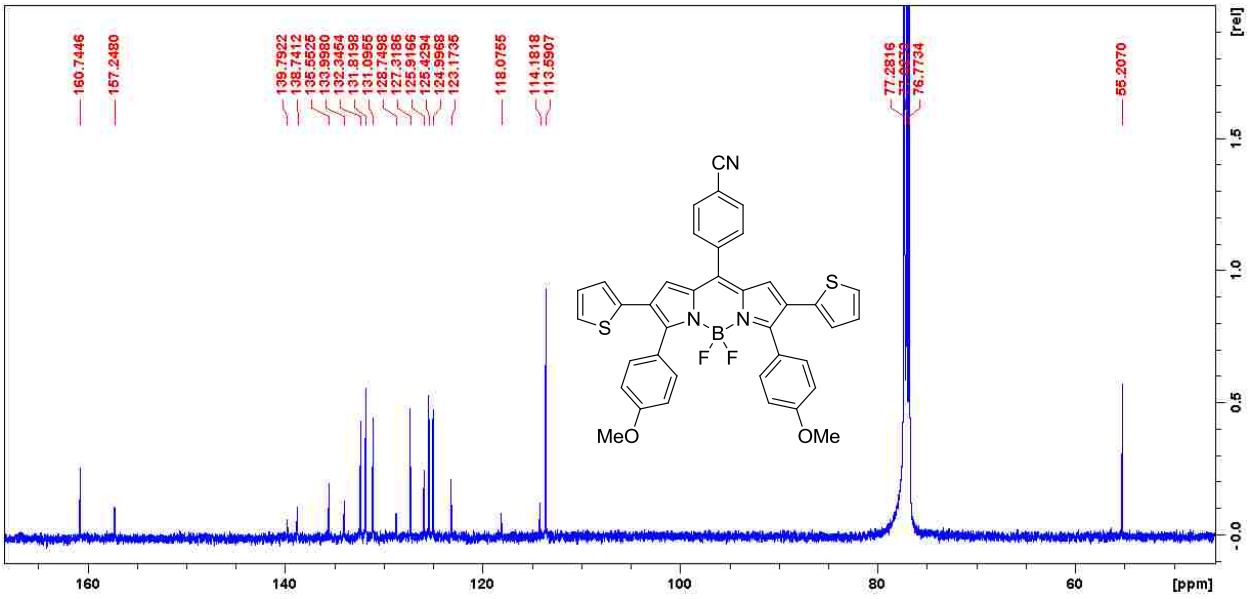

Figure 7.15. ^{13}C {^{1}H} NMR spectrum of BODIPY **7**.

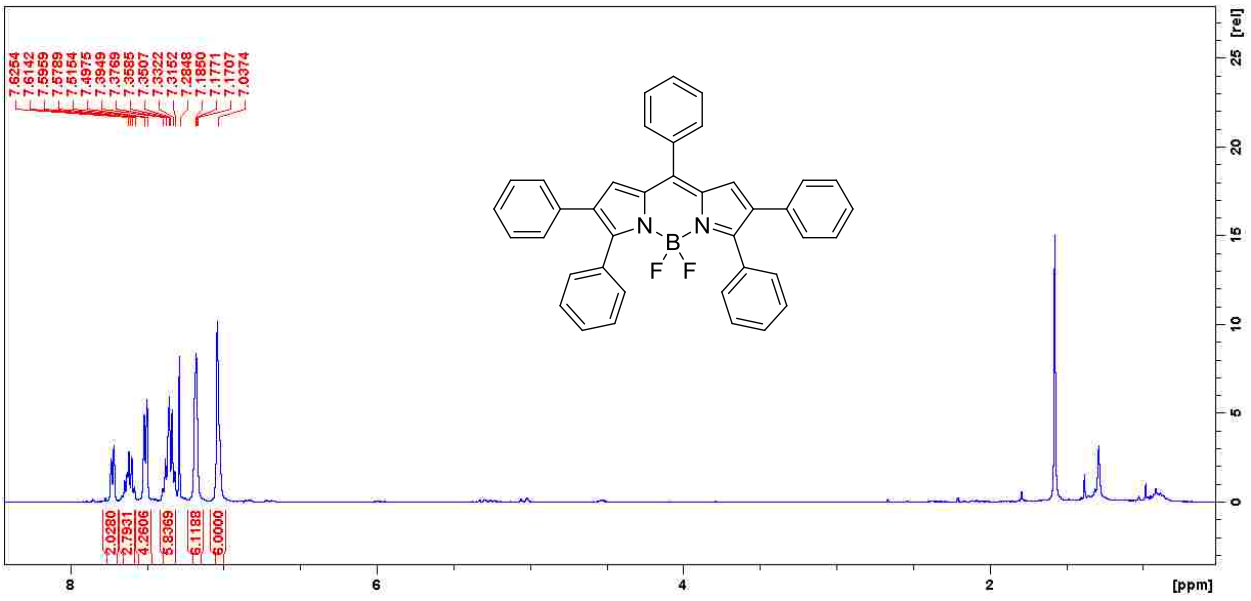

Figure 7.16. ^{1}H NMR spectrum of BODIPY **4**.

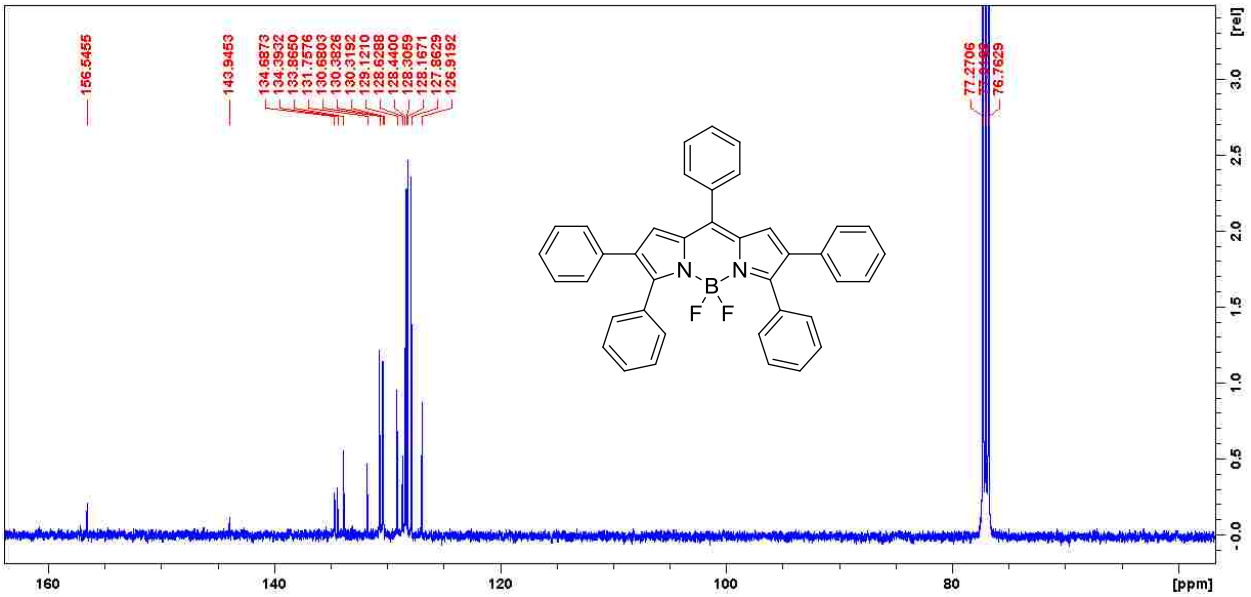

Figure 7.17. ^{13}C {^{1}H} NMR spectrum of BODIPY **4**.

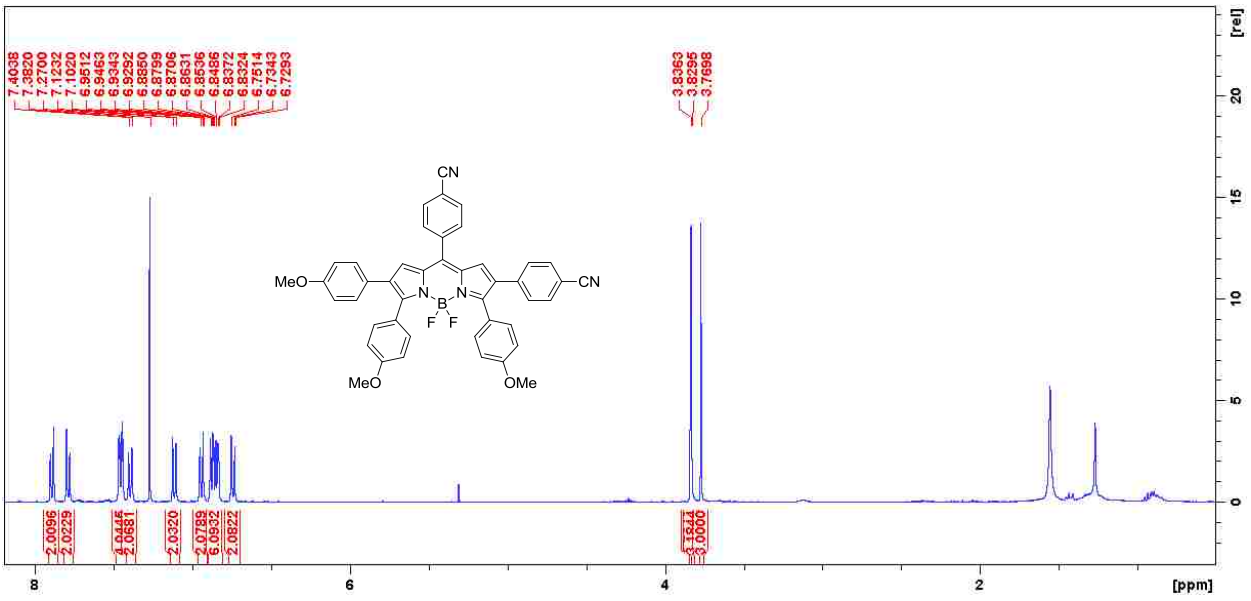

Figure 7.18. ^{1}H NMR spectrum of BODIPY **8**.

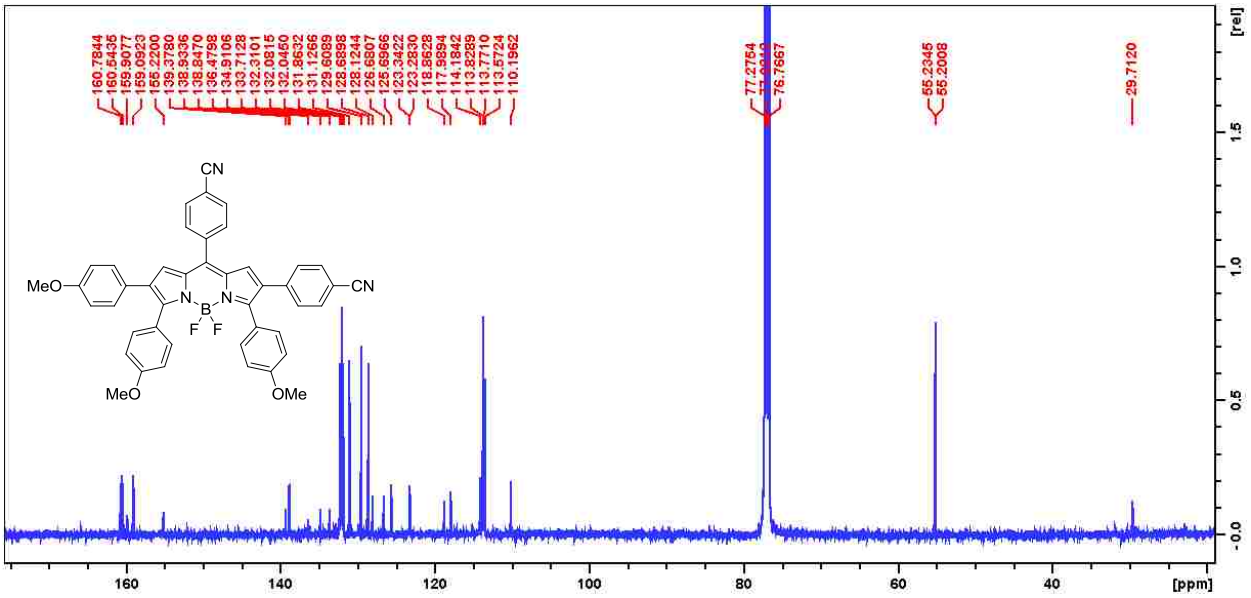

Figure 7.19. ^{13}C {^{1}H} NMR spectrum of BODIPY **8**.

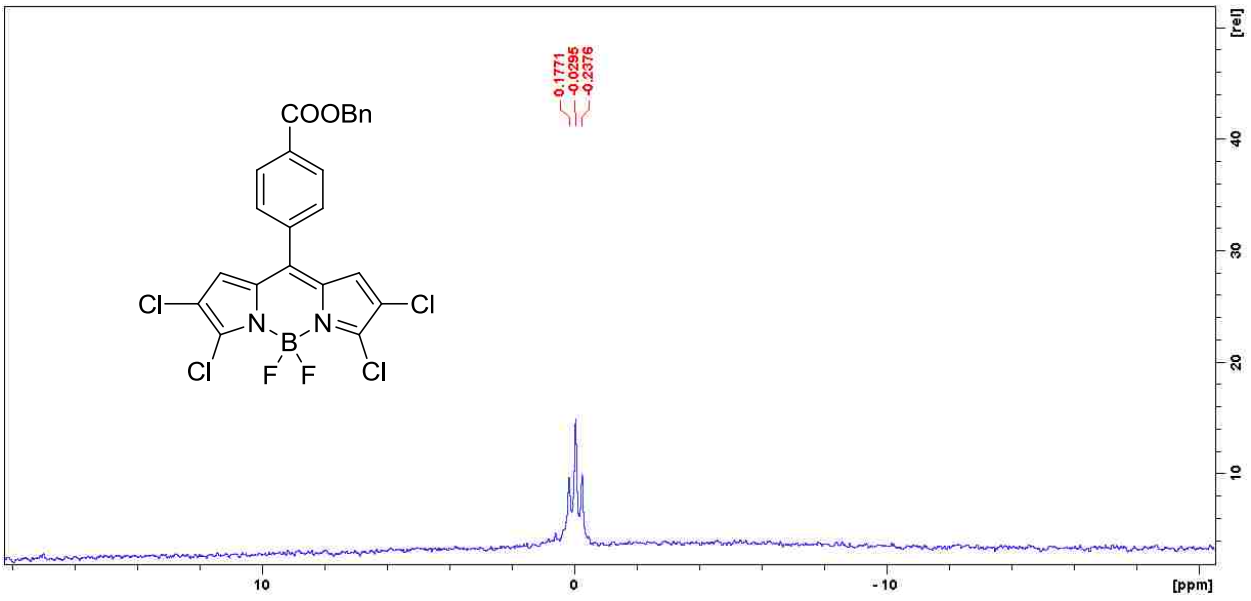

Figure 7.20. ^{11}B NMR spectrum of BODIPY **5a**.

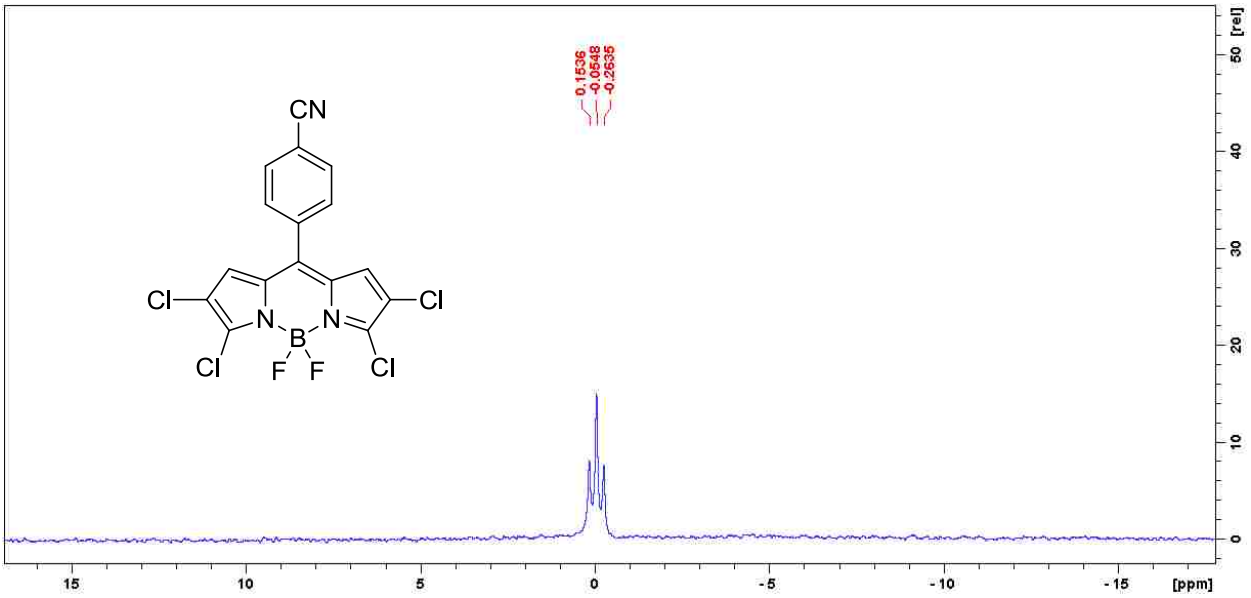

Figure 7.21. ^{11}B NMR spectrum of BODIPY **5b**.

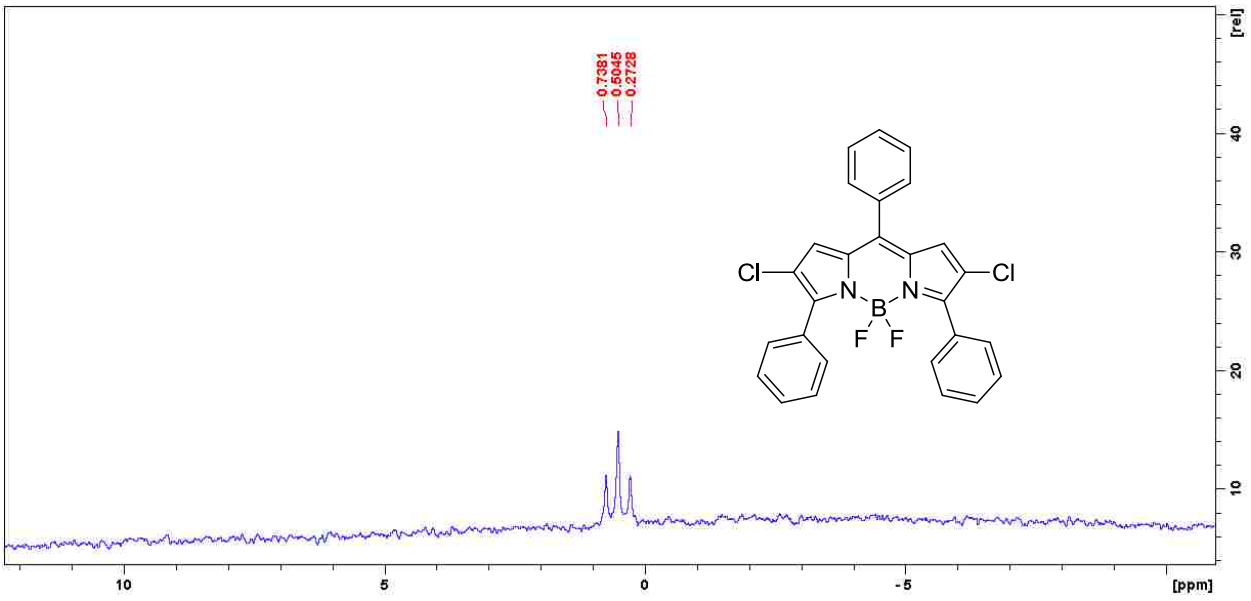

Figure 7.22. ^{11}B NMR spectrum of BODIPY **2**.

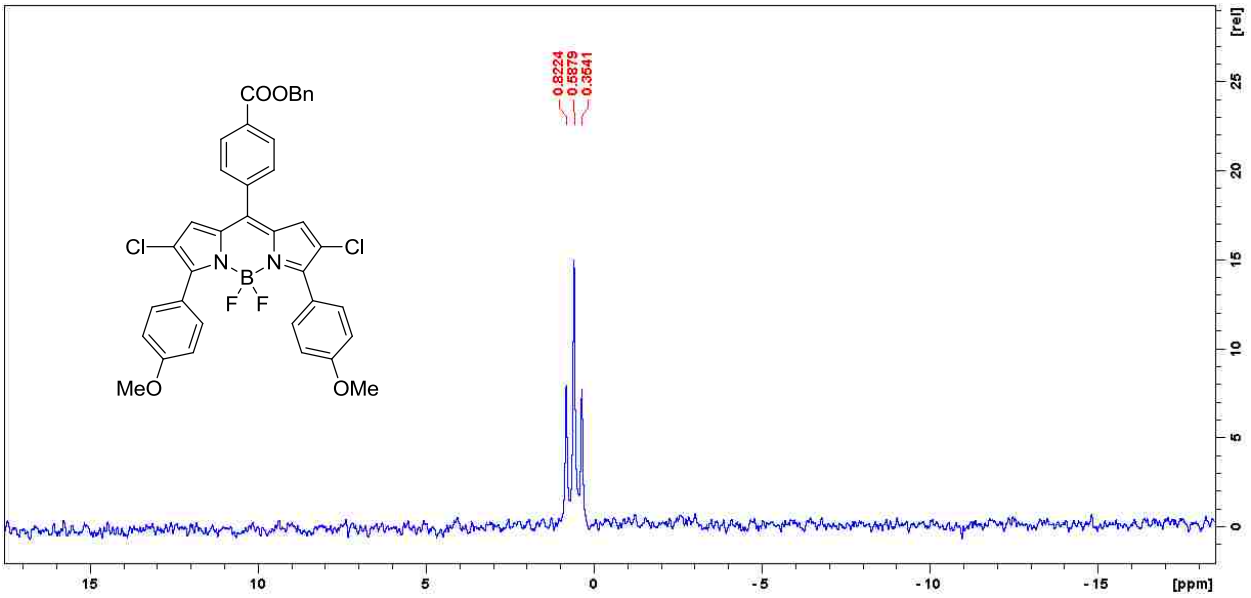

Figure 7.23. ^{11}B NMR spectrum of BODIPY **6a**.

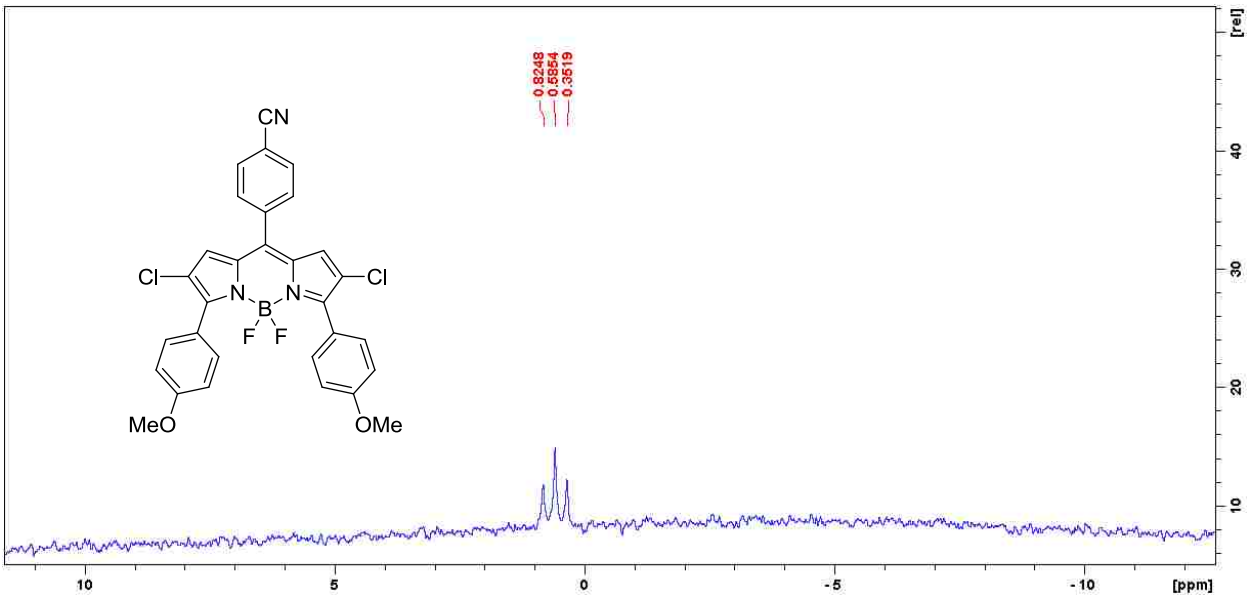

Figure 7.24. ^{11}B NMR spectrum of BODIPY **6b**.

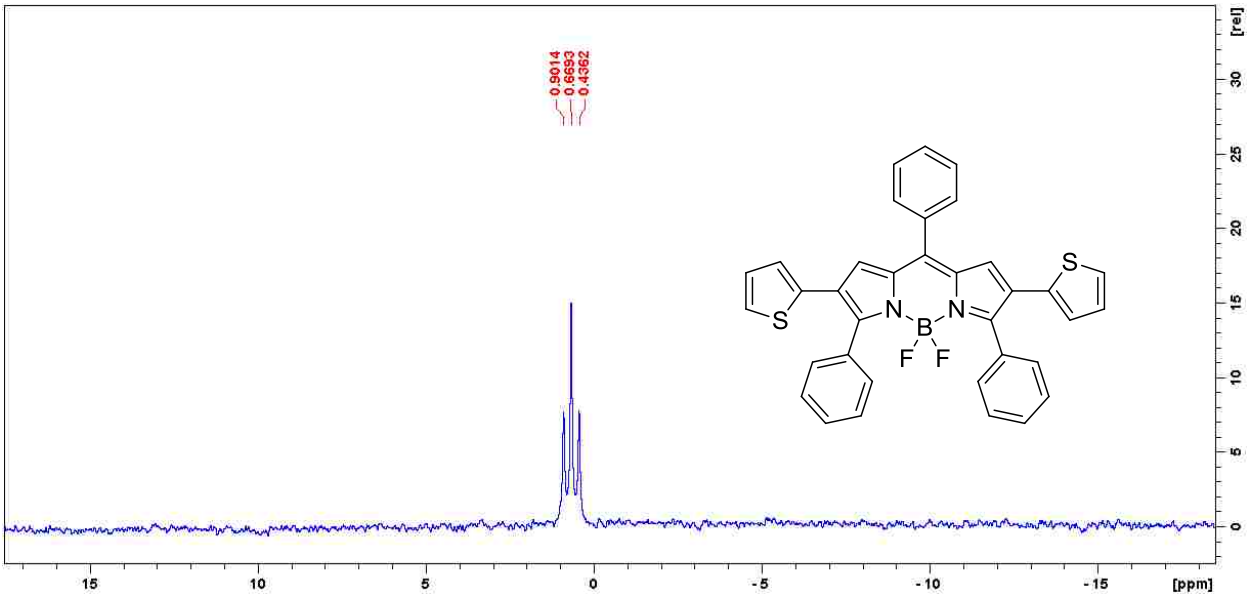

Figure 7.25. ^{11}B NMR spectrum of BODIPY **3**.

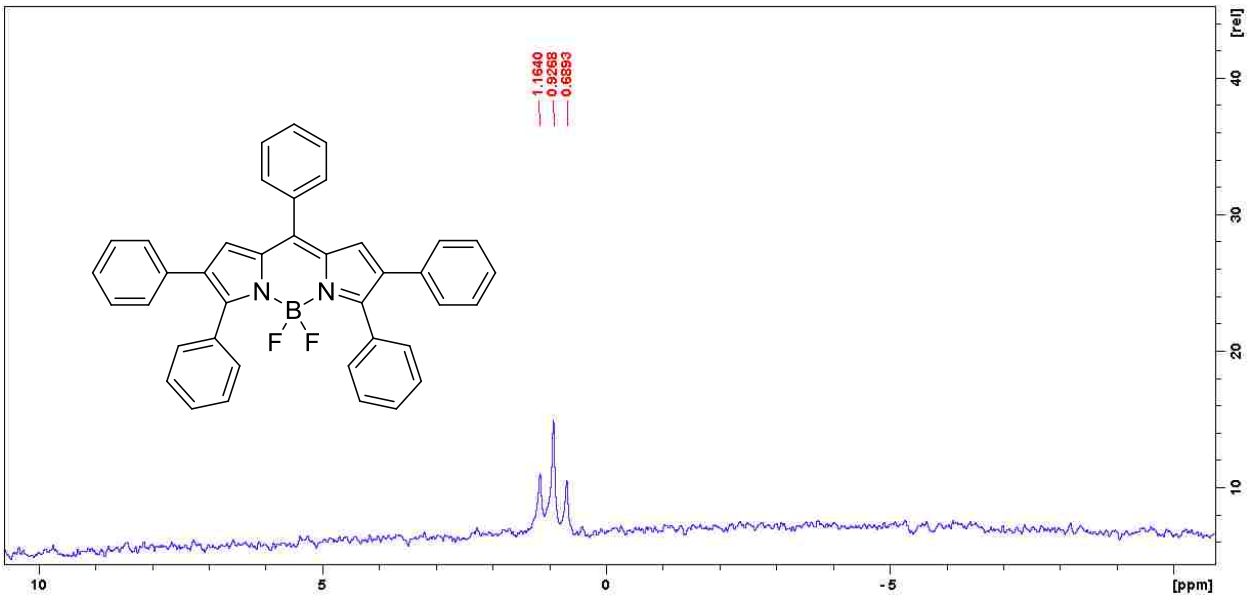

Figure 7.26. ^{11}B NMR spectrum of BODIPY **4**.

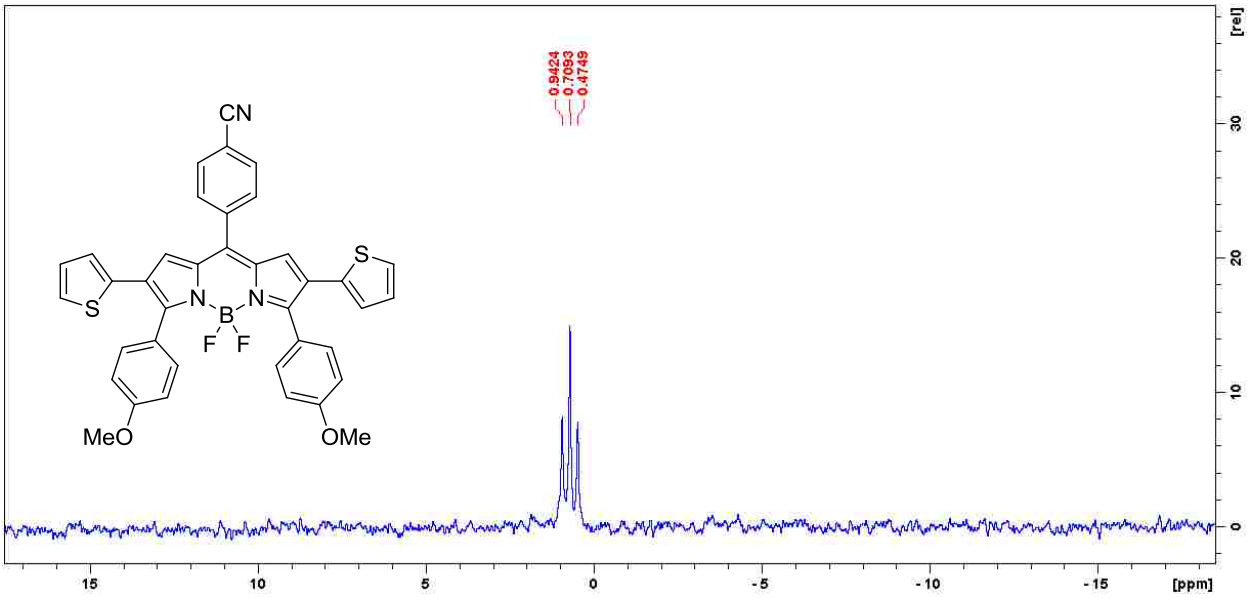

Figure 7.27. ^{11}B NMR spectrum of BODIPY **7**.

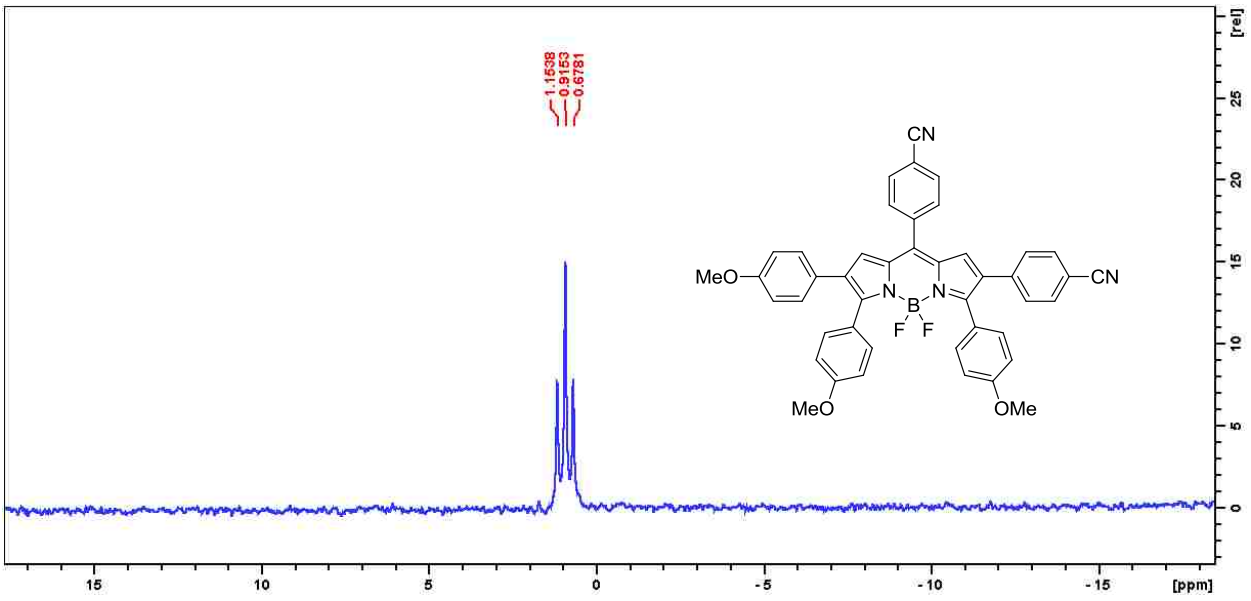

Figure 7.28. ^{11}B NMR spectrum of BODIPY **8**.

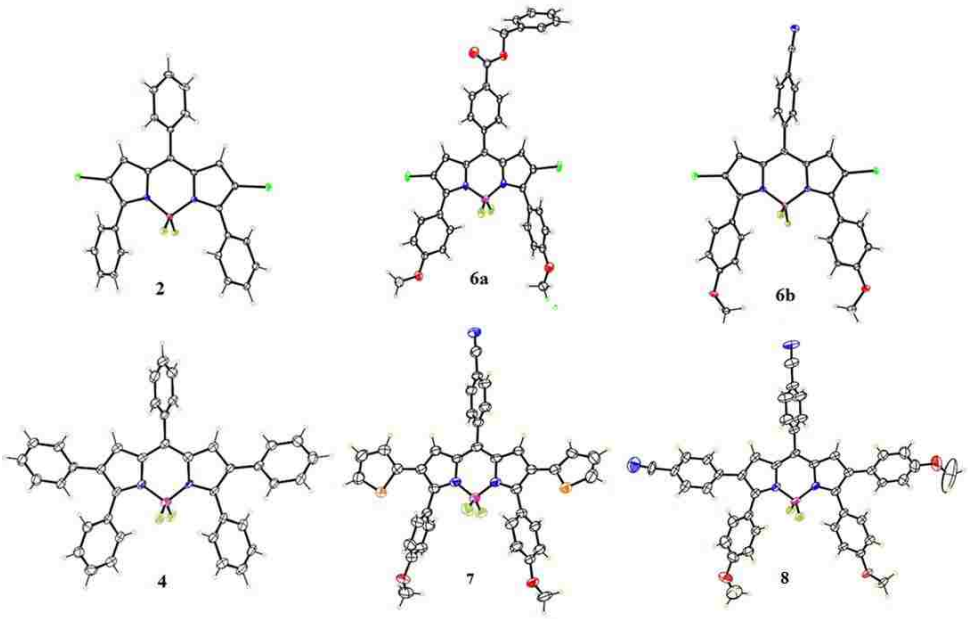

Figure 7.29. Crystal structures of BODIPY **2**, **6a**, **6b**, **4**, **7** and **8**.

7.3.2 X-ray crystallography

According to the crystal structures, the dihedral angles of meso substituents with the 12-atom BODIPY core for **2**, **4**, **6a**, **6b**, **7** and **8** were 62.0, 59.4, 56.6, 63.7, 54.1, and 60.7°, respectively. With substituents (*e.g.*, phenyl, thiophene) on 1,7 positions, the meso plane is almost perpendicular (~90°) with the BODIPY core.[37, 43] The dihedral angle of these BODIPYs without 1,7 substituents was much smaller (about 30° decrease) due to less steric interaction around the meso positions. The decrease of the dihedral angle could lead to better conjugation of meso substituents to the BODIPY core, and therefore enhance the transfer of pull effect. The dihedral angle of the 3,5 substituents with the 12-atom BODIPY core is in the range of 45-65° for all the compounds, except for BODIPY **7** which has a dihedral angle of 70.3 and 86.1, respectively. The dihedral angle of 2,6 substituents, especially for BODIPY **7** with thiophene on 2,6 positions, is smaller than the dihedral angle of 8, 3, and 5 substituents with the 12-atom BODIPY core. This suggests that the push-pull moieties on the 2,6 positions have better electronic coupling with the BODIPY core.

7.3.3 Spectroscopic properties

The spectroscopic properties of the push-pull BODIPYs were evaluated in solvents with different polarities and the results are summarized in Table 7.1 and Figure 7.30-7.39. All the compounds show a strong S_0-S_1 transition with an absorption coefficients in 25000-72000 M^{-1} cm^{-1} range. A weak broad absorption band centered at around 400 nm was observed at higher energy, which can be attributed to the S_0-S_n ($n \geq 2$) transition of the BODIPY moiety.[16, 22, 24] The π-π* transitions at 230-320 nm were also observed for all the compounds.[24] In comparison with BODIPY **2**, BODIPY **6a** and **6b** with electron donor (MeO) on para positions of 3,5 phenyls and electron acceptor (-CN, -BOOCN) on para position of 8 phenyl exhibit 25-37 nm and 40-48 nm

bathochromic shifts for absorption and emission in different solvents, respectively. BODIPY **6b** displayed a larger red-shift for both absorbance and emission compared to **6a** as the -CN group (Hammett parameter σ_p = 0.66)[44] is more electron withdrawing than -COOBn group (Hammett parameter σ_p = 0.56)[44] and results in enhanced pull effect associated with smaller HOMO-LUMO gap, as evidenced by DFT calculation and cyclic voltammetry analysis (Table 7.2, Figure 7.40 and 7.42). Similarly, compared with BODIPY **3**, BODIPY **4** showed a bathochromic shift of 22-25 nm for absorption and 23-27 nm for emission in different solvents investigated. With three sets of push-pull moieties installed on BODIPY **5**, BODIPY **6** exhibited a bathochromic shift of 30-34 nm and 55-60 nm for absorption and emission in different solvents investigated, respectively. These results indicated that the substituents of different push and pull ability on BODIPYs can cause bathochromic shift to different extent. In solvents with different polarities, BODIPY **4** having two thiophene groups at 2 and 6 positions showed the longest λ_{max} for absorption (635-653 nm) and emission (706-707 nm) and the largest Stokes shift (54-71 nm), which is consistent with the reported studies showing that thiophene group, especially at 2,6 positions, can cause large bathochromic shift and Stokes shift on BODIPYs.[35, 37, 43] The larger Stokes shift was presumably due to the geometry difference between S_0 and S_1 states upon excitation, resulting in increased geometry relaxation.[43, 45-46] As the polarity of solvents increased from toluene (solvent polarity E_T^N=0.099) to acetonitrile (solvent polarity E_T^N=0.460)[47], hypsochromic shift was observed to different extent for both absorption (6-22 nm) and emission (0-15 nm) associated with a gradual decrease of quantum yield. The slight hyperchromic shift of both emission and absorbance is probably due to the decrease of dipole moment (μ) of BODIPY upon excitation associated with the intromolecular charge transfer (ICT) between donor and acceptor ($\mu_g > \mu_e$, where μ_g and μ_e are the ground- and excited-state dipole moments) and thus the ground state is better stabilized in polar

Table 7.1. Spectroscopic properties of BODIPYs in toluene, tetrahydrofuran and acetonitrile at 298 K.

Cpds	[a]Solvent	λ_{ab}(nm)	λ_{em}(nm)	Stokes Shift (nm)	ε ($L \cdot mol^{-1} \cdot cm^{-1}$)	Φ^{b}
2	Tol	572	603	31	71258	0.30
	THF	566	597	31	67346	0.13
	CH_3CN	558	588	30	51609	0.12
6a	Tol	604	643	39	54004	0.13
	THF	594	637	43	31809	0.077
	CH_3CN	583	632	49	40192	0.061
6b	Tol	609	650	41	50350	0.085
	THF	597	643	46	39753	0.048
	CH_3CN	587	636	49	44983	0.038
3	Toluene	628	680	52	32361	0.079
	THF	620	680	60	26262	0.042
	CH_3CN	613	683	70	25952	0.013
7	Toluene	653	707	54	38630	0.027
	THF	645	706	61	32363	0.015
	CH_3CN	635	706	71	33438	0.0055
4	Toluene	592	622	30	67517	0.64
	THF	586	620	34	54568	0.33
	CH_3CN	576	616	40	57143	0.34
8	Toluene	626	677	51	29550	0.055
	THF	618	676	58	25219	0.025
	CH_3CN	606	676	70	23216	0.0072

[a]Solvent polarity (E_T^N): toluene=0.099; THF=0.207; CH_3CN=0.460.[47] [b]Cresyl violet perchlorate (0.55 in methanol) and methylene blue (0.03 in methanol) were used as external standards for BODIPY **2**, **6a**, **6b**, **4** and **3**, **7**, **8**, respectively.

solvent.[47-48] The decreased quantum yield with the increase of solvent polarity was consistent with many reported results and was attributed to the increase of nonradiative decay in more polar solvents.[24, 26, 33-34, 49] A 2-4 fold decrease of quantum yield was observed from BODIPY **2** to **6a** and **6b**, **3** to **7**, and **4** to **8**, which could be attributed to the ICT between donor and acceptor[25, 29] and the internal conversion between narrower band gaps[50-51]. ICT is known to affect the rate of nonradiative relaxation of fluorophores and results in decreased quantum yields.[52] Another reason associated with the low quantum yield of BODIPYs **3** and **7** is the greater freedom of rotation of

the smaller thiophene groups in comparison with phenyl, increasing the energy lost to nonradiative decay.[43] Interestingly, the quantum yield of BODIPY **8** was decreased 11-48 fold in different solvents compared to BODIPY **4**, which could be due to the enhanced ICT resulting from the multiple sets of push-pull moieties in the compound. The Stokes shift was increased as the polarity of solvent increased for all the compounds. Among them, the Stokes shift of BODIPY **8** increased the most (19 nm) from toluene to acetonitrile and indicated a large difference in dipole moment between ground and excited state.[24, 49]

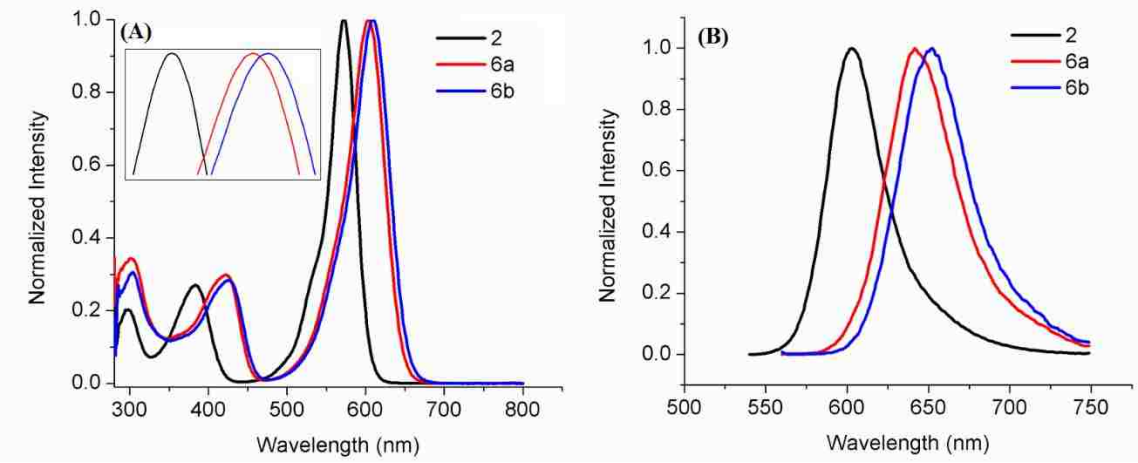

Figure 7.30. Absorbance (A) and fluorescence (B) of BODIPY **2**, **6a** and **6b** in toluene.

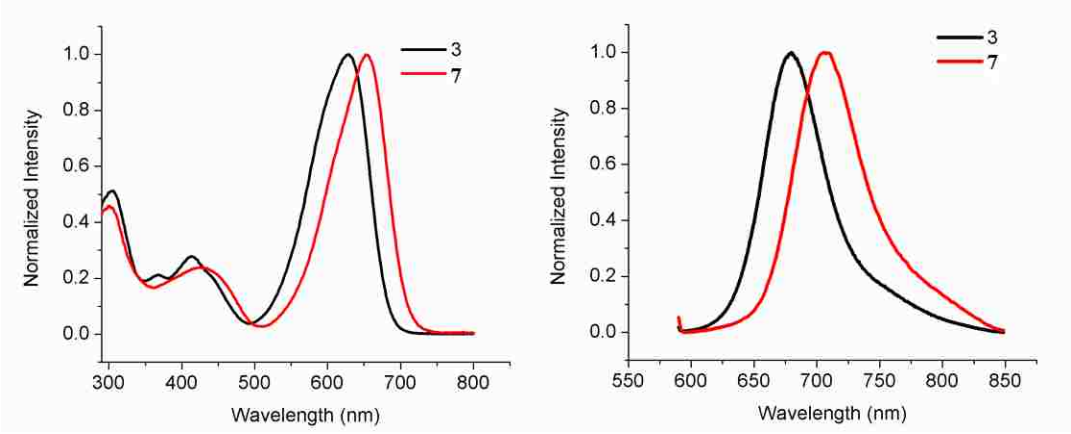

Figure 7.31 Absorbance (A) and fluorescence (B) of BODIPY **3** and **7** in toluene.

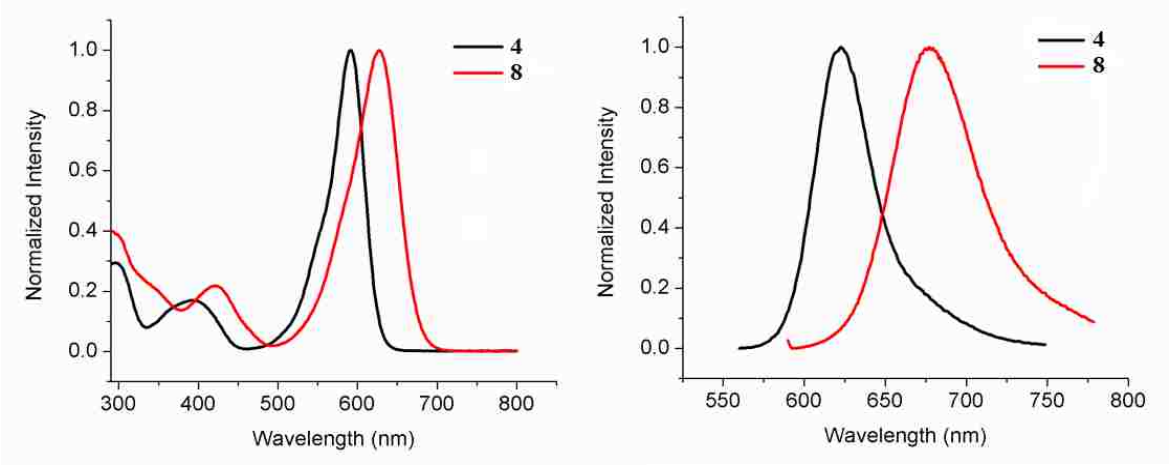

Figure 7.32. Absorbance (A) and fluorescence (B) of BODIPY **4** and **8** in toluene.

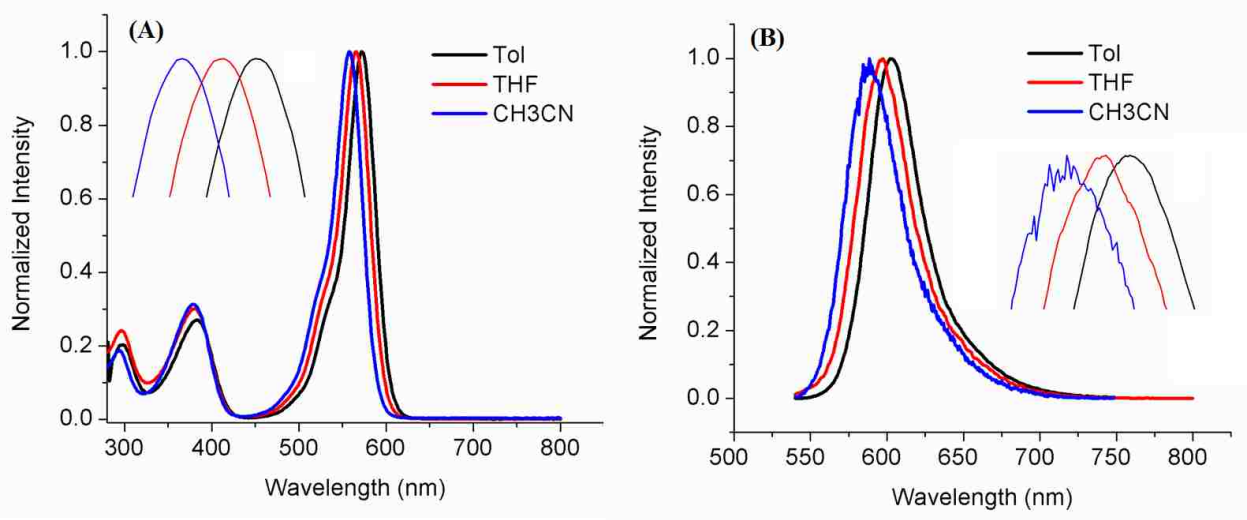

Figure 7.33. Absorbance (A) and fluorescence (B) spectra of BODIPY **2** in toluene, tetrahydrofuran and acetonitrile.

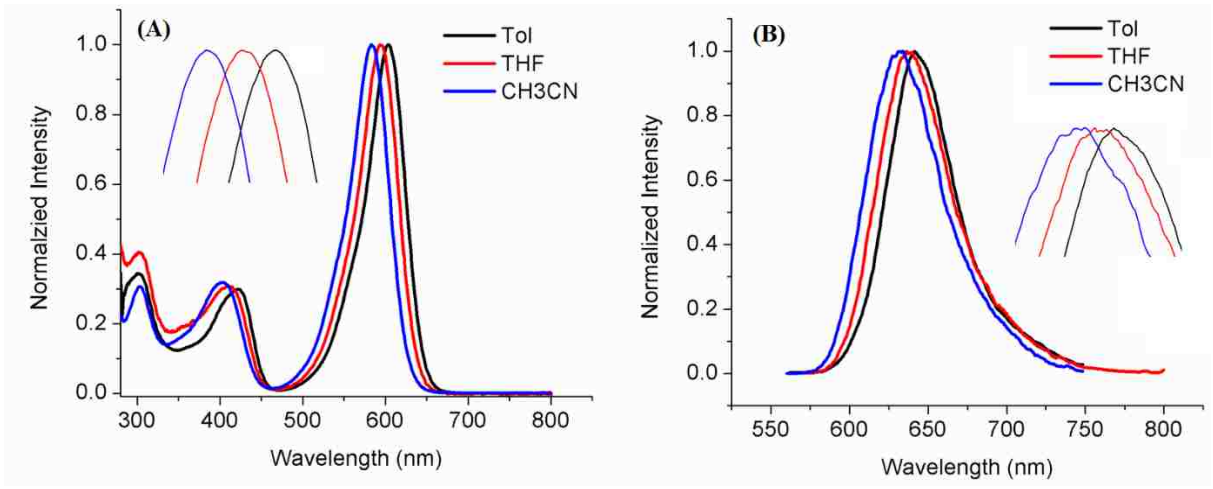

Figure 7.34. Absorbance (A) and fluorescence (B) spectra of BODIPY **6a** in toluene, tetrahydrofuran and acetonitrile.

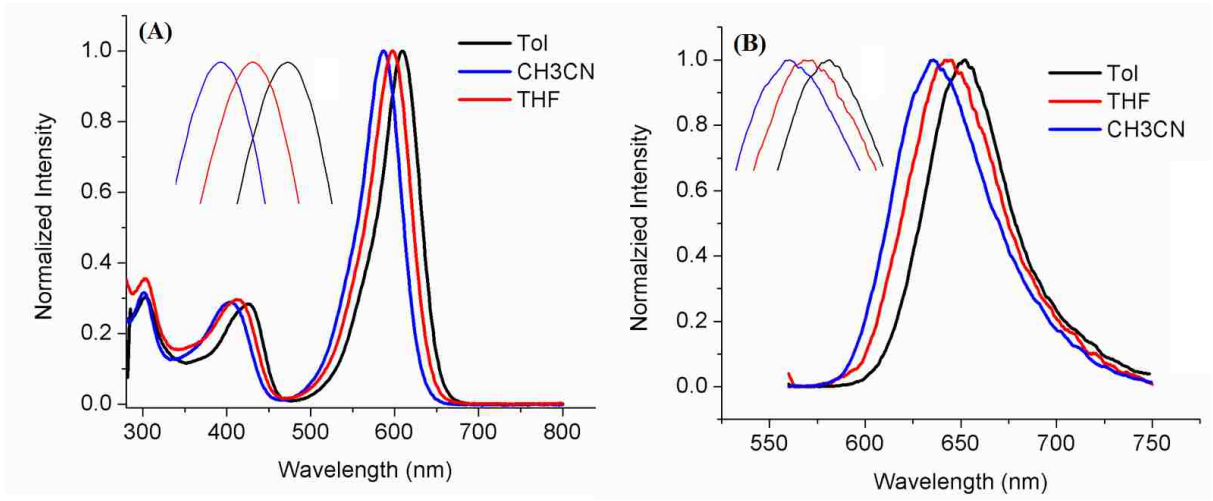

Figure 7.35. Absorbance (A) and fluorescence (B) spectra of BODIPY **6b** in toluene, tetrahydrofuran and acetonitrile.

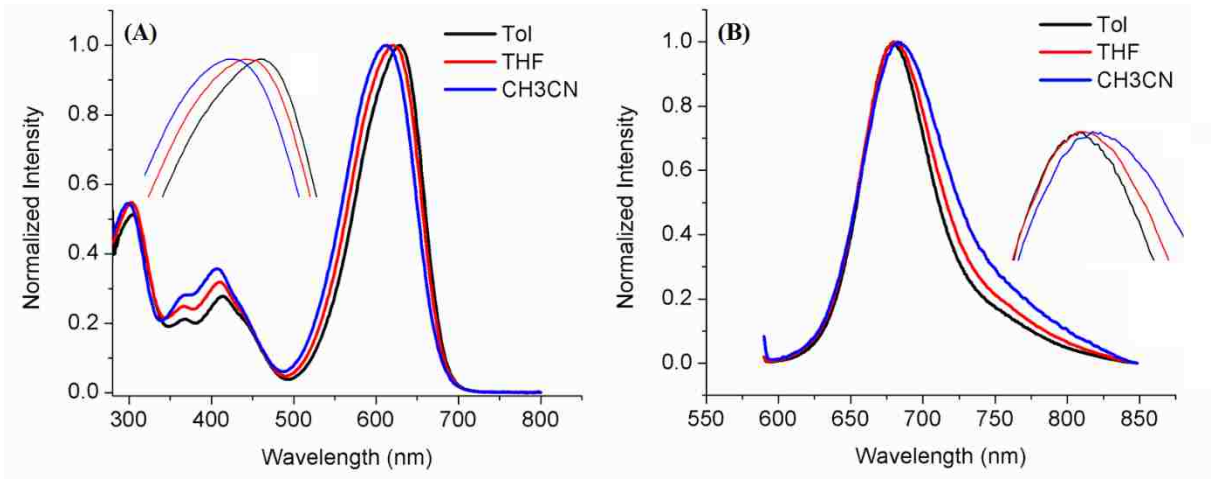

Figure 7.36. Absorbance (A) and fluorescence (B) spectra of BODIPY **3** in toluene, tetrahydrofuran and acetonitrile.

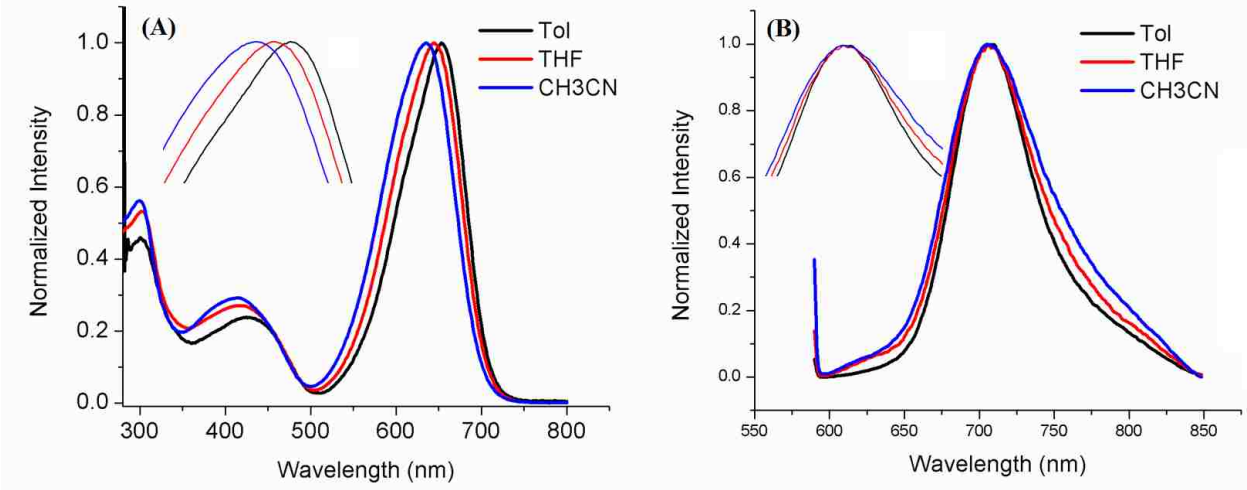

Figure 7.37. Absorbance (A) and fluorescence (B) spectra of BODIPY **7** in toluene, tetrahydrofuran and acetonitrile.

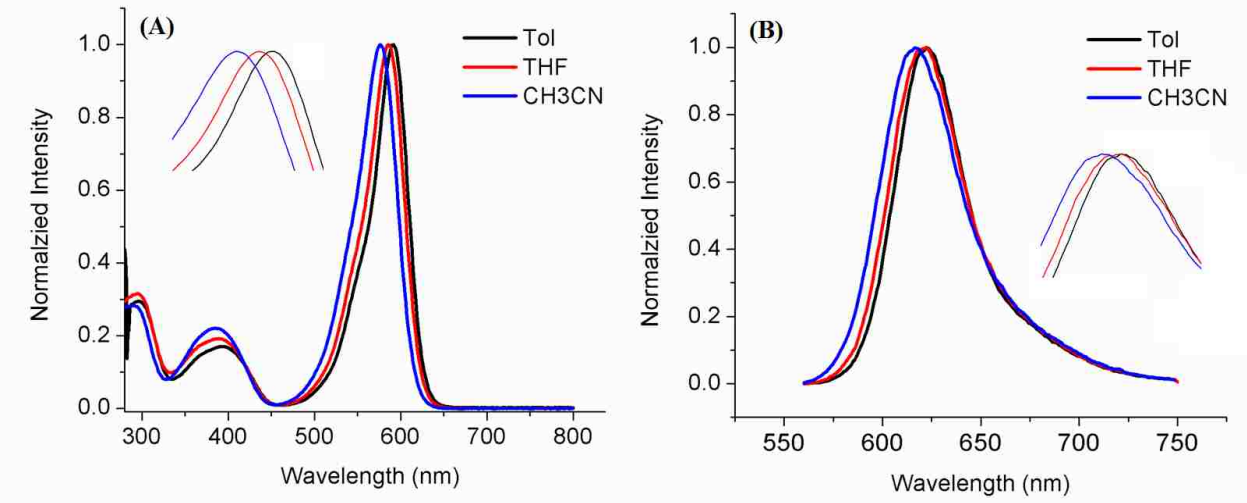

Figure 7.38. Absorbance (A) and fluorescence (B) spectra of BODIPY **4** in toluene, tetrahydrofuran and acetonitrile.

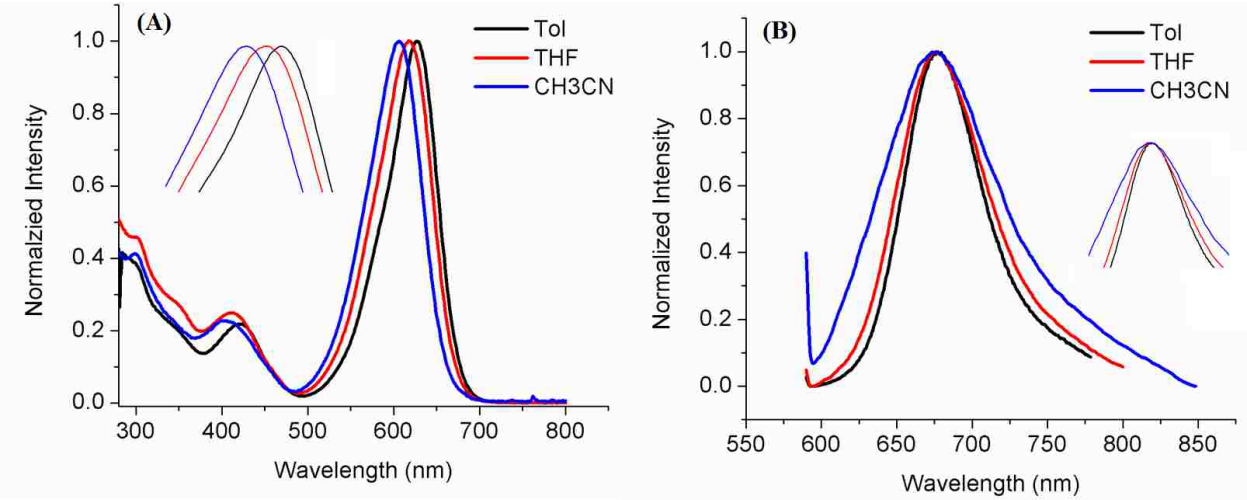

Figure 7.39. Absorbance (A) and fluorescence (B) spectra of BODIPY **8** in toluene, tetrahydrofuran and acetonitrile.

7.3.4 Cyclic voltammetry

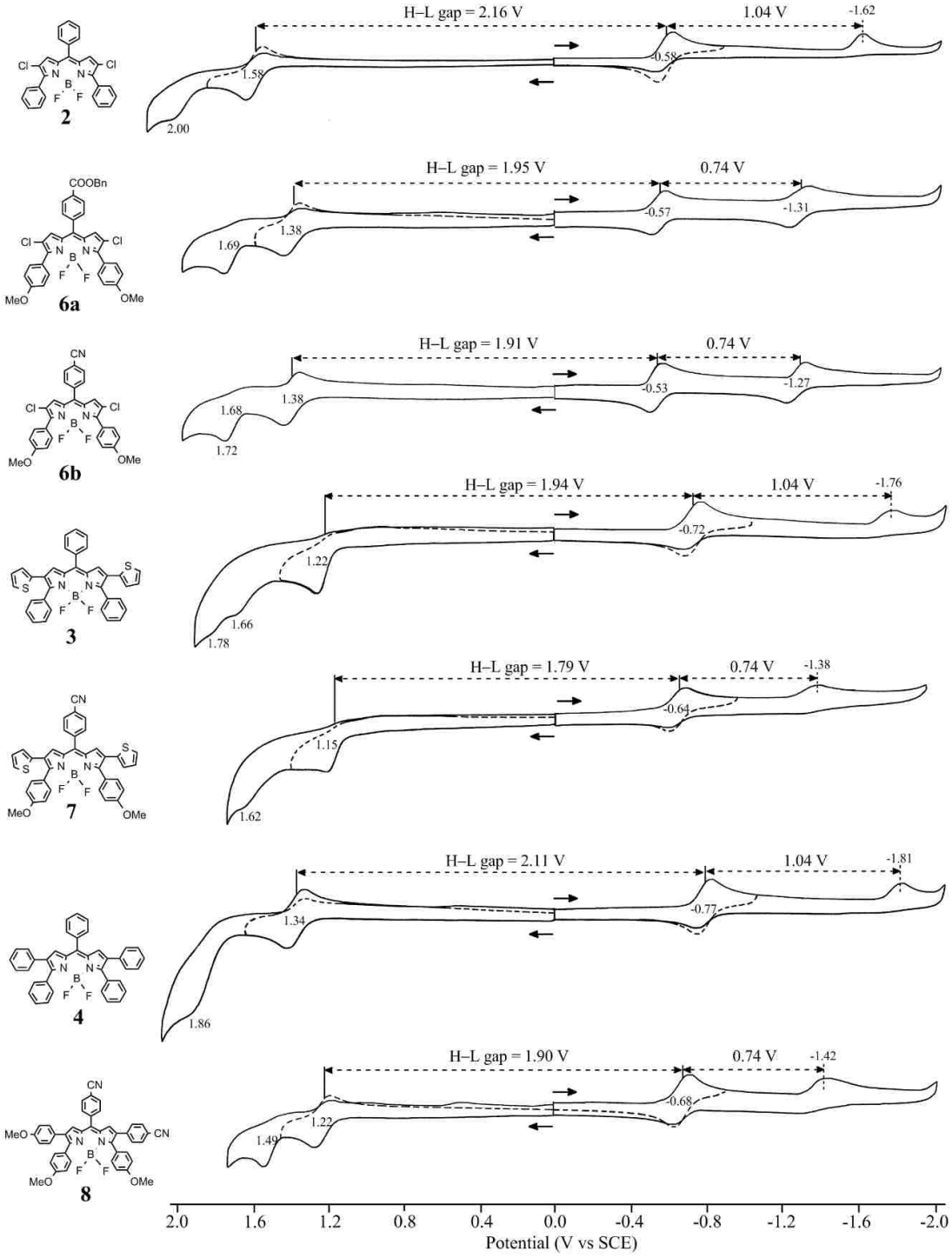

Figure 7.40. Cyclic voltammograms of BODIPY **2**, **3**, **4**, **6a**, **6b**, **7** and **8**.

Table 7.2. Oxidation and reduction potentials from cyclic voltammetry.

Cpds	Oxidation			Reduction		H-L (V)[b]
	3rd	2nd	1st	1st	2nd	
1		2.00[a]	1.58	-0.58	-1.62[a]	2.16
6a		1.69	1.38	-0.57	-1.31	1.95
6b		1.68	1.38	-0.53	-1.27	1.91
3	1.78[a]	1.66[a]	1.22	-0.72	-1.76[a]	1.94
7		1.62[a]	1.15	-0.64	-1.38[a]	1.79
4		1.86[a]	1.34	-0.77	-1.81[a]	2.11
8		1.49	1.22	-0.68	-1.42[a]	1.90

a. peak potential

b. Half-wave potential difference between 1st oxidation and 1st reduction

7.3.5 DFT calculations

To provide insights into the photophysical and electrochemical properties of the BODIPYs, DFT calculations are conducted on all the compounds and the results are summarized in Table 7.3, Figure 7.41 and 7.42, The installation of electron donating group (-MeO) and electron withdrawing group (-CN and –COOBn) to the BODIPYs caused the electron density on the HOMO and HOMO-1 shifted to the substituents bearing the electron donating groups, whereas the electron density on the LUMO and LUMO+1 shifted to the meso substituent bearing the electron withdrawing group. As a result, the overall HOMO-LUMO gap was decreased after introducing the push-pull moieties from **2** to **6a** and **6b**, **3** to **7**, and **4** to **8** (Table 7.3, Figure 7.42), which was in agreement with the spectroscopic result that the maximum λ_{ab} and λ_{em} was red-shifted after installation of push-pull moieties to the BODIPYs. The trend of the HOMO-LUMO gap (**2**> **6a** and **6b**, **3** > **7**, **4** > **8**) was consistent with the result from cyclic voltammetry (Figure 7.42).

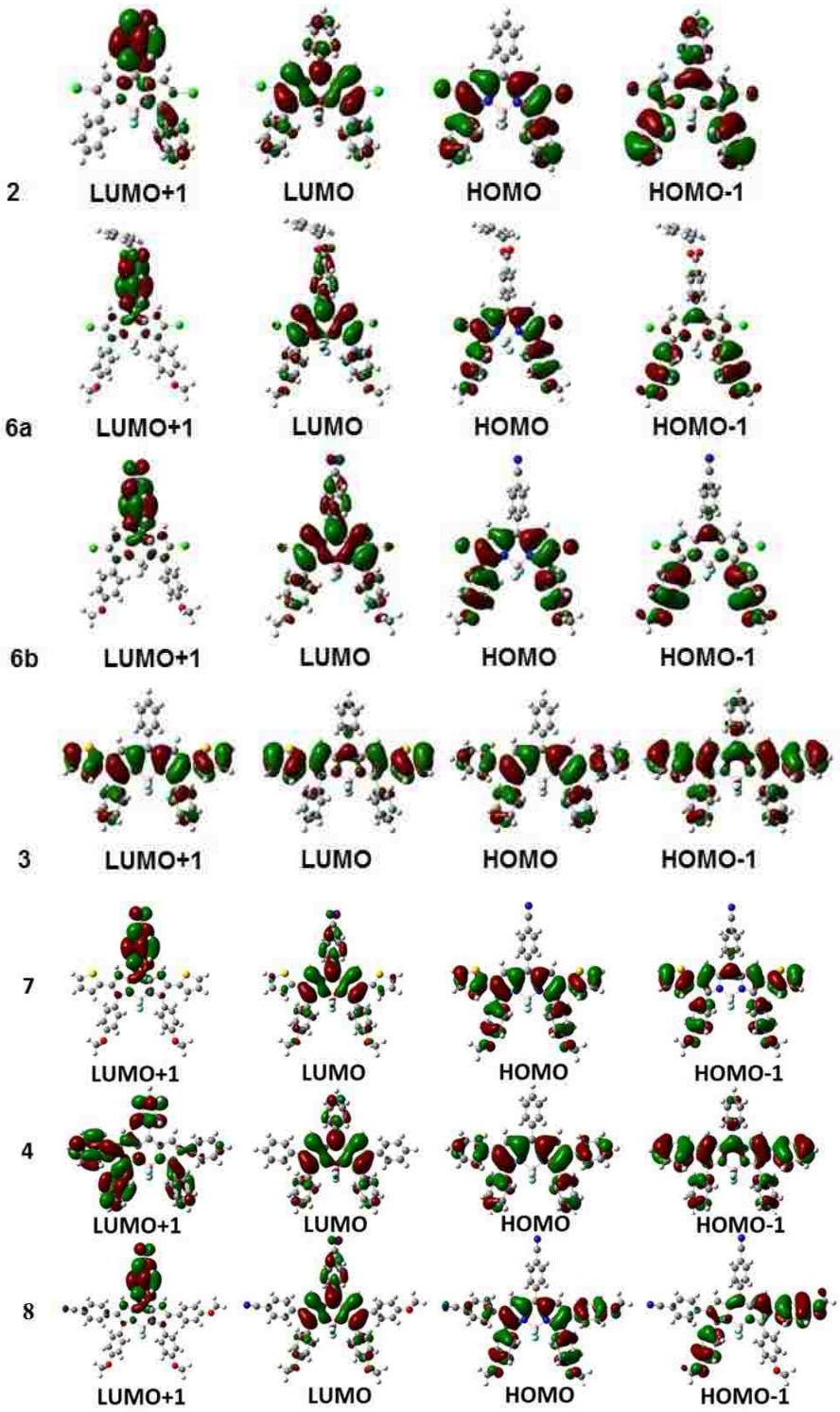

Figure 7.41. DFT calculated frontier orbitals for all the BODIPY **2**, **3**, **4**, **6a**, **6b**, **7** and **8** (B3LYP/6-31G(d)).

Table 7.3. DFT calculated molecular orbital energy levels for the BODIPYs.

Cpds	E_{HOMO} (ev)	E_{LUMO} (ev)	[a]ΔE (ev)
2	-5.83	-3.25	2.58
6a	-5.32	-2.94	2.37
6b	-5.45	-3.13	2.32
3	-5.18	-2.78	2.40
7	-5.13	-2.92	2.21
4	-5.26	-2.71	2.55
8	-5.29	-2.71	2.27

[a]$\Delta E = E_{LUMO} - E_{HOMO}$

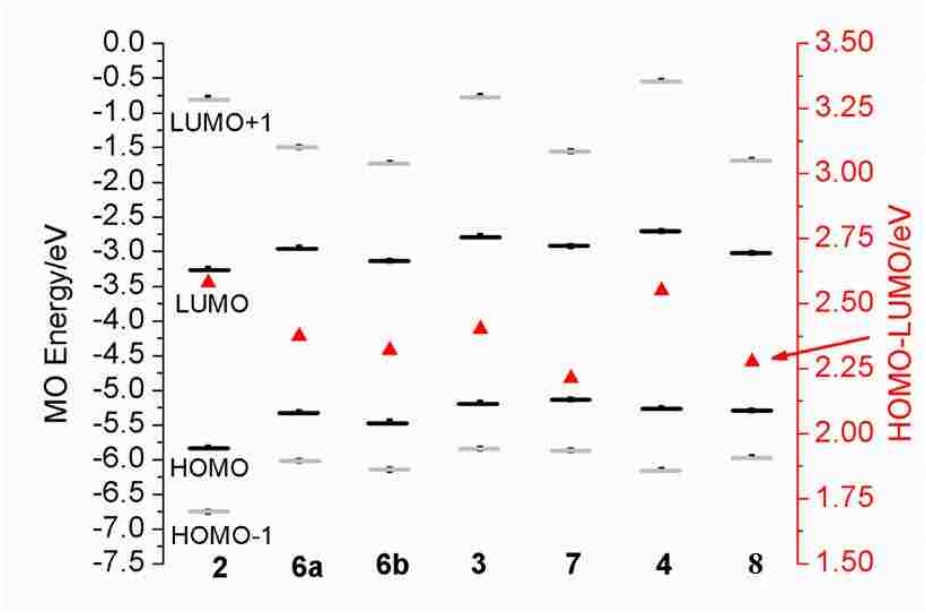

Figure 7.42. Molecular orbital energies of BODIPYs in DFT calculations. The HOMO-LUMO gaps are plotted against a secondary axis and are denoted by red triangles.

7.3.6 Cytotoxicity and uptake in human HEp2 cells

The concentration-dependent dark and phototoxicity (1.5 J/cm^2 light dose) and the time-dependent cellular uptake of all the BODIPYs were evaluated in HEp2 cells, and the results were summarized in Table 7.4, Figure 7.43 and 7.44. These results were obtained in collaboration with Ms. Zehua Zhou. All of the BODIPYs showed minimum both dark toxicity (IC_{50} > 200 μM) and phototoxicity (IC_{50} > 100 μM). All the BODIPYs, with the exception of **2** and **8**, were taken up

nearly linearly with time. BODIPY **2** and **8** were taken up rapidly in the first 2 h after which slower uptake was observed and in the case of **8** a plateau was reached after 8 h. BODIPY **3**, **5**, **6a**, and **7** exhibited very low uptake in HEp2 cells, which could be due to their poor water solubility. The higher cellular uptake of **6b** and **8** compared to other compounds probably was due to the introduction of –MeO and –CN groups which enhance their water solubility. It's interesting that BODIPY **2** accumulated the most within cells at 24 hours, probably as a result of its lower MW and favorable lipophilicity.

Table 7.4. Dark and phototoxicity and cellular uptake of BODIPYs using human HEp2 cells.

Cpds	Dark toxicity IC_{50} (μM)	Phototoxicity IC_{50} (μM)	Cellular uptake at 24 h (nM/cell)
2	>200	>100	1.2±0.10
6a	>200	>100	0.14±0.01
6b	>200	>100	0.51±0.01
3	>200	>100	0.14±0.01
7	>200	>100	0.12±0.01
5	>200	>100	0.058±0.028
8	>200	>100	0.79±0.13

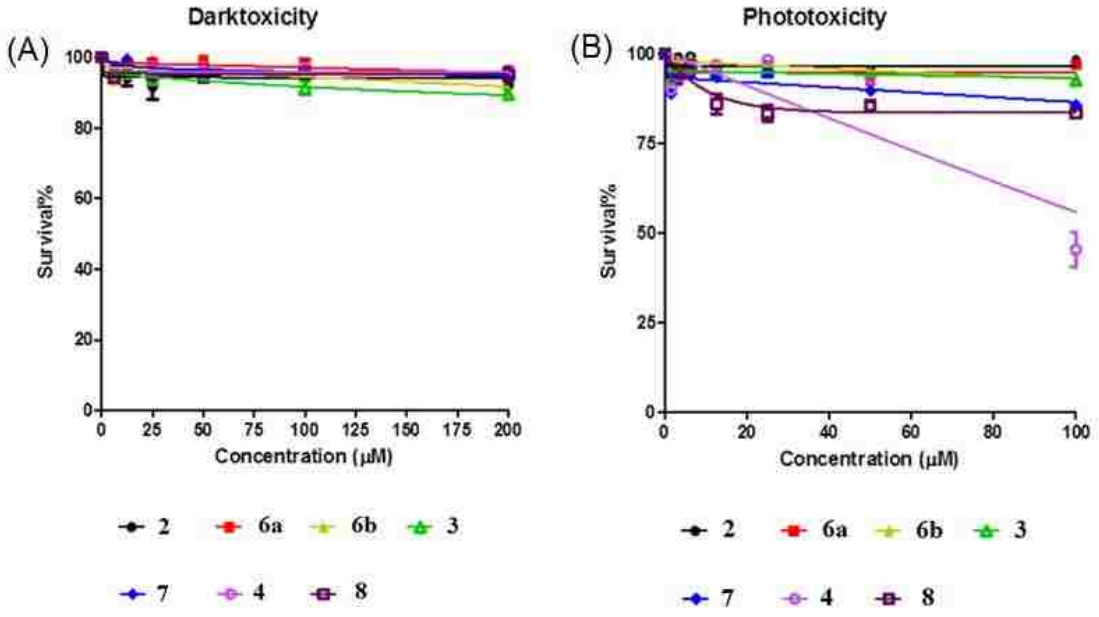

Figure 7.43. Concentration dependent dark toxicity (A) and phototoxicity (1.5 J/cm^2 light dose) (B) of BODIPYs in human HEp 2 cells.

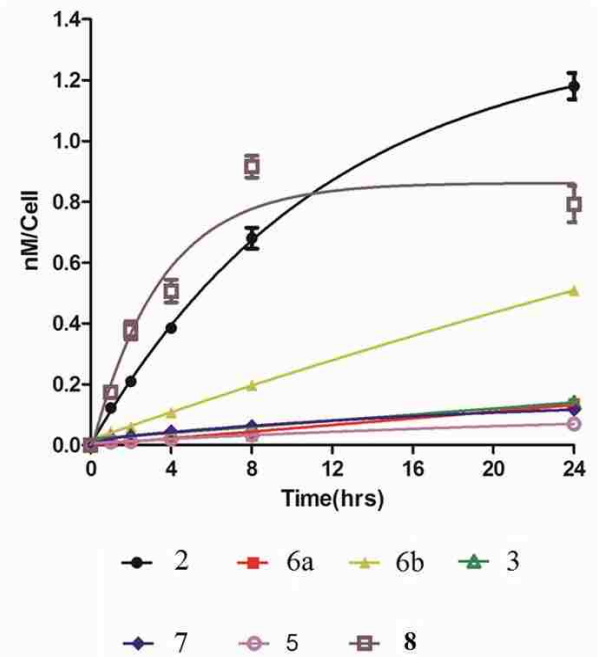

Figure 7.44. Time-dependent uptake of BODIPYs **2** (black), **6a** (red), **6b** (yellow), **3** (green), **5** (pink), **7** (navy) and **8** (brown) in human HEp2 cells.

7.4 Conclusion

A series of push-pull BODIPYs were synthesized in good yields by facile Suzuki and Stille-cross coupling reactions from 2,3,5,6,8-penta-chloro-BODIPY. The structures of all the compounds were characterized by HRMS, NMR, and X-ray crystallography (except for BODIPY **3**). A systematic comparison was made before and after installation of electron-withdrawing and electron-donating group to the BODIPYs to investigate the influence of push-pull effect on their spectroscopic and electrochemical properties. Bathochromic shift was observed for both absorbance (up to 37 nm) and emission (up to 60 nm) in different solvents after the installation of electron donor (-MeO) and acceptor (-CN and –COOBn). This result was in agreement with the DFT calculation that the HOMO-LUMO energy was decreased with the installation of push-pull moieties. The trend of the HOMO-LUMO energy (**2** > **6a** and **6b**, **3** > **7**, **4** > **8**) was consistent with the HOMO-LUMO trends obtained from cyclic voltammetry. BODIPY **4** bearing thiophene

groups at 2 and 6 positions exhibited the longest λ_{max} for absorption (635-653 nm) and emission (706-707 nm) and the largest Stokes shift (54-71 nm). The quantum yield was decreased up to 48 fold after introducing the push-pull moieties and was probably due to ICT between donor and acceptor and the internal conversion. All BODIPYs tested showed minimum dark (IC_{50} > 200 μM) and phototoxicity (IC_{50} > 100 μM) in human HEp2 cells. BODIPY **3**, **5**, **6a** and **7** displayed very low cellular uptake and was probably due to their poor water solubility. BODIPY **6b** and **8** showed higher cellular uptake, which could be attributed to the enhanced water solubility with the –MeO and –CN groups. It's interesting that BODIPY **2** accumulated the most within cells at 24 hours, probably as a result of its lower MW. The systematic investigation of these push-pull BODIPYs on their spectroscopic and electrochemical properties may provide guidance for the future design of new BODIPYs for different uses.

7.5 Reference

1. Li, J.; Liu, D.; Hong, Z.; Tong, S.; Wang, P.; Ma, C.; Lengyel, O.; Lee, C.-S.; Kwong, H.-L.; Lee, S. A New Family of Isophorone-Based Dopants for Red Organic Electroluminescent Devices. *Chem. Mater.* **2003,** *15* (7), 1486-1490.

2. Pawlicki, M.; Collins, H. A.; Denning, R. G.; Anderson, H. L. Two-Photon Absorption and the Design of Two-Photon Dyes. *Angew. Chem. Int. Ed.* **2009,** *48* (18), 3244-3266.

3. Reinhardt, B. A.; Brott, L. L.; Clarson, S. J.; Dillard, A. G.; Bhatt, J. C.; Kannan, R.; Yuan, L.; He, G. S.; Prasad, P. N. Highly Active Two-Photon Dyes: Design, Synthesis, and Characterization toward Application. *Chem. Mater.* **1998,** *10* (7), 1863-1874.

4. Ren, X.; Jiang, S.; Cha, M.; Zhou, G.; Wang, Z.-S. Thiophene-Bridged Double D-π-A Dye for Efficient Dye-Sensitized Solar Cell. *Chem. Mater.* **2012,** *24* (17), 3493-3499.

5. Higashino, T.; Imahori, H. Porphyrins as excellent dyes for dye-sensitized solar cells: recent developments and insights. *Dalton Trans.* **2015,** *44* (2), 448-463.

6. Hagfeldt, A.; Boschloo, G.; Sun, L.; Kloo, L.; Pettersson, H. Dye-Sensitized Solar Cells. *Chem. Rev.* **2010,** *110* (11), 6595-6663.

7. Trukhina, O.; Rudolf, M.; Bottari, G.; Akasaka, T.; Echegoyen, L.; Torres, T.; Guldi, D. M. Bidirectional Electron Transfer Capability in Phthalocyanine–Sc3N@Ih–C80 Complexes. *J. Am. Chem. Soc.* **2015,** *137* (40), 12914-12922.

8. Chou, H.-H.; Reddy, K. S. K.; Wu, H.-P.; Guo, B.-C.; Lee, H.-W.; Diau, E. W.-G.; Hsu, C.-P.; Yeh, C.-Y. Influence of Phenylethynylene of Push–Pull Zinc Porphyrins on the Photovoltaic Performance. *ACS Appl. Mater. Interfaces* **2016,** *8* (5), 3418-3427.

9. Mai, C.-L.; Moehl, T.; Hsieh, C.-H.; Décoppet, J.-D.; Zakeeruddin, S. M.; Grätzel, M.; Yeh, C.-Y. Porphyrin Sensitizers Bearing a Pyridine-Type Anchoring Group for Dye-Sensitized Solar Cells. *ACS Appl. Mater. Interfaces* **2015,** *7* (27), 14975-14982.

10. Yella, A.; Mai, C.-L.; Zakeeruddin, S. M.; Chang, S.-N.; Hsieh, C.-H.; Yeh, C.-Y.; Grätzel, M. Molecular Engineering of Push–Pull Porphyrin Dyes for Highly Efficient Dye-Sensitized Solar Cells: The Role of Benzene Spacers. *Angew. Chem. Int. Ed.* **2014,** *53* (11), 2973-2977.

11. Ripolles-Sanchis, T.; Guo, B.-C.; Wu, H.-P.; Pan, T.-Y.; Lee, H.-W.; Raga, S. R.; Fabregat-Santiago, F.; Bisquert, J.; Yeh, C.-Y.; Diau, E. W.-G. Design and characterization of alkoxy-wrapped push-pull porphyrins for dye-sensitized solar cells. *Chem. Commun.* **2012,** *48* (36), 4368-4370.

12. Kang, M. S.; Kang, S. H.; Kim, S. G.; Choi, I. T.; Ryu, J. H.; Ju, M. J.; Cho, D.; Lee, J. Y.; Kim, H. K. Novel D-π-A structured Zn(II)-porphyrin dyes containing a bis(3,3-dimethylfluorenyl)amine moiety for dye-sensitised solar cells. *Chem. Commun.* **2012,** *48* (75), 9349-9351.

13. Maufroy, A.; Favereau, L.; Anne, F. B.; Pellegrin, Y.; Blart, E.; Hissler, M.; Jacquemin, D.; Odobel, F. Synthesis and properties of push-pull porphyrins as sensitizers for NiO based dye-sensitized solar cells. *J. Mater. Chem. A* **2015,** *3* (7), 3908-3917.

14. Loudet, A.; Burgess, K. BODIPY Dyes and Their Derivatives: Syntheses and Spectroscopic Properties. *Chem. Rev.* **2007,** *107* (11), 4891-4932.

15. Boens, N.; Leen, V.; Dehaen, W. Fluorescent indicators based on BODIPY. *Chem. Soc. Rev.* **2012,** *41* (3), 1130-1172.

16. Lu, H.; Mack, J.; Yang, Y.; Shen, Z. Structural modification strategies for the rational design of red/NIR region BODIPYs. *Chem. Soc. Rev.* **2014,** *43* (13), 4778-4823.

17. Yuan, L.; Lin, W.; Zheng, K.; He, L.; Huang, W. Far-red to near infrared analyte-responsive fluorescent probes based on organic fluorophore platforms for fluorescence imaging. *Chem. Soc. Rev.* **2013,** *42* (2), 622-661.

18. Kowada, T.; Maeda, H.; Kikuchi, K. BODIPY-based probes for the fluorescence imaging of biomolecules in living cells. *Chem. Soc. Rev.* **2015,** *44* (14), 4953-4972.

19. Bessette, A.; Hanan, G. S. Design, synthesis and photophysical studies of dipyrromethene-based materials: insights into their applications in organic photovoltaic devices. *Chem. Soc. Rev.* **2014,** *43* (10), 3342-3405.

20. Kaur, N.; Kaur, P.; Singh, K. Ferrocene-BODIPY Push–Pull dyad: A common platform for the sensing of Hg2+ and Cr3+. *Sensors Actuators B: Chem.* **2016,** *229*, 499-505.

21. Flores-Rizo, J. O.; Esnal, I.; Osorio-Martínez, C. A.; Gómez-Durán, C. F. A.; Bañuelos, J.; López Arbeloa, I.; Pannell, K. H.; Metta-Magaña, A. J.; Peña-Cabrera, E. 8-Alkoxy- and 8-Aryloxy-BODIPYs: Straightforward Fluorescent Tagging of Alcohols and Phenols. *J. Org. Chem.* **2013,** *78* (12), 5867-5877.

22. Zhao, Y.; Lv, X.; Liu, Y.; Liu, J.; Zhang, Y.; Shi, H.; Guo, W. The emission enhancement of the NIR distyryl Bodipy dyes by the indirect S0 [rightward arrow] S2 excitation and their application towards a Hg2+ probe. *J. Mater. Chem.* **2012,** *22* (23), 11475-11478.

23. Ziessel, R.; Retailleau, P.; Elliott, K. J.; Harriman, A. Boron Dipyrrin Dyes Exhibiting "Push–Pull–Pull" Electronic Signatures. *Chem. Eur. J.* **2009,** *15* (40), 10369-10374.

24. Niu, S.; Ulrich, G.; Retailleau, P.; Ziessel, R. BODIPY-bridged push–pull chromophores: optical and electrochemical properties. *Tetrahedron Lett.* **2011,** *52* (38), 4848-4853.

25. Shi, W.-J.; Lo, P.-C.; Singh, A.; Ledoux-Rak, I.; Ng, D. K. P. Synthesis and second-order nonlinear optical properties of push-pull BODIPY derivatives. *Tetrahedron* **2012,** *68* (42), 8712-8718.

26. Ulrich, G.; Barsella, A.; Boeglin, A.; Niu, S.; Ziessel, R. BODIPY-Bridged Push–Pull Chromophores for Nonlinear Optical Applications. *Chemphyschem* **2014,** *15* (13), 2693-2700.

27. Erten-Ela, S.; Yilmaz, M. D.; Icli, B.; Dede, Y.; Icli, S.; Akkaya, E. U. A Panchromatic Boradiazaindacene (BODIPY) Sensitizer for Dye-Sensitized Solar Cells. *Org. Lett.* **2008,** *10* (15), 3299-3302.

28. Kolemen, S.; Cakmak, Y.; Erten-Ela, S.; Altay, Y.; Brendel, J.; Thelakkat, M.; Akkaya, E. U. Solid-State Dye-Sensitized Solar Cells Using Red and Near-IR Absorbing Bodipy Sensitizers. *Org. Lett.* **2010,** *12* (17), 3812-3815.

29. Sutter, A.; Retailleau, P.; Huang, W.-C.; Lin, H.-W.; Ziessel, R. Photovoltaic performance of novel push-pull-push thienyl-Bodipy dyes in solution-processed BHJ-solar cells. *New J. Chem.* **2014,** *38* (4), 1701-1710.

30. Bonnier, C.; Machin, D. D.; Abdi, O.; Koivisto, B. D. Manipulating non-innocent π-spacers: the challenges of using 2,6-disubstituted BODIPY cores within donor-acceptor light-harvesting motifs. *Org. Biomol. Chem.* **2013,** *11* (22), 3756-3760.

31. Didier, P.; Ulrich, G.; Mely, Y.; Ziessel, R. Improved push-pull-push E-Bodipy fluorophores for two-photon cell-imaging. *Org. Biomol. Chem.* **2009,** *7* (18), 3639-3642.

32. Wang, Y.; Chen, L.; El-Shishtawy, R. M.; Aziz, S. G.; Mullen, K. Synthesis and optophysical properties of dimeric aza-BODIPY dyes with a push-pull benzodipyrrolidone core. *Chem. Commun.* **2014,** *50* (78), 11540-11542.

33. Nano, A.; Ziessel, R.; Stachelek, P.; Harriman, A. Charge-Recombination Fluorescence from Push–Pull Electronic Systems Constructed around Amino-Substituted Styryl–BODIPY Dyes. *Chem. Eur. J.* **2013,** *19* (40), 13528-13537.

34. Jiao, L.; Wu, Y.; Wang, S.; Hu, X.; Zhang, P.; Yu, C.; Cong, K.; Meng, Q.; Hao, E.; Vicente, M. G. H. Accessing Near-Infrared-Absorbing BF2-Azadipyrromethenes via a Push–Pull Effect. *J. Org. Chem.* **2014,** *79* (4), 1830-1835.

35. Zhao, N.; Xuan, S.; Fronczek, F. R.; Smith, K. M.; Vicente, M. G. H. Stepwise Polychlorination of 8-Chloro-BODIPY and Regioselective Functionalization of 2,3,5,6,8-Pentachloro-BODIPY. *J. Org. Chem.* **2015,** *80* (16), 8377-8383.

36. Wang, H.; Vicente, M. G. H.; Fronczek, F. R.; Smith, K. M. Synthesis and Transformations of 5-Chloro-2,2′-Dipyrrins and Their Boron Complexes, 8-Chloro-BODIPYs. *Chem. Eur. J.* **2014,** *20* (17), 5064-5074.

37. Zhao, N.; Vicente, M. G. H.; Fronczek, F. R.; Smith, K. M. Synthesis of 3,8-Dichloro-6-ethyl-1,2,5,7-tetramethyl–BODIPY from an Asymmetric Dipyrroketone and Reactivity Studies at the 3,5,8-Positions. *Chem. Eur. J.* **2015,** *21* (16), 6181-6192.

38. Jinadasa, R. G. W.; Fang, Y.; Kumar, S.; Osinski, A. J.; Jiang, X.; Ziegler, C. J.; Kadish, K. M.; Wang, H. β-Functionalized Push–Pull opp-Dibenzoporphyrins. *J. Org. Chem.* **2015**.

39. Frisch, M. J. e. a. *Gaussian 09*, Revision B.01; Gaussian Inc. : Wallingford, CT, 2010.

40. Xuan, S.; Zhao, N.; Zhou, Z.; Fronczek, F. R.; Vicente, M. G. H. Synthesis and in Vitro Studies of a Series of Carborane-Containing Boron Dipyrromethenes (BODIPYs). *J. Med. Chem.* **2016,** *59* (5), 2109-2117.

41. Priestley, E. S.; De Lucca, I.; Zhou, J.; Zhou, J.; Saiah, E.; Stanton, R.; Robinson, L.; Luettgen, J. M.; Wei, A.; Wen, X.; Knabb, R. M.; Wong, P. C.; Wexler, R. R. Discovery and gram-scale synthesis of BMS-593214, a potent, selective FVIIa inhibitor. *Biorg. Med. Chem. Lett.* **2013,** *23* (8), 2432-2435.

42. Ishiyama, T.; Ishida, K.; Miyaura, N. Synthesis of pinacol arylboronates via cross-coupling reaction of bis(pinacolato)diboron with chloroarenes catalyzed by palladium(0)–tricyclohexylphosphine complexes. *Tetrahedron* **2001,** *57* (49), 9813-9816.

43. Wang, H.; Fronczek, F. R.; Vicente, M. G. H.; Smith, K. M. Functionalization of 3,5,8-Trichlorinated BODIPY Dyes. *J. Org. Chem.* **2014,** *79* (21), 10342-10352.

44. Hansch, C.; Leo, A.; Taft, R. W. A survey of Hammett substituent constants and resonance and field parameters. *Chem. Rev.* **1991,** *91* (2), 165-195.

45. Chen, Y.; Zhao, J.; Guo, H.; Xie, L. Geometry Relaxation-Induced Large Stokes Shift in Red-Emitting Borondipyrromethenes (BODIPY) and Applications in Fluorescent Thiol Probes. *J. Org. Chem.* **2012,** *77* (5), 2192-2206.

46. Chen, Y.; Zhao, J.; Xie, L.; Guo, H.; Li, Q. Thienyl-substituted BODIPYs with strong visible light-absorption and long-lived triplet excited states as organic triplet sensitizers for triplet-triplet annihilation upconversion. *RSC Advances* **2012,** *2* (9), 3942-3953.

47. Reichardt, C. Solvatochromic Dyes as Solvent Polarity Indicators. *Chem. Rev.* **1994,** *94* (8), 2319-2358.

48. Reichardt, C.; Welton, T., Solvent Effects on the Absorption Spectra of Organic Compounds. In *Solvents and Solvent Effects in Organic Chemistry*, Wiley-VCH Verlag GmbH & Co. KGaA: 2010; pp 359-424. 10.1002/9783527632220.ch6.

49. Qin, W.; Baruah, M.; Van der Auweraer, M.; De Schryver, F. C.; Boens, N. Photophysical Properties of Borondipyrromethene Analogues in Solution. *J. Phys. Chem. A* **2005,** *109* (33), 7371-7384.

50. Lin, S. H. Energy Gap Law and Franck–Condon Factor in Radiationless Transitions. *J. Chem. Phys* **1970,** *53* (9), 3766-3767.

51. Rurack, K.; Kollmannsberger, M.; Daub, J. Molecular Switching in the Near Infrared (NIR) with a Functionalized Boron–Dipyrromethene Dye. *Angew. Chem. Int. Ed.* **2001,** *40* (2), 385-387.

52. Umezawa, K.; Matsui, A.; Nakamura, Y.; Citterio, D.; Suzuki, K. Bright, Color-Tunable Fluorescent Dyes in the Vis/NIR Region: Establishment of New "Tailor-Made" Multicolor Fluorophores Based on Borondipyrromethene. *Chem. Eur. J.* **2009,** *15* (5), 1096-1106.

COPYRIGHT RELEASES

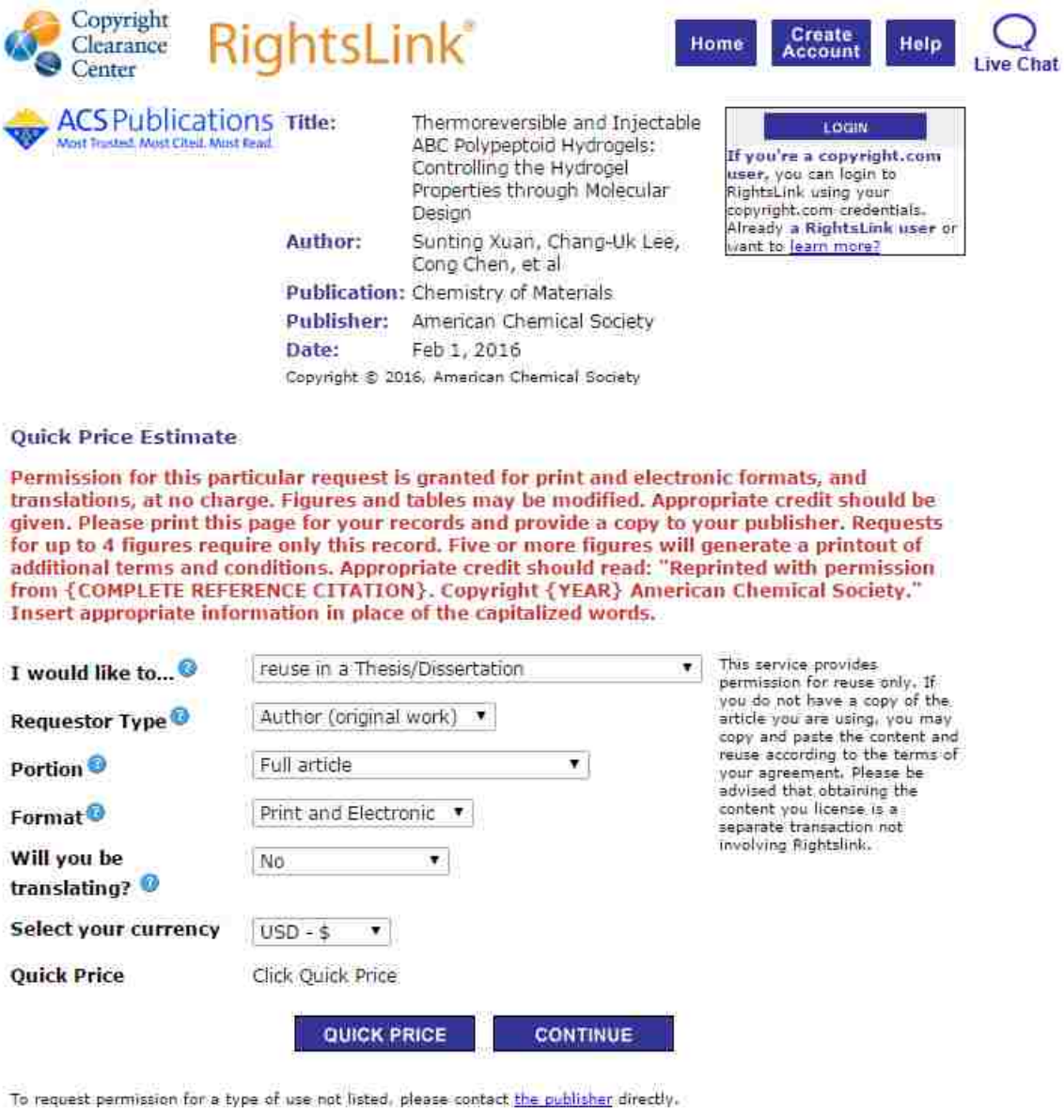

Copyright Clearance Center RightsLink

Home | Create Account | Help | Live Chat

ACS Publications
Most Trusted. Most Cited. Most Read.

Title: Thermoreversible and Injectable ABC Polypeptoid Hydrogels: Controlling the Hydrogel Properties through Molecular Design

Author: Sunting Xuan, Chang-Uk Lee, Cong Chen, et al

Publication: Chemistry of Materials

Publisher: American Chemical Society

Date: Feb 1, 2016

Copyright © 2016, American Chemical Society

LOGIN

If you're a copyright.com user, you can login to RightsLink using your copyright.com credentials. Already a RightsLink user or want to learn more?

Quick Price Estimate

Permission for this particular request is granted for print and electronic formats, and translations, at no charge. Figures and tables may be modified. Appropriate credit should be given. Please print this page for your records and provide a copy to your publisher. Requests for up to 4 figures require only this record. Five or more figures will generate a printout of additional terms and conditions. Appropriate credit should read: "Reprinted with permission from {COMPLETE REFERENCE CITATION}. Copyright {YEAR} American Chemical Society." Insert appropriate information in place of the capitalized words.

I would like to...	reuse in a Thesis/Dissertation
Requestor Type	Author (original work)
Portion	Full article
Format	Print and Electronic
Will you be translating?	No
Select your currency	USD - $
Quick Price	Click Quick Price

This service provides permission for reuse only. If you do not have a copy of the article you are using, you may copy and paste the content and reuse according to the terms of your agreement. Please be advised that obtaining the content you license is a separate transaction not involving Rightslink.

QUICK PRICE | CONTINUE

To request permission for a type of use not listed, please contact the publisher directly.

VITA

Sunting Xuan was born in Zhejiang, China. She attended Lanzhou University in Gansu, China, and received a B.S. degree in Chemistry in 2010. She then joined the graduate program in the Department of Chemistry at Miami University in Ohio in August, 2011. After one semester, she transferred from Miami University to Louisiana State University and joined the graduate program for her Ph.D. degree in the Department of Chemistry in January, 2012. She conducted graduate research under the supervision of Professor Donghui Zhang and Professor Graca Vicente, and successfully defended the Ph.D. dissertation on November 2nd, 2016.